Laser metal deposition repair of stainless steel 316L parts

Thomas Cailloux

Sorbonne Université
Nanyang Technological University

Ecole doctorale 388

LISL - CEA Paris-Saclay

MAE - NTU Singapore

Laser metal deposition repair of stainless steel 316L parts

Par Thomas CAILLOUX

Thèse de doctorat de Chimie Physique et Chimie Analytique de Paris Centre

Dirigée par Fanny BALBAUD-CELERIER et Kun ZHOU

Présentée et soutenue publiquement le 20 juin 2023

Devant un jury composé de :

Cécile LANGLADE, Professeure des universités, UTBM, LERMPS	Présidente, rapportrice
Christophe TOURNIER, Professeur des universités, ENS-PS, LURPA	Rapporteur
Oumaïma GHARBI, Chercheuse CNRS, SU, LRS	Examinatrice
Hejun DU, Professeur des universités, NTU, MAE	Examinateur
Fanny BALBAUD-CELERIER, Directrice de recherche, CEA, SCCME	Directrice de thèse
Kun ZHOU, Professeur des universités, NTU, MAE	Co-directeur de thèse
Salima BOUVIER, Professeure des universités, UTC, DIM	Invitée
Wilfried PACQUENTIN, Encadrant, CEA, LANIE	Invité
Srikanth NARASIMALU, Co-encadrant, NTU, ERIAN	Invité

Abstract

The nuclear and offshore wind industries are of great interest to meet the current challenges of producing carbon-free electrical energy in the context of the global energy and climate crisis. However, the structural materials used in these facilities are exposed to aggressive environments that damage components, limiting their lifespan and requiring their replacement. In the context of a circular economy, repair technologies make it possible to limit these replacements, thus reducing the time and costs associated with plant shutdowns. They also allow for minimizing the mineral resources required for the development of new components, as well as the carbon footprint associated with the manufacturing processes and transportation of the components. The objective of this thesis is to develop a process for the repair of metal parts that meets the following deposition criteria: dense, without cracks, with metallurgical bonding to the substrate, and imperceptible in terms of mechanical behavior and corrosion resistance. This process must ultimately be able to repair the initial defect with a return to the original dimensions without damaging the rest of the part. Laser Metal Deposition (LMD) technology, which is based on additive manufacturing, appears to be a promising way to meet these requirements. The LMD process has demonstrated its ability to repair metal parts while maintaining high deposition density and good mechanical properties. The energy provided by the laser allows the material to be fused without significantly affecting the substrate thermally, thereby avoiding distortion of the repaired part. Finally, the implementation of deposition heads on computer numerical control machines allows the repair process to be automated and to achieve a high level of precision compared to manual repair. The thesis, therefore focused on understanding and optimizing two main steps of the repair process: (i) the pre-machining to remove damaged material and (ii) the laser fused powder deposition to replace the material. An understanding of the synergy between these two steps is also essential to obtain a good quality deposit while machining a minimum volume of damage. For this purpose, a study was conducted to optimize the shape and dimensions of the machined defect. An ellipsoidal pre-machining with an opening angle of 120° and optimized deposition parameters were determined. The influence of substrate preheating,

interlayer dwell time, and different post-heat treatments on the repair was also studied. The results have allowed proposing a method to homogenize the characteristics of the repaired parts in terms of microstructure, mechanical properties, and corrosion resistance during the deposition of the material, aiming at the imperceptibility of the repair in the part. This work has also allowed the implementation of all these optimized steps in an additive/subtractive hybrid machine to demonstrate the feasibility and efficiency of this emerging technology. Repair times are thus reduced while maintaining a dense repair and slightly improving mechanical properties.

Résumé

Les industries nucléaires et éoliennes offshore présentent un intérêt majeur pour répondre aux enjeux actuels de production d'énergie électrique décarbonée dans un contexte de crise énergétique et climatique mondiale. Cependant, les matériaux de structure utilisés dans ces installations sont soumis à des environnements agressifs qui conduisent à l'endommagement des composants, limitant leurs durées de vies et nécessitant leur remplacement. Dans un contexte d'économie circulaire, les technologies de réparation permettent de limiter ces remplacements, diminuant ainsi les temps et coûts liés aux arrêts des installations. Elles permettent également de minimiser les ressources minérales nécessaires à l'élaboration de nouveaux composants ainsi que l'empreinte carbone liée aux procédés de fabrication et au transport des composants. L'objectif de cette thèse est de développer un procédé de réparation de pièces métalliques qui respecte les critères de déposition suivants : dense, sans fissures, avec une liaison métallurgique avec le substrat, imperceptible en termes de comportement mécanique et de résistance à la corrosion. Ce procédé doit in fine permettre de réparer le défaut initial avec un retour aux dimensions d'origine, sans endommager le reste de la pièce. Pour respecter ce cahier des charges, la technologie Laser Metal Deposition (LMD) issue de la fabrication additive apparait prometteuse. Le procédé LMD a en effet démontré sa capacité à réparer des pièces métalliques en conservant une haute densité de déposition et de bonnes propriétés mécaniques. L'énergie apportée par le laser permet de fondre le matériau d'apport sans sensiblement affecter thermiquement le substrat, évitant les distorsions de la pièce réparée. Enfin, l'implantation des têtes de déposition sur des machines à contrôle numérique permet d'automatiser le procédé de réparation et d'avoir une haute précision en comparaison d'une réparation manuelle. La thèse s'est donc focalisée sur la compréhension et l'optimisation de deux grandes étapes du procédé de réparation : (i) le pré-usinage pour l'enlèvement de matière endommagée et (ii) le dépôt de poudres fondues par laser pour remplacer la matière. La compréhension de la synergie entre ces deux étapes est également essentielle pour obtenir des dépôts de bonne qualité en usinant un volume endommagé minimum. Pour cela une étude a permis d'optimiser la forme

et les dimensions du défaut usiné, un pré-usinage ellipsoïdal avec un angle d'ouverture de 120° et des paramètres de déposition optimisés a ainsi été déterminé. Les travaux de thèse ont également investigué l'influence du préchauffage du substrat, du temps d'attente intercouche et de différents post-traitements thermiques sur la réparation. Ils ont ainsi permis de proposer une méthode pour homogénéiser les caractéristiques des pièces réparées en terme de microstructure, propriétés mécaniques et résistance à la corrosion lors du dépôt de matière pour viser l'imperceptibilité de la réparation dans la pièce. Ces travaux ont également permis de mettre en œuvre l'ensemble de ces étapes optimisées dans une machine hybride additive/soustractive pour démontrer la faisabilité et l'efficacité de cette technologie émergente. Les temps de réparation sont ainsi réduits tout en conservant une réparation dense et en améliorant légèrement les propriétés mécaniques.

À mes parents et à ma fiancée Margaux,

Acknowledgements

Cette thèse a été réalisée au CEA à Paris-Saclay au sein du LISL pendant deux ans et demi et à NTU à Singapour au sein de MAE pendant un an. Je souhaite remercier Hicham MASKROT, Lionel GOSMAIN, et Frédéric SCHUSTER pour leurs aides et leurs appuis afin de mener à bien cette thèse.

Je tiens à remercier mes deux directeurs de thèse, Fanny BALBAUD et Kun ZHOU, de m'avoir permis de réaliser ce projet et pour la confiance qu'ils m'ont accordé pendant ce parcours. Je souhaite également remercier mes encadrants, Srikanth NARASIMALU et Wilfried PACQUENTIN pour sa disponibilité permanente, et ses précieux conseils.

Je remercie l'ensemble des membres du jury de thèse pour leurs remarques pertinentes et les échanges scientifiques le jour de ma soutenance. J'exprime ma plus grande reconnaissance envers Cécile LANGLADE et Christophe TOURNIER pour avoir rapporté mon travail de thèse et pour leur qualité de relecture. Je remercie les examinateurs Oumaïma GHARBI et Hejun DU d'avoir évalué mon travail de thèse, ainsi que Salima BOUVIER pour ces remarques pertinentes lors de ma soutenance.

Je remercie l'ensemble du personnel du LISL et de MAE pour leur accueil, leur aide et leur bonne humeur quotidienne. Merci à tous les permanents, doctorants et stagiaires du LISL et de MAE avec qui j'ai pu partager cette aventure : Gautier, Vincent, Timothée, Quentin, Ulysse, Angélique, Florent, Christina, Nicolas, Alexandre, Jérôme, Clément, Cécile, Marion, Théo, Ayse, Chengcheng, Desmond et Yung.

Un grand merci à toi Vincent, qui m'a initié à la fabrication additive dès le début de ma thèse et avec qui j'ai passé de longues journées à démonter, analyser, réparer et remonter cette machine OPTOMEC qui sera notre outil de travail récalcitrant mais formidable. Un grand merci à toi aussi Timothée, cher roommate, pour toutes ces discussions scientifiques et moins scientifiques et les soirées Call of bloqués au Puzzle pendant les confinements. Merci à toi aussi Pouille pour nos bons moments de rigolade et de me souvenir de la force de notre formation d'ingénierie de Besac. Et merci à Desmond pour m'avoir fait découvrir la culture singapourienne et avec qui j'ai pu apprendre à utiliser le procédé hybride.

Enfin, je souhaiterais énormément remercier toute ma famille et en particulier mes parents, qui m'ont toujours soutenu en permanence dans mes études et mes loisirs et qui m'ont permis d'aboutir à cette conclusion de mon parcours universitaire. Je tiens également à te remercier Margaux, ma future épouse, d'avoir toujours été là avec un soutien constant dans les bons et les mauvais moments et sans qui tout ceci n'aurait même pas débuté si tu ne m'avais pas motivé à réaliser ce rêve. Saches que cela n'aurait pas été pareil sans toi.

Merci à vous tous d'avoir fait en sorte que j'aille au bout de ce parcours.

Contents

List of Figures

List of Tables

Acronyms

AM Additive Manufacturing.

ASHM Additive/Subtractive Hybrid Manufacturing.

BJ Binder Jetting.

CAD Computer Aided Design.

CAM Computed Aided Manufacturing.

CAS Cellular Arm Spacing.

CEA Commissariat à l'énergie atomique et aux énergies alternatives.

CNC Computer Numerical Control.

CR Cooling Rate.

DDC Ductility Dip Cracking.

DED Directed Energy Deposition.

DOE Design of Experiments.

EAB Elongation At Break.

EBSD Electron BackScattered Diffraction.

EDS Energy Dispersive X-ray Spectroscopy.

FCP Free Corrosion Potential.

FZ Fusion Zone.

GDMS Glow Discharge Mass Spectrometry.

GED Global Energy Density.

GMAW Gas Metal Arc Welding.

HAZ Heat Affected Zone.

ICP-AES Inductively Coupled Plasma Atomic Emission Spectrometry.

IPF Inverse Pole Figure.

LENS Laser Engineered Net Shaping.

LISL Laboratoire d'Ingénierie des Surfaces et Lasers.

LMD Laser Metal Deposition.

LPM Linear Powder Mass.

LSP Laser Shock Peening.

MAE School of Mechanical and Aerospace Engineering.

MIC Microbiologically Influenced Corrosion.

MZ Mixed Zone.

NTU Nanyang Technological University.

OM Optical Microscopy.

PBF Powder Bed Fusion.

PREN Pitting Resistance Equivalent Number.

SAW Submerged Arc Welding.

SC3DP Singapore Center for 3D Printing.

SCC Stress Corrosion Cracking.

SCE Saturated Calomel Electrode.

SEM Scanning Electron Microscopy.

SL Sheet Lamination.

SLM Selective Laser Melting.

SM Subtractive Manufacturing.

SS Stainless Steel.

TIG Tungsten Inert Gas.

USP Ultrasonic Shock Peening.

UTS Ultimate Tensile Strength.

WAAM Wire Arc Additive Manufacturing.

WEAM Wire Electron Additive Manufacturing.

WEDM Wire Electrical Discharge Machining.

WLAM Wire Laser Additive Manufacturing.

XRD X-Ray Diffraction.

YS Yield Strength.

Introduction

The nuclear and offshore wind industries are of great interest to meet the current challenges of producing carbon-free electrical energy in the context of the global energy and climate crisis. Extreme conditions such as high temperatures, vibrations or pressures are often found in industrial equipment and machinery. As a result, metal parts can be damaged due to wear, fatigue or accidents, reducing their service lifespan and performance [1, 2]. To ensure proper operation of the equipment, damaged parts must be repaired or replaced. In many cases, the traditional solution to these problems is complete replacement of the damaged component. However, this can be a costly solution, especially in cases where parts are in short supply or no longer manufactured [3]. In addition, it can lead to production downtime, which can have a negative impact on the company's costs and profitability.

Therefore, repairing damaged parts is an interesting alternative to extend their life and reduce costs associated with plant shutdowns. It also allows for minimizing the mineral resources required for the development of new components, as well as the carbon footprint associated with the manufacturing processes and transportation of the components. However, existing repair processes, such as welding or brazing, have limitations in terms of accuracy, quality and reliability [4]. They can introduce residual stresses that can reduce the strength and life of the part. In addition, these processes can change the microstructure of the part, which can also affect its mechanical properties. In addition, the heat generated during these processes can cause distortion of the part and change its geometry. These techniques can also be costly and time-consuming to repair because they require a high level of expertise.

In this context, the development of innovative repair processes that are in line with the needs of the industry is of paramount importance. Additive manufacturing technologies, also known as 3D printing, offer new perspectives for the repair of damaged metal parts. Indeed, these technologies make it possible to produce parts with high precision and surface quality, while reducing production costs and minimizing material losses. Therefore, the development of innovative repair processes based on additive manufacturing represents

a major challenge for the industry and can contribute to the implementation of more sustainable and economical practices in the context of the circular economy.

The objective of this work is to develop and optimize a process for repairing metal parts damaged by mechanical or corrosion phenomena, while respecting particular specifications. The deposit made by additive manufacturing must be of excellent quality, *i.e.* dense and without cracks. It must also have a strong metallurgical bonding with the part to be repaired. The repair area must be imperceptible in terms of microstructure, mechanical properties, and corrosion resistance to restore the initial properties of the damaged part. Finally, the repair process must not further damage the original part, removing the least amount of original material.

Laser Metal Deposition (LMD) technology, which is based on additive manufacturing, appears promising for meeting these requirements [5]. The LMD process has demonstrated its ability to repair metal parts while maintaining high deposition density and good mechanical properties. The energy provided by the laser allows the material to be melted without significantly affecting the substrate thermally, thus avoiding distortion of the repaired part. Finally, the implementation of projection nozzle on numerical control machines allows the repair process to be automated and to achieve a high level of precision compared to manual repair. However, problems with this process for repair have been reported in the literature, such as fusion problems on certain part geometries, heterogeneity of part characteristics, and difficulties in implementation compared to manual repair.

A better understanding of the LMD process and the interactions between the different steps of the repair process, as well as the metallurgical phenomena involved in the laser process on the characteristics of the repaired parts, is necessary to obtain a quality repair process that respects the imposed specifications. The following questions can be asked to explore this research work:

- How can the LMD process be optimized to achieve dense, crack-free repairs that are metallurgically bonded to the repaired part?
- How can the pre-machining preparation of the damaged part be improved to reduce the volume of material to be removed and ensure a dense repair?
- What are the resources available and how can they be used to restore the original properties and dimensions of the damaged part?

These questions were explored using a standard material, which is commonly used in the energy industry, namely Stainless Steel 316L. It has a good corrosion behavior, thanks to its high chromium and molybdenum content associated with a low carbon content. It

also has good mechanical properties, through a high elastic and mechanical resistance. This steel is weldable by all conventional welding processes and is widely used in additive manufacturing in wire and powder form. These elements make it a perfect candidate for use in those industries subject to aggressive environments [6].

The investigation will be presented in six chapters. The first chapter is a state-of-the-art of the existing repair processes and their limitations, as well as the stainless steel 316L material. Then, the different additive manufacturing processes will be presented and compared to determine their ability to perform repairs on damaged parts. The laser metal deposition process appears to be a promising technique for this application and is presented in more detail with the influential factors on the process. Finally, the difficulties experienced in the literature with the LMD process for the repair of damaged components are discussed.

The second chapter describes the materials and experimental methods used in this thesis work. Characteristic and operating conditions of the LMD machines are detailed first. Then, the preparation methods for sample observations are described. At last, techniques for material characterization are presented, including the microstructural observation, mechanical properties and corrosion resistance determination techniques.

The third chapter is dedicated to the additive manufacturing process, through the optimization of the deposition parameters and the adaptation of the deposition pattern for the repair application. The positioning of the parts to be repaired is discussed to achieve a good quality of repair. This part aims at understanding and optimizing the basic principles of the repair process, in order to satisfy the requirements of dense deposition, without cracks and having a metallurgical bonding with the substrate.

Chapter 4 discusses the influence of the pre-machining geometry on the quality of the final repair, in order to achieve a dense repair with the removal of a minimum of material during the pre-machining operation. Firstly, in order to determine an optimized angle for the repair, the influence of the opening angle of the pre-machining on the mechanical behavior of the repaired parts is studied. The second part focuses on the technical conditions to be imposed on the opening angle for the repair of deep defects. Finally, a minimization of the repair volume is carried out on the basis of the results obtained previously.

The 5th chapter evaluates the influence of substrate preheating, interlayer cooling and post heat treatment on the intrinsic characteristics of the repairs, such as the microstructure and the microhardness. The corrosion resistance and the microorganism formations in

seawater of the heat-treated repairs is tested and discussed. This part aims to make the repair imperceptible by homogenizing the properties of the repair with additional thermal treatments added to the repair process. These techniques must also meet the requirements of a dense, metallurgically bonded repair to the substrate without damaging the original part.

Finally, Chapter 6 discusses the effect of using hybrid additive/subtractive manufacturing in improving the repair process. Performing a complete repair process in a single machine allows us to observe the time savings for repairing damaged parts, highlighting the issues of coupling additive and subtractive processes in a single enclosure. The alternation of machining and material deposition operations or the application of a thermal post-treatment during the repair process allows to evaluate the interest of this process on the repair time and the final characteristics of the repaired parts.

This thesis was conducted within the framework of a tripartite agreement between the Commissariat à l'énergie atomiques et aux énergies alternatives in Paris-Saclay, Sorbonne Université in Paris and the Nanyang Technological University in Singapore. The Joint PhD agreement stipulated that the student would spend two years at CEA/SU and one year at NTU to validate the two degrees. Due to the COVID-19 health crisis and the closure of international borders, a PhD extension of 8.5 months was validated, in order to spend a full year in Singapore. The first studies carried out at the CEA made it possible to carry out repairs under optimal conditions on an OPTOMEC additive manufacturing machine with an argon atmosphere and by dissociating each stage of the repair process, in order to optimize them. The work performed in Singapore on a DMG Mori additive/subtractive hybrid manufacturing machine has enabled the implementation of a complete repair process including the steps of machining and printing under air atmosphere, representing the industrial application of this process.

Chapter 1

Repair of stainless steel 316L for the industry

Abstract

This chapter is dedicated to a literature review of the replacement and repair methods currently used to restore component functionality in the industry. Then, a review of metal Additive Manufacturing (AM) processes is performed to show the potentialities of the Laser Metal Deposition (LMD) process to perform this type of repair. Finally, the LMD repair process is detailed and its technical limitations are highlighted in order to discuss the means to achieve a specification-compliant repair.

Contents

1.1 SS316L repair technologies in the industry

1.1.1 Stainless steel 316L

Stainless Steel (SS)316L is an iron base alloy with alloying elements mainly composed of nickel, chromium and molybdenum. The chemical composition of this alloy is given in Table 1.1 according to ASTM A276 [7], ASTM A240 [8] and RCC-M [9], which governs the construction of nuclear power plants in France. The high chromium content gives it its stainless properties with the formation of a compact and impervious Cr_2O_3 passivating layer on the surface of the material when in contact with oxygen. The addition of molybdenum hardens the material and improves its resistance to localized corrosion in aggressive environments (chlorinated, salty and acidic environments). The stainless steel 316L (L for "low carbon") has less than 300 ppm of carbon, in order to avoid the formation of chromium carbide at the grain boundaries during welding, which leads to a depletion of chromium and a strong sensitivity of the structure to inter-granular corrosion. Nickel is present in large quantities as a γ-gene agent, which stabilizes the austenite face-centered cubic structure of the steel at room temperature. The manganese content provides increased resistance to hot cracking during rapid solidification.

Table 1.1: Chemical composition of SS316L according to ASTM A276, ASTM A240 and RCC-M specifications (in wt%).

	Mass percentage							Mass ppm		
Element	Fe	Cr	Ni	Mn	Mo	Si	Cu	C	P	S
ASTM A276	Bal.	16-18	10-14	<2	2-3	<7.5	-	<300	<450	<300
ASTM A240	Bal.	16-18	10-14	<2	2-3	<7.5	-	<300	<450	<300
RCC-M	Bal.	16.5-18.5	10-13	<2	2.3-2.7	<7.5	<1	<300	<300	<150

In conventional production, the austenite FCC structure is obtained by hyperquenching. The steel is heated to a fixed temperature of 1050°C to 1150°C to dissolve the intermetallic phases and homogenize the chemical composition, and then rapidly cooled by quenching with water. Precipitation hardening can be carried out with a heating phase between 700°C and 800°C. As observed in Figure 1.1, the final microstructure is composed of fine and equiaxed austenite FCC grains with an average size of a few tens of microns, depending on the work hardening and heat treatments applied. Lamellar grains of ferrite can be formed at the austenite FCC grain boundaries. The microstructure does not have a crystallographic texture.

The mechanical properties of SS316L are listed in Table 1.2. This stainless steel is known for its high strength even at high temperatures, as well as for its high ductility.

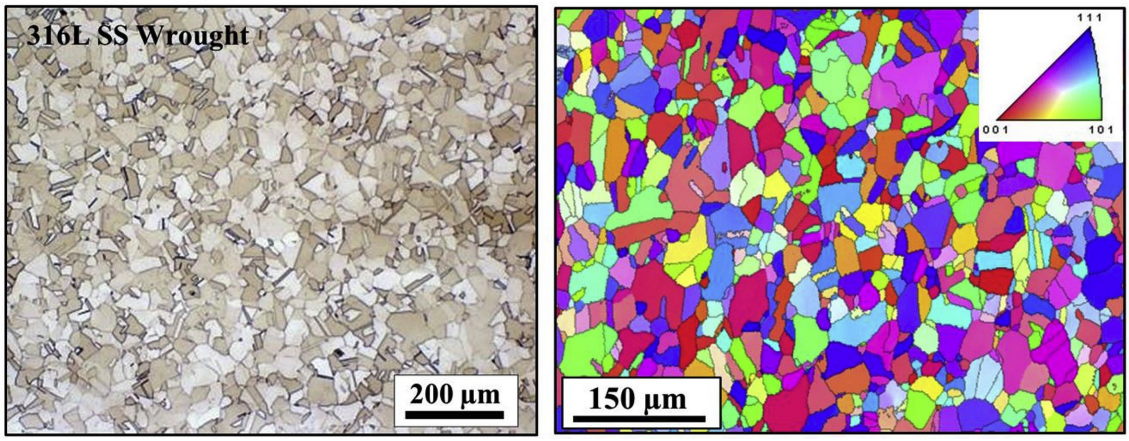

Figure 1.1: Microstructure of a wrought stainless steel 316L [10].

Table 1.2: Mechanical properties of SS316L according to the litterature.

Vickers Hardness (HV)	Ultimate tensile strength (MPa)	Yield strength (MPa)	Elongation at break (%)	References
150-220	485-585	170-245	40-60	[11, 7, 9, 8]

1.1.2 Damage encountered in the industry

Industry uses a large amount of stainless steel, especially SS316L, for internal components that are essential to the operation of equipment. Its excellent mechanical and corrosion resistance properties and low cost make it a material of great interest for many applications. For example, it is used in primary and secondary piping, pumps, valves and heat exchangers in nuclear power plants [6]. It can also be found in electrical enclosures, safety cables and floating structures in offshore wind turbines [12].

However, the aggressive environments and high mechanical stresses present in these industrial applications can cause mechanical and corrosive damage to components over time. Despite its high resistance to general corrosion, SS316L can thus present localized corrosion such as crevice corrosion, pitting or Stress Corrosion Cracking (SCC). The presence of chlorides, for example, enhances the formation of pitting corrosion by triggering an autocatalytic process. The pits are charged with positive metal ions following oxidation of the base metal in the anodic zone. Cl^- and H^+ ions concentrate in the pits, forming poorly soluble metal hydroxides and an acid solution respectively that accelerates the phenomenon.

Moreover, the presence of microorganisms in natural seawater induces biofilm formation on the surface of SS316L and can lead to Microbiologically Influenced Corrosion

(MIC). This is defined as the degradation of materials due to the physical presence and metabolic activity of these organisms on surfaces, according to mechanisms involving either electrochemical at the metal-solution interface, or chemical reactions (production of aggressive metabolites, etc.)

In addition, wear due to prolonged friction on a surface causes a reduction in the amount of material. In some cases, excessive stresses, mechanical fatigue of parts, or SCC can initiate and propagate cracks in the steel.

These phenomena damage the stainless steel parts, as can be seen in the examples in Figure 1.2. They can cause the deterioration of the seals of the pipes or even the complete breakage of the parts by weakening the mechanical properties, while they are subjected to the same constraints with less material or by becoming porous.

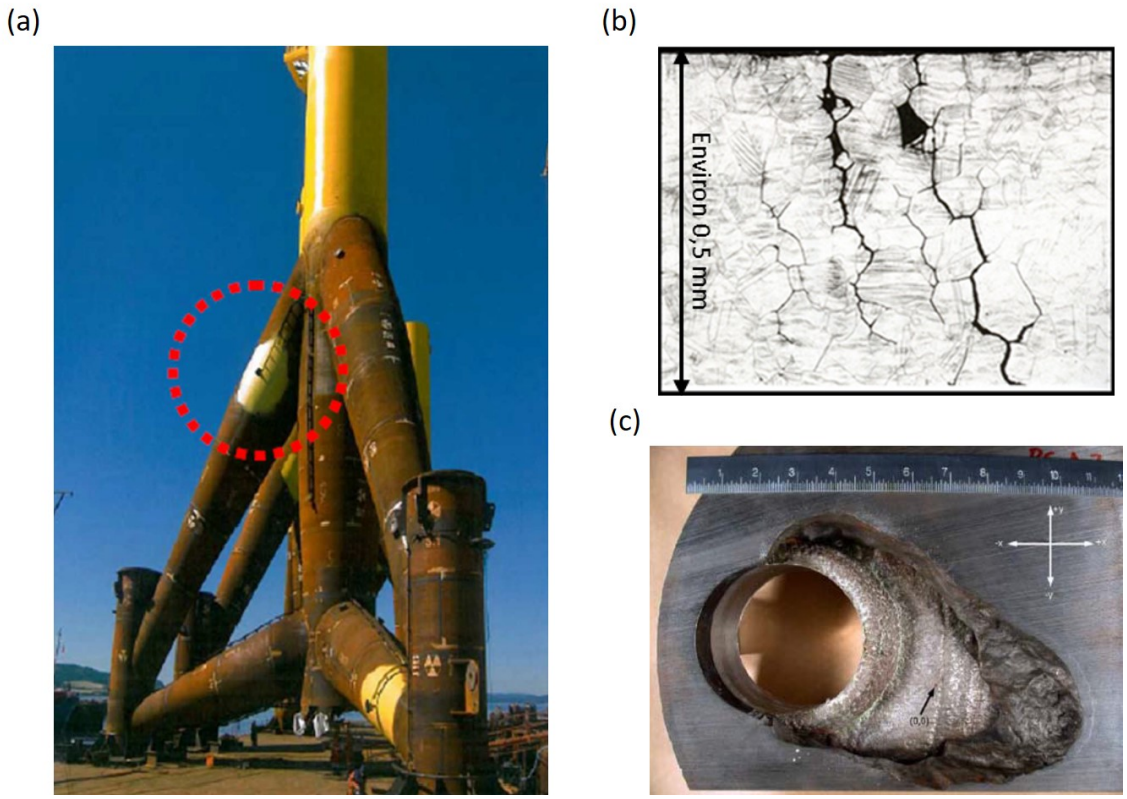

Figure 1.2: Observation of (a) uniform corrosion on wind turbine monopile [13], (b) SCC in the emergency cooling circuits of the primary circuit at the Civaux nuclear power plant [14] and (c) nuclear reactor head corrosion [15].

1.1.3 Replacement of a damaged component

The restoration of the equipment after the damage of the components can be achieved by the use of two solutions, which will be chosen according to the intensity of the damage to the part and the costs involved. The first solution is to replace the component with a new one. The equipment is shut down, then the damaged part is disassembled and replaced with a new one.

Despite higher costs, time and logistics and higher consumption of material and energy, replacing the damaged part has several advantages, as the assurance of having a new part that meets the required dimensional and mechanical specifications and where the defects encountered on the old parts have been rectified. [3].

Indeed, industry equipment is continuously upgraded throughout its lifetime. Some parts may change design or even material. For example, 600 alloy tubes in the steam generator of nuclear power plants are being replaced with the more intergranular corrosion resistant 690 alloy. Thus, damaged parts are replaced with more efficient ones [2].

As part of preventive maintenance, a component that has exceeded a certain period of use should be replaced to prevent damage and a complete shutdown of the system. This application reduces costs and unplanned maintenance time [16].

However, for reasons of cost, material and energy savings, repairing a damaged part is preferable to replacing it. But sometimes, repair is simply not possible because the component is too degraded to be repaired, as in the case of a part that is so corroded that it is pierced. Or the repair with the current techniques does not allow to achieve the necessary or expected characteristics for the good functioning of the system. Finally, the repair seems impossible or delicate in contaminated or irradiated areas, where the implementation of additive or subtractive processes could be dangerous. In these situations, replacement of the damaged part is preferred [16].

These situations are extreme cases where changing the part is justified and necessary. But this method consumes a lot of energy and materials to extract and transport raw materials, manufacture the component, and distribute it. This results in long waiting times, high maintenance costs and carbon emissions. In addition, unplanned maintenance can significantly increase downtime if spare parts are not readily available, as well as the cost due to production interruption.

1.1.4 Repair process

Definition

The second solution is to repair the damaged component, preferably on site, and then return it to service in the industrial installation. With this method, material and energy consumption is significantly reduced as only the damaged material is replaced. This results in a significant reduction in maintenance costs, production downtime and carbon emissions. This technique is an integral part of the circular economy. The component is reused rather than discarded. As described in the literature [17, 18] and illustrated in the Figure 1.3, the repair process for damaged components consists of five major steps.

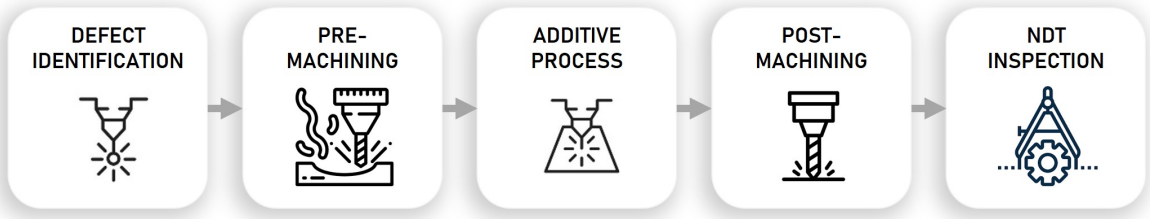

Figure 1.3: Flow chart of the repair process.

The first step is to identify the defect caused by mechanical or corrosive phenomena. The part is cleaned using mechanical techniques such as sandblasting or chemical immersion in degreasing baths, and then analyzed. Defects are identified using non-destructive methods such as dye penetration, X-ray or neutron radiography or ultrasound. However, after identification, a cross section of the part with metallographic observation is required to determine the dimensions of the defect. Another technique under development is to scan the damaged part with a 3D scanner or coordinate measuring machine equipped with a probe that reconstructs the actual volume of the part. This reconstructed volume is then compared to the original CAD drawing of the part to identify defects.

The second step is the pre-machining step. The material around the flaw must be machined because it contains stresses and contaminants resulting from the damage phenomenon. In fact, when grinding cracked welds, if the crack is not abraded enough, it will start again at the point where the abrading was stopped [19]. Machining makes it possible to eliminate the defect, to remove the existing contaminants, but also to allow access to the equipment used in the next step.

The next step is the addition of material thank to a metal deposition process. This operation is crucial, because the deposited material will replace the damage material and

it will determine the quality and durability of the repair over time. The purpose is to replace the previously removed damaged material with new material. The control of the deposition parameters is essential to ensure a dense, crack-free deposit of material that is metallurgically bonded to the part to repair.

The fourth step consists in performing a post-machining finish on the repaired part. This phase enables the removal of the excess material deposited by the process previously presented, but also to restore the part to its original dimensions.

Finally, the last phase aims to determine the quality and the success or failure of the repair process. The repaired part must be inspected with non-destructive methods to evaluate the presence of porosities in the deposited material or at the interface that could compromise the mechanical or corrosion resistance of the repaired part in service.

Specifications

Throughout the different steps of the repair process, a number of specifications must be followed to ensure that an excellent quality repair is achieved, allowing the repaired part to be returned to service with characteristics close to those of the original part.

The repair process must:

- Eliminate completely the flaw in the material due to mechanical or corrosive phenomena with the least amount of material removal possible;
- Produce a dense, crack-free deposit with material diffusion to the substrate and between layers or metallurgical bonding;
- Obtain a homogeneous microstructure, mechanical properties and corrosion resistance of the repaired area;
- Return the part to its original pre-damage dimensions;
- Do not damage the rest of the part during the repair.

These guidelines should be closely followed throughout the repair process, but special attention should be given to the deposition step, as the deposited material will be the replacement material and must be of dense. Furthermore, this step is the more aggressive for the part due to the energy source used to melt the material.

1.1.5 Traditional repair processes

Repair is a complementary technique to replacement of damaged parts. In the industry, it is primarily studied for the return to service of a damaged part in order to reduce the material and energy consumption compared to the complete replacement of the part, but above all to reduce the cost and time of maintenance.

Welding processes

Traditionally, repairs are performed using manual wire welding techniques. These include Tungsten Inert Gas (TIG), Gas Metal Arc Welding (GMAW), Submerged Arc Welding (SAW), friction and laser welding. In fact, welding is one of the oldest and best mastered process to melt a metal and deposit it locally. Each welding technique has its advantages and disadvantages depending on the geometry of the part, the material, the amount of material to be deposited and the environment [20].

In the nuclear industry, the TIG process is used mainly to repair the stainless steel piping because it provides excellent deposit quality with good metallurgical continuity with the substrate [9]. It is suitable for welding thin sections and minimizes part deformation compared to other processes. However, it requires skilled welders and has a low productivity [21]. In the offshore environment, laser welding techniques with water drainage heads allow for underwater repairs without the need to remove the component from the water. The deposition quality is excellent and the technique is less dangerous to the welder than an electric arc process [22].

When mastered, these techniques represent promising, inexpensive, and easy-to-implement processes for repairing damaged components. Moreover, repairs made by welding processes allow to obtain high material densities if no cracks, cavities, inclusions or lack of fusion are introduced during the process. However, due to the nature of the processes and, in particular, the energy source, they have a number of limitations that cannot be eliminated or that would require in-depth optimization studies.

The main disadvantage of these welding processes is the very powerful energy source used to fuse the material, especially in the case of arc welding. A high voltage is applied between the part and the deposition tool to create an electric arc. While this technique is simple to implement, it has a significant thermal impact on the part. The energy introduced into the part during welding can be quantified using Equation 1.1.

$$H_{net} = f_1 * \frac{U * I}{V} \tag{1.1}$$

where H_{net} is the welding energy in J/mm, V is the transverse arc speed in mm/s, U is the welding voltage in V, I is the welding current in A, and f_1 represents a transfer coefficient expressed as the ratio between the amount of heat actually transferred to the workpiece and the total power generated by the heat source

Based on welding repairs reported in the literature, Table 1.3 summarizes the energy introduced into the part by the heat source.

Table 1.3: Energy introduced during welding repair.

Process	Material	d(mm)	U(V)	I(A)	V(mm/s)	f_1	H_{net} (J/mm)	References
GMAW	H08Mn2Si/Q235	1.2	24	110	5.2	0.8	406	[23]
TIG	SS316L	1.25	19	105	1.5	0.7	931	[24]
SMAW	SS316L	3.25	25	120	3.3	0.8	727	[25]

Figure 1.4 (a) presents a common example of the microstructure of austenitic stainless steel after welding. Three zones can be observed globally. The fusion zone is composed of dendrites caused by the rapid solidification of the melt pool. The base metal is far enough away to not undergo major changes. On the other hand, the literature shows that the high energy supplied by the heat source to melt the wire affects a large thickness of the base metal, which is called the Heat Affected Zone (HAZ). The zone has not been melted, but it has enough energy to undergo microstructural changes such as grain coarsening on a width of approximately 1 mm in this case (Figure 1.4 (a)). For materials with low thermal conductivity, such as stainless steel, the heat dissipates slowly through the base metal and causes recrystallization of the microstructure as it passes through the area near the Fusion Zone (FZ) [24].

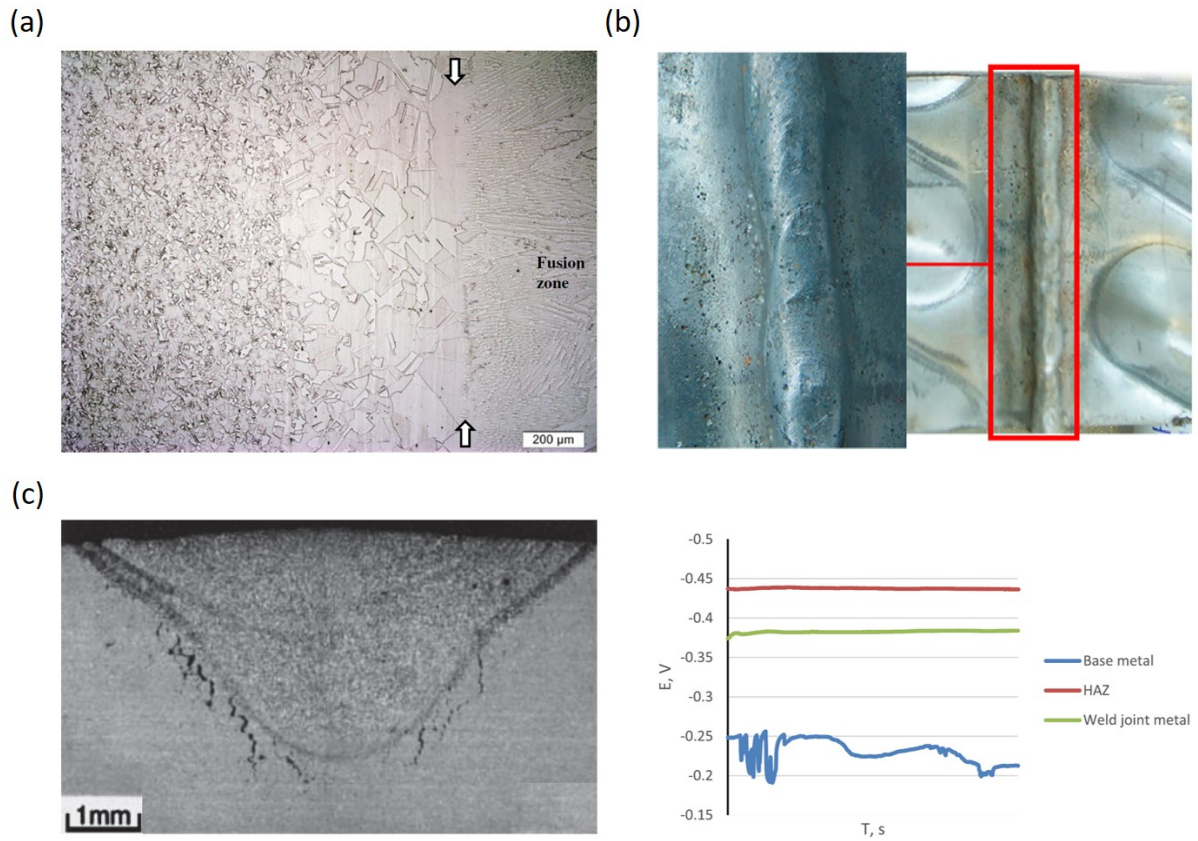

Figure 1.4: (a) HAZ in fine-grained austenitic stainless steel after GTAW process [24], (b) pitting corrosion of the weld and corrosion potential of each area [26] and (c) cracking of the HAZ in irradiated stainless steel 316 after welding [27].

Similarly, AghaAli *et al.* [25] indicate that a phase change is observed in repeated repairs of SS316L parts. The ferrite content in the substrate decreases from 7% to 3% after four repairs, but the lathy shaped grains between the austenite grains gradually change to vermicular grains dispersed in the matrix. This decrease and change in morphology results in lower Brinell hardness and lower energy absorbed during impact tests.

These microstructural changes caused by these welding processes result in reduced mechanical properties and corrosion resistance. Yu *et al.* [28] showed that an FC300 steel specimen repaired by arc welding had Ultimate Tensile Strength (UTS) and Elongation At Break (EAB), which decrease of 17.6% and 20.6% compared to an unrepaired reference specimen due to martensite formation in the HAZ.

Furthermore, the problem of weld corrosion is a common phenomenon in the field of welding. As shown in Figure 1.4 (b), Kovalev *et al.* [26] has observed that the different zones present in a weld in SS304, *i.e.* the base metal, the HAZ and the FZ, have different corrosion potentials of -0.25 V, -0.37 V and -0.44 V respectively. The HAZ corresponds to

the less noble zone, because of the formation chromium carbide along the grains boundaries leading to chromium depleted zone in the vicinity of the grain boundary. This explains why this zone is more susceptible to corrosion. A wide HAZ, as in the case of welding, therefore implies a larger area susceptible to intergranular corrosion.

The use of welding processes also introduces high residual tensile stresses into the parts. This is due to the heating cycles during the passage of the heat source and the subsequent shrinkage of the melt pool as it solidifies, creating residual tensile stresses. This phenomenon is amplified in large beads and is generally located in the HAZ. If they are near the surface or in the FZ and exceed the UTS of the material, the residual tensile stresses can cause the weld to crack or hot cracking respectively [24]. In other cases, they cause SCC [29], as observed in the emergency circuits of the primary circuits of many nuclear reactors in France [14]. Finally, under certain conditions, these stresses associated with high temperature and irradiated material cause cracking of the weld repair. In fact, helium is produced by the transmutation of nickel and boron present in stainless steel. When high temperatures and high tensile stresses are applied, helium bubbles form at the grain boundaries and cause cracking of the weld (Figure 1.4 (c)) [30, 27]. Residual stresses can also cause warpage of the repaired part, which will no longer have the correct geometry to be reused in the original equipment [23].

Cold spray

Unlike fusion deposition processes, cold spray technology uses the kinetic energy of powder particles propelled at high velocity against a substrate at room temperature to plastically deform them, create a metallurgical bond and coat the surface of a part [31]. These technologies have become increasingly popular in recent years and are used for coating, repair and, more recently, creating complex parts.

This deposition method has the advantage of being flexible and inexpensive. The deposition is performed at room temperature without melting the powders, so oxidation-sensitive materials such as aluminum can be used. The kinetic energy is used to create the metallurgical bond and does not thermally affect the part as in the case of welding [32]. Finally, this process introduces residual compressive stress into the surface of the parts, which is beneficial for wear, fatigue and corrosion resistance [33, 34]. Numerous studies in the literature demonstrate the feasibility of the cold spray process for repairing parts with reloading of material followed by finishing to restore the original dimensions of the part. Industrial tests, particularly on aluminum parts, have been carried out on cones [35], gears [36], S-92 and UH-60 helicopter gearbox sump [37], blades [38] or Caterpillar engine oil pump housing [39] after wear.

However, the literature highlights porosity rates of 2% in cold spray which is considered low, but still very high compared to other deposition processes [31, 32]. The reason for this is the angle between the substrate and the projection nozzle. The optimal angle is 90° to allow the particles to come to rest on the surface of the material because it has only a normal velocity vector. If the angle is other than normal, the particles may bounce off the surface because the angle creates a tangential velocity vector, resulting in poor deposition rates and even abrasion [32]. Despite optimized deposition parameters, the literature shows the presence of porosities and metal oxide impurities in the deposits with a porosity rate of about 2%. This rate increases significantly when deposition is performed in a confined area, such as the pre-machining of a repair, as shown in Figure 1.5. This is because this area consists of inclined surfaces on which the sprayed particles bounce. In addition, the accumulation of these unbound particles in the area will interfere with the deposition of the last sprayed particles and may cause porosity [40].

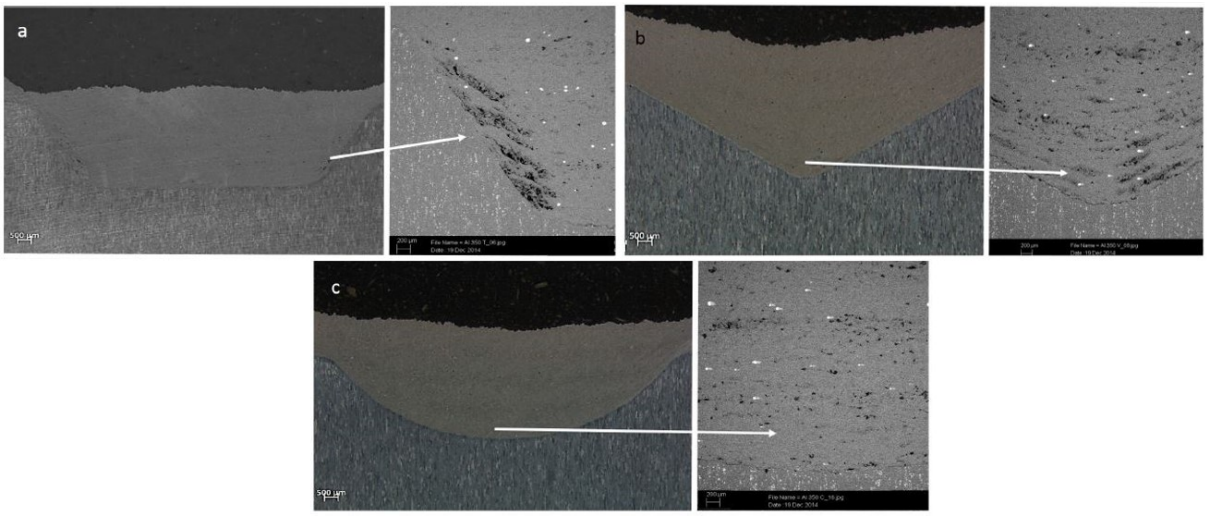

Figure 1.5: Cross-section of different pre-machining with porosity on non-horizontal surface in (a) trapezoid shape, (b) conical shape and (c) circular shape [40].

The deposit results in poor mechanical properties for the as-built specimens, especially with a low elongation at break due to the presence of a high porosity rate and strain-hardening of the coating. Despite low mechanical properties, the literature shows that cold spray repairs of aluminum alloy parts have high fatigue resistance close to the reference substrate or even better fatigue properties. Crack initiation usually occurs at the deposit/substrate interface or in interparticle porosities [32].

Finally, this technique is limited to certain materials because it cannot be used for hard materials due to the difficulty of plastic deformation of the particles. In addition, the process leads to coatings with a low geometric accuracy, requiring a post-manufacturing

machining to recover the original dimensions of the repaired part [32]. As-sprayed stainless steel coatings are not known to be more corrosion resistant than conventional stainless steel. In fact, pores in the deposits can be corrosion initiation points, especially for pitting corrosion. In addition, fine areas of high plastic deformation locally change the potential of the atoms to the point of creating areas that are highly susceptible to pitting and cracking of the protective oxide layer [41].

Post-manufacturing heat treatment is the most efficient method of improving the properties of cold-spray coatings. As shown in Figure 1.6, annealing of as-deposited coatings significantly improves tensile strength and ductility by attenuating defects in the coatings. For stainless steel, a high temperature heat treatment is required to homogenize the microstructure of the deposit and reorganize the dislocations to obtain viable mechanical properties [31].

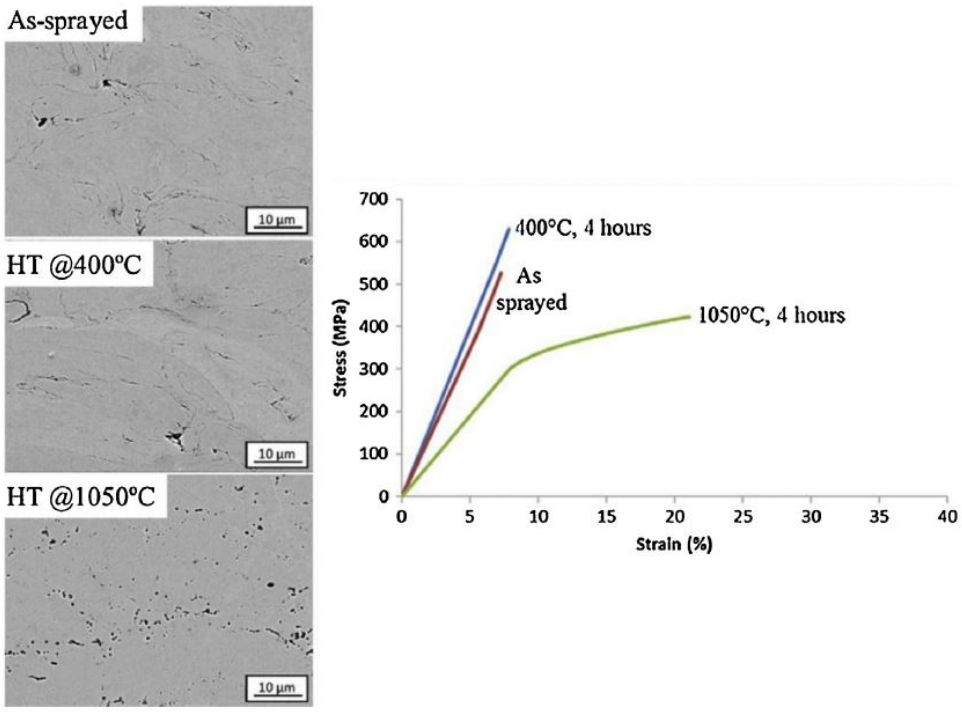

Figure 1.6: SEM cross-section observations and mechanical properties of cold-sprayed 304L stainless steel as-built and with heat treatments for a SS304L [42].

Thermal spray

The thermal spraying processes such as wire arc spray, plasma spray or high velocity oxy-fuel coating spraying belong to the same family of processes as cold spray. The notable difference is that the particles are pre-heated or pre-melted in the spray nozzle

with different heating methods (flame, arc, plasma, ...) before being sprayed onto the substrate to be repaired.

These processes have been used for several decades to repair damage to parts due to corrosion and cavitation in the oil & gas [43], power generation industries [44, 45], and also in the US Navy [46]. They are losing interest in favor of the cold spray process, which is less restrictive to implement, more efficient and offers more advantages.

Despite better resistance to corrosion and cavitation than cold spray deposition due to more homogeneous oxide layers, these "hot" processes suffer from a problem of particle oxidation that is enhanced by preheating prior to deposition. This problem leads to an increase in the rate of porosity and oxide inclusions in the deposits. The solution is to use vacuum manufacturing chambers, which are not designed for on-site repair. In addition, they thermally affect the part to be repaired or coated, causing distortions that are detrimental to the repair. In fact, the cooling of the particles bonded to the substrate creates residual tensile stresses in each layer that can cause the deposit to crack [47].

Heating or melting of the particles leads to unwanted phase transformations and even vaporization of the most volatile elements, resulting in a change in chemical composition between the starting material and the deposited material [47].

Thermal spray processes have been used for years to repair damaged components because they were the only methods available, other than welding, to perform this type of operation. However, they have a number of problems that have not been overcome with the development of new material deposition techniques.

1.1.6 Summary

Conventional methods for repairing damaged parts have interesting aspects. They are easy to implement on-site and are well known to industrial operators. In addition, their technology is inexpensive because they have been used in various forms for several decades. They therefore appear to be useful tools for repair in the industrial environment.

However, although some characteristics are restored after repair, the repaired parts have degraded properties compared to the original part due to the nature of the process used. In the case of welding, the high energy input causes microstructural changes in the part to be repaired and distortions due to the residual stresses introduced. Thus, the criteria of the repair process regarding the imperceptibility of the repair and the non-damage of the original part are not satisfied.

Also, the cold and thermal spray processes do not achieve high density deposits

equivalent to the reference substrate, and the mechanical properties of the repaired specimens are of poor quality. The criteria of dense deposits metallurgically bonded to the substrate and imperceptibility of the repair are also not achieved with these processes, despite remarkable fatigue properties.

These results from the literature imply the need to study new possibilities for the deposition of material during the repair of damaged components in order to obtain a repair process that meets all the criteria imposed by the specifications established in Section 1.1.4. In recent years, with the development of AM, new processes have matured that allow the application of thin metal layers ranging ,from a dozen µm to several mm, with excellent geometric precision.

1.2 Additive manufacturing laser metal deposition

1.2.1 Generalities of additive manufacturing

Since the 1980s, AM has evolved from building parts layer by layer with polymers for rapid prototyping to rapid tooling with metallic materials. Nowadays, it gathers a set of different technologies that allow the production of complex parts with a wide availability of material grades. The ISO-ASTM 52900-15 standard defines AM as *"process of joining materials to make parts from 3D model data, usually layer upon layer, as opposed to subtractive manufacturing and formative manufacturing methodologies"* [48]. The manufacturing process consists of four main steps. A Computer Aided Design (CAD) model of the part to be manufactured is created on the computer, then software meshes it into a discrete value by creating a .stl file. This file is sliced into a set of layers to be deposited, which are translated by the AM machine using heat source trajectories, which melt the layers and create the final part.

AM has become very popular in recent years due to the maturation of deposition technologies coupled with CNC machines. Moreover, unlike traditional manufacturing processes such as forging or Subtractive Manufacturing (SM), AM has significant advantages, such as the ability to produce complex parts that cannot be achieved by traditional methods, the ability to optimize the topology of parts to reduce the amount of material used, and the number of assemblies. These technologies allow the deposition of multi-material coatings adapted to harsh environment applications such as nuclear fusion. Finally, the manufactured parts are near-net shape and require only finishing operations to achieve the correct surface roughness. These advantages make manufacturing an asset for developing new parts at reduced cost [49].

As described in the ISO 17296-2 standard [50], AM has seven process categories. They are categorized according to the method of material deposition and the bonding technique between the layers, as shown in the Figure 1.7. Metal AM is possible using Sheet Lamination (SL), Binder Jetting (BJ), Powder Bed Fusion (PBF) and Directed Energy Deposition (DED). However, not all of these technologies are suitable for repairing damaged components.

In SL technology, thin sheets of material (typically fed by a roll feed system) are joined together layer by layer using ultrasonics or lamination to form a single part. However, the material is fed from a roll onto a flat surface. Therefore, this process cannot be used to repair parts with complex geometries that require the material to be placed in a confined, pre-machined area.

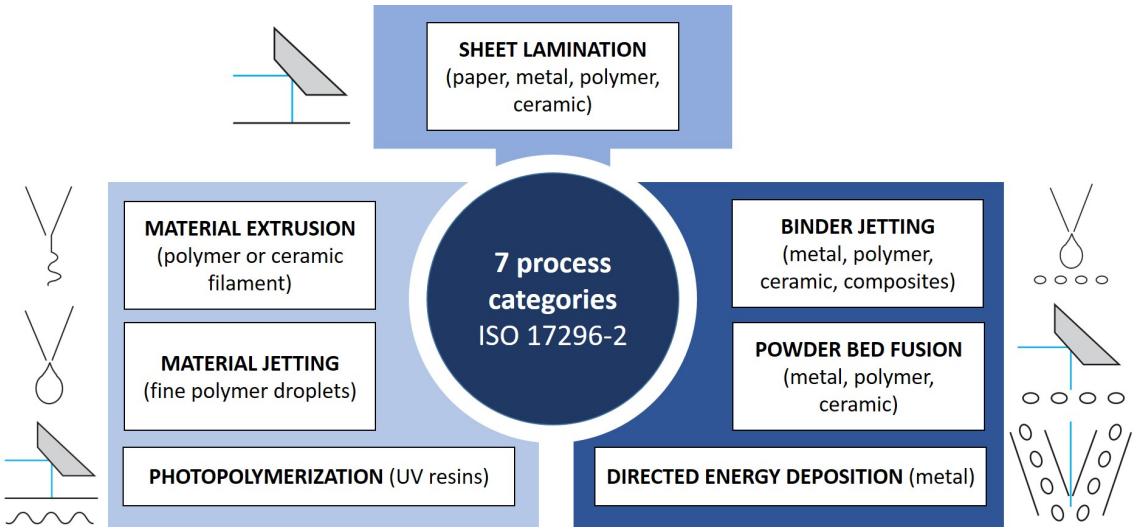

Figure 1.7: Overview of the AM process categories, adapted from Obaton *et al.* [51].

In BJ technology, a binder is selectively applied to the powder bed and these areas are bonded together, layer by layer, to form a solid part. A sintering treatment is then applied to solidify the part. However, the deposit, which shrinks as the binder evaporates, is only 90% to 97% dense, depending on the technique. In addition, there is no metallurgical continuity with the substrate, making this technology unsuitable for repair.

The PBF technique works on the same principle as sheet lamination. The difference is that the powder is applied to a flat, horizontal surface with a scraper and then melted with a laser or electron beam. Therefore, the configuration of the machine does not allow the powder to be deposited in confined areas or on complex non-horizontal surfaces.

Unlike previous technologies, the material feed of DED technology is more suitable for repairing complex and confined surfaces. In fact, the material in the form of wire or powder is delivered coaxially to the energy source. From now on, the focus will be on DED technology, which has the technical capability to repair components. This technique allows the production of metal, polymer or ceramic parts in successive layers. The process uses focused thermal energy to fuse materials by melting them as they are deposited. It is most commonly associated with Computer Numerical Control (CNC) machines used in machining that allow 5 axes of motion. As shown in the Figure 1.8, there are different process names depending on the type of energy source or method of feedstock deposition.

The DED process can be divided into two types of feeding, powder feeding and wire feeding, as displayed in the Figure 1.8. Compared to handling micrometric powders, using wire filler is easier and safer for the operator. The main characteristics of the different processes are detailed in Table 1.4. The DED processes developed for powder feeding

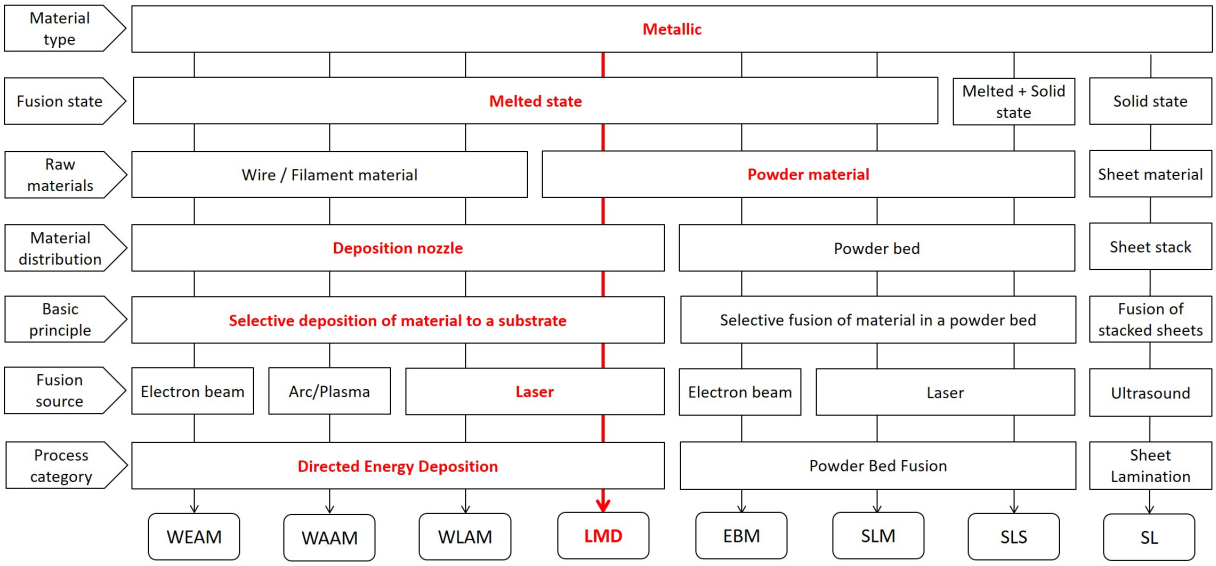

Figure 1.8: Overview of the single-step AM metallic processes, adapted from [48].

use laser as thermal energy, while the DED processes developed for wire feeding use electric arc, plasma arc, laser, and electron beam as heat sources. The DED process uses both coaxial and lateral feed technologies to feed the raw material into the melt pool. Known as the LMD, the process consists of a powder feeder and a laser. Wire-feed processes are classified as Wire Arc Additive Manufacturing (WAAM), Wire Laser Additive Manufacturing (WLAM), and Wire Electron Additive Manufacturing (WEAM). As shown in Table 1.4, the arc, laser and electron beam energy densities for DED processes are 10^4, 10^6 and $10^8 W/mm^2$, respectively. A shielding gas is used to prevent oxidation of the melt pool during the deposition process in the LMD, WAAM, and WLAM processes. A vacuum furnace is used for the WEAM process. The cost of the WAAM process is relatively lower than that of the LMD, WLAM and WEAM processes. The surface roughness (Ra) of the part produced by the LMD process is about 20-30% higher than that of the WLAM process in a flat deposit. The deposition rate and film thickness of the wire DED processes are significantly higher than those of the powder DED processes, while the dimensional accuracy and residual stress of the part produced by the wire DED processes are higher than those of the powder DED processes, as shown in Table 1.4 [52].

Table 1.4: DED process characteristics, adapted from Ahn et al. [52].

Process	Feedstock	Energy source	Layer thickness (mm)	Minimum bead size (µm)	Heat flux density (W/mm^2)	Energy efficiency (%)	Deposition rate (g/min)	Building efficiency (%)
LMD	Powder	Laser	200-500	380-1000	$\approx 10^6$	<40	<8.3	<90
WAAM	Wire	Arc	1000-2000	1000-2000	$\approx 10^4$	<90	16.7-66.7	$\approx$ 100
WLAM	Wire	Laser	>1000	5-15*d_{wire}	$\approx 10^6$	2-5	1.5-48.0	$\approx$ 100
WEAM	Wire	Electron	<3000	<1600	$\approx 10^8$	15-20	<330	$\approx$ 100

The LMD process is a promising technique for repairing damaged metal components. In fact, this process has several features that are advantageous for the repair process. The heat flux density with a laser is higher than with an arc, which means that the energy is more focused on the material being deposited. As a result, the thermal energy is less dispersed to the rest of the part, limiting distortion of the part being repaired and reducing the size of the thermally affected area while maintaining strong metallurgical continuity with the substrate. In addition, the laser process is easier to implement for component repair than the electron beam process, which requires a vacuum manufacturing chamber. The use of powders allows for finer beads, which allows for better control of bead deposition within a confined pre-machining environment as used in repair processes. Finally, systematic assembly on CNC machines makes it possible to automate the repair process [5].

Table 1.5 summarizes the advantages and disadvantages of all processes that have the technical capability and flexibility to deposit material on damaged parts prepared as part of a repair process, according to my personal review of the studies read in the literature. The results show the particular interest in focusing on the LMD process, which has a large number of advantages over the other processes. For each characteristic, a score is assigned by comparing the ability of each process to perform the task. A score of - - corresponds to the least suitable process and ++ corresponds to the most suitable process.

Table 1.5: Performance comparison of processes capable of repair.

	Manual welding	Cold spray	Thermal spray	WEAM	WAAM	WLAM	LMD
Bead size	++	- -	- -	++	++	++	-
Deposit material efficiency	++	- -	- -	++	++	++	+
Build rate	+	-	-	++	++	++	+
Resolution	-	- -	- -	-	-	-	+
Surface finish	-	- -	- -	-	-	-	++
Porosity rate	-	- -	- -	+	-	+	++
Introduction of residual stress	- -	++	-	+	- -	+	+
Multimaterials	-	+	+	-	-	-	++
Automation capability	- -	-	-	+	+	+	++
Complex geometry	-	- -	- -	+	+	+	++
On-site application	++	+	+	- -	+	+	-
Operator safety	+	- -	- -	++	++	++	-
Repair	+	-	-	-	+	+	++

1.2.2 Laser metal deposition principle

LMD is a developed AM process for repairing damaged components, considering the many advantages that this technique offers. The flexibility of implementation and the quality of deposition with interesting performances make it a mature process. A wide range of materials can be deposited: stainless steel, maraging steel, nickel alloys, titanium alloys, aluminum alloys, copper alloys, cobalt alloys. This process is also known under other names such as Laser Cladding (LC), Laser-Powder Directed Energy Deposition (LP-DED), Direct Metal Deposition (DMD), Direct Laser Deposition (DLD), Laser Energy Deposition (LED) or Laser Energy Net Shaping (LENS) [53].

The principle is illustrated in Figure 1.9. It consists in creating a melt pool with a laser focused on the surface of a substrate. The powder is transported in tubes with a neutral carrier gas (helium or argon) from the powder tanks to the coaxial nozzle, which concentrates the powder stream in the melt pool that feeds it with feedstock. The deposition unit, which includes the coaxial nozzle and the optical path, is moved in translation in the three spatial directions to create the beads. Some machines have two additional rotational axes for complex fabrications. The fabrication chambers can be in a controlled environment under argon to prevent oxidation, or under air [52].

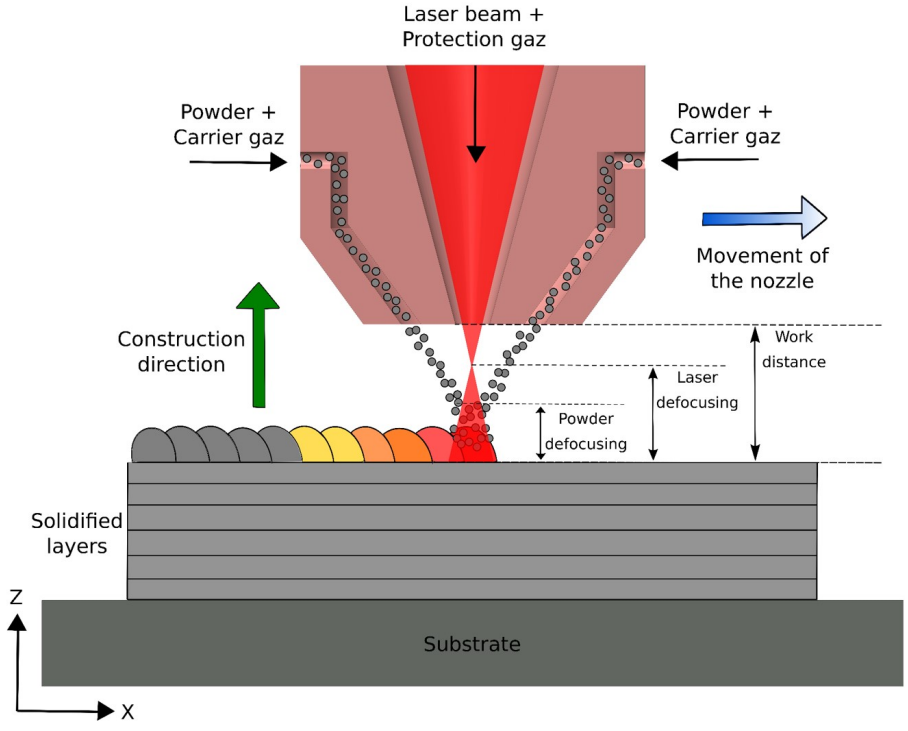

Figure 1.9: Principle of the LMD process.

1.2.3 Influential factors in laser metal deposition

Parameters

The literature lists a number of parameters that influence the characteristics of the manufactured parts [53, 52]. They are grouped into five categories and are summarized in the Table 1.6.

Table 1.6: Influential factors of laser metal deposition.

Laser	Powder	Substrate	Motion	System
Power	Material	Material	Deposition pattern	Oxygen content
Beam diameter	Internal porosity	Geometry	Scanning speed	Carrier gas flow rate
Beam profil	Morphology	Dimensions	Overlapping rate	Heat treatment
Working distance	Diameter distribution	Surface condition	Interlayer increment	
Wavelength	Mass flow rate	Temperature	Interlayer dwell time	

Many studies have been conducted to determine the most influential parameters on the microstructure of parts produced by LMD [54, 55, 56, 57]. The deposition pattern and the following LMD parameters: laser power (W), scanning speed (mm/min), powder mass flow rate (g/min), and overlapping rate (%), are those that most influence the bead and layer geometry, density ratio, and microstructure of the parts produced.

The Global Energy Density (GED) (J/mm^2), described by the Equation 1.2, is a key quantity widely used in the literature to quantify the energy delivered per unit area of material [53]. Knowing that the energy delivered by the laser is focused on the spot diameter, which is approximately the width of a bead.

$$GED = \frac{P}{d_{beam} * V} \tag{1.2}$$

Another parameter that can be introduced is the Linear Powder Mass (LPM), described by the Equation 1.3. This parameter determines the amount of powder delivered to the melt pool from the nozzle per unit length. Not all of the sprayed powder is melted in the process and a yield factor η can be introduced. The latter varies little with variation of the deposition parameters, but depends on the configuration of the machine and the nozzle. Typically, this yield is 13% on a LENS technology for H13 powder spraying [58].

$$LPM = \eta * \frac{Q}{V} \tag{1.3}$$

Interaction and solidification mechanism

The adsorption of the laser onto the substrate creates a melt pool, which is the liquid molten metal allowing the material deposition, and that is fed by the powder supplied from the coaxial nozzle. This powder is also melted by the combined effect of the laser and the melt pool. Sufficient laser energy absorbed by the substrate and particles causes rapid heating and melting of the area. When the laser leaves the molten pool area, rapid solidification of the molten metal takes place. The cooling and solidification mode depends mainly on the laser energy density and the interaction time [53].

The LMD process is a complex interaction of physical processes. In particular, the energy absorbed by the laser beam melts the substrate and powders, forming a melt pool in which strong fluid flow occurs, driven primarily by the surface tension gradient (or Marangoni shear stress). Heat transfer and fluid flow are strongly influenced by the local arrangement of the beads and the substrate surface, which can vary from location to location. Due to the highly transient nature of fluid flow, the shape of the melt surface (a free surface) is constantly changing, affecting the final surface quality [59]. The resulting solidification bead consists of a deposited layer and a remelted area in the substrate, as shown in Figure 1.10.

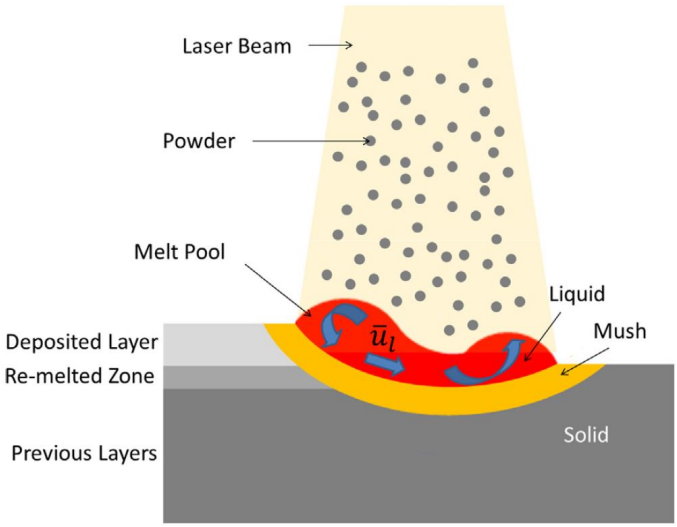

Figure 1.10: Presentation of the melt pool and the resulting bead [53].

As illustrated in Figure 1.11 and explained by Lippold *et al.*, the solidification mode is influenced by the combination of the temperature gradient G and the solidification growth rate R. The cooling rate G*R influences the size of the microstructure and the ratio G/R influences the morphology [24]. The scanning speed of about 1000 mm/min causes a very fast solidification of the melt pool. The temperature gradient between the melt pool and

the substrate is very high. Although the material has a low thermal conductivity, the energy is dissipated quickly and the solidification rate is in the order of $10^3 - 10^5$ K/s [60]. The cellular substructure is produced in LMD with a relatively large size around few µm compared to the PBF, where the cell have a size around 1 µm [61].

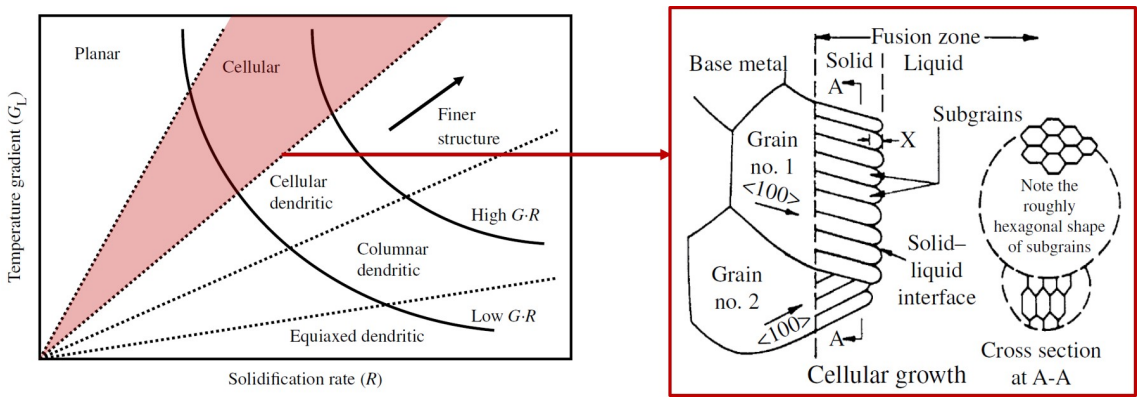

Figure 1.11: Effect of temperature gradient in the liquid, GL, and solidification growth rate, R, on solidification mode and cellular solidification modes that occur in LMD deposit [24].

LMD defect

The main objective of LMD manufacturing is to obtain a material with a relative density greater than 99%, with good mechanical strength after manufacturing. However, defects can occur in several forms. Porosity is the most common defect in AM and can be categorized into two forms: interlayer porosity and intralayer porosity, each of which is shown schematically in Figure 1.12.

Interlayer porosity is due to insufficient energy input to melt the powder, resulting in lack of fusion. These porosities are observed at the substrate/deposit interface, between layers, or between beads. They result from either too low GED or too high a powder mass flow rate, or a combination of both. Their geometry is usually irregular and large, caused by too rapid solidification of the melt pool that failed to fuse with the previous layer [56].

Intra-layer porosities are generally spherical in shape and occur at random locations. They are the result of vaporization of the elements at the low vaporization temperature point or keyholing [62]. If the GED supplied by the LMD process is high enough, the temperature under the beam can exceed 3000°C. Elements with low vaporization temperature vaporize, such as manganese (2061°C), chromium (2671°C), nickel (2913°C). High dilution corresponds to the appearance of intra-layer porosity. Intra-layer porosity also depends on the properties and uniformity of the starting powder [63]. If the starting

powders do not have a uniform particle size distribution and contain internal porosity, the porosity in the final product will be higher [64].

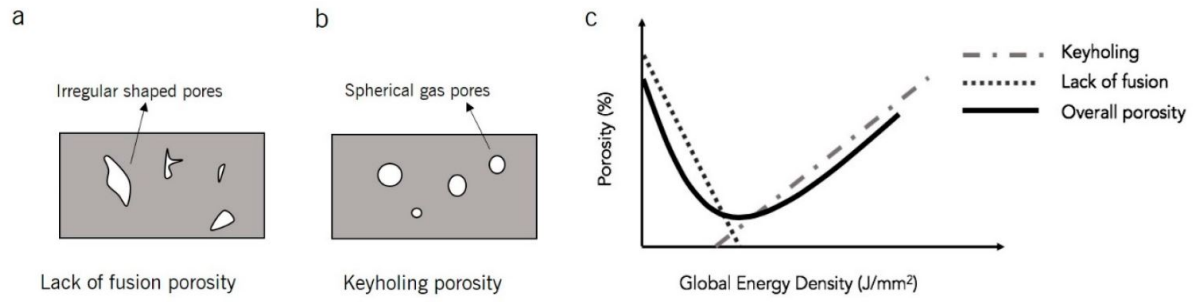

Figure 1.12: (a) Interlayer porosity, (b) intralayer porosity and (c) the intersection of interlayer and intralayer porosity with respect to GED [56].

Cracks or distortions may also occur in LMD parts due to the introduction of high residual stresses caused by the laser process. The sudden release of stress leads to the formation of cracks in the material [51].

Deposit geometry

Most parametric optimizations performed on the LMD process aim to determine the influence of process parameters on bead and layer geometries [65, 66, 67, 68, 69]. These geometries are important features for controlling the porosity rate in the part to be minimized. They make it possible to obtain a dense deposit with metallurgical continuity between the layers. As shown in Figure 1.13, three output parameters are sought:

- the width of the bead (W);
- the effective height (H_{eff}), which corresponds to the added height to the structure;
- the diluted height (H_{dil}), which corresponds to the thickness of the lower layer remelted with the deposited bead.

The remelted area in the previous layer is defined by the dilution rate, which can be calculated thanks to Equation 1.4, can also be calculated from these data. According to the literature, sufficient metallurgical continuity with the substrate and between the layers can be obtained with a dilution rate between 10% and 30% [56]. Below 10%, the dilution rate is not considered sufficient to avoid the formation of porosities and, in particular, lack of fusion between the beads and between the layers. Above 30%, keyholes are reported in the literature.

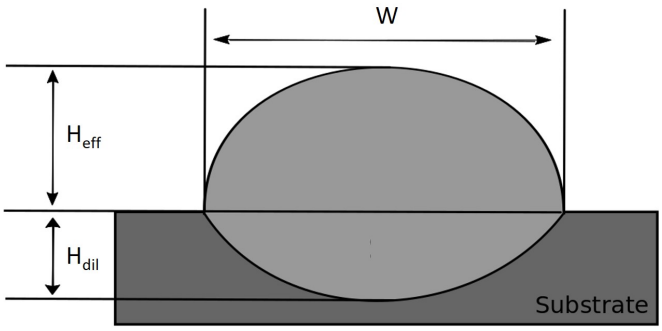

Figure 1.13: Illustration of a bead cross-section exhibiting the geometric parameters studied.

$$D\% = \frac{H_{dil}}{H_{dil} + H_{eff}} \tag{1.4}$$

Laser power, scanning speed and powder mass flow rate are correlated parameters through Equations 1.2 and 1.3. The variation of a single deposition parameter will cause a linear trend on the geometric parameters of the LMD-deposited bead. In fact, the work of El Cheikh *et al.* [66] on the influence of process parameters on the geometry of SS316L single tracks showed that at constant LPM, increasing power resulted in wider, taller, and more dilute beads as the GED increased with increasing power. Similarly, at constant GED, increasing the powder mass flow rate results in wider, taller and less dilute beads because more material is added to the melt pool and less energy is transferred to the substrate. Finally, increasing the scanning speed results in thinner beads in height and width because less energy and material is available per unit length. These trends can be seen in Figure 1.14. Other examples of parametric optimization in the literature follow these trends [65, 67, 68, 69].

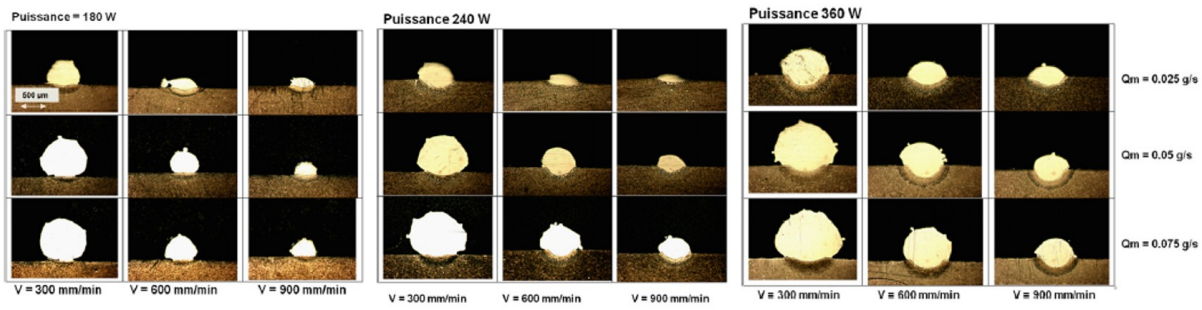

Figure 1.14: Single-track cross-sections according to the variation of the process parameters P, V and Q [66].

If the GED is too low and/or the LPM too high, the deposited beads exhibit a lack of fusion with the substrate, resulting in porous deposits, as shown by de Oliveira *et al.* [65] for nickel-chromium based alloy powder deposits on C45 steel substrates. From an LPM of 63 g/m, a power of at least 1000 W for a spot diameter of 3.2 mm is required to allow metallurgical continuity of the beads to the substrate.

This data is used to calculate the step-over (SO) in mm, which is the distance between two beads. This value is a function of the overlapping rate (OR) in % and the bead width (W) in mm, as described in the Equation 1.5.

$$SO = W * (1 - OR) \tag{1.5}$$

The bead geometry resulting from the deposition parameters combined with the overlapping rate determines the height of the built-up layer. Nenadl *et al.* [70] and Li *et al.* [71] have shown that increasing the overlapping rate (or decreasing the step-over) results in an increase in the layer height (Figure 1.15). Indeed, more material is deposited in the same area than with a large spacing between the beads, which leads to the increase of the overall height. In both studies, it is observed that doubling the overlap rate between two consecutive beads results in a doubling of the layer height.

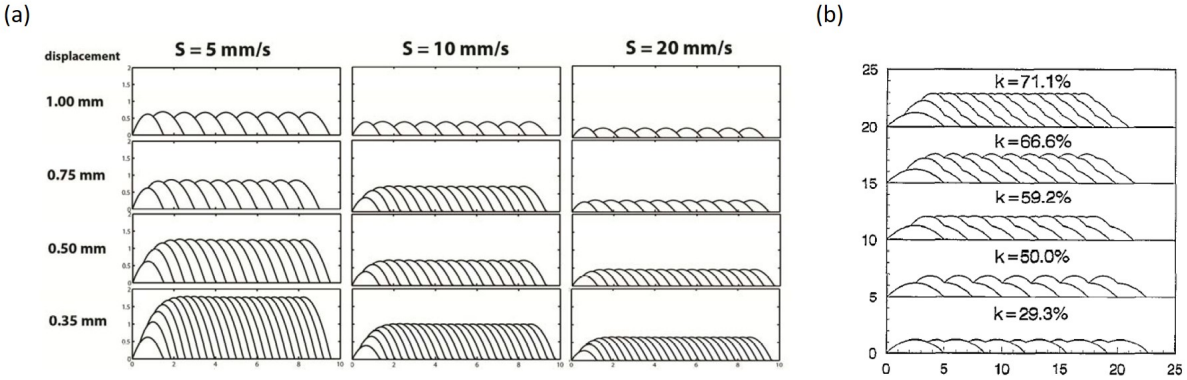

Figure 1.15: Study of the influence of the overlapping rate on the layer height from (a) [70] and (b) [71].

However, if the overlapping rate is too high or the step-over is too low, the layer requires the deposition of several beads to reach a constant height. There is also a risk of interbead porosity. Therefore, it is necessary to determine an optimal overlapping rate. The literature indicates that an overlapping rate of 30% is commonly used in LMD fabrication to avoid the formation of interlayer lack of fusion [54].

To successfully produce high density parts with a satisfactory surface finish, the various

manufacturing parameters must be optimized. The objective is to avoid the formation of interbead or interlayer porosity due to low GED. In contrast, a too high energy density would lead to the formation of keyholes or gas bubbles trapped in the metal matrix. Porosity must be avoided to achieve good mechanical properties and corrosion resistance [56].

Residual stress

Besides the geometry of the beads and layers, the residual stress in a manufactured part is an important issue. If tensile stresses are too high, the part may eventually crack prematurely, rendering it unusable. These stresses are caused by the heating and cooling cycles of successive laser passes. As explained in the Figure 1.16, during the laser pass, the heat creates a compressive stress as the material expands. Then, during the cooling phase of the bead, the shrinkage of the material causes tensile stress in the upper layers and compressive stress in the lower layers [72].

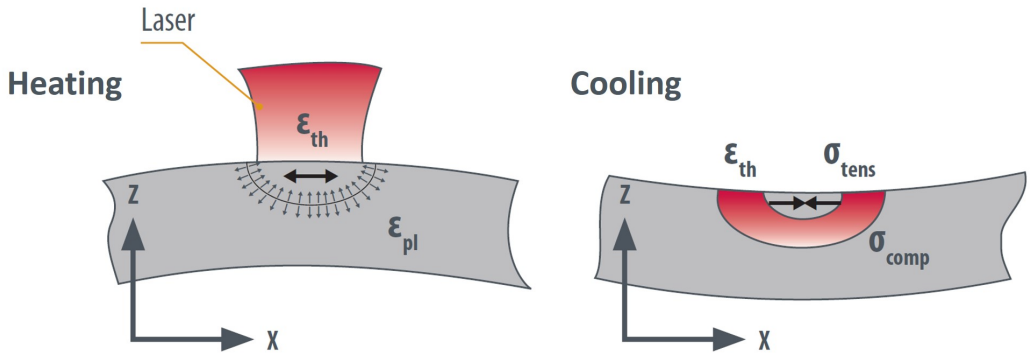

Figure 1.16: Mechanisms at the origin of residual stresses [72].

Residual stress is a result of the material melting process. The distribution of residual stresses in the part is complex due to the succession of liquid-solid passages during the manufacturing process. On the other hand, there are methods to reduce the intensity of residual stresses by reducing the thermal gradient between the melt and the substrate and thus the solidification rate.

Piscopo *et al.* [73] explain that increasing the GED power by increasing the power or decreasing the feed rate reduces residual stresses in an SS316L cube produced by LMD. The results of the study show an overall reduction in residual stresses in the part and up to a 61% reduction in tensile residual stresses at 1 mm depth in the cube with doubling the laser power. Similarly, reducing the feed rate by 37.5% reduced residual stresses overall and up to 42% at 1 mm depth.

Ding *et al.* [74] suggest preheating the substrate for 12CrNi2 deposition to reduce the thermal gradient between the melt and the workpiece. As shown in Figure 1.17, their work demonstrated a reduction in residual stress intensity of the order of 29% and 28% for longitudinal and transverse stresses, respectively, by preheating the substrate to 300°C compared to a substrate with an initial temperature of 20°C.

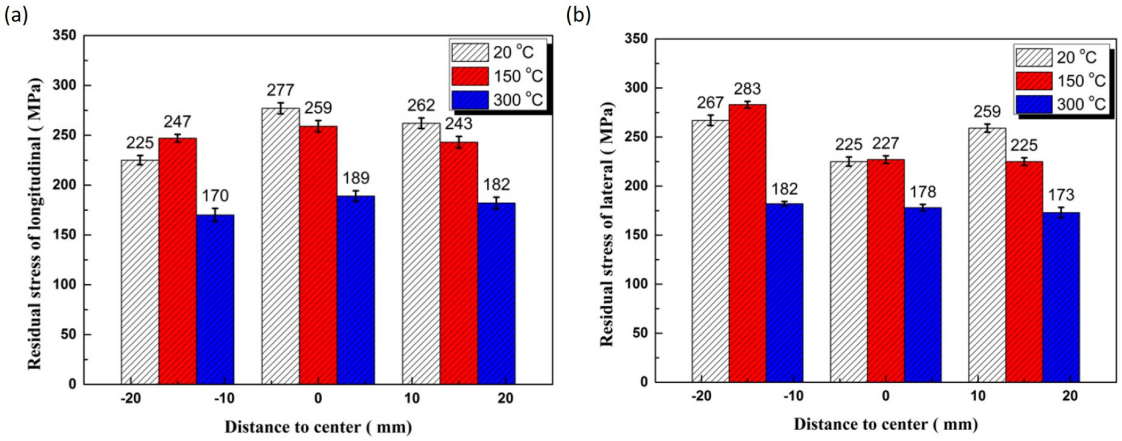

Figure 1.17: (a) Longitudinal stress and (b) lateral stress of test specimen preheated at different temperatures. [74].

Another method is to reduce the size of the substrate as much as possible in order to increase the overall temperature of the part and thus reduce the thermal gradient [75]. However, this technique results in greater distortion of the substrate under stress intensity. Finally, Saboori *et al.* [76] suggest using a zigzag deposition strategy with 67° rotation between each layer instead of 90° to reduce stress intensity.

1.2.4 LMD-printed SS316L

Microstructure

The microstructure of SS316L samples deposited by LMD is characterized from the macroscopic to the nanoscopic scale. As shown in Figure 1.18 (a), the melt pool boundaries are visible after etching at the macroscopic scale. These are the boundaries left by the melt pool as it is diluted in the lower layer. Still at the same scale, observations highlight the columnar morphology of the grains oriented toward the center and the advance of the melt pool, as shown in Figure 1.18 (b). Epitaxial growth of grains between layers is also observed in the <100> crystallographic direction. The grain size can vary from 50 µm to a few mm [60].

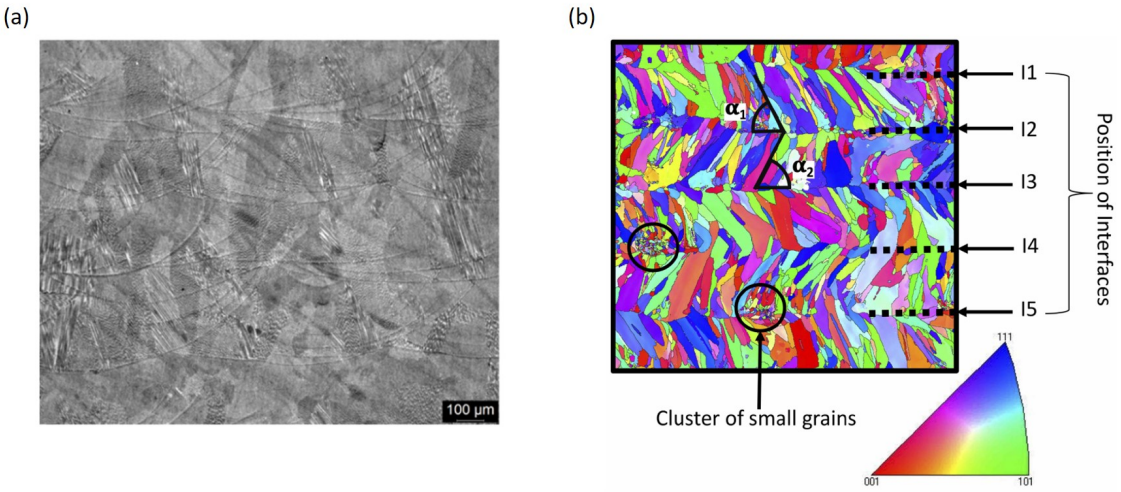

Figure 1.18: (a) SEM observation after chemical etching and (b) IPF mapping of LMD-printed SS316L [77].

At the microscopic scale, the grains contain a cellular substructure formed by the high cooling rate of the melt pool, as explained in Section 1.2.3. The three-dimensional structure of the cell structure is similar to a honeycomb structure, and the morphology of the cell structure is different depending on the direction of observation. The Figure 1.19 shows the cross, horizontal and longitudinal sections of the cell structure in an LMD-printed SS316L. Thus, depending on the cross-section of the cell structure extract, it can be a circle, an ellipse or two parallel lines, widely observed in AM metals and alloys [61]. This substructure is sensitive to the cooling rate of the part, as shown in Figures 1.19, since its dimensions increase significantly from the order of 1 µm for the LPBF process to 16 µm for the LMD process due to cooling rates in the order of 10^6 and 10^4, respectively. Even within the LMD process, the different GED used influence the cell size. In fact, according to the work of Ma *et al.* [78], the 90% increase in GED from 51 J/mm^2 to 85 J/mm^2 results in a 533% increase in cell size from 3 µm to 16 µm due to the different projection nozzle configurations.

The cell substructure is the result of a hexagonal network arrangement of dislocations, but also of segregation of chemical elements [61]. Several authors have emphasized the difference in chemical composition between the center of the cells and the cell boundaries [79, 80, 81]. The results show that the cell edges are enriched in iron, chromium, molybdenum and manganese and depleted in nickel. The exact chemical compositions of each zone given by Tan *et al.* [80] indicate that the cell centers correspond to austenite and the cell junctions to residual delta ferrite.

Using Equations 1.6 and 1.7, which determine the equivalent chromium and nickel of

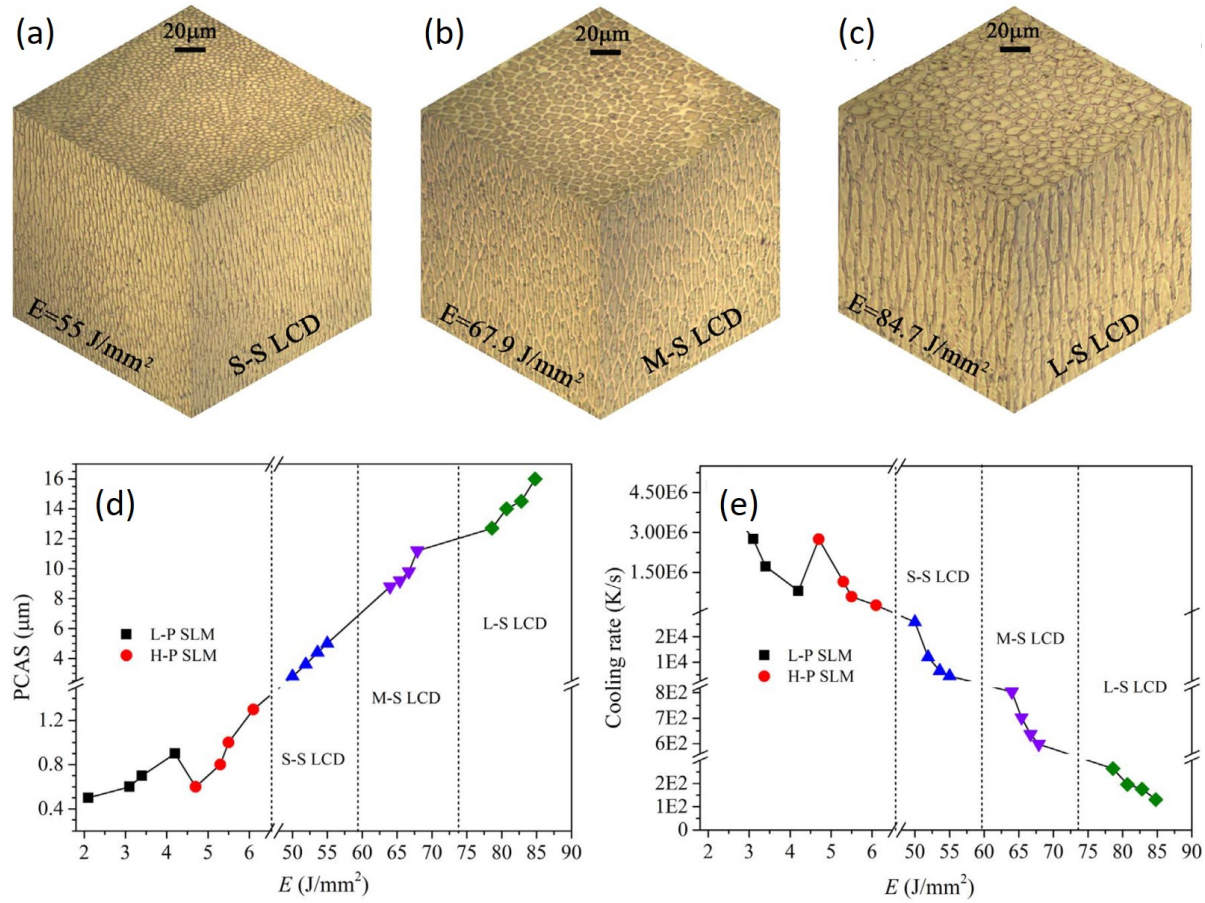

Figure 1.19: (a), (b) and (c) cellular substructure of SS316L samples produced by LMD using different GED and effect of GED on (d) PCAS and (e) cooling rate of SS316L samples produced using LPBF (SLM) and LMD (LCD) [78].

a stainless steel from its chemical composition and the Schaeffler diagram (Figure 1.20 (a)), it is possible to determine the proportion of austenite and ferrite in the steel studied. The solidification mode described in Figure 1.20 (b) is framed by the values given in Table 1.7. In the previously cited papers [79, 80, 81], the ratio Cr_{eq}/Ni_{eq} was in the interval allowing solidification in the AF mode. This explains the difference in chemical composition between cell centers and cell boundaries and the presence of ferrite in the LMD-printed deposits.

$$Cr_{eq} = Cr + Mo + 1.5 * Si + 0.5 * Nb \tag{1.6}$$

$$Ni_{eq} = Ni + 30 * C + 0.5 * Mn \tag{1.7}$$

Finally, at the nanoscale, oxide inclusions are detected and uniformly distributed

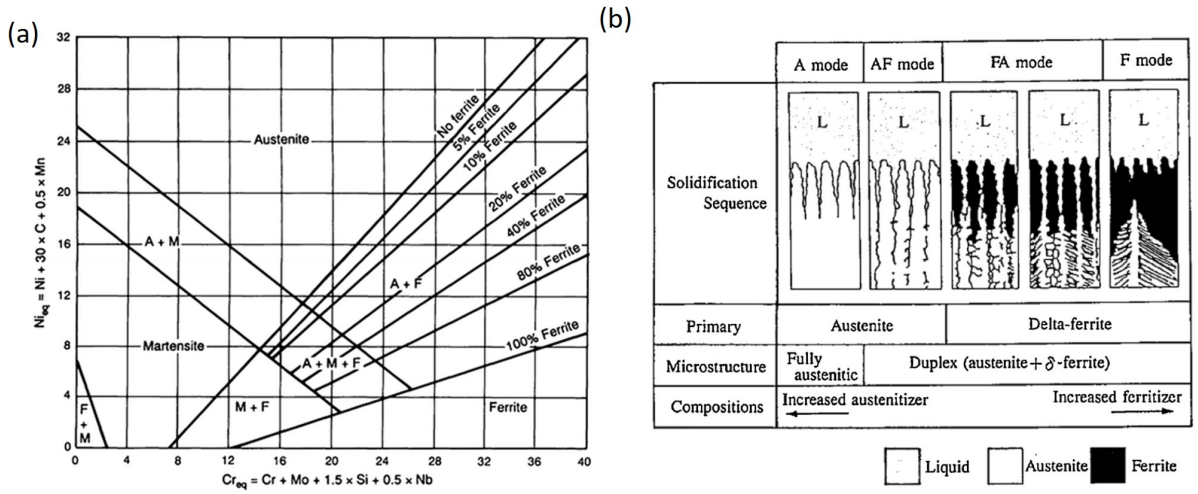

Figure 1.20: (a) Schaeffler's diagram and (b) austenitic steel solidification diagram [80].

Table 1.7: Solidification mode identification.

Solidification mode	$Cr_{eq}/Ni_{eq} ratio$
Ferritic (F) mode	$1.95 \leq Cr_{eq}/Ni_{eq}$
Ferritic-Austenitic (FA) mode	$1.48 \leq Cr_{eq}/Ni_{eq} \leq 1.95$
Austenitic (A), Austenitic-Ferritic (AF) mode	$Cr_{eq}/Ni_{eq} \leq 1.14$

in the cell boundaries. The formation of these inclusions is the result of oxidation of highly oxygen-reactive elements such as manganese, silicon, titanium, and aluminum. The oxygen comes from the atmosphere in the manufacturing chamber or from the passive layer that forms on the powders during manufacturing. Under laser energy, this layer breaks down and oxygen diffuses into the melt by reacting with elements with an affinity for oxygen [61]. Barkia *et al.* [81] found silicon oxides and precipitates rich in Mn, Mo and Cr. Similar results are found in the work of Tan *et al.* [80] and Zietala *et al* [79].

Mechanical properties

The mechanical properties of the specimens produced by LMD have higher tensile strength but lower elongation at break than SS316L produced by conventional methods, like represented in Figure 1.21. According to the authors, the magnitude of the elongation varies depending on the proportion of defects in the deposit that lead to premature cracking of the specimen. For example, Barkia *et al.* [81] found an elastic strength of 440 MPa and an elongation at break of about 52% for the LMD process instead of 170 MPa for YS for a wrought SS316L. In contrast, Zhang *et al.* [82] found a higher UTS

of about 560 MPa, but an elongation at break of only about 20%. This difference is due to the different deposition parameters used in each study, which cause variations in the morphology and size of the cell substructure, as well as the concentration of defects. Despite this variation, the high performance of these parts is attributed to the unique microstructure composed of small cell sizes, the presence of residual delta ferrite, a dense network of dislocations, and the presence of nano-oxides dispersed in the matrix, which strengthens the material [83].

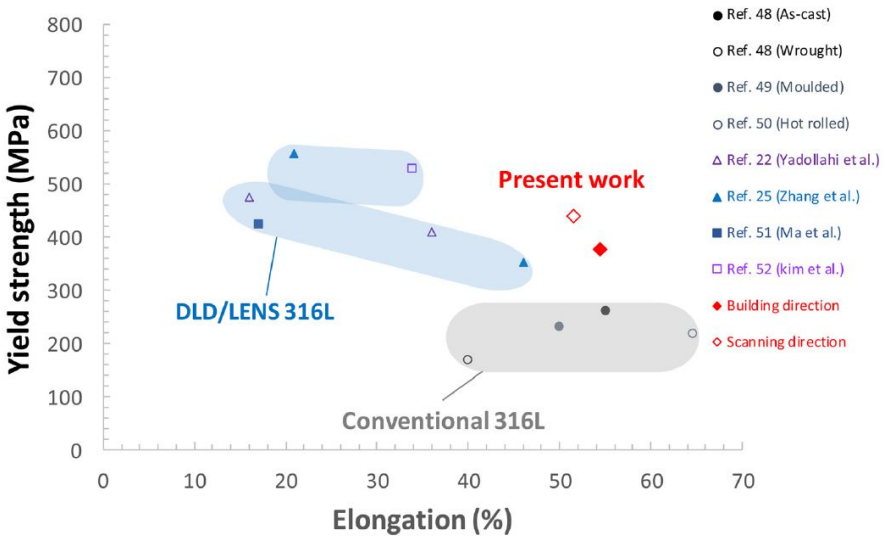

Figure 1.21: Tensile properties of LMD-produced SS316L [81].

Similarly, the literature shows an anisotropy in the mechanical properties of the specimens produced by LMD. In fact, the tensile specimens extracted in the horizontal direction have better mechanical properties than those collected in the vertical direction. The presence of elongated porosities due to the deposition direction of the beads in the direction perpendicular to the vertical specimen is a cause of the low elongation in this direction [83]. Moreover, the particular microstructure with columnar and elongated grains in the building direction causes different dislocation movements in the microstructure and results in heterogeneous tensile properties [84].

Corrosion resistance

The corrosion resistance of stainless steels in chlorinated solutions such as seawater is due to the formation of a layer of chromium oxide $Cr2O3$ on the surface of the material. This compact, adherent and therefore protective layer is called the passive layer: it forms a barrier separating the steel from its environment. Other elements, such as molybdenum,

can improve the corrosion resistance of the steel by stabilizing the layer, especially in acidic environments. How the material is going to be elaborated will thus influence the formation and resistance of this passive layer.

As seen in the previous section, the microstructure of an LMD-printed part is different from that of a conventional SS316L. The literature shows differences in corrosion behavior. Revilla *et al.* [85] compared the corrosion behavior of conventional, SLM, and LMD printed SS316L in a 3.5 wt.% NaCl solution. The results show similar corrosion potentials for each sample around -73 ± 10 mV due to very similar chemical compositions. However, the stability of the passive layer varies greatly depending on the fabrication technique. The passive layers of the samples have a stability interval $E_{breakdown} - E_{corr}$ of 499 mV, 571 mV and 1155 mV for the conventional, LMD and SLM methods respectively. The differences in passivity between the samples appear to be related to the marked differences observed in the dimensions of the microstructural features. The fineness of the microstructure (distribution of alloying elements) in the SLM < LMD < wrought order could lead to the growth of a more compact, stable and less defective passivation layer.

These observations are confirmed by Shen *et al.* [86] who show in stainless steel coatings produced by LMD that pitting occurs at the interface between the dendritic and interdendritic regions due to the potential difference between the two zones caused by the difference in chromium concentration. As illustrated in Figure 1.22, they show that by obtaining a finer grain substructure, the number of nucleation sites of the passive oxide layer can be increased, resulting in a thicker passive layer that is more resistant to corrosion. The comparison between standard stainless steel and LMD stainless steel is subjective because it depends on the quality of each steel. Therefore, using a lower GED results in a finer cellular substructure and therefore improved corrosion resistance in chlorinated environments.

As observed in the work of Revilla *et al.* [85] and shown in Figure 1.23, corrosion takes place within the cells of the grain substructure, which are less rich in chromium than the cell boundaries. These observations are reported several times in the literature dealing with the corrosion of SS316L in chloride solution [87, 88, 86]. However, changes in the solidification mode and chemical composition of the powders may alter this mode of attack on the cellular substructure and require further study to draw conclusions.

A chemical composition of SS316L rich in minor elements such as sulfur and phosphorus can reduce the corrosion resistance. In fact, these elements can form inclusions in the matrix such as MnS. These inclusions are pitting initiation sites as observed in the work of Laleh *et al.* [89].

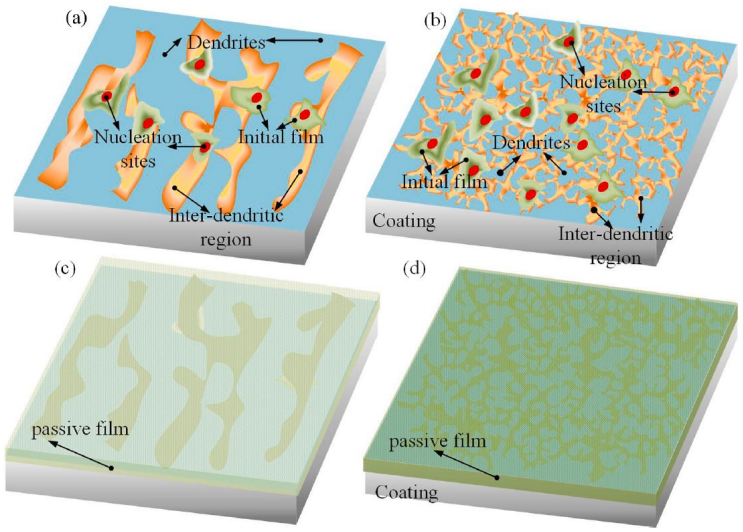

Figure 1.22: Role of the dendrite size on the nucleation and formation process of passive film, (a) and (c) on coarsened dendrites, and (b) and (d) on refined dendrites [86].

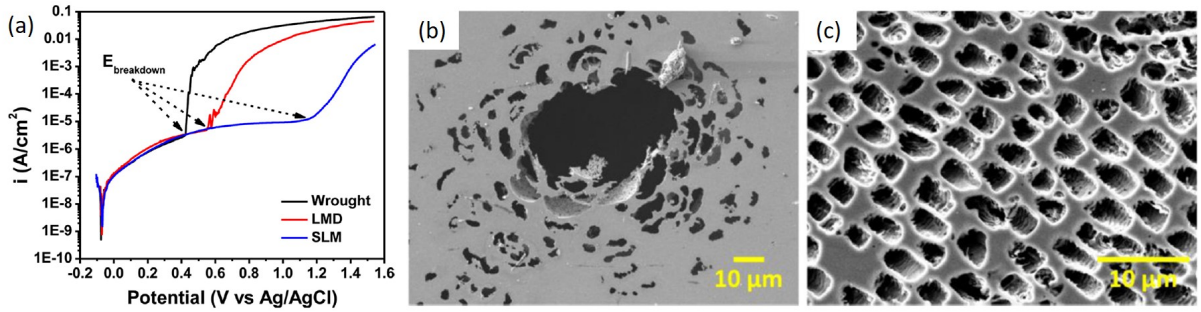

Figure 1.23: (a) Potentiodynamic polarization curves of wrought, LMD, and SLM 316 L stainless steel specimens in 3.5 wt.% NaCl and high magnification secondary electron images of the corrosion attack after the potentiodynamic polarization experiments for the (b) wrought and (c) LMD [85].

1.2.5 Summary

As AM has evolved over the past few decades, many technologies have matured. Some of these technologies have specialized in the production of metal parts, but only DED technology has the ability to deposit material on existing parts, making it suitable for repair. Of all the processes in this technology, the LMD process has the finest deposition bead (380-1000 µm) due to the use of powders that allow the thermal affected area to be limited and a better resolution of the deposition compared to the others DED processes (minimum 1000 µm for WAAM), as observed in Table 1.4.

This fusion process involves complex physical phenomena that take into account a

large number of process parameters (laser power, scanning speed, powder mass flow rate, overlapping rate, deposition pattern). These parameters must be optimized to control the geometry of the beads and layers and to achieve dense and crack-free deposits.

LMD parts printed in SS316L have a coarse columnar microstructure that is elongated in the direction of fabrication, due to the thermal gradient between the melt pool and the part. There is a cellular substructure with a size of around few µm within the grains resulting from segregation of chemical elements and dislocations. This unique microstructure results in different mechanical properties than a conventional stainless steel. YS and UTS are higher with 170 MPa and 440-560 MPa respectively, but EAB is reduced (20-52%). For corrosion resistance in seawater, dense LMD-printed parts have better passive film stability than conventional stainless steel due to better distribution of chemical elements.

The LMD process has demonstrated its ability to produce dense SS316L parts with interesting properties. However, it is necessary to study the condition and behavior of a part repaired by this process, mixing a printed LMD deposit and a conventional substrate, to determine the influence of the LMD process parameters on the quality of the repair.

1.3 Laser metal deposition repair

1.3.1 Generalities

With the will to circularize the economy and to develop the 9Rs method "refuse, rethink, reduce, reuse, repair, refurbish, remanufacture, repurpose, recycle, recover" for AM, repair with AM methods has developed rapidly in the literature since the 2000s, as shown in Figure 1.24 (a). The authors study most of the materials commonly used in the industry, such as cast iron, steel, Inconel, titanium alloys, cobalt alloys [90]. The repair is applied to a large number of parts, such as turbine blades, injection molds, mechanical equipment, gears... (Figure 1.24 (b)). Finally, as shown in Figure 1.24 (c), half of the publications in the literature concern repairs performed with the LMD process [91]. The interest of researchers in this promising process is due to its flexibility and the quality of its deposits, while limiting its effect on the original part.

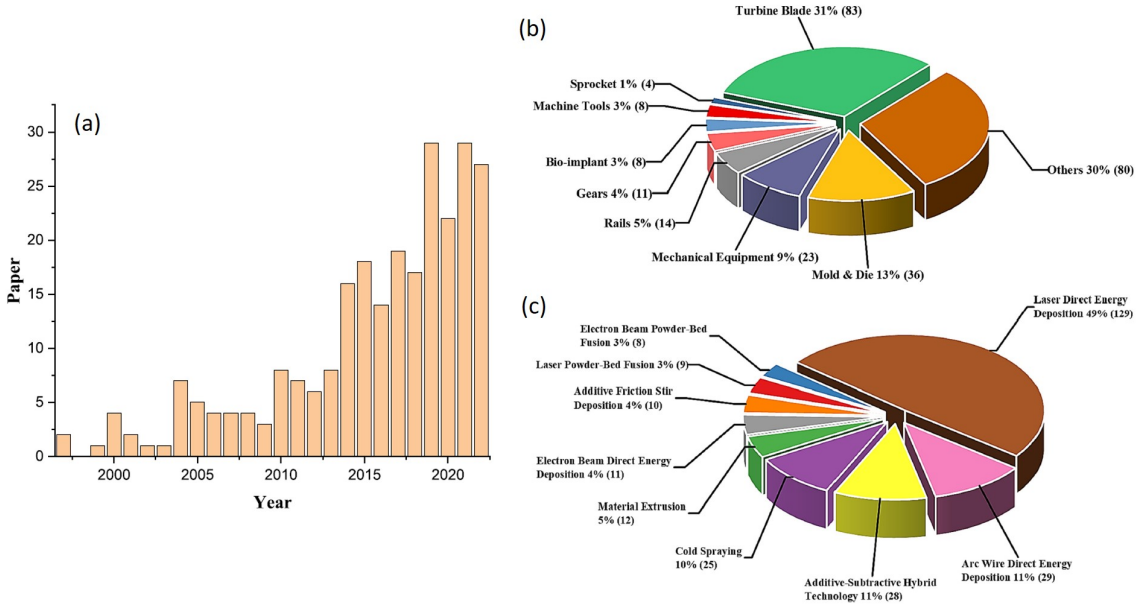

Figure 1.24: (a) Research articles published about repair, (b) product-specific deployment and (c) relative status of AM technologies for repair [91].

Numerous studies of repairing damaged components using the LMD process focused on turbine blades. In fact, turbine blades in the power generation and aerospace industries are often damaged at their tips. However, as shown in Table 1.4, LMD beads are the smallest of the DED technologies in the 200 to 500 µm range. This parameter is very important when repairing thin turbine blades. In addition to the standard advantages of this process, the epitaxial growth of the grains between the layers was sought because the blades are produced with a single crystal microstructure, which allows them to buckle more than

with a polycrystalline microstructure. Brandt *et al.* [92] demonstrated the feasibility of using this process to repair steam turbine blades in fossil-fired power plants. The authors developed the technique and founded a company to commercialize it. Subsequently, several articles were published on optimizing the deposition parameters to obtain a single crystal microstructure [93], observing their influence on the properties of the blade after repair [94], and recovering the original dimensions of the part by limiting the machining [95], as shown in Figure 1.25. The thinness and low dilution of the deposited beads is also an attractive feature for repairing metal joints, as shown in Figure 1.25 (b).

As shown in Figure 1.25 (c), the LMD process can be used to repair more massive parts, such as boat engine crank pins, which require reloading of material after the surface is abraded as the piston rod rotates. Other studies focused on the repair of cast iron, such as engine blocks, because the small HAZ made it possible to avoid the formation of martensite in the part and the cracking of the block during engine operation. To reduce the risk of martensite formation during the repair process, laser preheating steps were proposed [96]. Moreover, the geometric precision of the deposits and the low distortion of the parts are an advantage for the repair of foundry or plastic injection molds, which can return to their original dimensions after repair. Foster *et al.* [97] demonstrated the feasibility of this process for repairing foundry molds with Stellite-21. The part is easy to repair with LMD and the wear resistance is excellent compared to other repair processes.

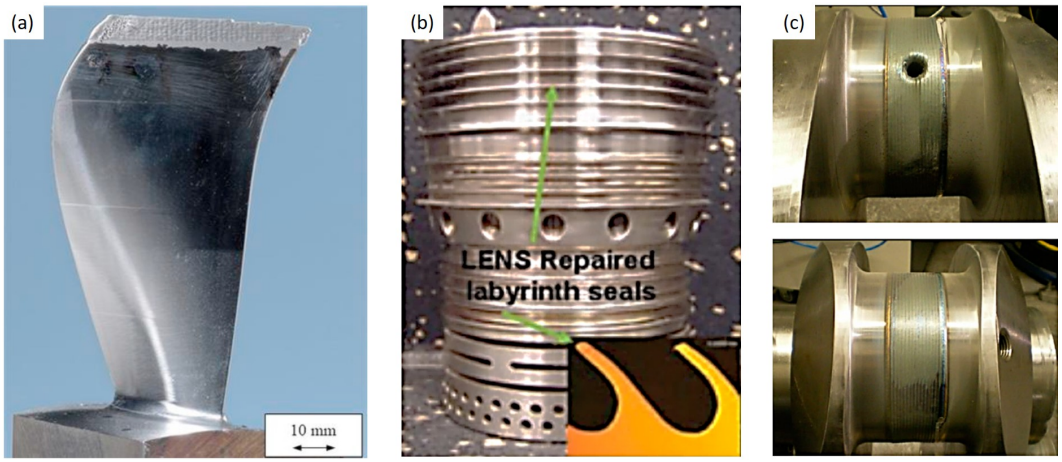

Figure 1.25: Examples of repair for (a) turbine blade in Inconel 718 [95], (b) Inconel 718 compressor seal [98] and (c) crankshaft segment [99].

In addition, some companies are beginning to patent LMD repair techniques to protect this know-how, which is in full development like Westinghouse, which offers a solution for the repair of stainless steel components used in the nuclear industry with pre-machining, material removal by LMD, then inspection by non-destructive methods [17].

1.3.2 Heterogeneous characteristics of repaired parts

In the literature about LMD-repaired parts, the recurring observation is the heterogeneity of the microstructure and the residual stresses in the repairs. These characteristics influence the mechanical behavior and the corrosion resistance of the repair and can lead to degraded properties.

The presence of porosity in the deposits and the lack of fusion at the deposit/substrate interfaces is frequently cited in the literature among the defects that lead to these degraded properties. This phenomenon is usually caused by poor optimization of the deposition process parameters. As observed in the work of Oh *et al.* [100], who studied the repair of SS316L grooves using various repair methods, the insufficient dilution of the beads caused porosity on the pre-machining surfaces that were not perpendicular to the laser. Thus, what the authors consider to be cracks are simply lack of fusion that does not provide metallurgical continuity with the substrate. This results in a severe degradation of the mechanical properties of the order of 50% for the UTS and 90% for the EAB compared to the reference substrate, as shown in Figure 1.26.

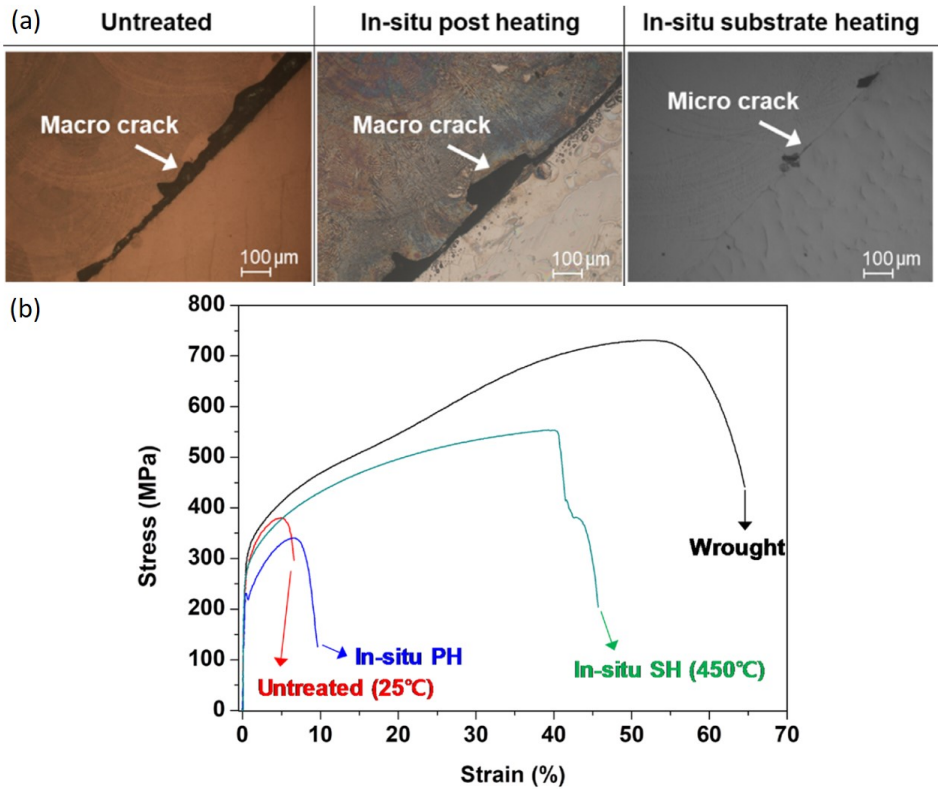

Figure 1.26: (a) Repair cross-sections with different methods exhibiting the lack of fusion at the interface and (b) the resulting degraded tensile mechanical properties [100].

Another specificity is the particular microstructure of the repair. It is the result of a combination of a conventional microstructure and a microstructure typically found in additive manufactured parts. In the works of Balit *et al.* [101], a grain size gradient between the SS316L wrought substrate and the SS316L LMD-printed part is observed (Figure 1.27 (a)). On one side the grains are fine and equiaxed with an average grain size of 7.2 ± 3.9 µm and on the other side they are long and columnar with an average grain size of 36 ± 20.9 µm. In addition, the grains of the first layer do not follow the trend of the rest of the deposit because of epitaxial growth from the fine grains of the substrate. This leads to an increase in hardness of 200 µm on both sides of the interface (Figure 1.27 (d)). This is explained by a reinforcement effect on the substrate side and a moderate grain growth area compared to the rest of the deposit on the deposit side (Figure 1.27 (a)). In addition, in-situ SEM tensile tests showed that the repaired samples have the lowest mechanical properties (Figure 1.27 (b)). In fact, this result is explained by a homogeneous deformation in the substrate due to fine and equiaxed grains and a heterogeneous deformation in the deposit due to long and columnar grains. On the other hand, the interface exhibits little deformation due to its higher hardness (Figure 1.27 (c)). Incompatibility of deformation between these three zones leads to degradation of mechanical properties. In fact, the Yield Strength (YS) of the repaired sample (430 MPa) is higher than that of the substrate (347 MPa), largely due to the LMD printed part. The repaired part shows a decrease in its UTS, 630 MPa versus 650 MPa, and a greatly reduced EAB, 46% versus 91% for the substrate. Similar results are found in the work of Guévenoux *et al.* [102] using the same analysis techniques but with an Inconel 718 assembly.

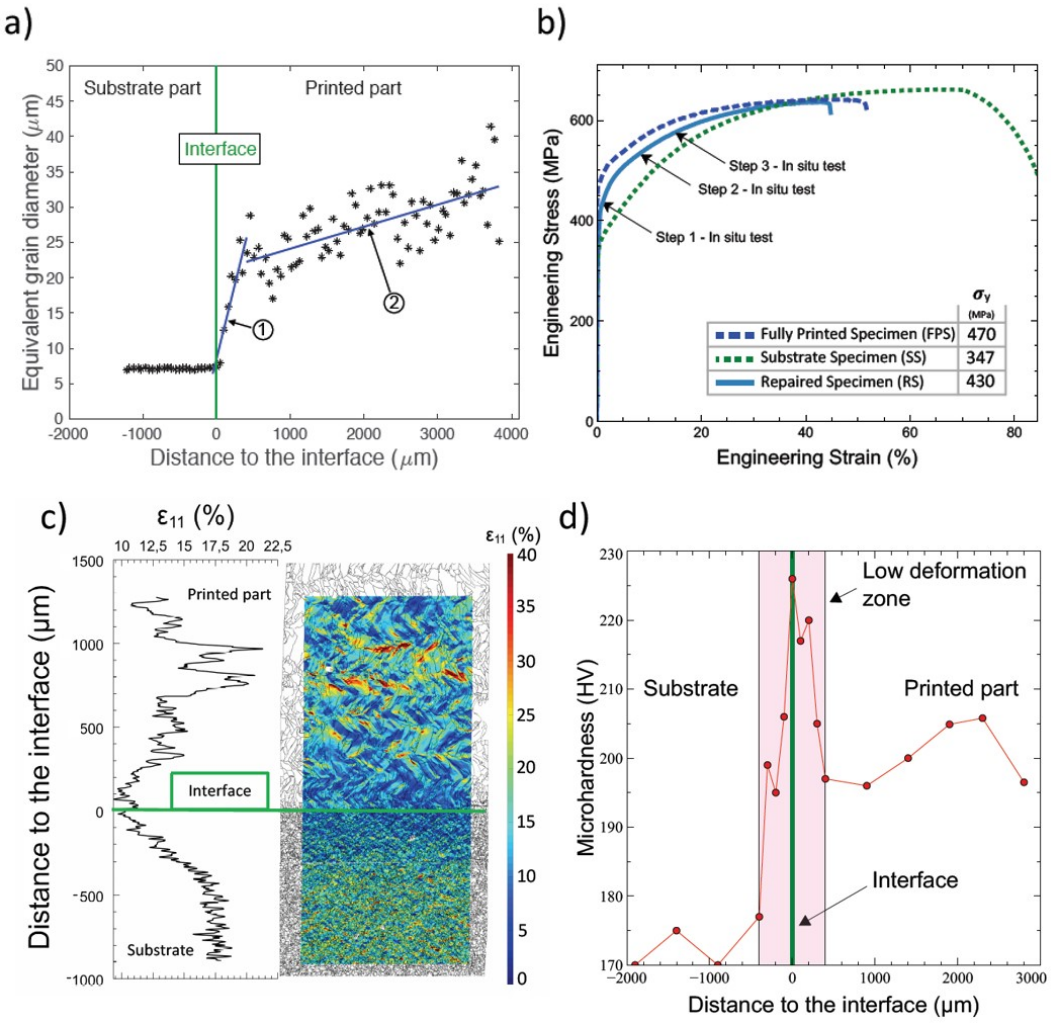

Figure 1.27: (a) Evolution of the grain size in the substrate/deposit interface, (b) tensile stress-strain curves of different tests, (c) evolution of the axial strain for the step of deformation of 17% and (d) microhardness distribution in the interface highlighting the peak [101].

The microstructure is highly dependent on the process parameters and the variation of a single parameter locally can significantly change the properties of the zone. Marazani *et al.* [103] repaired grooves with a variation of the different deposition parameters (laser power, spot size, scanning speed, ...) for Ti-6Al-4V material. For all the deposition parameters, the microhardness appears to be higher in the center of the deposit, with some variation depending of the parameter values. Similar results are found in the work of Paydas *et al.* [104] as shown in Figure 1.28. According to the authors, the thermal history of the part is involved in the increase of this hardness in the deposit and the variation of the hardness according to the different manufacturing parameters used. In fact, the rapid solidification of the melt pool creates a fine cell substructure that causes

a high hardness. This increase in hardness is accentuated when the GED is low, as in Figure 1.28 (a), compared to a high GED (Figure 1.28 (b)), caused by the difference in cell size according of the used GED, as observed in Figure 1.19 and which remains similar for titanium alloys.

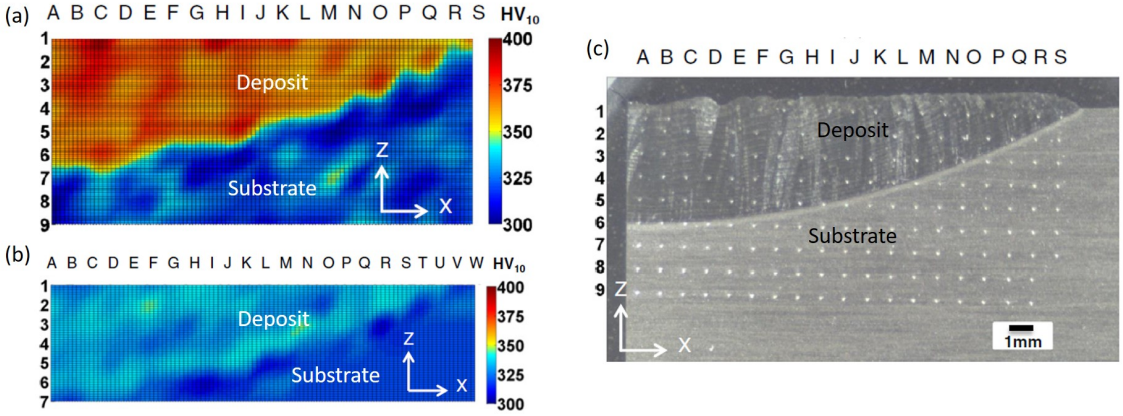

Figure 1.28: Hardness mapping in the repair cross section with (a) high GED, (b) low GED and (c) position of the indentation [104].

Liu *et al.* [105] deposited AISI4140 and INC718 on AISI4140 substrates to observe the tensile behavior of these hybrid specimens. The fractures all initiated and propagated within the deposit, indicating lower yield strength in these areas. On the other hand, as shown in Figure 1.29 (b), the cast AISI4140 and LMD-printed INC718 materials have the same hardness, but the interface between the two has a lower hardness. This condition results in heterogeneous properties and potentially different fatigue behavior.

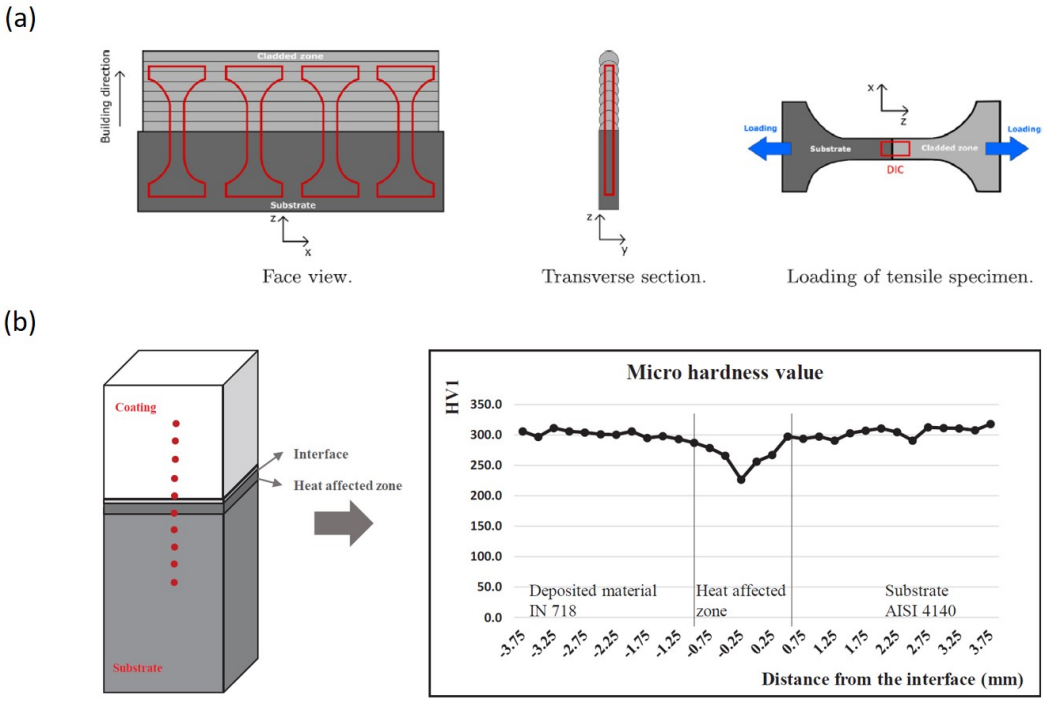

Figure 1.29: (a) Geometry of the repaired specimen and loading configuration [102] and (b) hardness distribution on the hybrid specimen [105].

As explained in Section 1.2.4, the corrosion potential of wrought and LMD-printed SS316L are close but the stability of the protective oxide layer depends on the chemical composition, porosity and microstructure of each part of the repair. Moreover, the repaired parts are heterogeneous in terms of microstructure, but also in terms of chemical composition between the substrate and the deposit, since it is difficult to use a filler material with the same average chemical composition as the part to be repaired. Thus, these differences can cause galvanic corrosion of the parts, with damage to the less noble part, as observed on the weld beads in chlorinated solution in Figure 1.4 (b).

The quality of a repair depends on the quality of the material deposition. If this step is poorly performed, the repaired parts will have very poor mechanical properties and low corrosion resistance. However, even with high density, the heterogeneity of the microstructure leads to degraded properties of the repaired parts compared to the reference substrate. An important work is to be done on the repair process with respect to the criteria of dense deposition and metallurgical bonding with the substrate, imperceptibility of the repair without damaging the original part, as indicated in our initial specifications.

1.3.3 Influence of the pre-machining geometry in the repair

As it is observed, the interface between the substrate and the deposit is an essential part to be characterized and controlled as it is a place of microstructural and mechanical heterogeneities. This interface can also be studied through the geometry of the pre-machining. However, the pre-machining step prior to material deposition is poorly studied in the literature. Indeed, this step is important because it allows the defect and the surface contaminants to be removed, and give good accessibility to the powder projection nozzle. The confinement of the pre-machined area, related to the geometry, will impose geometrical constraints on the deposition of material. As shown in the literature, this issue will also affect the quality of the repair, especially the density rate of the repair.

Pinkerton *et al.* [106] were among the first to demonstrate that the shape of the pre-machining has a strong influence on the density of the repair using a triangular and a rectangular groove. The vertical walls of the rectangular groove cannot absorb the laser energy and cause a lack of fusion between the deposit and the substrate as shown in Figure 1.30 (a). These observations are also reported in the work of Graf *et al.* [107] (Figure 1.30 (b)). They emphasize that the use of a too limited premachining with edges close to the vertical causes problems with the powder and laser delivery into the groove due to the mask created by the top surface of the substrate.

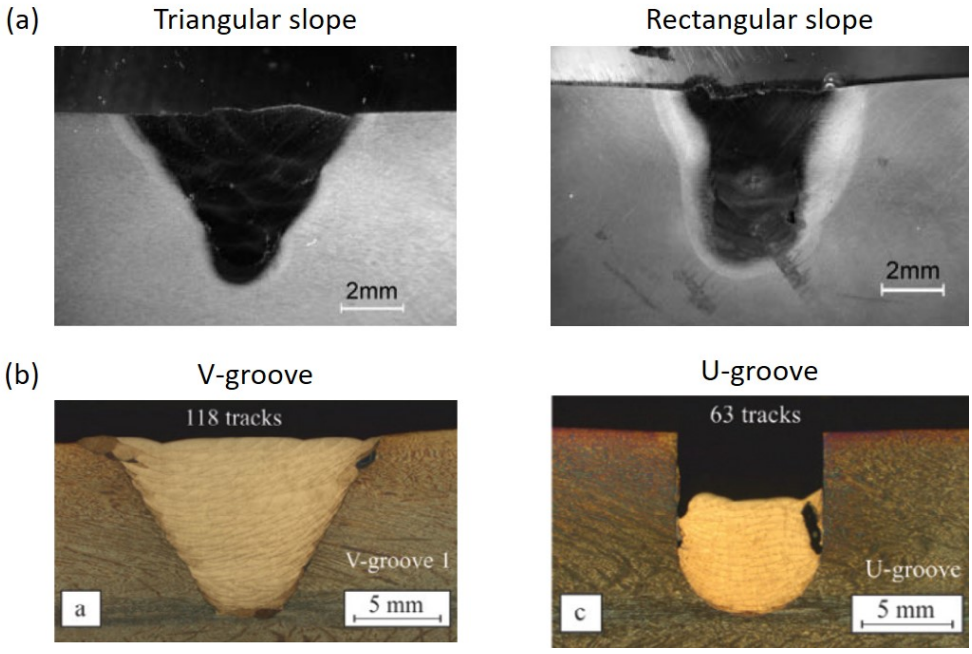

Figure 1.30: Repair using LMD process of (a) triangular et rectangular slopes in [106] and (b) V-groove and U-groove in [107].

In a similar approach, the work of Oh *et al.* [108] focuses on the repair of hot-rolled and PBF-printed substrates using grooves of different depths (Figure 1.31 (a)). The results show the presence of large porosities at the deposit/substrate interface when the groove depth exceeds 1 mm, as observed in Figure 1.31 (b). This results in strongly reduced mechanical properties for these samples and cracking at the interface (Figure 1.31 (c)). The authors consider that these porosities occur as a result of delamination of the deposits due to residual stresses. On the other hand, increasing the groove depth for the same bottom width results in steeper edges. The dilution of the beads is not sufficient to provide sufficient metallurgical bonding at the steeper edges, resulting in the lack of fusion observed.

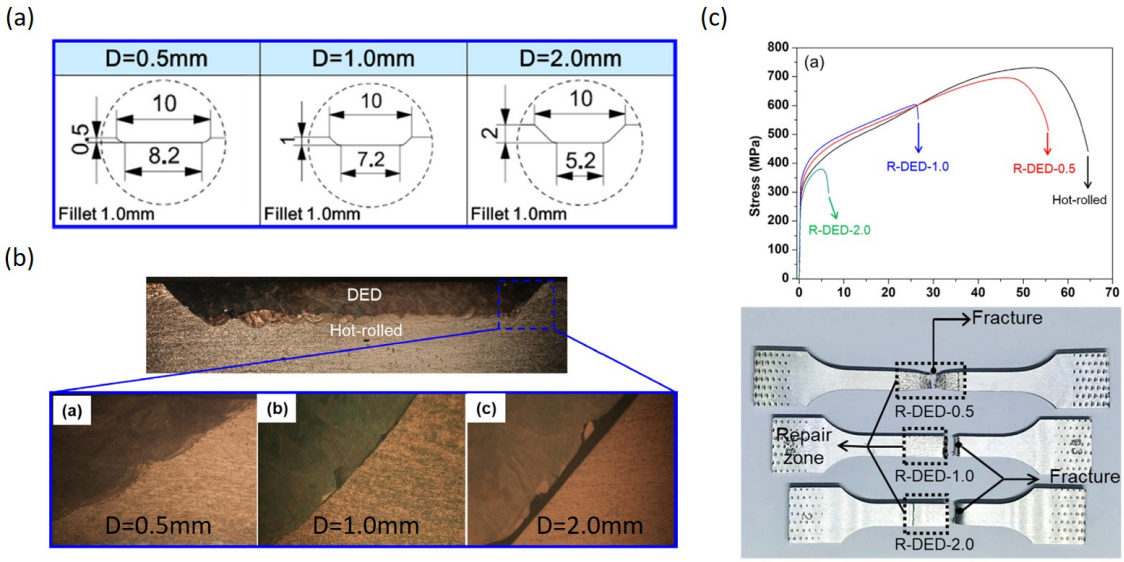

Figure 1.31: (a) Premachining geometries with different depths, (b) optical microscopy of cross-section and zoom at the interface and (c) tensile stress-strain curves and crack position of the tensile specimens [108].

These articles highlight the variation in repair density as well as the decrease in mechanical properties with different premachining geometries and, in particular, the strong influence of the groove opening angle on deposition quality. When this angle approaches 90°, *i.e.* verticality, lack of fusion appear at the edges, resulting in poor quality repairs. Similarly, the interface is a zone with a strong microstructural and mechanical gradient that will affect the mechanical strength of the repair depending on its orientation and, therefore, the opening angle.

Another point defined by our specifications is to remove as little material as possible to minimize the risk of damaging the part to be repaired during the repair process. It is therefore necessary to optimize the repair volume. As shown in the literature, this

optimization requires modifying the shape of the pre-machining and its dimensions through its opening angle, depth and width.

Zhang *et al.* [18] worked on the steps of scanning, machining volume optimization, and pre-machining. They used U-shaped shapes with different opening angles to try to fully integrate the damaged area into this shape while minimizing the volume. As mentioned, the larger the opening angle, the better the access to the projection nozzle, but the larger the volume to be machined, which means more cutting time and more material to be deposited. Thus, a function of the material to be machined is determined by the damaged cross section and the opening angle of the pre-machining. As shown in Figure 1.32, angles of 26° and 31° are calculated for cross sections A and B, respectively. These results show that the optimization of the premachining volume to meet the specifications is highly dependent on the initial defect. However, given the variations in opening angle required to minimize the volume, it is necessary to know the influence of this opening angle on the quality of the repair. Depending on the results, conditions are imposed on the volume optimization algorithm.

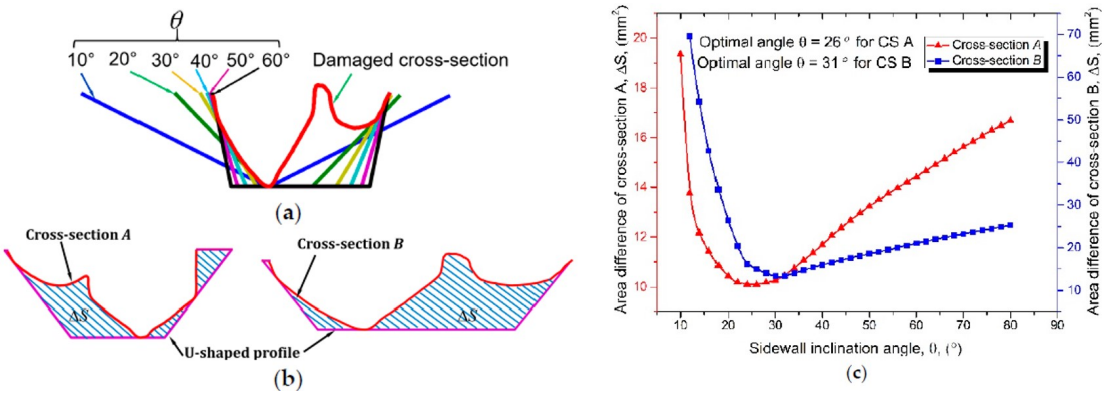

Figure 1.32: (a) Different U-shaped boundaries containing the damaged cross-section, (b) cross-sections A and B contained in optimized U-shaped boundaries and (c) function of removal section versus opening angle for the cross-sections A and B [18].

The pre-machining geometry plays an important role in the repair process. The shape and dimensions of the pre-machined part leads to technical constraints on the deposition of material with the LMD process, particularly due to the difficulty of accessing the bottom of the defect with the projection nozzle and the degraded interactions between the laser and the substrate if the edges are too steep. Moreover, volume optimization is highly dependent on the shape of the defect and the opening angle of the premachining.

Therefore, optimization of the shapes, depths and opening angles of the pre-machined part is essential to increase the quality of the repair in terms

of density and mechanical properties. Particular attention should be paid to the substrate/deposit interface to understand the deformation mechanisms involved and to observe their effect on the overall repair. Depending on the results obtained, volume-optimization conditions could be applied using complex shapes that are not widely used today and that allow a significant reduction in the volume to be pre-machined while maintaining an excellent repair quality.

1.3.4 Repair imperceptibility seeking

The heterogeneity of the microstructure and its impact on the mechanical properties of the repaired parts highlighted in the Section 1.3.2 is a major problem of the LMD repair process. It is thus necessary to study methods to reduce, or even eliminate, the microstructural and mechanical differences between the various repair zones in order to achieve imperceptibility of the repair. A return to the original characteristics of the repaired part allows it to be returned to service.

To limit the effects of fusion processes such as welding on parts and to control the microstructure, conventional and AM often use thermal treatments to modify the thermal history of parts. Different heat treatments can be applied Substrate preheating, application of inter-layer dwell times, and post-heat treatments are effective and easy to implement methods for controlling the properties of manufactured parts.

Substrate preheating is performed to reduce the presence of undesirable phases and residual stresses introduced during the welding and laser cladding process. Reducing the thermal gradient between the melt pool and the substrate limits the introduction of residual stresses, excessive solidification rates and the formation of certain phases [74, 109].

Baek *et al.* [110] preheated D2 and M4 steel substrates from 100°C to 500°C and deposited M4 steel powder in a premachined groove. M4 steel is susceptible to cracking during melting processes, and this observation is validated by repair with preheating to 100°C, where internal cracks are detected. On the other hand, by increasing the preheating temperature, cracks are avoided because, according to the authors, the introduction of residual stresses in the part is reduced due to a lower thermal gradient between the melt and the part to be repaired. The authors also observed an increase in the size of the dendrites with the preheating temperature. A decrease in mechanical properties for preheating above 500°C is noted with, for example, 18% less energy absorbed in Charpy impact tests.

Similar observations are found in the work of Moheimani *et al.* [111] who studied the impact of preheating to 250°C on the deposition of SS316L by LMD. It is observed an increase in the size of the cell substructure with a cell size in the 2.5 mm deposition of the substrate of 2.9 µm for a cold substrate against 3.9 µm for a preheated substrate. This difference is caused by the cooling rate, which is modified by the preheating. Also, the hardness of the preheated samples is more homogeneous and lower than with a cold substrate due to the modification of the cellular sub-structure, as observed in Figure 1.33.

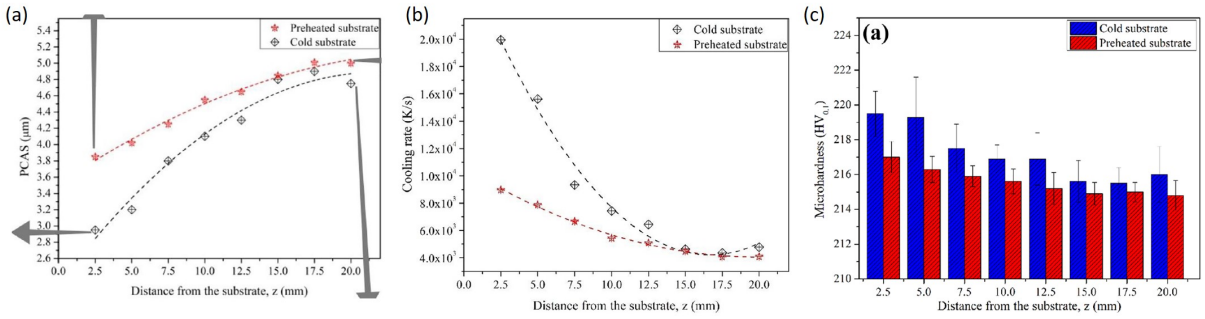

Figure 1.33: (a) Variation of cells size, (b) variation of the cooling rate and (c) microhardness along the building direction of SS316L cube produced on the cold and preheated substrates; [111].

Ding *et al.* [74] worked on 12CrNi2 deposition by laser cladding using three substrate preheating temperatures (20°C, 150°C, and 300°C). They showed that increasing the preheating temperature reduced the hardness (Figure 1.34 (a)), the residual stress (Figure 1.34 (b)), and increased the ductility of the parts by slightly decreasing the mechanical properties of the deposit (Figures 1.34 (c) and (d)).

The change in microstructure, mechanical properties, and partial relaxation of residual stresses with substrate preheating appears to be a significant advantage in achieving near-imperceptible repairs. However, an investigation of the preheating temperature to be applied to the substrate is necessary to obtain near imperceptible repairs.

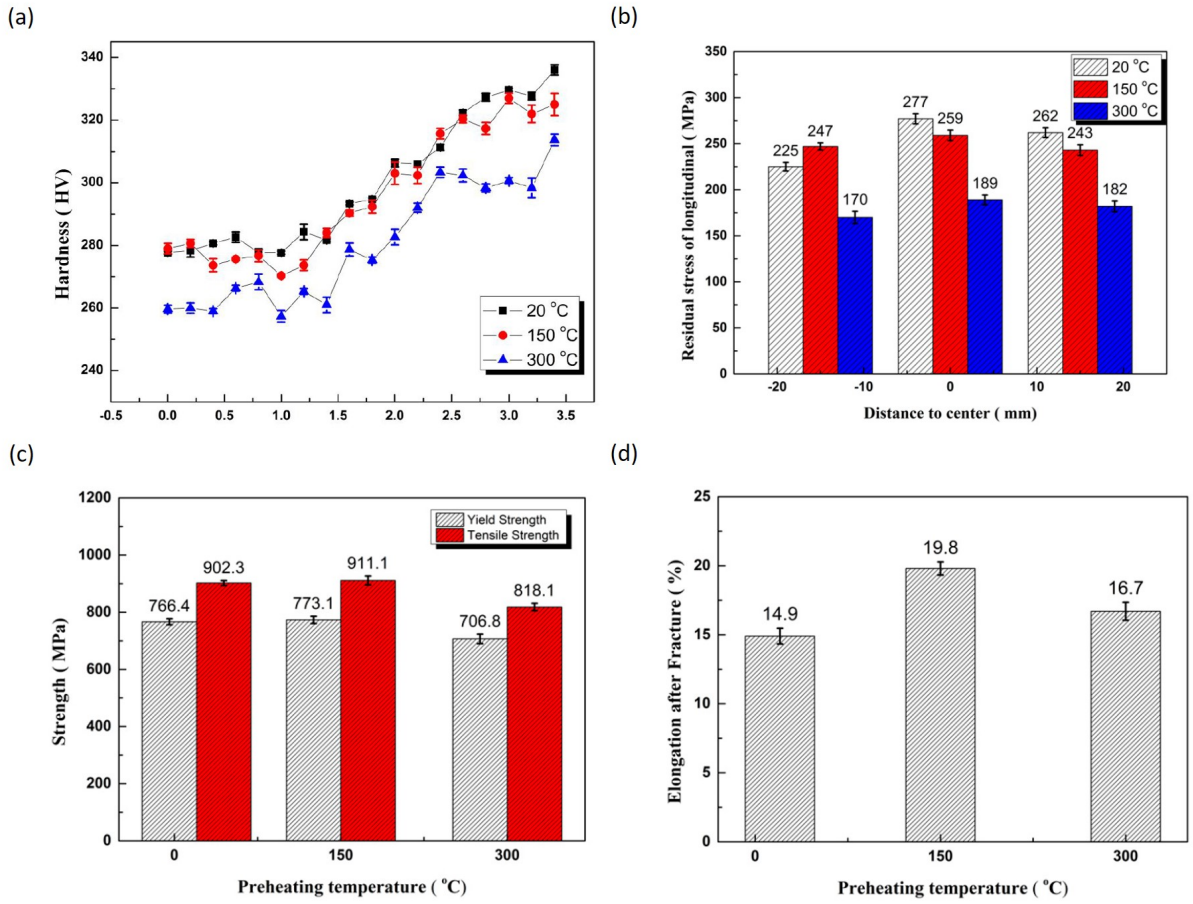

Figure 1.34: Analyses of 12CrNi2 deposit with different substrate preheating: (a) hardness distribution along the deposit, (b) longitudinal stress of the test specimen, (c) YS and UTS and (d) elongation at break of tensiles specimens [74].

Interlayer dwell time is a method used in the literature to increase the cooling rate between the melt pool and the part at each layer, thereby reducing the grain size of the deposits, which can then approximate the microstructure of the substrate.

Guévenoux *et al.* [102] demonstrated that applying a 10-s dwell time between layers in the construction of a single-strand wall in Inconel 718 for substrate repair of the same material reduced the grain size in the fabricated part, as observed in Figure 1.35. This microstructural difference allows the YS and UTS mechanical properties of the dwell time repairs to improve to 510 MPa and 880 MPa, respectively, compared to 390 MPa and 740 MPa of the no dwell time repair. However, they are still lower than the wrought with YS and UTS mechanical properties of 1012 MPa and 1260 MPa.

In the same approach, Mohr *et al.* [112] observe a decrease in grain substructure cell area with increasing dwell time between each layer. This work was performed on SS316L in the LPBF process, but is applicable to the LMD process, which follows the same trends

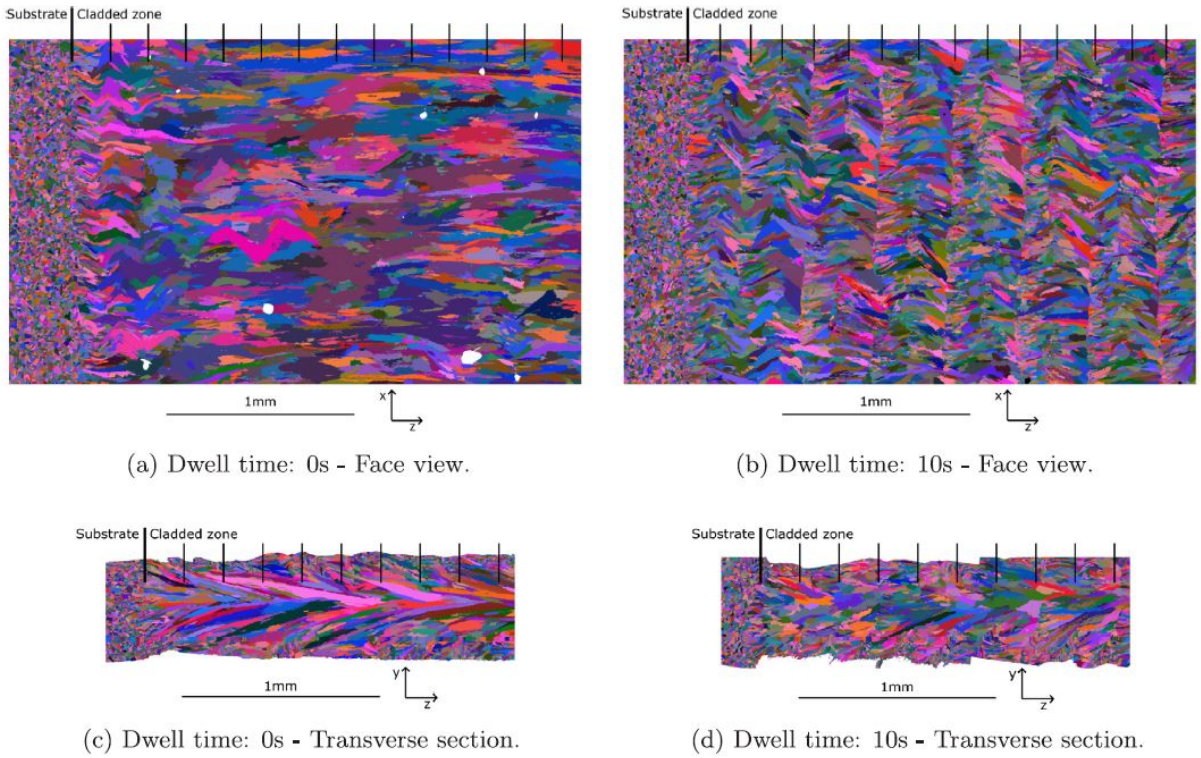

(a) Dwell time: 0s - Face view.

(b) Dwell time: 10s - Face view.

(c) Dwell time: 0s - Transverse section.

(d) Dwell time: 10s - Transverse section.

Figure 1.35: Differences of the microstructures obtained without (a) (c) and with 10s (b) (d) dwell time [102].

at different cooling rate scales. Thus, between long and short interlayer dwell times, we observe a decrease in cell area from 980 µm² to 320 µm².

Yadollahi *et al.* [113] highlight that hardness increases with interlayer dwell time, as well as UTS, but reduces significantly the elongation at break for SS316L, like illustrated in Figures 1.37 (b) and (c), where the sample with dwell time is called "nine-built" and without dwell time "single-built".

Moreover, Denlinger *et al.* [114] show that the residual stresses in single-track wall in Inconel 625 and Ti-6Al-4V made with interlayer dwell times can increase or decrease depending on the nature of the material and the residual stress intensity varies with the time applied due to the increase of the cooling rate between the melt pool and the part, like observed in Figure 1.36.

The application of an interlayer dwell time in the repairs could allow to reduce the grain size of the SS316L deposits and to approach the grain size of the substrate in order to homogenize the microstructure. On the other hand, the increase in hardness and residual stresses are parameters to be studied and minimized by optimizing this waiting time.

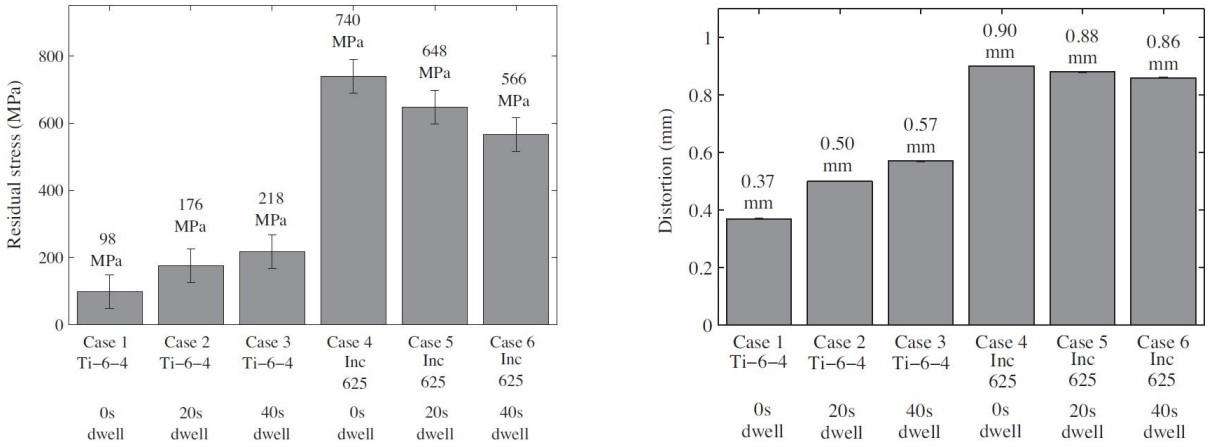

Figure 1.36: (Left) Residual stress measurements taken using the hole-drilling method and (right) distortion calculated using the CMM results [114].

Post heat treatment is a widely used method in the industry because of its overall effect on a part and its ease of application in furnaces. These treatments can be applied at both low and high temperatures, depending on the purpose and duration of the application.

Low temperature heat treatments for SS316L are typically applied at 300°C and 900°C. Below 600°C, these heat treatments can relieve the residual stresses introduced during the laser process without changing the microstructure, as observed in the work of Shiomi *et al.* [115], a 70% reduction in residual stresses was observed in a chromium-molybdenum steel produced by LPBF by treating it at 600°C for one hour. Between 600°C and 900°C, residual stresses are further relaxed, but this temperature range is conducive to the formation of sigma phase in SS316L, which is detrimental to the mechanical properties of additive manufactured parts, as shown by Wang *et al.* [116].

High temperature heat treatment can be applied to the repairs, in order to totally relax the residual stresses by annealing or rearranging dislocations , recrystallizing the deformed microstructure, controlling the grain size and promoting dissolution of the residual elements [117]. As observed in Figures 1.37 (a) and (b), these phenomena are observed in the work of Yadohalli *et al.* where the columnar grains of the microstructure have recrystallized into equiaxed grains with no cellular substructure and where the residual ferrite phase of an SS316L produced by LMD is completely dissolved by a heat treatment at 1150°C for two hours.

Heat treatments have the effect of softening steels. As shown in Figures 1.37 (c) and (d) of the Yadohalli *et al.* paper [113], the microhardness of the heat-treated sample is reduced to about 160 HV compared to 215 HV of the as-welded sample, a reduction of

25%. Similarly, the YS and UTS of the heat-treated specimen are reduced compared to the as-built specimen, but its ductility is improved with an increase in EAB from 33% to 43%. These trends are also observed in the work of other authors [118, 119, 120].

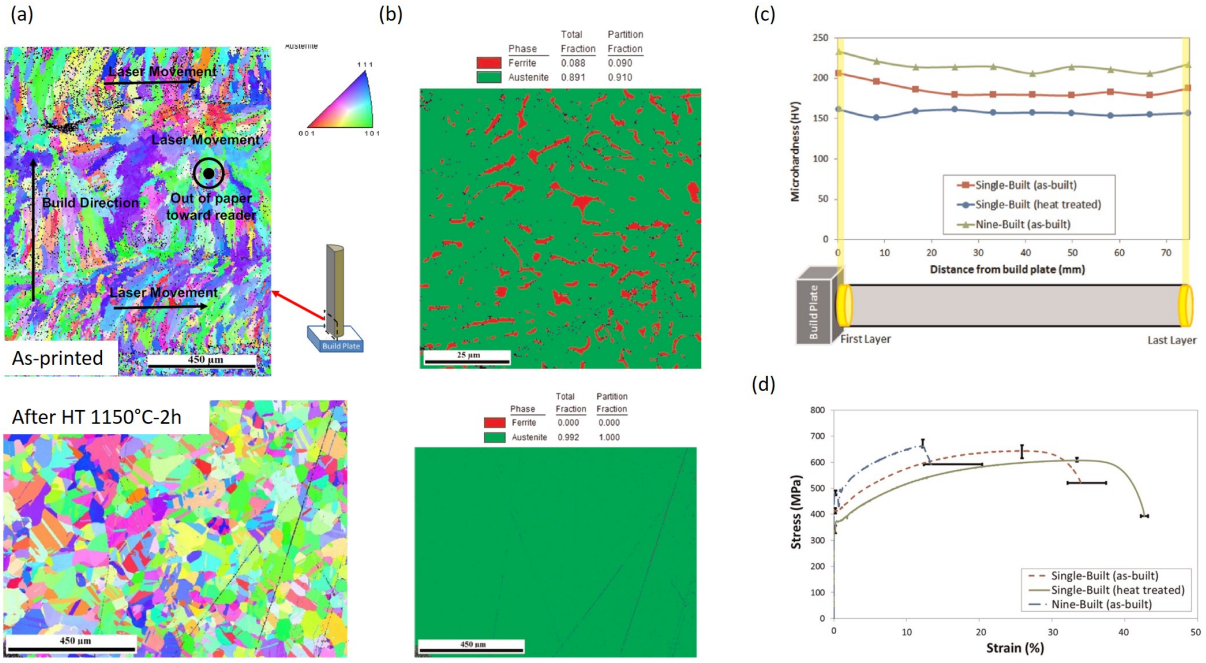

Figure 1.37: Observations of as-built deposit (single-built as-built), heat treated deposit (single-built heat treated) and deposit with dwell time (nine-built as-built): (a) IPF maps (b) phase map of the microstructure of single-built before and after heat treatment, (c) microhardness along the deposit and (d) tensile stress-strain curves [113].

Shim *et al.* [121] demonstrated that the application of an annealing solution treatment at 1040°C for 1 hour to a ferritic SS630 repair homogenized the microstructure and microhardness throughout the substrate, interface, and deposit, as shown in Figure 1.38. The repair followed by heat post-treatment is shown in blue and named SA-repaired-SA, compared to the SA-repaired sample, which is the as-repaired sample. The final sample, SA-repaired-SA-PH, has undergone an additional precipitation hardening treatment but is not the subject of this comparison.

Moreover, the corrosion resistance in sea water increases with the application of high temperature heat treatment, attributed to a more homogeneous microstructure than the as-built LMD deposit [88]. However, as shown by Laleh *et al.* [89], heat treatment can form inclusions that are detrimental to the corrosion resistance of some samples. Heat treatments above 1000°C cause the transformation of MnS inclusions into manganese-silicate and manganese-chromite inclusions in SS316L LPBF specimens. This type of transformation can occur in SS316L LMD specimens, which have the same morphology of

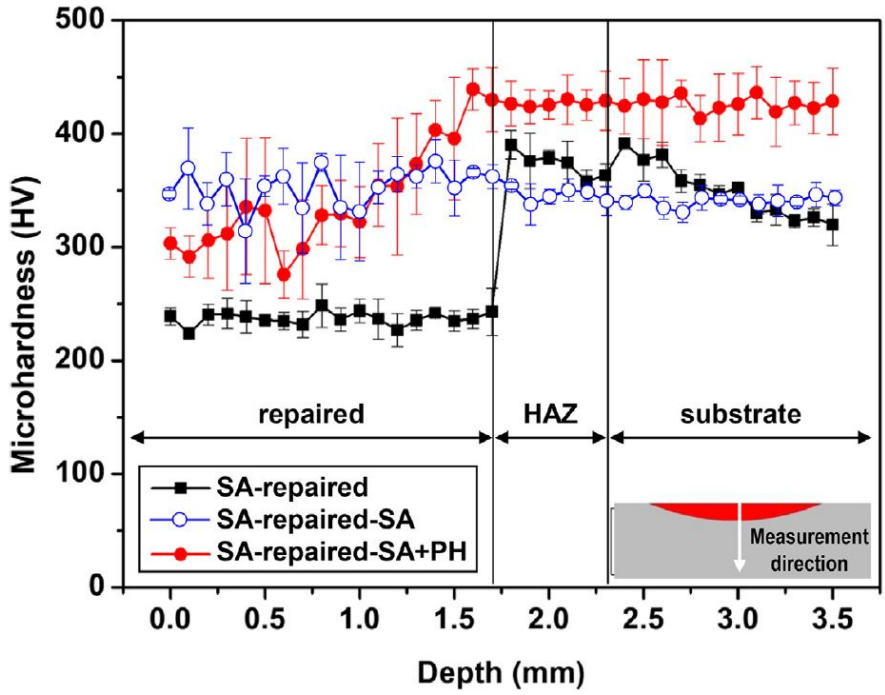

Figure 1.38: Microhardness values along the substrat, interface and deposit in a SS630 repair with different thermal treatments [121].

microstructure.

Heat treatments, especially at high temperatures, have shown great interest in controlling the microstructure by dissolving the cellular substructure and residual ferrite of SS316L, but also by recrystallizing the columnar grains. Similarly, homogenization of microhardness and improvement of ductility are of great interest for repairs known to have low EAB. However, it is important to avoid a strong decrease in mechanical properties and an excessive coarsening of the grains, as well as the formation of undesirable phases such as the sigma phase.

LMD repairs suffer from material heterogeneity, which can lead to deformation incompatibilities and premature failure of the repaired part. To overcome these heterogeneities and restore the performance (mechanical, corrosion) of the repaired part, thermal treatments are considered to homogenize the microstructure. However, these treatments were developed and studied in the context of parts manufactured entirely by conventional or AM. Few studies using these methods are applied to the repair. Indeed, the application of these homogenization treatments can cause a different behavior in the overall repair,

in particular at the interface between the conventional substrate and the LMD deposit. This needs to be studied to increase the quality of the repair process.

1.3.5 The additive/subtractive hybrid process for repair

Additive/Subtractive Hybrid Manufacturing (ASHM) is a manufacturing method that allows the use of an additive material deposition process (e.g. powder/laser) and a subtractive process (e.g. milling) within a single machine. Existing machines are either machining machines with an additive unit integrated in parallel and numerically controlled [122], or machines designed for this type of manufacturing, which use a single tool spindle to control and move the machining tools and the projection nozzle [123].

As explained by Cortina *et al.* [123] in their diagram shown in Figure 1.39, the production of new parts by LMD requires finish machining after material deposition and, in the case of repair, a machining before and after the deposition. Hybrid technology offers the ability to take advantage of both additive and subtractive technologies in a single workstation, opening up new manufacturing possibilities. In fact, the development of hybrid manufacturing is a key element in increasing the complexity of AM by exploiting the synergy of the two technologies. The use of a single machine requires only one zero setting of machine coordinates, reduces the movement of parts, takes up less space than multiple machines, and simplifies operator actions. Moreover, the combination of the two processes makes it possible to reduce material consumption with near-net-shape parts and to increase the complexity and quality of the parts produced by alternating between additive and subtractive processes. Finally, this technology represents a time and cost saving.

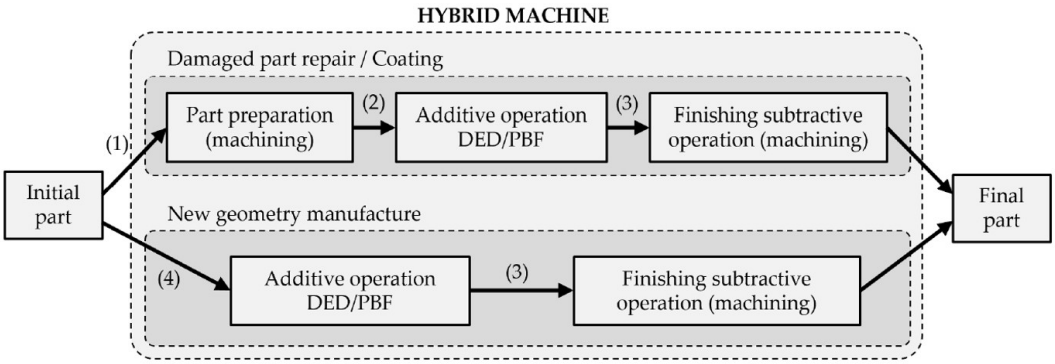

Figure 1.39: Flow chart and interactions in hybrid process for the damaged part repair or new part fabrication [123].

As mentioned earlier, the repair requires pre-machining, then material deposition and

finishing post-machining. Performing all of these steps in a single machine would be a significant time savings. As early as 2006, Ren *et al.* [124] demonstrated the possibility of repairing a mold by combining the LMD process to reload the material with finishing post-machining to restore the original dimensions of the part. A similar study was performed by Jones *et al.* [125] for the repair of turbine blades and the results were encouraging for the feasibility of this process for repair. Nevertheless, few studies have been carried out on the influence of the hybrid process on the final quality of the parts and even fewer on the repair.

In any case, the analyses performed show the time savings of the hybrid process compared to separate additive and subtractive processes. Felhausen *et al.* [126] found a time savings of 68% on a complete hexagonal production with the material deposition and finishing steps using the hybrid process.

In addition to the process gain, a better quality of the repaired parts is obtained with the hybrid process. In fact, Feldhausen *et al.* [126] and Kannan *et al.* [127] produced two groups of hexagons under different deposition and machining conditions. In the first group, called additive, the 127 mm high hexagons are fabricated in one step by material deposition and then post-machined. In the second group, called hybrid, five 25.4 mm sections are deposited and fully machined before material is deposited for the next section. The results indicate a lower rate of porosity in the parts produced by the hybrid process. Also, the mechanical properties in tension of the parts produced by the hybrid process are better and much more homogeneous, as shown in the Figure 1.40. The elongation of the first group is low due to the high porosity rate and a higher rate of twinning within the microstructure than for the hybrid group. On the other hand, the homogenization of the mechanical properties of the specimens taken vertically and horizontally is important and is not explicitly explained by the authors. Between the specimens taken horizontally and vertically, there is a difference of 55 MPa and 25 MPa for YS, 120 MPa and 40 MPa for UTS, and 9% and 4% for EAB between the additive technique alone and the hybrid respectively. A modification of the microstructure with the hybrid process could be the explanation, but the EBSD analyses carried out in the studies are focused on the inside of a bead and do not allow to draw any conclusions.

Besides better density and mechanical properties, an improvement in residual stress state is observed when using the hybrid process. In fact, Yang *et al.* [128] fabricated blocks using the LMD process in two ways. Similar to the previous study, one block was fabricated by LMD in a single step and then post-machined. For the second block, milling was performed between each layer, machining a portion of the previous layer. As noted in the Figure 1.41, the analyses highlight a decrease in residual stresses in the block for the

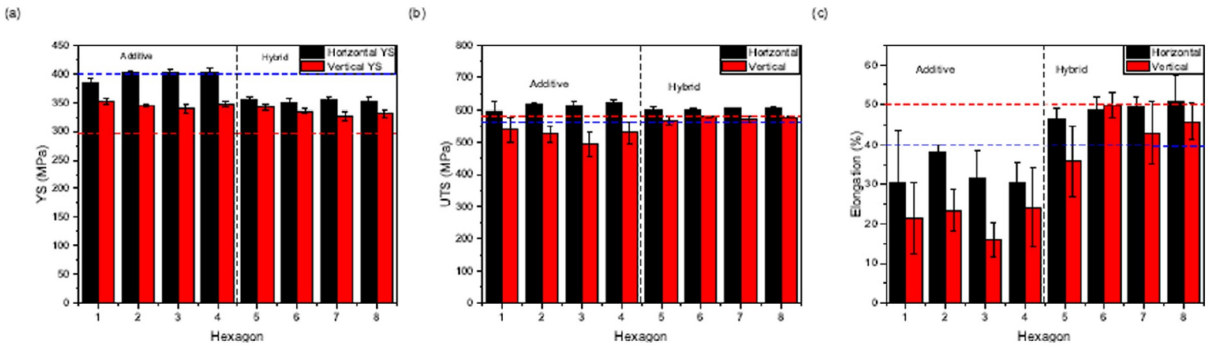

Figure 1.40: Mechanical properties of the tensile specimens extracted from the hexagon (a) yield strength, (b) ultimate tensile strength and (c) elongation at break [127].

second case, as milling a portion of the layer in each pass allowed for the release of some of the residual stresses introduced by the laser process. Residual stress relaxation of up to 60% is observed in the center of the cube.

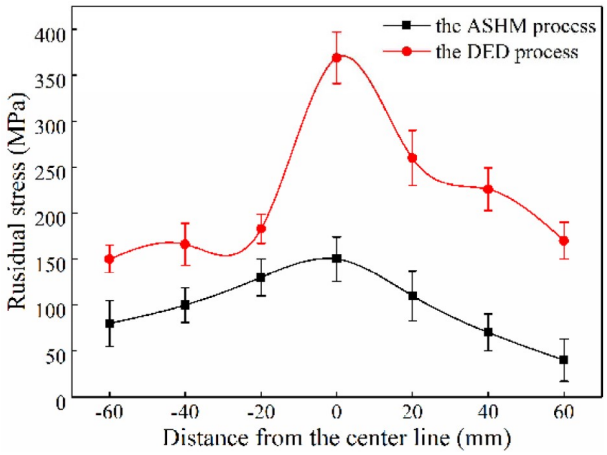

Figure 1.41: Residual stresses measured in the samples produced by LMD only and ASHM processes [128].

However, the hybrid process must deal with issues that do not arise when additive and subtractive processes are separated. In fact, the protection and safety issues related to powders and lasers are elements that are not present in subtractive machines, but can be adapted to additive processes. The use of powders can pose a problem of infiltration into the movement mechanisms and cause damage to the spindles and rotary axes. Additionally, machining usually requires the use of cutting fluids to cool and lubricate the tool to limit overheating and wear, but also to improve surface finish. These cutting fluids must be cleaned from the part surfaces after each machining operation to prevent contamination of the melt pool with water or oil. Moreover, the water vapor evaporated by the laser heat

could alter the powder jet or damage the optical system [123]. For example, Kannan *et al.* [129] have worked on the influence of the humidity level in the manufacturing chamber on the quality of the manufactured parts. In fact, the water molecules can dissociate and lead to dissolution of oxygen and hydrogen in the parts, especially in iron alloys, which would cause brittleness. Density and mechanical property results show negligible differences between dry and wet chambers. However, it is important to understand the phenomena involved and their effects on the manufactured parts.

Repair includes pre-machining, material deposition and finishing machining the surface, which require the use of additive and subtractive modules. A major advantage in reducing repair time and cost would be to perform these three steps in one machine. The hybrid additive/subtractive process is currently maturing to take advantage of the synergies between the two technologies to achieve fast, high quality repairs. However, there is a lack of knowledge about hybrid repair and the few articles in the literature show that there are precautions to take when compared to the use of separate machines.

The parts produced by the hybrid process show an improvement in the density ratio and in the mechanical properties in addition to a better isotropy. Furthermore, residual stresses appear to be reduced compared to the conventional additive process due to the relaxation of surface stresses after the cutting tool. These results are encouraging and demonstrate the interest in using the hybrid process to achieve better quality repairs at reduced cost. However, further studies are needed to know the exact impact of the process and material interactions and to observe if the improvements reported in the literature for manufacturing new parts also apply to repairing.

1.4 Conclusions and objectives

The industry faces the problem of damage to their components from mechanical and corrosive phenomena. This deterioration can lead to premature failure of the parts and unplanned shutdown of the system. Replacing the damaged part with a new one is in some cases not suitable due to its size, the environment or the unavailability of spare parts. When possible and in a circular approach, repair of damaged parts presents many advantages such as the reduction of maintenance costs and time, and the material and energy savings achieved. The repair must meet a set of criteria defined in the following specifications:

- Eliminate completely the flaw in the material due to mechanical or corrosive phenomena with the least amount of material removal possible;
- Produce a dense, crack-free deposit with material diffusion to the substrate and between layers or metallurgical bonding;
- Obtain a homogeneous microstructure, mechanical properties and corrosion resistance of the repaired area;
- Return the part to its original pre-damage dimensions;
- Do not damage the rest of the part during the repair.

Existing repair processes do not meet the above specifications. For example, arc welding damages the part and the microstructure is heterogeneous. Similarly, cold spray does not provide a dense deposit in the as-built condition. Therefore, the development of AM, and in particular LMD process, combined with machining in hybrid machines to achieve complete repairs, is one of the most promising technologies to obtain repairs with excellent dimensional and material quality. This process has the advantage of producing thin, dense deposits that are metallurgically bonded to the substrate with good mechanical properties and corrosion resistance without thermally affecting the damaged part in depth. The deposition parameters (*i.e.* laser power, scanning speed, powder mass flow rate, overlapping rate, deposition pattern...) results in changes in the density of the deposits, but also in the microstructure and therefore in the mechanical properties and corrosion resistance of the parts produced using LMD. This LMD printed microstructure is columnar with a cellular substructure of a few microns, in contrast to the fine, equiaxed microstructure of a conventional stainless steel 316L.

Literature studies have shown the importance of the deposition/substrate interface on the repair properties, as well as the shape of the pre-machining on the density of the repaired parts, which decreases as the area becomes too confined. However, there were no results that allowed a choice of shape or dimensions for the repair to maximize density while minimizing the volume to be repaired. Furthermore, the microstructural heterogeneity between the substrate and the deposit has been highlighted and the consequences on the degraded mechanical properties of the repairs are still poorly understood. Very few studies have attempted to homogenize the intrinsic properties of repairs using complementary processes such as heat treatments, despite interesting results when applied to conventional materials, such as a reduction in residual stresses, recrystallization of the microstructure or softening of the steel. Similarly, ASHM is a great asset to the repair process for its time savings and return to original dimensions, but there are limited results in the literature on

the quality of parts repaired by hybrid manufacturing. However, some authors have made promising observations on the production of new parts using the hybrid process, such as the reduction of residual stresses and the homogenization of the mechanical properties of LMD-printed parts.

The AM process, through the optimization of the deposition parameters and the deposition pattern for the repair application. The objectives are to understand and optimize the basic principles of the repair process, in order to satisfy the requirements of dense deposition, without cracks and having a metallurgical bonding with the substrate.

A study on the influence of the pre-machining geometry on the quality of the final repair need to be investigated, in order to achieve a dense repair with the removal of a minimum of material during the pre-machining operation through the optimization of the repair volume. The results should allow a selection of the type of pre-machining to be used and the conditions to be imposed on its geometry to maximize the chances of a dense repair.

In order to investigate the effect on the properties of the repaired parts, there is a need of carry out a study on the application of thermal treatments in the context of repair using the LMD process. The objective is to determine which treatment is best suited to homogenize the repairs, particularly in terms of microstructure, in order to improve mechanical properties and corrosion resistance, while maintaining dense deposits and bonding to the substrate.

The opportunity of using ASHM in improving the repair process, in terms of repair time and repair quality will be discussed. Performing a complete repair process in a single machine allows us to observe the time savings for repairing damaged parts, highlighting the issues of coupling additive and subtractive processes in a single enclosure. Coupling the two processes will allow us to determine if the technology can be of interest in obtaining a repair that meets our specifications.

These different analyses of the optimization of the LMD process for the repair case, of the understanding of the influence of the premachining geometry on the quality of the deposit for its volume optimization, of the homogenization of the repaired area properties to increase the repair performances and of its implementation in a additive/subtractive hybrid process have been treated within this PhD thesis and are subsequently presented to you in this manuscript.

Chapter 2

Experimental methods

Abstract

This chapter is dedicated to the presentation of the materials and methods used in this work. A first section exposes the manufacturing machines and the elaboration of repairs. Then, the material that are going to be studied: substrate and powder are characterized. The last section describes the methods used to characterize the density, the microstructure, the mechanical properties and the corrosion resistance of the repaired parts.

Contents

2.1 Laser metal deposition process

2.1.1 OPTOMEC LENS MTS-500

During the first part of the thesis, which took place at the Laboratoire d'Ingénierie des Surfaces et Lasers (LISL) at Commissariat à l'énergie atomique et aux énergies alternatives (CEA) Paris-Saclay, an OPTOMEC MTS-500 machine represented the LMD process used in this work (Figure 2.1 (a)). The system is a CNC machine equipped with a laser projection unit and three linear axes of movement (XY: moving table and Z: laser projection unit). The commands are edited in G-code program, commonly used on CNC machines. It is manufactured by OPTOMEC located in Albuquerque, USA and uses the patented Laser Engineered Net Shaping (LENS) technology [130].

The manufacturing chamber is in a controlled environment under argon to limit oxidation at high temperature and the influence of oxygen on the manufacturing process. Ultra-pure 99.9999% argon is used to fill the chamber, and a recirculating atmosphere system keeps the oxygen concentration below 100 ppm. The samples are inserted into the manufacturing chamber through an antechamber that performs a vacuum and then a recharge of ultra-pure argon three times. The samples are handled in the chamber through a glove box, as shown in Figure 2.1 (a). The substrates are deposited on two ceramic plates connected to the moving platform under which an inductor is placed to preheat the substrates in-situ to a temperature of 900°C. A spiral inductor was already present at the beginning of the thesis and was modified by a rectangular shape to allow a better distribution of the magnetic field in the substrates. The heat is created by the Joule effect of the eddy currents induced in the material by the strong magnetic field generated by the copper inductor traversed by a strong electric power. A pyrometer focused on the surface of the substrate analyzes in real time the temperature of the part and a feedback loop can adjust the power of the inductor to obtain a stable preheating temperature.

This machine has the particularity of being equipped with four powder feeders, which permit to mix different types of powder during the insertion in the melt pool. In the case of the study, only one powder will be used. It is transported by an argon carrier gas, which brings it to the laser projection unit. Then, the powder is focused by a coaxial nozzle and feeds the melt pool, like exhibited in Figure 2.1 (b). The powder mass flow rate is regulated by the rotation speed of a perforated disk located at the bottom of the feeder and by the gas flow.

The melt pool is generated by a YLS-3000-CT laser with a wavelength of 1064 nm, pseudo-Gaussian type and a maximum power of 3 kW. The working distance between the

nozzle and the substrate is 12 mm and generates a laser spot after focusing of 1.2 mm in diameter. The laser is emitted in the axis of the nozzle and the powder is projected by the external cone. A protective gas is used to prevent possible projections of material and smoke that could damage the optics. The laser projection unit is water cooled to prevent deterioration of its elements during construction.

The repairs carried out with the OPTOMEC MTS-500 machine made it possible to carry out fabrications with the LMD process under optimal conditions in an argon atmosphere and to focus in a first part of the work only on the material deposition step.

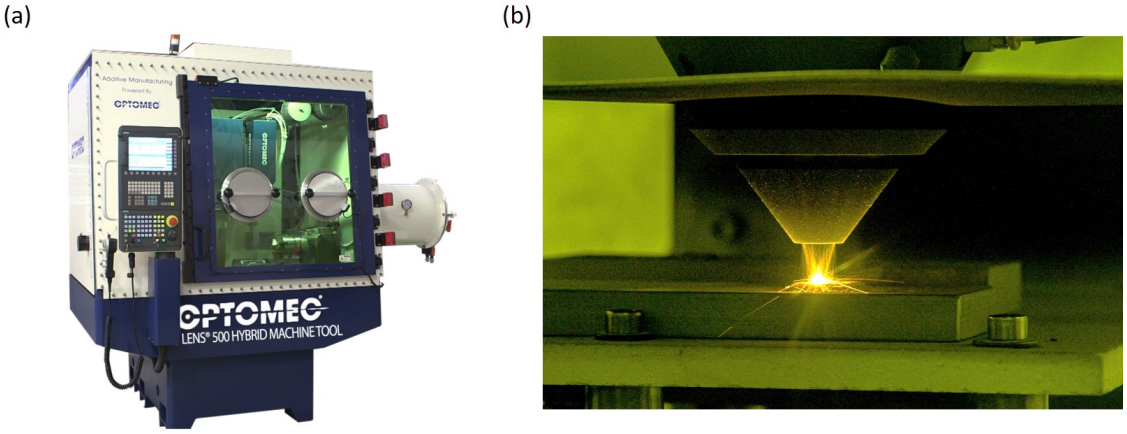

Figure 2.1: Overview of (a) the OPTOMEC MTS-500 and (b) the laser projection nozzle during deposition.

2.1.2 DMG Mori LaserTec 65 3D

The fabrications carried out during the second part of the thesis took place at Singapore Center for 3D Printing (SC3DP) at Nanyang Technological University (NTU) Singapore and were performed with a DMG Mori LaserTec 65 3D hybrid machine (Figure 2.2 (a)). It is a 5-axis hybrid CNC machine (AC: moving table and XYZ: laser projection unit) originally dedicated to machining with the possibility to interchange tools automatically, to which a laser unit has been added. Thus, the tool holder can be equipped with the laser projection unit for the AM (Figure 2.2 (b)) as well as with a tool for the SM (Figure 2.2 (c)). The G-code language is used to send the manufacturing instructions. The machine is manufactured by DMG Mori in Pfronten in Germany [131].

The manufacturing chamber is under air. A local argon gas shield is present to protect the melt pool from excessive oxidation. The substrates are placed on a support equipped with jaws that block the position of the substrate during the rotation of the moving table

and prevent distortion of the substrate during the laser process.

The machine is equipped with a Coax14 projection nozzle, which creates a 3 mm diameter powder jet at the focal point. The working distance between the nozzle and the substrate is optimized to 13 mm, which generates a laser spot of 2.96 mm diameter with a top head profile. The laser has a maximum power of 2.5 kW.

The milling is performed thanks to a milling cutter of 8 mm diameter and a length of 120 mm. The tool has a rotation speed of 3500 rpm and a cutting feedrate speed of 1000 mm/min. The tool change is automated with a tool changer. The same tool holder is compatible with the milling cutter and the laser projection nozzle. All the components are water cooled to avoid damage to the equipment.

The repair tests performed with the DMG Mori LaserTec 65 3D hybrid machine made it possible to achieve all the steps of the repair process in a single operation within the same tool.

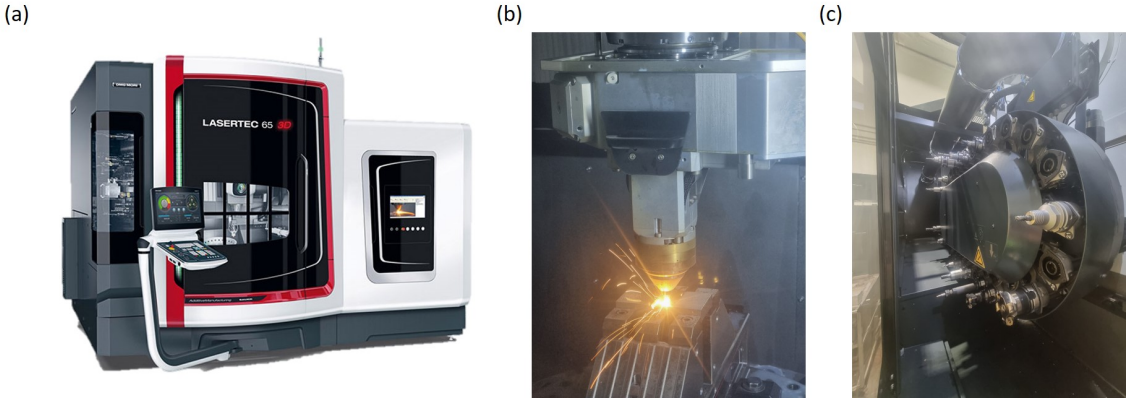

Figure 2.2: Overview of (a) the DMG Mori LaserTec 3D hybrid, (b) the tool holder with the laser projection nozzle during deposition and (c) the tool magazine.

2.2 Raw materials and repair terms

The raw material is SS 316L, largely used in the nuclear and marine environment. The substrates represent the parts to be repaired. The powder constitutes the filler metal, which will be used to replace the damaged, polluted and missing material.

The chemical composition of the raw materials is shown in the Table 2.1. Major elements were measured by Inductively Coupled Plasma Atomic Emission Spectrometry (ICP-AES) and minor elements by Glow Discharge Mass Spectrometry (GDMS). These elements can represent parts used in current French nuclear reactors, when the chemical

composition is compared to the RCC-M code [9].

The substrate is less rich in alloying elements than the powder, particularly nickel and molybdenum. In addition, molybdenum is low and the sulfur and phosphorus content is relatively high compared to the specifications of the RCC-M standard. This difference reflects a real situation where the substrate and the powder do not have exactly the same chemical composition. This difference can lead to differences in microstructure formation during solidification, as well as differences in mechanical and corrosion resistance behavior between the substrate and the LMD printed deposit, which must be considered in the analyses. Regarding corrosion resistance of the materials, this low molybdenum content and high S and P contents of the substrate could lead to a lower resistance compared to the powder.

Table 2.1: Chemical composition of SS316L powder and substrate compared to RCC-M specification (in wt%).

Analysis method	ICP-AES					GDMS							
Element	Fe	Cr	Ni	Mn	Mo	C	Co	P	Si	S	V	Cu	N
Subsrate	Bal.	17.3	10.0	1.5	1.6	<0.02	0.092	0.029	0.194	0.019	0.052	0.36	0.099
Powder	Bal.	18.1	13.7	1.7	2.6	<0.02	0.014	0.013	0.44	0.012	0.024	0.03	0.09
SS316L RCC-M	Bal.	16.5-18.5	10-13	<2	2-2.5	<0.03	-	<0.03	<1	<0.015	-	<1	<0.11

2.2.1 SS316L substrate

The substrates are produced by casting and are then hot rolled to strain harden the microstructure and give the blums the desired cross section. A heat treatment of the annealing solution type at 1050°C is applied to the parts to dissipate the residual stresses and recrystallize the microstructure. The substrates are machined in blocks of 100 x 50 x 15 mm^3 in length, width and thickness respectively.

The substrates used in this work have a fine and equiaxed microstructure with an average diameter of 38.5 ± 16.3 µm and presented in Figure 5.5. The matrix consists mainly of an austenite FCC phase, but also contains about 1% of ferrite BCC phase. The latter is lamellar and has developed at the austenite grain boundaries in the direction of bloom rolling. The hardness of the substrate is about 190 HV. The mechanical properties are as follows UTS = 610 MPa, YS = 310 MPa, EAB = 65%.

In the case of the study, the substrates are intact and not previously damaged by mechanical or corrosive phenomena. However, different shapes were machined inside the substrates to represent the pre-machining stage of the repair process. It consists of the removal of the damage defect after its identification and should be representative of what

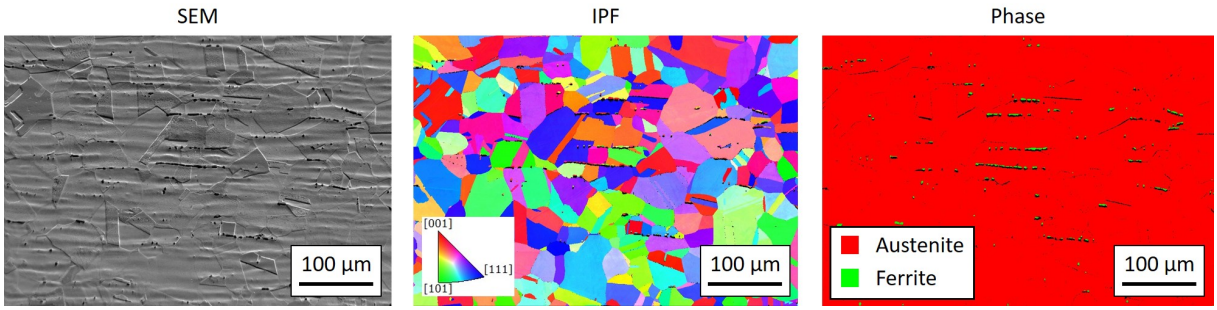

Figure 2.3: SEM observation, IPF map and phase map of the SS316L substrate.

is done on a real damaged part. The pre-machining shapes are described in detail in the corresponding sections.

2.2.2 SS316L powder

SS316L powder from Pearl Micro® is supplied by the manufacturer Erasteel in Sweden. It is gas atomized. The particle size distribution was measured by dry laser particle size analysis Partica LA960. This instrument can measure particle sizes between 0.01 µm and 5000 µm. The results show a particle size range between 45 and 150 µm and centered around 75 µm (Figure 2.4 (a)). It is adapted to OPTOMEC and DMG Mori machines, which use this spectrum of powder particle sizes.

The SEM observations of the powders are presented in Figure 2.4 (b). The particles are mostly spherical with the presence of satellites on the surface of the particles, which do not cause any flow problem in the projection nozzle.

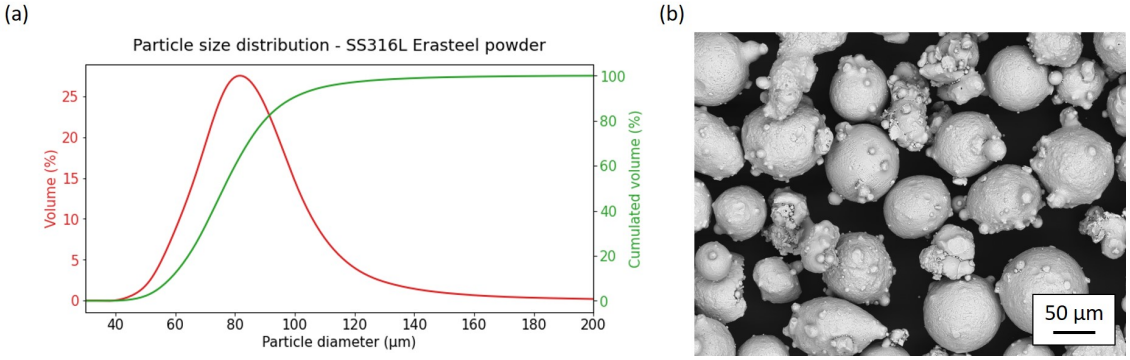

Figure 2.4: (a) Particle size distribution of the SS316L Erasteel powder and (b) SEM observation exhibiting the powder morphology.

2.2.3 Repair terminology

Examination of a repair, which represent the entire part, reveals distinct microstructural regions. The FZ is associated with melting. The base metal, though not melted, is partially affected by the heat from the LMD process. The fusion zone and base metal can be further subdivided, as described in this section and in Figure 2.5.

The deposit region represents the portion of the FZ where the powder is fused to replace the missing material. Surrounding this region along the fusion boundary, the Mixed Zone (MZ) can be defined. It consists of melted and resolidified base metal mixed with powder, which form the first beads in contact with the base metal.

The HAZ is the substrate near the FZ, which has not received enough energy from the laser to melt, but enough to undergo microstructural reactions, like recrystallization, grain growth, phase transformations, dissolution of precipitates, precipitate formation or residual stress and stress relaxation [24]. The interface is the line between the MZ and the HAZ. Finally, the substrate is the base metal far enough of the fusion zone, which is also not affected by the repair process.

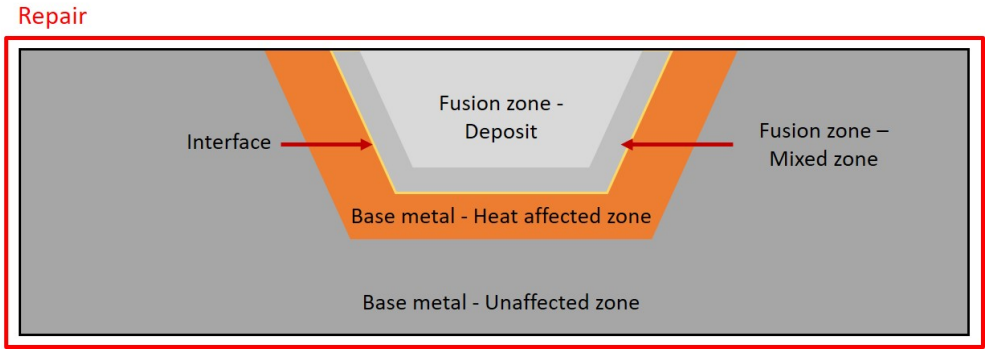

Figure 2.5: Terminology used to indicate the different areas in the repair.

2.3 Materials characterization methods

2.3.1 Specimen preparation

The preparation of the samples is different for the preparations made on the OPTOMEC machine and DMG Mori, because the equipment and consumables of metallographic preparation were different in the French and Singaporean laboratories. The cuts are usually made in the plane orthogonal to the repair in order to observe the microstructure in the cross section of the repaired substrates.

In order to be analyzed, the repairs made on the OPTOMEC machine are cut with a metallographic micro-saw. After cutting, the samples are hot mounted in PolyFast resin. They are then mechanically polished on a Struers Tegramin-20 automatic polishing machine with 240, 500, 1200 and 2000 grit size SiC paper.

- A mirror surface is obtained with a 0.04 µm oxide polishing suspension diamond solution on drape. This polishing is used for the detection of porosities and lack of fusion by Optical Microscopy (OM);
- To obtain a good surface finish and reveal the microstructure, the mirror-polished samples are electropolished with a 10% diluted oxalic acid solution at a voltage of 15 V for 45 s. This surface finish is used for the observation of the microstructure by OM, Scanning Electron Microscopy (SEM), Electron BackScattered Diffraction (EBSD) and for microhardness mapping.

The samples made on the DMG Mori machine are cut using Wire Electrical Discharge Machining (WEDM). They are then hot-coated in a phenolic conductive resin. Mechanical polishing is done on a Struers Tegramin-25 automatic polishing machine starting with SiC 320 paper, then Diapro Largo 9 µm, Dac 3 µm and Nac 1 µm.

- A 0.04 µm oxide polishing suspension diamond solution on drape is used for a mirror surface finish. Internal defects are observed after this preparation with an OM;
- To reveal the microstructure of the repairs, the surface is etched with a Kroll solution, which is constituted of 93% water, 6% HNO3 and 1% HF. OM, SEM and EBSD observations are performed after chemical etching.

2.3.2 Density analysis

Archimedes method

Density measurements by the Archimedes method were performed according to ASTM B311-22 [132]. The method consists in measuring the mass of a sample in air and in a fluid, here water as explained in the Figure 2.6. The principle of Archimedes based this measurement method: *"A body wholly or partly immersed in a fluid is buoyed up by a force equal to the weight of the fluid displaced"*. Thus, the volume and density of the sample can be determined.

Considering the density of air and water at a given temperature, and the mass of the sample in air and water, it is possible to determine the density of the sample according to the following formula 2.1 [133].

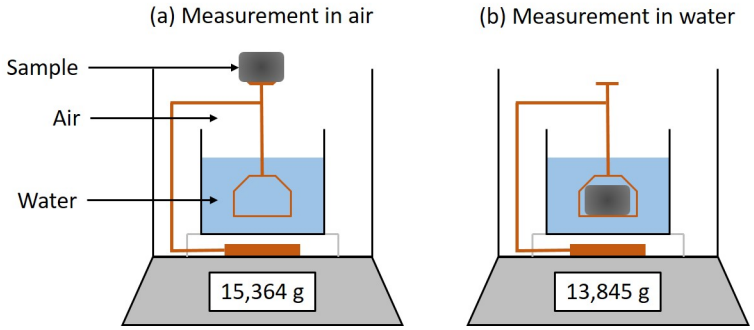

Figure 2.6: Overview of the Archimedes measurement process.

$$\rho_{sample} = \frac{m_{air}}{m_{air} - m_{water}} * (\rho_{water} - \rho_{air}) + \rho_{air} \tag{2.1}$$

With ρ_{sample}: sample density measured ($g\,cm^{-3}$), m_{air}: the mass of the sample in air (g), m_{water}: the mass of the sample in water (g), ρ_{air}: the air density ($g\,cm^{-3}$) and ρ_{water}: the water density ($g\,cm^{-3}$).

Using the formula 2.2 and the theoretical density of the material, it is possible to determine the porosity of the sample.

$$\%_{density} = \frac{\rho_{measured} * 100}{\rho_{theoretical}} \tag{2.2}$$

The mass of each specimens was measured independently five times in air and water at 20°C using an electronic balance with a resolution of 0.1 mg.

Cross section analysis

The density of the samples is also measured by observing the cross-section of the samples after mechanical polishing on a mirror polished surface using an OM, as described below and in Figure 6.8. A black and white image is obtained and converted to an 8-bit image. By image analysis, the dark areas are detected and measured. The porosity rate is the percentage of dark pixels in the image, then the density can be calculated. The resolution of the OM used enables the detection of a defect with a minimum size of 1 µm.

Three cross sections are observed for each measurement. This measurement is less accurate than the Archimedean density measurement, because it detects porosities in only the cross-sectional planes of the measured part. However, this method enables to observe the morphology of the porosities present.

They are defined by the ISO 6520 [134] standard and represent defects commonly encountered in fusion welding and are applicable to additive manufacturing. These defects can be divided into six groups:

- Crack, which is an imperfection produced by a local rupture in the solid state which may arise from the effect of cooling or stresses;
- Cavity like a gas pore, which is a gas cavity of essentially spherical form;
- Solid inclusions, which is a solid foreign substances entrapped in the weld metal;
- Lack of fusion, which is a lack of union between the fusion zone and the base metal or between the successive layers of the deposit;
- Imperfect shape of the external surfaces of the bead;
- Miscellaneous imperfections, which cannot be included in the previous groups, like the temper colour (visible oxide film) or spatter of molten metal.

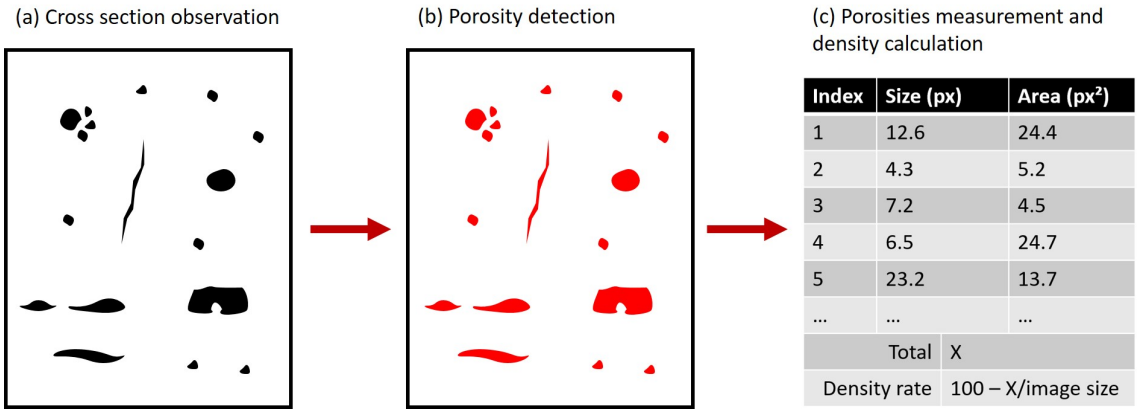

Index	Size (px)	Area (px²)
1	12.6	24.4
2	4.3	5.2
3	7.2	4.5
4	6.5	24.7
5	23.2	13.7
...	...	...
Total	X	
Density rate	100 – X/image size	

Figure 2.7: Process of detecting porosities in a cross section by image analysis.

2.3.3 Metallurgical observations

Optical microscope

The first observations of the samples were made on a Zeiss Axio Imager optical microscope at the CEA and on a Keyence Digital Microscope VHX-7000 at NTU. The surfaces were observed under white light after mechanical polishing. OM image mappings provided an overview of the defect characteristics like their size and location within the repair. The size and shape of the grains, the melting baths and the interface between the deposit and the substrate on the etched samples could be visualized.

Scanning electron microscopy

The SEM enables to obtain images with an important depth of field. The topology of the sample, the chemical distribution of the elements constituting it and the nature of the phases in presence can be observed.

A FEG JEOL JSM-7000F SEM and a FEG JEOL JSM-7600F SEM were used respectively at CEA and NTU to perform the microstructural observations. These observations were performed after the revelation of the microstructure as described in the section 2.3.1.

As described in the Figure 2.8, a SEM equipment focuses an electron beam on the material to be observed and scans the surface to obtain an image. The material reacts in different ways by releasing secondary and backscattered electrons, as well as X-rays. A pear-shaped analysis area with a thickness of a few µm is impacted under the surface [135], as shown in Figure 2.8. The secondary electrons will give the topography of the sample surface, the backscattered electrons the chemical contrast and the X-rays will be captured by Energy Dispersive X-ray Spectroscopy (EDS) analysis to define the nature of the elements present.

The parameters used for the topographic and chemical contrast analysis are a voltage of 15 kV and a current of 0.5 to 2.0 nA. The detection of chemical elements by X-ray measurement is performed at a voltage of 20 kV and a current of 2 nA.

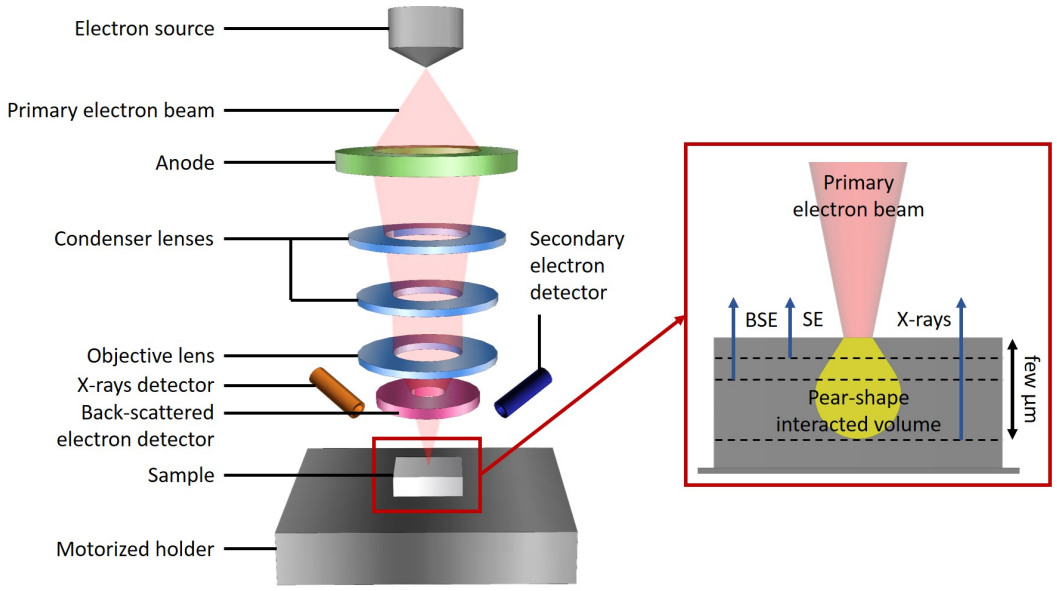

Figure 2.8: Schematic diagram of the core components of an SEM microscope and the response of the sample exposed to primary radiation.

Electron backscattered diffraction

SEM used in this thesis are all equipped with an EBSD detector. This crystallographic analysis technique determines the crystallographic orientation of single or polycrystalline materials. All seven crystal systems can be identified and can be used for crystal orientation mapping, defect studies, phase identification or grain boundary studies.

Like illustrated in Figure 2.9, in the secondary vacuum analysis chamber, the sample is steeply tilted at 70° from the horizontal towards the EBSD detector. This angle optimizes the detection of backscattered electrons. The detector is composed of a phosphorescent screen, which is activated on contact with an electron. These backscattered electrons come from the sample exposed to the primary beam and diffract according to the Bragg condition which links the atomic lattice spacing to the crystal structure [136]. These EBSD analyses can highlight the grain size gradient between the different zones of the repair and the nature of the phases present locally.

An acceleration voltage of 20 kV and a current intensity of 7 nA were used. The analyses were performed at CEA and NTU respectively with an integration time of 10 ms and 3 ms and post-processed on Esprit 2.0 and Tango/Mango software. The grains were defined for a joint disorientation angle >5°.

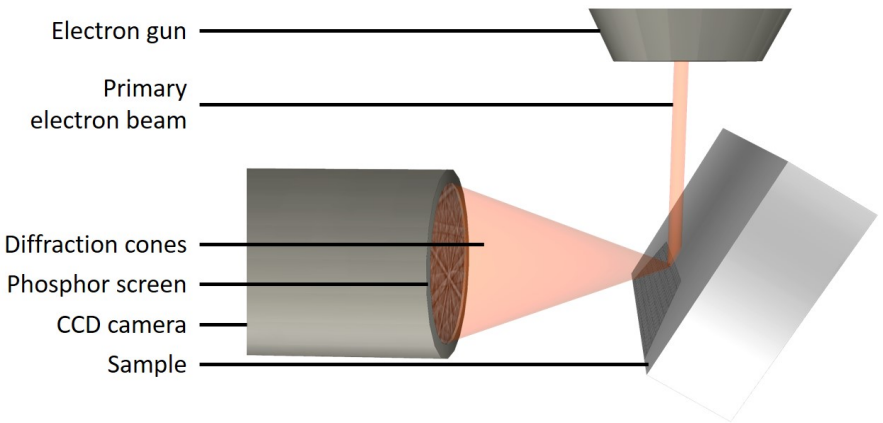

Figure 2.9: Schematic diagram of the principle of the EBSD process in the SEM chamber.

X-ray diffraction

X-Ray Diffraction (XRD) is a non-destructive analysis technique to characterize the crystal structure of materials. It provides information on structures, phases, preferred crystal orientations and residual stress state within a sample. In this work, this technique was used to measure the residual stresses within three zones (*i.e.* substrate, interface and deposit). The diffractometer used is a BRUKER D8 Discover with a copper anode, which emission wavelength $K_\alpha 1$ is 0.154 nm.

Elastic residual stresses are mechanical stresses present at room temperature in a part without mechanical loading. The stress state can be defined according to a symmetrical third order tensor σ_{ij} where i is the direction of the acting force and j is the area on which the force rests as defined in Equation 2.3. The stresses acting in the plane are called normal stresses and those acting in the parallel plane are called shear stresses [137].

$$\sigma_{ij} = \begin{pmatrix} \sigma_{11} & \sigma_{12} & \sigma_{13} \\ \sigma_{21} & \sigma_{22} & \sigma_{23} \\ \sigma_{31} & \sigma_{32} & \sigma_{33} \end{pmatrix} \tag{2.3}$$

The method of measuring residual stresses by X-ray is based on the interatomic distance of the planes (hkl). Under the action of a mechanical stress, the lattice spacing can increase or decrease compared to a stress-free lattice. Like descripted in the Equation 2.4, the position of the diffraction peak initially at the angle $2\theta_0$ will be shifted to the angle 2θ and can be used to determine the state of residual stress in the microstructure [137].

$$\epsilon^{hkl}(\phi,\psi) = \frac{d^{hkl}(\phi,\psi) - d_0^{hkl}}{d_0^{hkl}} \tag{2.4}$$

Where $\epsilon^{hkl}(\phi,\psi)$ is the shift between the diffraction peak without and with residual stresses depending on the orientation of the sample, $d^{hkl}(\phi,\psi)$ is the lattice spacing of the (hkl) planes subjected to residual stresses and d_0^{hkl} is the stress-free lattice spacing.

However, depending on the orientation of the stress direction, the lattice spacing will be larger or smaller due to the contraction rate of Poisson's law (Figure 2.10 (a)). The measurements carried out with different ψ angles reach to a curve d^{hkl} as a function of $sin^2\psi$ as observed in Figure 2.10 (b). These curves can have different profiles depending on the nature of the forces present in the material (Figure 2.10 (c)), *i.e.* if the stresses are normal, shear, gradient, or nonlinear due to texturing, as shown in the Figure 2.10 (b). Only the first two curves can be accurately measured with the $sin^2\psi$ method [137].

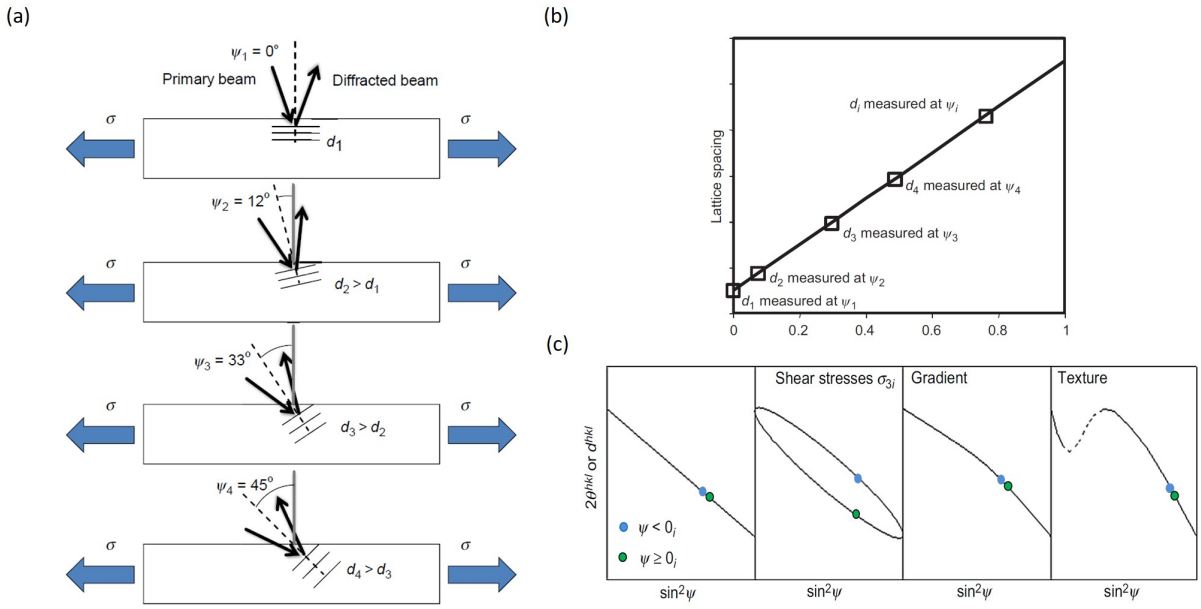

Figure 2.10: (a) Lattice spacing evolution according to the orientation of the crystal plane subjected to compressive stress, (b) resulting curve from the measurements with different ψ angle and (c) possible $sin^2\psi$ distributions depending on the stress state of the material

2.3.4 Mechanical properties identification

Microhardness mapping

Hardness measurements by mapping are intended to determine the local microhardness gradient within the repair between different zones. These measurements can be correlated with the microstructure and the residual stress state in the part.

The principle consists in using a diamond indenter in the shape of a straight pyramid with a square base and a 136° α angle, which is impressed on the surface of the sample with the application of a force F. After removal of the force, the diagonals d_1 and d_2 of the square indentation left are measured, as illustrated in Figure 2.11. The Vickers hardness is calculated according to the equation 2.5.

$$HV = \frac{Test\ force\ (kgf)}{Indentation\ area\ (mm^2)} = 0.1891 * \frac{F}{d^2} \tag{2.5}$$

Where HV is the Vickers hardness in HV, F is the applied force on the diamond indenter in N and d is the mean of d_1 and d_2 in mm.

The Vickers hardness measurements were performed on a STRUERS DuraScan70 motorized instrument. A load of 1 kg for 5 seconds was applied. Approximately 200

indentations are made on each samples with a distance of 0.3 mm between each indentation to obtain the microhardness mapping within a repair. The diagonals are observed after indentation with an OM with a magnification of X40. The measurements were carried out according to the standard ISO 6507-1 [138].

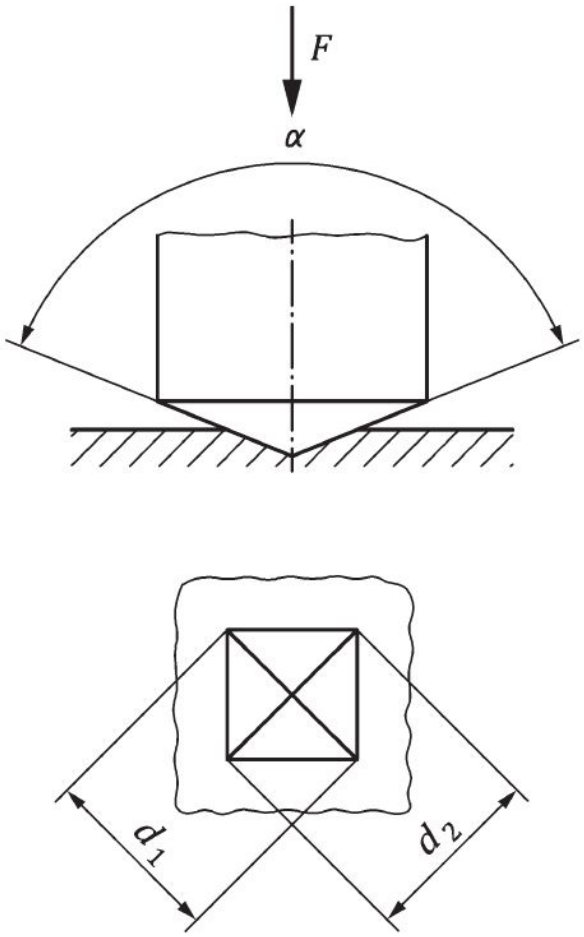

Figure 2.11: Vickers Hardness test principle [138].

Tensile tests

The tensile test is used to determine the mechanical properties of the repairs such as Young's modulus, UTS, YS and elongation at break. These values obtained for the repaired parts are compared to parts without repair and enable to determine the level of imperceptibility of the repair. For each study condition, between four and six flat 316L specimens are extracted from the repaired parts.

During this thesis, the tensile tests were carried out at room temperature using MTS

Criterion 43 electromechanical test system in CEA and Shimadzu AGS-50kNX in NTU at a displacement-controlled loading rate of 1 mm/min.

The dimensions of the specimens were calculated according to the ISO 6892-1 [139] standard and are presented in Figure 2.12 (a) for the tests carried out at the CEA and in Figure **??** (b) for the tests made at NTU. A reduction in the thickness and width of the specimens took place at NTU to accommodate the machining and testing machines.

The repairs are heterogeneous parts in terms of microstructure and mechanical properties as in the case of welded parts. The position of the repair in the tensile test specimen was inspired by the tensile test specimens extracted from the welded parts and which make it possible to determine their mechanical behaviour as explained in the ISO 4136 [140] for the destructive tests of welded parts. In the case of this study, the mechanical strength of the interfaces between the deposit and the substrate is studied. The position of the tensile specimens in the repair is described in the Figure 2.12 (c)

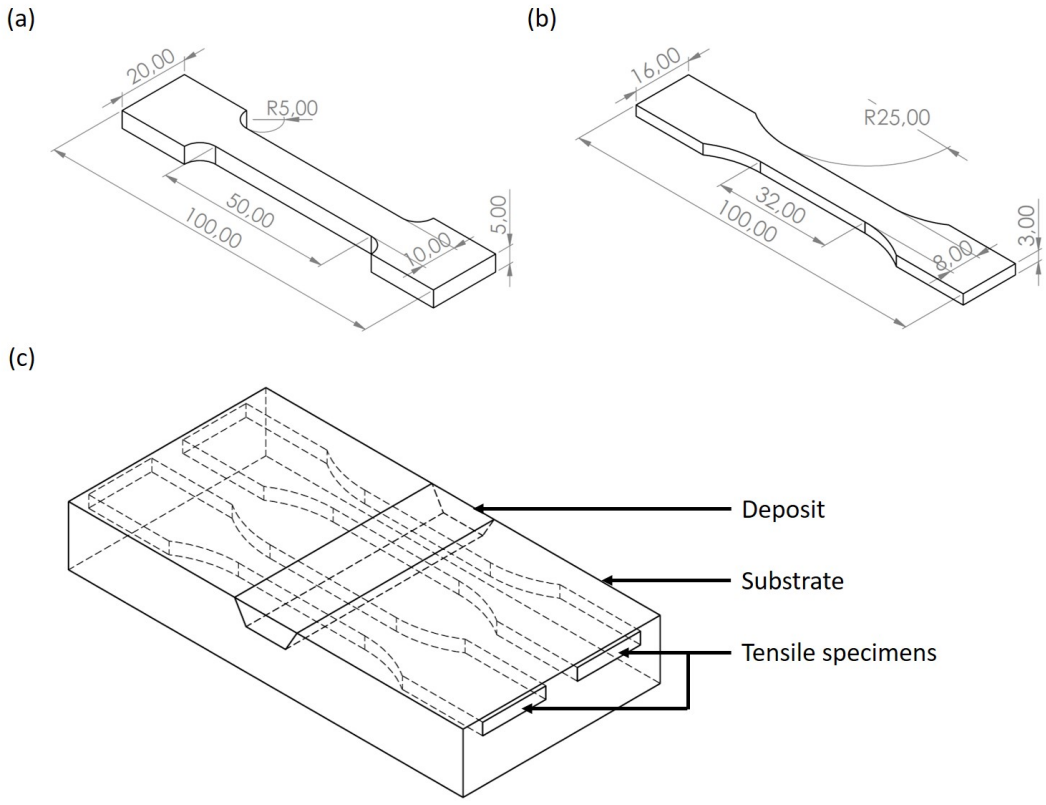

Figure 2.12: Dimensions of the tensile specimens in (a) chapter 4 and (b) chapter 6 and (c) position of the tensile specimens in the repaired parts.

Charpy impact tests

Charpy impact tests are used to determine the rapid deformation behavior of repaired parts compared to non-repaired samples. The values obtained by these tests are the energy absorbed by the specimen, the time for which the pendulum force reaches 0N and the crystallinity of the broken specimens.

The principle consists in breaking a notched specimen with a single impact of an oscillating sheep-pendulum. The notch has a specified geometry as described in ISO 148-1 [141] (Figure 2.13 (a)) and a position in the middle of the two supports, opposite the impact location. The V-notch have an inside angle of 45°, a depth of 2 mm and a bottom radius of 0.25 mm. The repair position is located in the middle of the specimen with the notch in the deposit as described in Figure 2.13 (b).

The Charpy impact tests were performed at room temperature using an instrumented Charpy impact machine (300 J). They were carried out in the Université de Technologie de Troyes (UTT) by Akram Alhussein. Four standard Charpy specimens were tested for each sample.

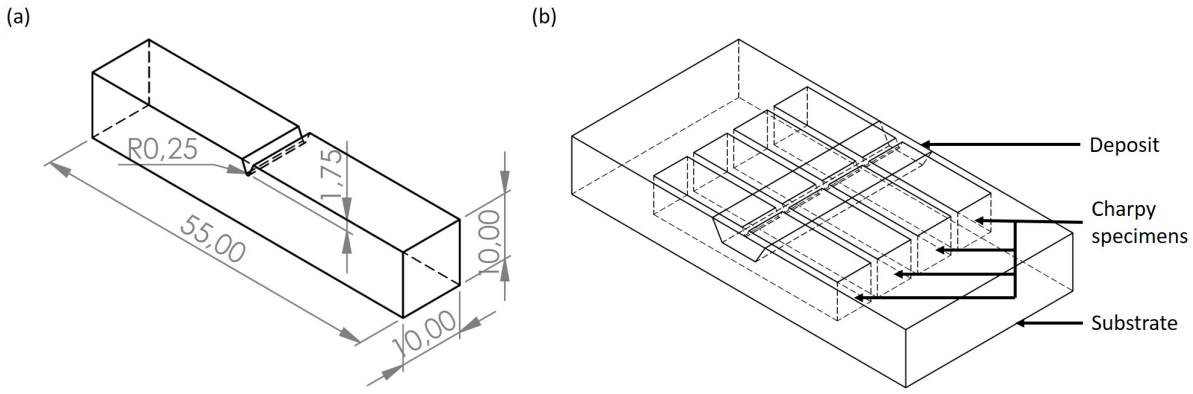

Figure 2.13: (a) Dimensions of the Charpy specimens and (b) position of the Charpy specimens in the repaired parts.

2.3.5 Corrosion resistance determination

Immersion tests in seawater

The immersion tests in natural sea water of repaired 316L stainless steel coupons were conducted by the company Corrodys based in Cherbourg. The objective of these tests is to compare the behavior of different repairs in natural sea water. The tested specimens are metal coupons of dimensions 30 x 50 mm and 15 mm thick. The coupons were drilled during preparation. Six families of coupons numbered 1 to 6 were provided in three units labeled A to C, *i.e.* 18 coupons in total.

The principle consists in immersing the repairs for 90 days in renewed natural sea water, in order to determine the corrosion behavior of the repairs in a natural environment. The free potential is monitored throughout the test and microbiological analyses are undertaken at the end of the test.

The installation of an electrical connection at the level of the drilling (protected by a resin) was prepared allowing an electrochemical follow-up, as shown in Figure 2.14 (a).

To obtain specimens with the same dimensions and a homogeneous oxide layer on the whole surface, the samples were machined with an WEDM machine and degreased in a half acetone half ethanol solution subjected to ultrasound. Then, the samples were etched in a solution composed of 60% demineralized water, 30% HNO_3, 6% HCl and 4% HF for 7h30 in order to remove 20 µm of thickness. Finally, a passivation is carried out to elaborate on the surface of the specimens a protective oxide layer, reproducible from one preparation to another and representative of that of an industrial product, using a solution composed of 85% demineralized water and 15% HNO_3 for a duration of 16h.

The samples are placed in a plastic tank with a volume of 500L. The tank is continuously renewed with natural seawater, which comes from the port of Flamands in Cherbourg, at a flow rate of 120 L/h allowing a complete renewal rate of the tank more than once a day. There is no current or agitation in the tank. Temperature, conductivity, salinity, pH, redox potential and dissolved oxygen were measured during the entire 90 days of testing.

The corrosion free potential was measured continuously on each of the coupons. Three Saturated Calomel Electrode (SCE) were used as reference to perform the corrosion free potential measurements. Figure 2.14 (b) shows the distribution of the coupons and reference electrodes in the tank.

At the end of the tests, the samples were taken and the biofilm swabbed for microbiological analysis. The biofilm was swabbed from the surface of each sample. The following microbiological analyses were performed on the collected biofilm:

- Total aerobic heterotrophic flora (viable and cultivable microbial communities), quantified according to the ISO 7218 petri dish dilution method;
- Total biomass (total dead and live microorganisms), quantified by epifluorescence microscopy;
- Total microalgae, quantified on Malassez cell.

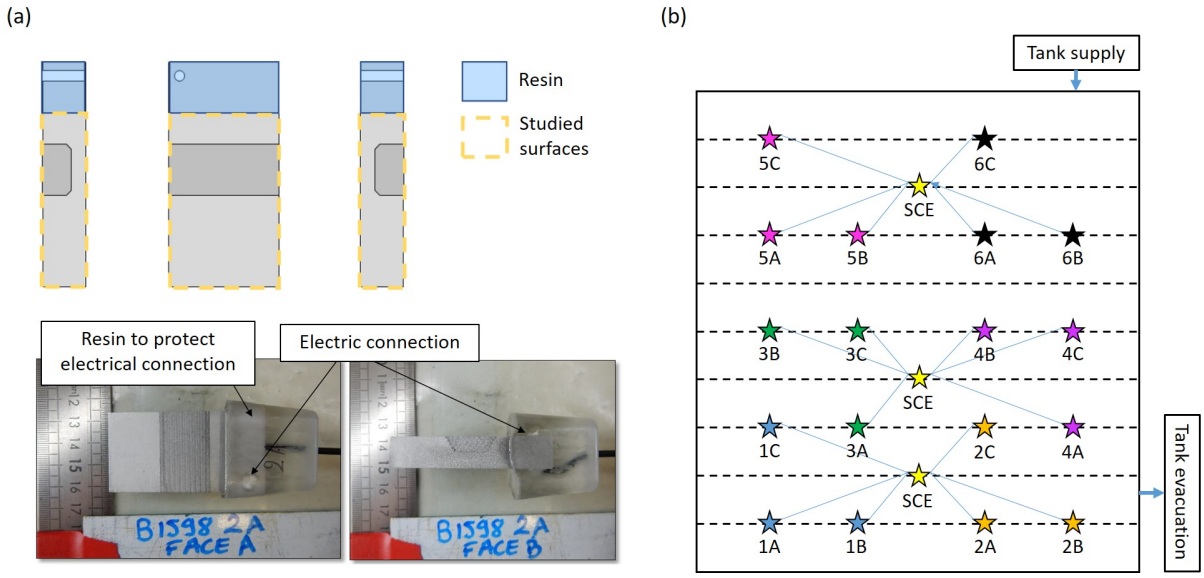

Figure 2.14: (a) Electrochemical assembly of the specimens for immersion and (b) distribution of samples marked A to C for each repair method numbered 1 to 6 in the immersion tank and position relative to the reference electrode (SCE).

Chapter 3

Optimization of the additive manufacturing process for repair

Abstract

This chapter presents the work performed on the generation of laser paths according to the position of the pre-machining and the optimization of the additive process for the repair. Three parts are described in this chapter. The first part presents the designs of experiment used to obtain dense and crack-free deposits metallurgically bonded with the substrate for the two machines used. Then, the importance of part positioning is explained in detail. Finally, the generation and optimization of the deposition pattern in G-code using the Python language is explained.

Contents

3.1 Introduction

The state of the art has identified several main parameters of the LMD process that influence the properties of the materials processed. Laser power, scanning speed, powder mass flow rate, overlapping rate, and deposition pattern are the manufacturing parameters that most affect part density. Prior to conducting the repair study, optimization of the process parameters was performed to achieve dense deposits with minimum porosity, no cracks, and metallurgical continuity with the substrate and between layers, which is the first point of the specification described in the Section 1.1.4 of Chapter 1 and is the most important aspect in order to achieve a healthy repair.

To meet this requirement, the literature highlights that a dilution rate in the previous layer between 10% and 30% is used by most researchers to produce new parts. This rate ensures the metallurgical bonding between the substrate and deposition and between the layers without interlayer porosity [56]. However, to avoid the lack of fusion observed in repair papers where these bead dilution rates are too low and pre-machining slopes are high, a dilution rate around 40% is used. The geometry of the beads and layers, as well as the dilution rate of the melt pool will be affected by the deposition parameters. The study focuses on four process parameters: the laser power (P), the scanning speed of the laser beam (V), the powder mass flow rate (Q) and the overlapping rate (OR).

The purpose of this study is to optimize the parameters of the additive process to obtain dense and crack-free SS 316L deposits metallurgically bonded to the substrate and produced by LMD, which can be used for the SS316L substrate repair in the next chapters to avoid porous repair like display in Figure 3.1 (a). This parametric optimization will be performed on the two machines used during the thesis, namely the OPTOMEC LENS MTS-500 machine and the DMG Mori LaserTec 65 3D machine. Two different optimization methods will be used according to the evolution of the PhD student's skills.

After optimizing the deposition parameters, the importance of substrate positioning and machine coordinate zeroing is highlighted. The strategies used on each machine according to the available measuring tools will be detailed in order to have the correct starting position and alignment of the parts to be repaired with the machine axes and avoid lack of fusion in the non-horizontal surfaces (Figure 3.1 (b)).

Finally, an explanation is given of the Python language program that was developed and used in this thesis to generate G-code machine programs adapted to the pre-machining repair. All variables and code lines are calculated and generated from the pre-machining geometry, bead geometry and process parameters. Adaptation of the overlapping rate at each layer according to the exact width to be filled is integrated into the deposition

pattern to prevent the formation of porosities during the deposition of the last bead of the layer like observed in Figure 3.1 (c)

The output criteria evaluated in this chapter will focus on the position and insertion of the beads in the deposit and pre-machining and the density of the manufactured or repaired parts. The ultimate objective of these optimizations is to achieve a dense and crack-free repair as shown in Figure 3.1 (d).

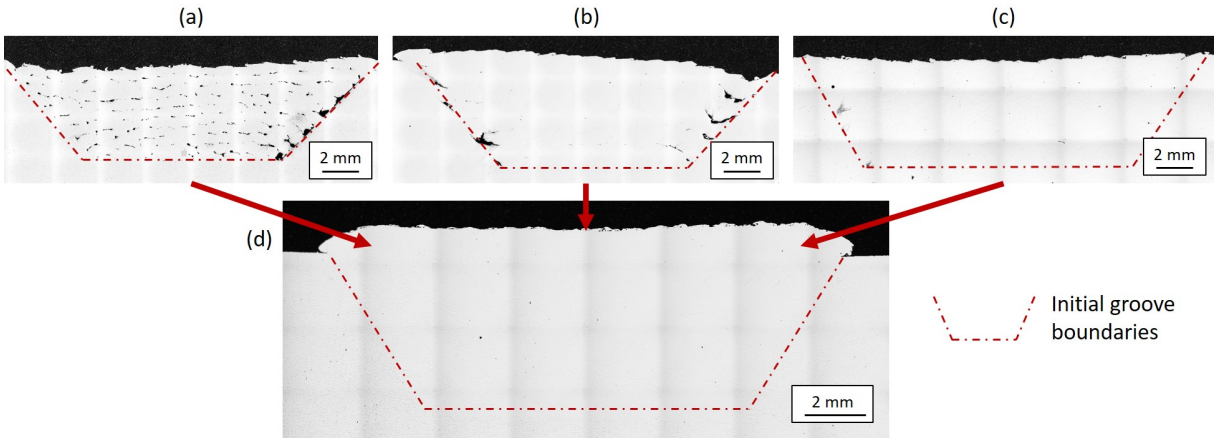

Figure 3.1: OM observations of cross sections of repair trials with (a) non optimized process parameters, (b) bad alignment of axis, (c) no adaptation of overlapping rate at each layer and (d) resolution of previous problems.

3.2 Deposition parameters optimization

3.2.1 OPTOMEC LENS MTS-500 (CEA Paris-Saclay)

Design of experiments

No set of optimized deposition parameters for depositing SS316L powder was available on this machine when the thesis began. The Latin Hypercube Sample method was used to develop a Design of Experiments (DOE) to evenly distribute a reduced number of samples over a range of parameters to reduce the search window. A Latin hypercube is the generalization of placing only one sample per row and column in a Latin square with an arbitrary number of dimensions, where each sample is the only one in each hyperplane aligned with the axis containing it. Cubes were fabricated and then analyzed by metallographic observation to determine the apparent porosity rate. Other parameter combinations were then added around the results of the densest cubes until optimized parameters were obtained.

Prior to this parametric optimization, single strand deposition tests were performed to determine the window limits for each parameter. Outside of these parameter windows, either the strands would separate from the substrate or smoke would escape from the melt. Variation of the deposition parameters was performed over the ranges shown below:

- Laser power P: [400W ; 700W]
- Scanning speed V: [300 mm/min ; 900 mm/min]
- Powder mass flow rate Q: [6.6 g/min ; 18.2 g/min]

The other manufacturing parameters were fixed during this study. The overlapping rate between the beads is fixed at 30%, following the observations made in the literature for the LMD process to avoid the formation interbead porosity [54]. According to this value and the laser spot size diameter of 1.2 mm, the step-over between each bead is 0.84 mm. The working distance between the projection nozzle and the part is maintained at 12 mm throughout the manufacturing process. Finally, the oxygen level is maintained at less than 50 ppm oxygen in the production chamber under argon to limit oxidation of the melt pool. The deposition pattern is to place the beads in parallel by going back and forth and rotating the next layer 90° along the build axis like described in Figure 3.2.

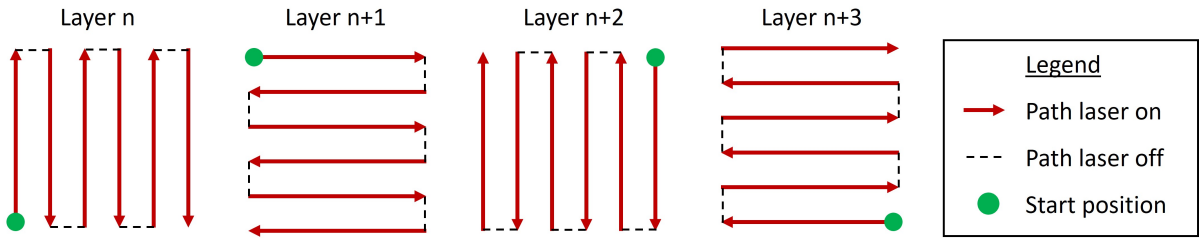

Figure 3.2: 90°-Zigzag deposition pattern used for the cube fabrication.

The size of the cubes is 16 mm on each side and 20 layers high. The final height of the cubes depends on the process parameters used. The first layer is deliberately extended to 30 beads wide to observe a single layer coating. 40 combinations of process parameters were tried to obtain the best deposition density.

Cubes fabrication and results

Figure 3.3 summarizes the parameter combinations used and the density rate results measured within each cube by metallographic observation.

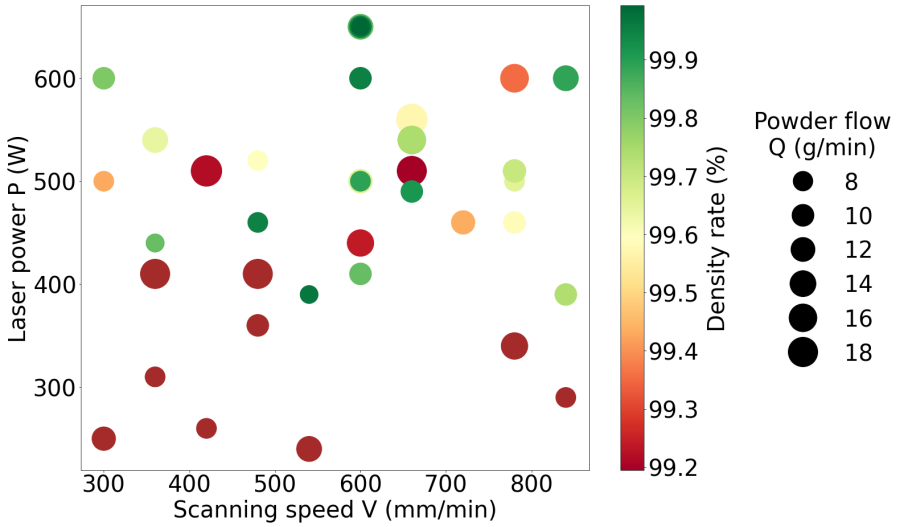

Figure 3.3: Cubes density in function of laser power, scanning speed and powder mass flow rate.

The density of the samples varies from 95.12% for the cube shown in Figure 3.4 (a) to 99.993% for the cube produced with the optimized parameters (Figure 3.4 (f)). The low density of many samples is caused by a too high laser power (Figure 3.4 (b)), which causes the vaporization of the elements with low melting point temperature and the formation of gas bubbles contained in the metal matrix [142]. Other cubes are made with too high powder flow rate combined with a too low power, which causes the melt pool to grow excessively without allowing it to remelt part of the previous layer. As a result, inter-layer lack of fusion are formed in the structure, as shown in Figure 3.4 (d). This phenomenon can be mitigated as the fabrication progresses as the accumulation of energy creates larger melt pools for the same amount of material to be melted and allows dilution in the previous layer (Figure 3.4 (e)).

A good density is measured in some samples, but these parameter combinations cannot be selected for further study because they do not respect another output data, which is a dilution rate around 40% to avoid the formation of porosities on the inclined surfaces of the pre-machining. The cube shown in Figure 3.4 (c) is a perfect example of a dense cube, but with insufficient dilution in the beads.

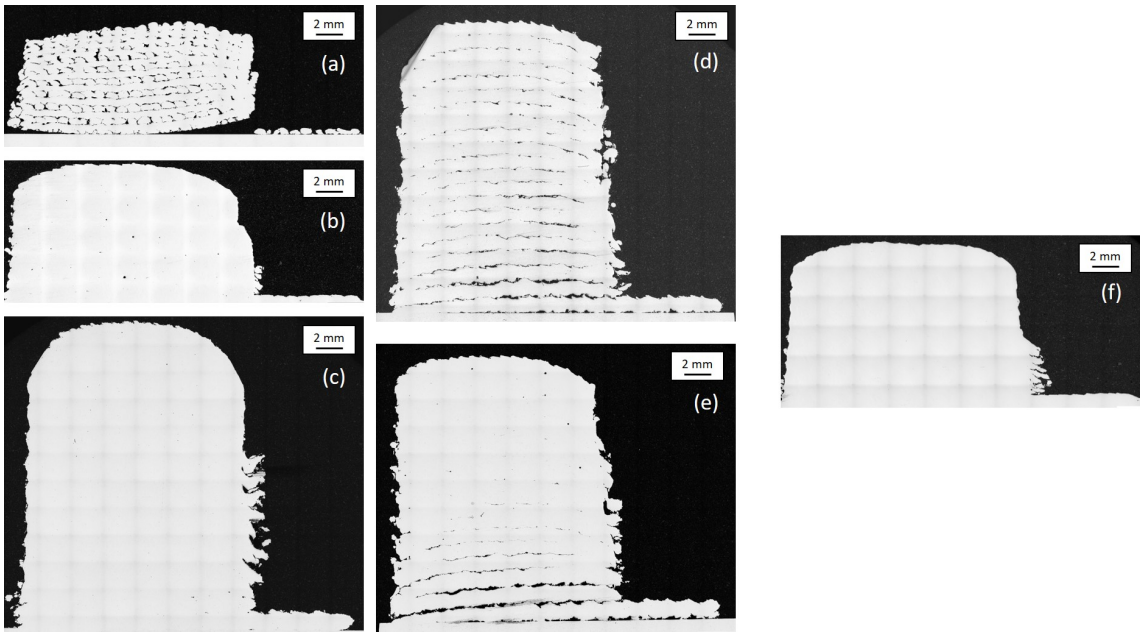

Figure 3.4: OM observations of cross sections of cubes from the DOE with some details: (a) no dilution, interbead and interlayer lack of fusion, (b) good dilution but gas porosities (too high laser power), (c) excellent density but not enough dilution in the first layer, (d) interlayer lack of fusion, (e) interlayer lack of fusion in the first layers only and (f) dense parts and bead with 45% dilution for the optimized parameters.

Based on the results of this investigation, the following deposition parameters were selected for the OPTOMEC LENS MTS-500 machine: P = 650 W, V = 600 mm/min and Q = 4 rpm = 6.6 g/min. These parameters produce deposits with a density of 99.993%, measured by metallographic observation, and a bead dilution rate of 45%. The effective height and width of the beads is 500 µm and 1200 µm, respectively.

According to the specific energy formula given by the Equation 3.1 [53], these parameters generate a specific energy of 54 J/mm^2.

$$E = \frac{P}{d_{beam} * V} \tag{3.1}$$

3.2.2 DMG Mori LaserTec 65 3D (NTU Singapore)

Design of experiment

The technique used in the previous Section has been of interest for understanding how parameters affect bead and layer geometry, melt pool evolution during construction, and porosity formation. On the other hand, it uses a large amount of material and is time

consuming in terms of fabrication, sample preparation and analysis. These were the first fabrications made with an additive manufacturing machine and were instructive for the future.

The parametric optimization performed on the DMG Mori LaserTec 65 3D machine is more precise because it involves three steps. The first consists of depositing single tracks to observe the influence of the process parameters on the geometry of the beads. The process parameters giving a bead with geometries close to the one given by the manufacturer with a dilution rate of about 40% are used to fabricate single-layer coatings with different overlapping rates. The aim is to find which value avoids the formation of inter-bead porosity and allow reaching a constant height after a minimum of deposited beads. Finally, the fabrication of cubes with these optimized parameters will allow the determination of the Z-increment to be achieved between each layer.

The parametric range studied is centered on the parameters provided by the machine manufacturer to produce parts in SS316L. As output criteria, the geometry and bead dilution are evaluated for single tracks, porosity formation and layer stabilization for single layers and cubes.

Single-tracks fabrication

Single-tracks of 20 mm are deposited on a SS316L substrate using different combinations of parameters. The factorial design method is used for this parametric optimization. It is a multi-parameter analysis method, which is most useful for applications in which a process depends on numerous parameters.

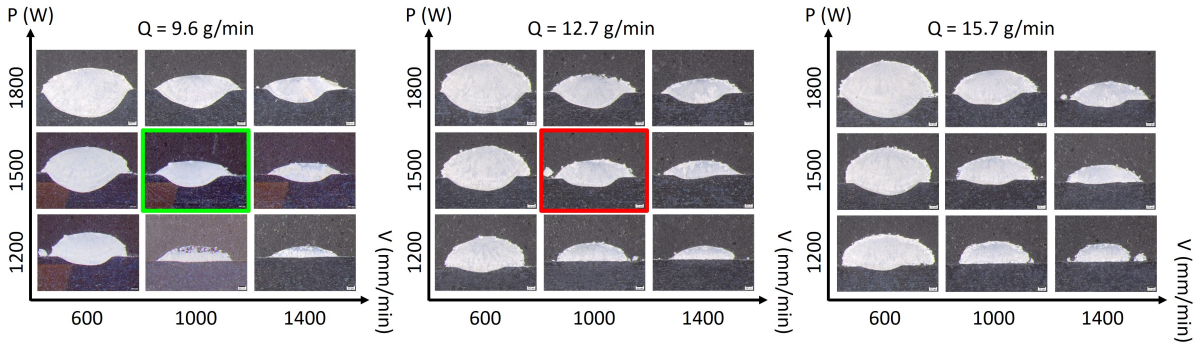

Figure 3.5: OM observations of cross sections of single tracks in function of the process parameters used with the parameters of the manufacturer in red and chosen for the repair study in green.

Figure 3.5 presents the geometry of the beads as a function of the process parameters

used, with the parameters given by the manufacturer in red. A dilution rate of 30% is observed for a bead height and width of 600 µm and 2500 µm, respectively. This geometry is acceptable for manufacturing new parts, but can be problematic for repairing pre-machined parts with edges that are not perpendicular to the laser. In order to maintain the bead proportions specified by the manufacturer and to increase the dilution rate, the parameters indicated by the green rectangle were chosen, which has a dilution rate of 45% for a height and width of 500 µm and 2500 µm, respectively.

The process parameters used for the rest of the study with the DMG Mori LaserTec 65 3D are P = 1500 W, V = 1000 mm/min and Q = 300 rpm = 9.6 g/min. These process parameters develop a specific energy of 50 J/mm^2, which is equivalent to that used on the OPTOMEC machine.

Coating fabrication

Single-layer coatings were fabricated with different overlapping rates to determine the overlap required to avoid lack of fusion between the beads and to quickly stabilize the layer height. As shown in the green box Figure 3.6, an overlapping rate of 40% allows to achieve this result. This parameter will be used for the rest of the repair study.

This recovery rate is higher than the 30% typically read in the literature [60, 52] and used on the OPTOMEC machine. However, this value may vary slightly, as it depends strongly on the configuration of the machine and the geometry of the beads. In the case of the DMG Mori, this value is the most suitable to meet the imposed criteria.

Below 40%, the layer height will not stabilize and the surface will consist of curves, which can introduce porosity when the next layer is deposited. Above 40%, interbead porosity begins to appear and the layer reaches a stable height after too many deposited beads.

Cube fabrication

The optimized parameters were used for the production of cubes. The objective is to determine the increment between each layer to be implemented in the programs. The final height of the layers is influenced by several parameters. For example, the accumulation of heat in the cube can lead to a larger melt pool than initially expected. This increases the overlapping rate and thus the height of the layer. Similarly, in order to remain in the focus of the laser and the powder stream, the working distance between the surface and the projection nozzle must be constant throughout the build. If it decreases or increases too much by an incorrect vertical increment, the melt pool will be modified by the defocusing

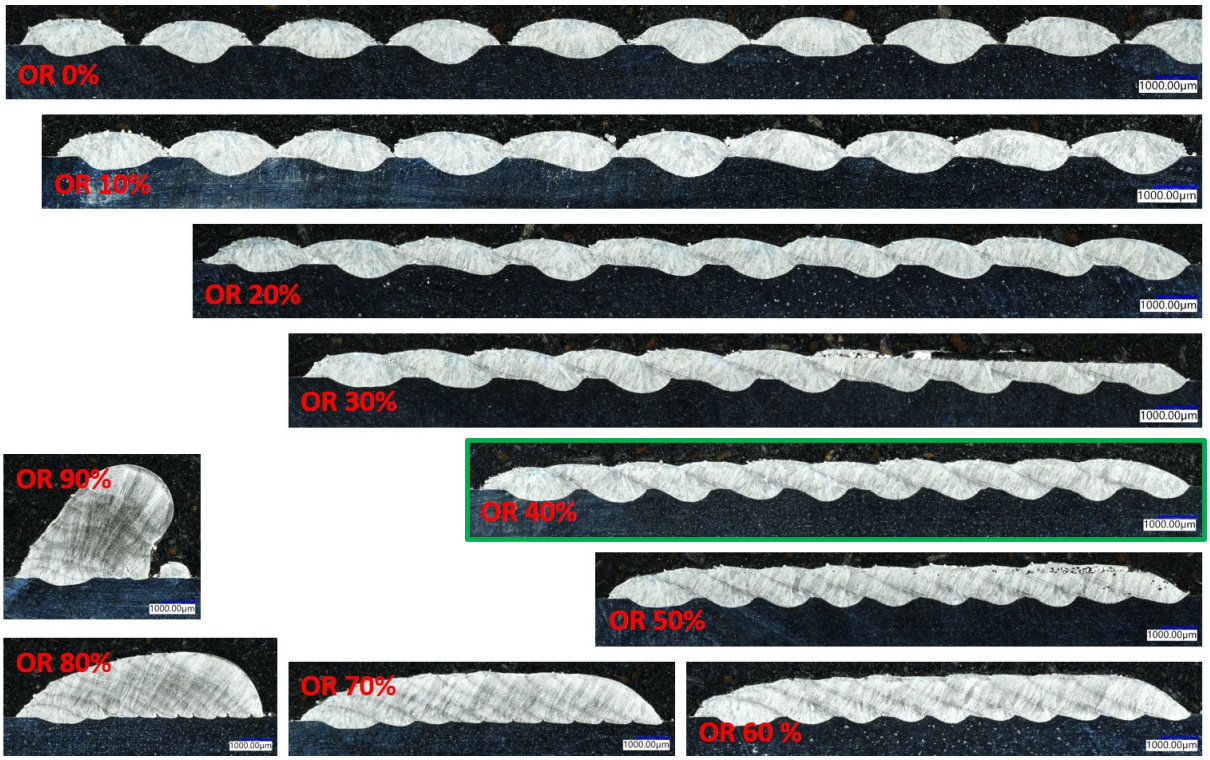

Figure 3.6: OM observations of cross sections of single layer coating with different overlapping rate for optimized process parameters.

of the beam and its passage outside the powder stream, resulting in wider melt pools but less or no powder feeding. Another point is to observe that no interlayer porosity is formed during production. Figure 3.7 (a) illustrates the interest in keeping the working distance constant.

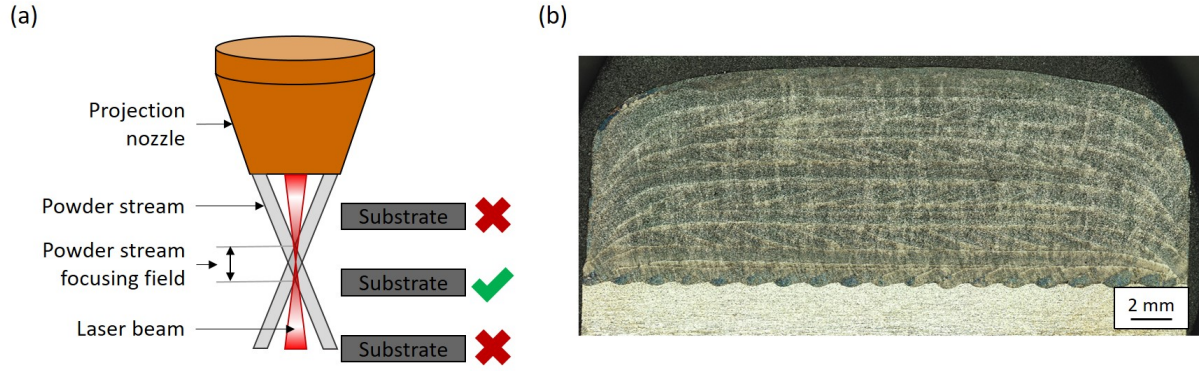

Figure 3.7: (a) Principle of adopting optimized vertical increment to remain in the powder stream focus and (b) OM observation of the cross section of a cube produced with the optimized parameters on the DMG Mori.

With a first increment determined by the height of the previously produced single-layer coating, a 20 mm wide cube with a height of 10 layers is produced. Three more cubes are produced with slightly different height increments and with the 90°-Zigzag deposition pattern. The total height of the cube is measured and divided by the number of layers to determine the Z-increment to be used per layer. The results are summarized in Table 3.1 and an example of one cube cross section is given in Figure 3.7 (b). Note the high density of the cube with a rate of 99.989% estimated by metallographic observation, which has no interbead or interlayer porosity. There is metallurgic continuity between the deposit and the substrate and between the different layers. This result can be obtained by sufficient remelting of the previous layer with the bead dilution rate of 45%.

Table 3.1: Results of cube height and optimized ΔZ.

ΔZ (mm)	Cube height (mm)	Optimized ΔZ (mm)
0.6	7.15	0.72
0.7	7.28	
0.8	7.19	
0.9	7.4	

The optimized parameters used for the repair study are as follows: P = 1500 W, V = 1000 mm/s, Q = 300 rpm = 9.6 g/min, OR = 40 % and ΔZ = 0.7 mm.

3.3 Substrate and machine axis alignment

3.3.1 Problems caused by misalignment

Optimizing process parameters allows to produce dense, crack-free deposits. The geometry of the bead and the layer provides the necessary information about the number and position of the beads to be placed in the pre-machining process to fill the layer. On the other hand, if the starting position of the machine is incorrectly set or the axes of the machine misaligned with the substrate reference frame, this can result in imperfect repairs and, in particular, lack of fusion with non-horizontal edges, as shown in Figure 3.1 (b). It is essential to know the pre-machining position and to correctly set the machine zero by adjusting the program start position. It is necessary to correlate the coordinates of the machine datum with those of the program datum.

3.3.2 Laser beam guide on OPTOMEC

The OPTOMEC LENS MTS-500 machine is equipped with a simple low power laser guide coaxial with the high power laser used to melt the powder. This laser guide was used to set the starting position of the machine in the XY plane.

Figure 3.8 (a) presents the method used to align the substrate to the machine axes and center it in the XY plane. An initial positioning of the sandblasted substrate was done visually using the laser guide. A program was then run to ensure the same shape movement at the top of the pre-machining with the laser guide activated. The substrate was moved until the top of the pre-machining matched the laser movement. This meant that the substrate axes were aligned with the machine and the starting point was centered.

To adjust the Z-axis working distance, the projection nozzle and the top substrate surface are aligned. Knowing the depth of the pre-machining, a simple addition determined the Z-axis position so that the working distance between the substrate and the nozzle was 12 mm, as shown in Figure 3.8 (b).

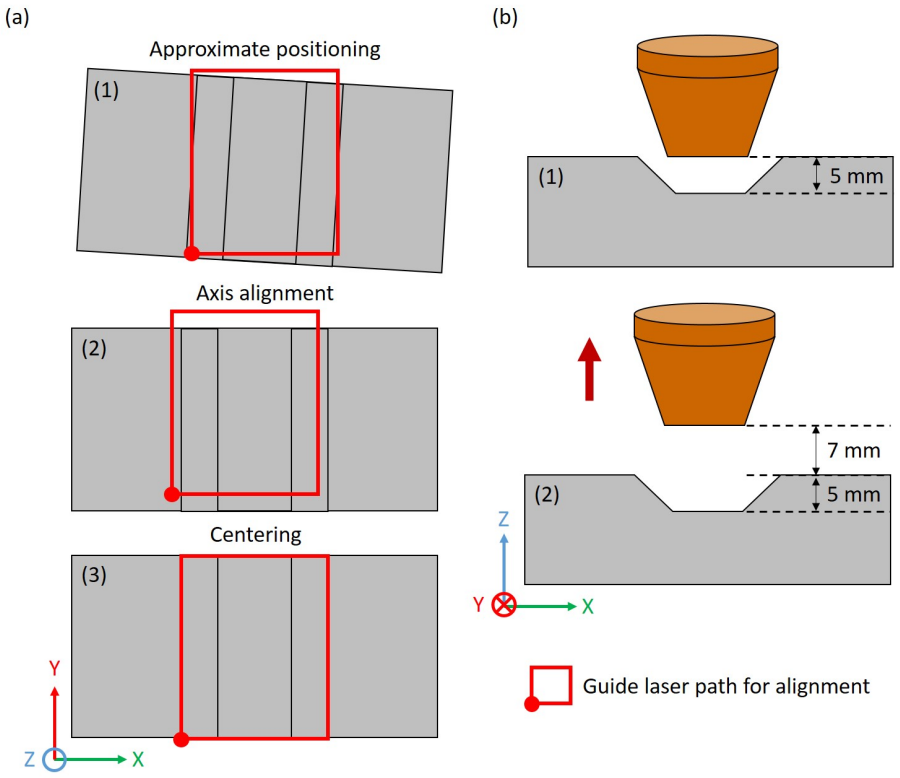

Figure 3.8: Axis alignment and centering method on the OPTOMEC machine for the (a) XY plan and (b) Z axis.

3.3.3 Automated probe head on DMG Mori

The DMG Mori LaserTec 65 3D machine is built on a machine center base and incorporates a ruby ball probe to accurately measure the position of the substrate surfaces. As illustrated in Figure 3.9, the position of the YZ and XZ planes in the machine frame is measured with the probe, and the center is calculated and directly integrated into the program reference frame. The position of the top is also measured with the probe, and adding the working distance to the Z coordinates gives the starting position of the projection nozzle.

The alignment of the axes is not necessary on this machine because the substrate is clamped in a support equipped with jaws, which clamping axes are aligned with the axes of the machine. It is sufficient to know the angle at which the pre-machining has been carried out in relation to the machine axes in order to adjust the material deposition program.

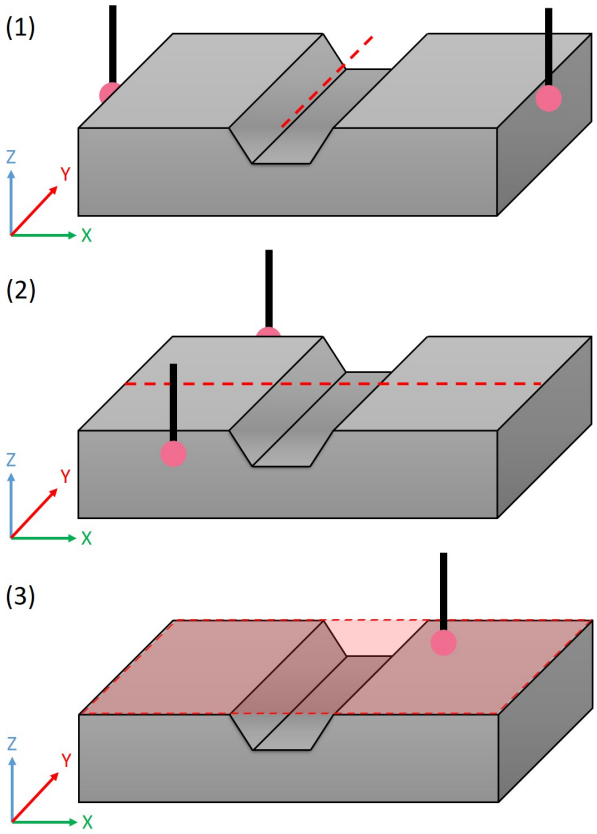

Figure 3.9: Centering method on the DMG Mori for the XY plan and Z axis.

3.4 G-code program generation using Python

Projection nozzles using LMD technology are mounted on CNC machines. G-code programs are used to define sequences of instructions to drive CNC machine tools. This programming is currently highly automated from CAD/Computed Aided Manufacturing (CAM) drawings. However, during this thesis, no CAD/CAM software was available to generate the programs, but this allowed us to understand and adapt the material deposition programs to the repair problem.

In short, these programs are composed of lines of codes that allow its start, its stop, the movement of the projection nozzle and the deposition of material. There are different elements to be found:

- the movement functions (G00, G01, G02, G03) or changes in coordinate systems (G90, G91);
- the coordinates of the points (X, Y, Z, A, C), which allow the machine to know the position of the tool within the manufacturing chamber
- the scanning and rotation speeds (S, F), which specify the speed of the tool;
- and the auxiliary functions (M), which enable the laser to be switched on or off, the powder or gas flow to be switched on, the lubrication to be switched on or the tool to be changed.

The bead deposition strategy can be adjusted by assembling these lines in a precise sequence. However, to achieve dense and metallurgically continuous repairs, it is necessary to have the right amount of material in the right place. A set of parameters and locations must be calculated from the input data and then compiled with machine language to achieve this result. The Python language was used in this thesis for the calculation, compilation and generation of the G-code files because of its simplicity and versatility.

3.4.1 Calculation of filling parameters

The input data is the information obtained during the parametric optimization and pre-machining steps described previously. It includes the optimized process parameters, deposition pattern, bead, layer and pre-machining geometries, which details are given in Table 3.2.

Figure 3.10 describes the initial calculations performed in the Python program with the data needed to determine the distance between each bead, the number of layers to

Table 3.2: Input data given entered in the Python program for groove pre-machining.

Process parameters	Bead and layer geometries	Pre-machining geometry
Laser power (W)	Layer height (mm)	Shape
Scanning speed (mm/s)	Bead width (mm)	Bottom width (mm)
Powder mass flow rate (rpm)	Overlapping rate (%)	Depth (mm)
Deposition pattern		Opening angle (%)
		Length (mm)

be deposited in the pre-machining, the width of each layer, and the number of beads needed to fill each layer. The objective of these calculations is to know exactly how many beads are needed in each layer to fill the pre-machining. Their start and end positions are calculated to be implemented in the line generation explained in the next section. These calculations allow to compartmentalize the pre-machined area, so that each location can receive a bead, corresponding to the right amount of material.

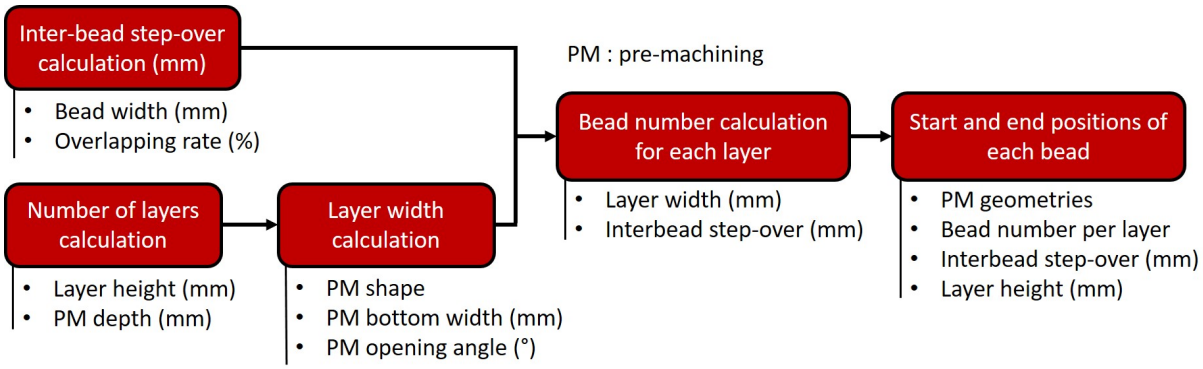

Figure 3.10: Calculation of the parameters necessary for the generation of G-code files.

3.4.2 Generation of G-code lines

The G-code programs used on the additive manufacturing machines are slightly different, but have the same structure in three blocks: the initialization phase, the movement phase, and the extinction phase. The generation of the .mpf G-code file with the Python program follows this pattern. It uses calculation lines, strings, for loops, and if conditions. The principle is illustrated in the flowchart Figure 3.11.

The first block initializes the program, the machine and its accessories. The variables are defined and sent to the machine in instructions. During this phase, the process parameters such as laser power, feed speed and powder mass flow are implemented. The start position of the nozzle is also set.

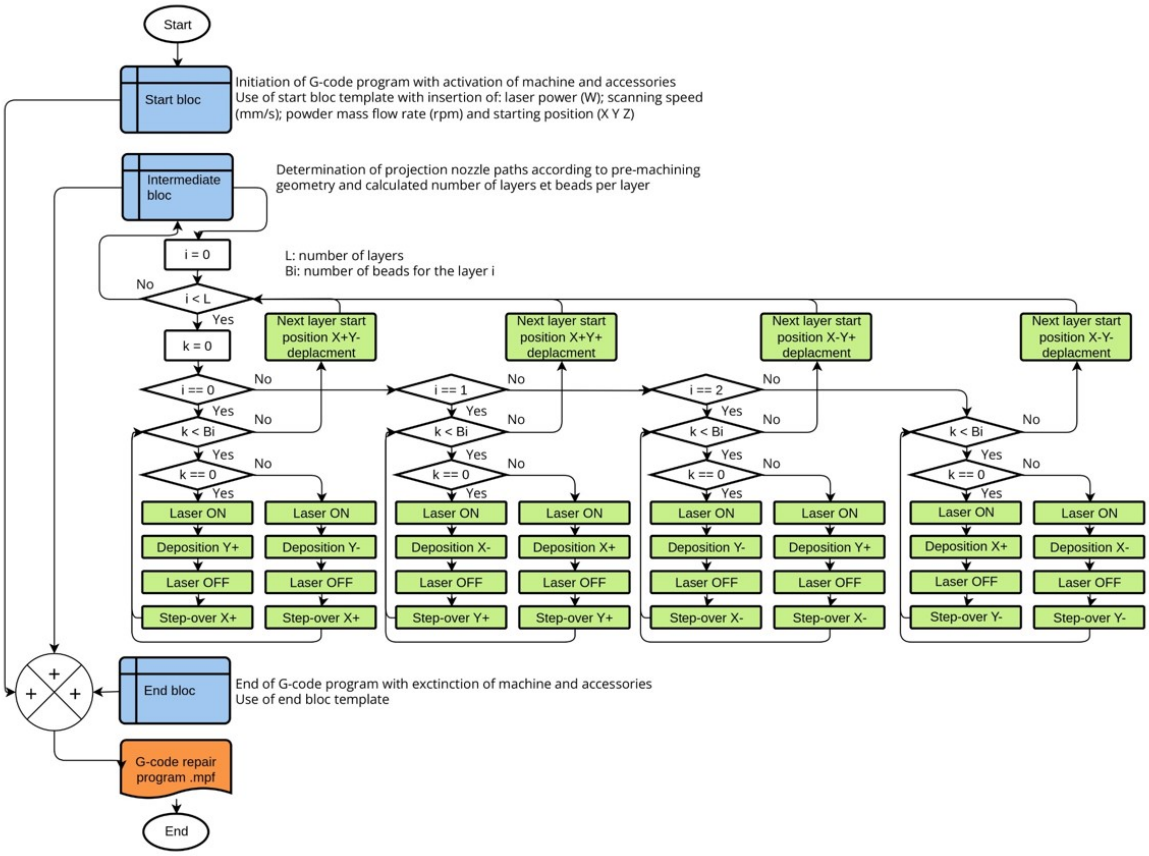

Figure 3.11: Chart example of Python program for the generation of G-code for the 90°-Zigzag deposition pattern developed during the thesis.

The intermediate block consists of all the lines of code that instruct the paths to be taken by the laser, how to maintain the working distance, and how to turn the laser on and off. Depending on the deposition strategy used and the shape of the pre-machining, for loops and if conditions allow, at each pass in the green boxes (Figure 3.11) the code lines necessary to fill each layer with the right number of wires are added. At the end of each layer, a move to the starting position of the next layer is performed laser off. These conditions depend on the parameters previously calculated with the number of layers and beads per layer, the width and length of the layers.

The end block has a calculation line that allows to know the duration of the deposition time in the pre-machining. The rest of the commands are fixed and allow to disable the machine accessories and to end the program.

Once these three blocks are generated and saved in lists, they are compiled and saved as a G-code file with .mpf extension, which can be read by the CNC machine.

3.4.3 DeltaHD optimization

The paths of the projection nozzle are usually generated by CAD/CAM software, which is optimized for manufacturing parts from a flat surface. The number of beads to be deposited depends on the width of the layer as well as the bead geometry and the deposition parameters of the additive process. The calculated number is rarely a whole number, which must be rounded to the nearest whole number. For the repair of a confined pre-machining, this results in two situations, the first where too many beads are calculated and the second where too few beads are calculated. In the first case, the last bead to be placed in the layer is geometrically constrained by the presence of the second last bead and the slope of the pre-machining according to the degree of rounding, which prevents it from penetrating to the desired position, as depicted in Figure 3.12. Porosity is formed due to lack of fusion. In the second case, the porosity is caused by a lack of material, as shown in Figure 3.12. Neither situation is a problem in conventional additive manufacturing because the next layer deposited would compensate for the approximation. In the case of repair, the porosity is present in the part and cannot be removed without re-machining. Therefore, the logic of this software is not adapted to the repair situation. The solution is to adjust the overlapping rate between the beads of a layer in real time after calculating the number of beads in that layer, so that this number matches the width to be deposited and results in the diagram in Figure 3.12.

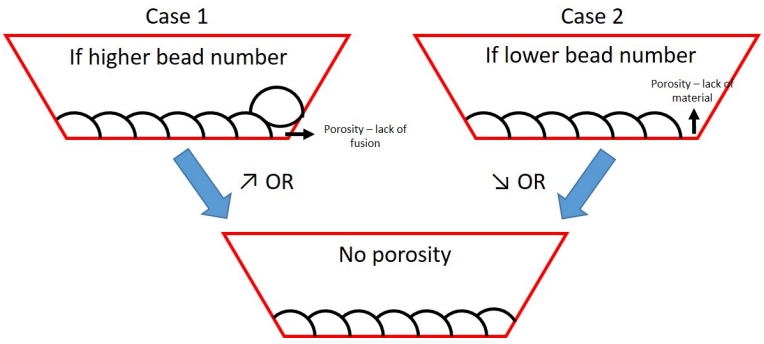

Figure 3.12: Illustration of the solution of the approximation problem using a feedback of the overlapping rate calculation at each layer during program generation.

In practice in the Python program, a feedback loop is used to recalculate the overlapping rate at each layer from the layer width and the approximate number of beads per layer. The exact position of each bead is calculated based on the complex shape of the pre-machining. This new method adapts the generation of tool paths to the case of the LMD process, which has thin and not very diluted beads, and to the situation of pre-machining repair, which is a significant geometrical constraint compared to conventional additive manufacturing on

open surfaces. The tests conducted using this technique demonstrate a clear improvement in repair density compared to repairs performed with a non-optimization strategy, as shown in Figure 3.13.

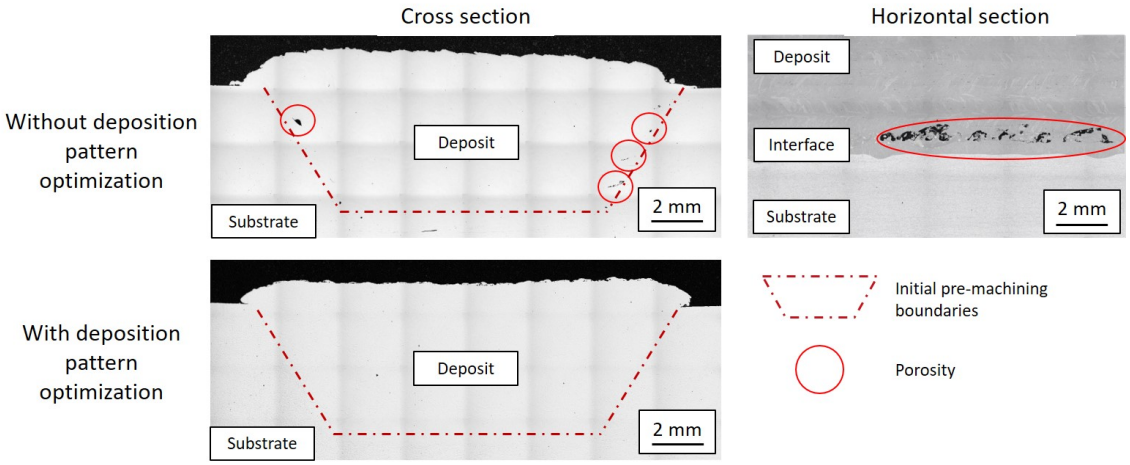

Figure 3.13: OM observations of cross-sections of the repair tests with and without adaptive deposition strategy.

Unfortunately, the integration of this adaptive strategy of the overlapping rate at each layer depending on the number of beads and the width to be deposited was not integrated into the Python program program as it was performed later in the research work. Therefore, repair work of various shapes and sizes of pre-machining presented in the following chapter still presents repairs with problems of lack of fusion at the substrate/deposit interface. However, this will demonstrate the importance of the shape of the pre-machining on the quality of the repair.

3.5 Summary

This chapter focused on the optimization of the LMD process as applied to the case of repairing pre-machined parts made of stainless steel 316L components. Combinations of process parameters had to be determined to achieve dense and crack-free deposits with beads metallurgically bonded to the substrate and between them. The method for alignment of the machine axes to the substrate axes and centering of the start position was detailed. Finally, the Python program for generating G-code files was explained and an improved deposition strategy applied to the repair was integrated.

The influence of four deposition parameters (laser power, feed rate, powder mass flow rate, and overlapping rate) on the deposition density was investigated. Optimized

deposition parameters were determined to obtain deposits with a density greater than 99.99% and diluted beads at a rate of 45% in the previous layer to avoid the formation of porosity in the confined areas of the repairs. These parameters are specific to the OPTOMEC LENS MTS-500 and DMG Mori LaserTec 65 3D machine configurations and to SS316L powder.

The technical problem of positioning and aligning the machine axes with those of the substrate was detailed. A method was developed for each machine, which has different accessories depending on the manufacturer's design. In one case, the positioning must be done visually with the use of a laser guide that comes to traverse a known path on the substrate. In the other case, the measurement is performed with a probe and the values are automatically entered in the program's reference frame.

Finally, a Python program for generating G-code files was developed during this thesis and explained in this manuscript. This program is adapted to the pre-machining filling and takes into account the process parameters, bead geometries, layers and pre-machining to have the right number of beads in the right place. The integration of an adaptive overlapping rate strategy at each layer allows for dense repairs, especially at the substrate/deposition interface. The use of measuring tools implemented in the CNC machines guarantees the accuracy of the alignment and the coordinates of the part to be repaired.

Chapter 4

Correlation between the pre-machining geometry and the characteristics of the repair

Abstract

The first part presents a study on the opening angle influence of the pre-machining on the mechanical behavior of the repaired parts in order to determine an optimized angle for the repair. The second part focuses on the technical conditions to be imposed on the opening angle for the repair of deep defects to have high density of deposition and avoid collision. Finally, a minimization of the repair volume is performed using the results obtained previously. Increasingly complex pre-machining geometries were used throughout the chapter to observe the ability of the LMD process to repair complex shapes.

Published paper associated to this chapter:

- T. Cailloux, W. Pacquentin, S. Narasimalu, F. Belnou, F. Schuster, H. Maskrot, C. Wang, K. Zhou, F. Balbaud-Celerier, Influence of trapezoidal groove geometry on the microstructure and mechanical properties of stainless steel 316L parts repaired by laser metal deposition, *Materials Science and Engineering A.* • (2022) Volume 859, 144218;
- B.S. Smail, T. Cailloux, Y. Quinsat, W. Pacquentin, S. Narasimalu, H. Maskrot, F. Balbaud-Celerier, Integrated approach to stainless steel 316L parts repair for pitting corrosion using laser metal deposition, *Journal of Manufacturing Processes.* 95 (2023), Volume 95, Pages 1-13.

Contents

4.1 Introduction

As mentioned in the state of the art, repair studies focus exclusively on the effect of LMD process parameters on the characteristics of the repaired parts. By varying the main deposition parameters like the laser power or the scanning speed or using powders of the same material from different manufacturers, the authors modified the microstructure of the deposit and correlated it to the overall repair properties [143, 144, 145]. However, for all the deposition microstructures produced in the LMD repair literature, an interface between the substrate and the deposit is observed. Moreover, the use of a single pre-machining geometry does not indicate whether the deposition parameters used are applicable in other situations.

Some studies on the repair of pre-machining on different shapes highlight the problem of the confinement of the deposition area and the inaccessibility of the spray nozzle. Lack of fusion on vertical or close edges is observed, caused by lack of dilution of the melt pool on theses walls [106, 107]. Therefore, the opening angle of the pre-machining is of great importance to obtain a dense repair that is metallurgically bonded to the substrate. However, the literature does not quantify limiting or optimized values of this opening angle. Oh *et al.* [108] attempted to demonstrate the influence of pre-machining depth on the mechanical properties of repairs, but lack of fusion at the substrate/deposition interface due to poor deposition parameters did not allow conclusive results.

In addition, the interface is a complex zone because it is the site of microstructural and mechanical heterogeneity between different zones of a repair. Balit *et al.* [101] observed an increase in hardness at the interface and a different distribution of stress and strain between substrate, interface and deposit in tensile tests. These deformation incompatibilities explain the degraded mechanical properties of conventional/additive composite parts. The addition of lack of fusion in this area, as explained above, would cause even more degraded mechanical properties. It is therefore essential to ensure proper fusion of the non-horizontal edges by knowing the influence of the pre-machining geometry on this parameter.

These observations from the literature highlight the lack of information on the effect of the pre-machining geometry, especially the opening angle, on the final quality of the repair. A specific study would thus allow the determination of optimized geometric values and the experimentation of the feasibility of the LMD process for the repair of different pre-machining geometries. Therefore, the first part of this chapter is dedicated to the study of the influence of the pre-machining opening angle on the density and mechanical properties of the repaired parts. The second part is dedicated to the correlation between

the depth and the opening angle of the pre-machining to allow the repair of deep defects while ensuring a good deposition quality and avoiding machine/part collisions. Finally, results obtained in the first two parts of the study are used to optimize the repair volume and minimize the material to be machined in the case of a typical defect. Increasingly complex defects are used in each part to demonstrate the ability of the LMD process to repair various forms of pre-machining.

Three shapes have been selected to represent pre-machining operations performed on substrates to remove the initial damage defect and to provide access to the projection nozzle. These shapes allow different types of damage to be treated by limiting the material removed during machining. They are shown in the Figure 4.1.

- The trapezoidal groove with inclined edges is the most frequently repaired geometry in the literature because it is easy to produce with conventional machining tools. This type of pre-machining allows the repair of defects that follow an axis over long lengths, such as cracks or welds between two severely corroded parts;

- The flat-bottom conical is a geometry similar to the groove, but more localized to a point. The important difference lies in these rounded edges, which require more complex machining than in the case of the groove. This type of pre-machining can be adapted to repair localized defects such as SCC or pitting corrosion;

- The ellipsoid is a more complex shape and has never been studied in the literature, except for a single repair using the cold spray [34]. However, this geometry makes it possible to greatly reduce the volume to be machined for pitting type defects, which have this ellipsoidal shape as shown in the literature [146, 147, 148]. In this study, this shape was used in an optimization process to reduce the repair volume.

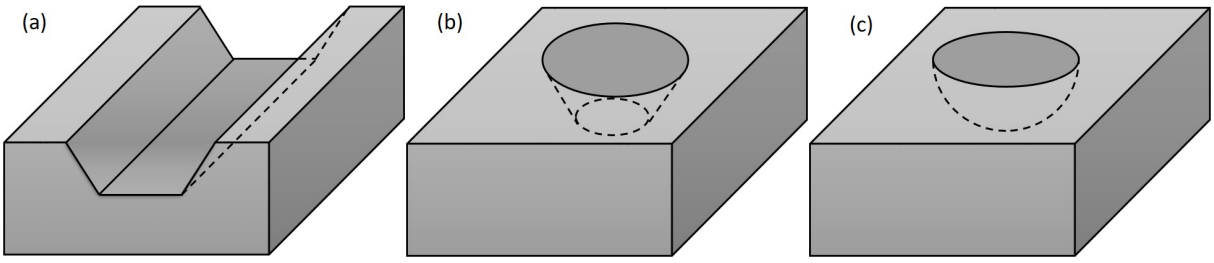

Figure 4.1: Pre-machining shapes used for the repair study: (a) trapezoidal groove, (b) flat-bottom conical hole and (c) ellipsoid hole.

4.2 Influence of the opening angle on the density and mechanical properties of repaired trapezoidal grooves

4.2.1 Experimental protocol

Trapezoidal grooves were milled lengthwise in the SS316L substrates. The cross-sectional geometry of the substrates with a groove opening angle θ having one of the following values is shown in Figure 4.2 (a): 105°, 120°, and 135°. A 100 mm length of the cross section was extruded.

The deposition parameters for the OPTOMEC machine determined in Chapter 3 were used in this study, namely P = 650 W, V = 600 mm/min, Q = 6.6 g/min and OR = 30%. The strategy of adjusting the overlap rate between the beads for each layer has not yet been implemented in this study.

The deposition pattern consists of using zigzag paths along the longitudinal direction with a 180° rotation between each layer, as illustrated in Figure 4.2 (b). This could help stabilize the different layers in height [149] and avoid the formation of grains with a single preferential growth direction to prevent a crack from propagating easily in the material [150]. This strategy facilitates the deposition of the beads in the groove, especially in the case of small opening angles. Furthermore, studying the insertion of the beads in a confined area is achievable.

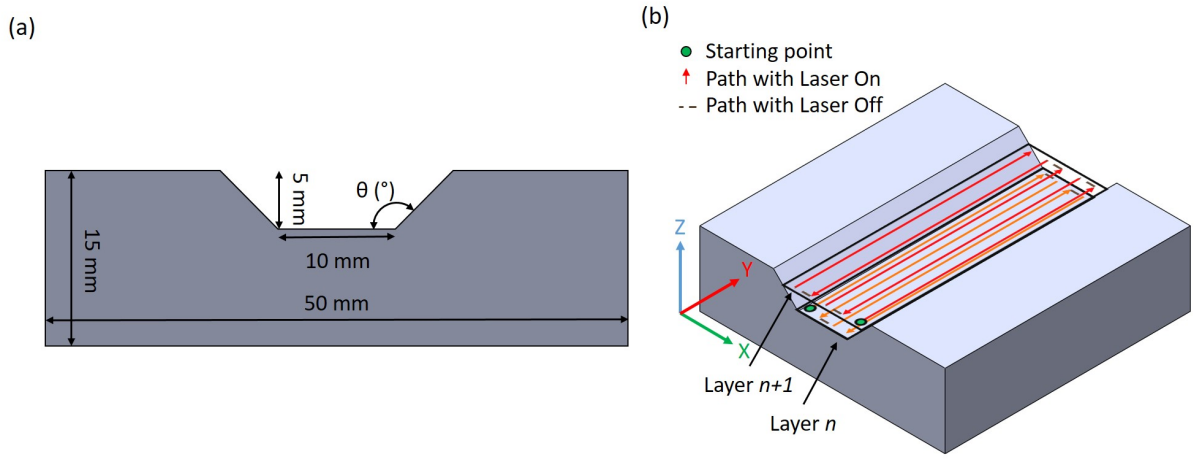

Figure 4.2: (a) Cross-section of the groove pre-machining in the substrate and (b) 180°-Zigzag deposition pattern used for this study.

4.2.2 Density rate

The repaired samples were subjected to dye penetration tests and radiography. The results show the absence of porosity on the surface of the repairs. The radiographs confirm that no macro-porosity, incomplete fusion, or macro-cracks are present in the repair volume, as shown in the radiographic films Figure 4.3. Note that the deposit appears brighter than the substrate on the film, probably due to differences within the material. The Image Quality Indicator specifies that any defect smaller than 300 µm may appear blurred on the image, indicating that more advanced analysis needs to be performed to detect smaller defects.

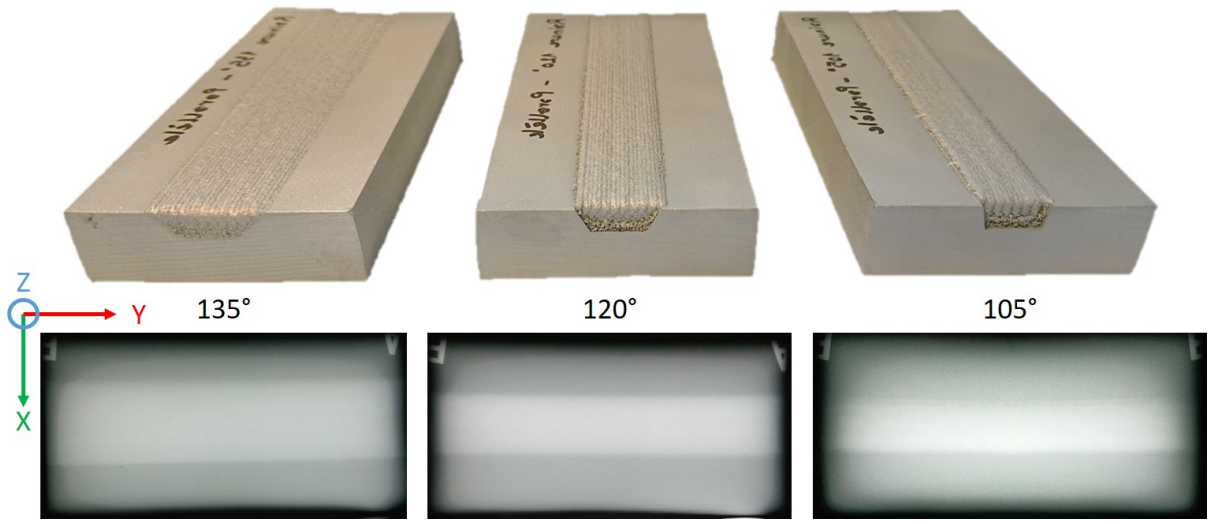

Figure 4.3: Radiographic films of the different repairs.

The density of the samples was calculated by image analysis on several cross sections as a complementary method to validate the results of the non-destructive tests. A defect with a minimum size of 1 µm can be detected with the resolution of the OM used. Present porosity is a result of gas entrapment. Due to the use of inert shielding gas, this phenomenon is commonly observed in LMD-printed parts [56]. In addition, lacks of fusion between the deposit and the substrate are observed. These types of porosities are more noticeable as the groove opening angle decreases, as shown in Figure 4.4 (a), due to the poor accessibility of the projection nozzle. Relative densities of 99.93%, 99.97%, 99.95%, and 99.92% were measured for the substrate and the 135°, 120°, and 105° grooves, respectively (Figure 4.4 (b)).

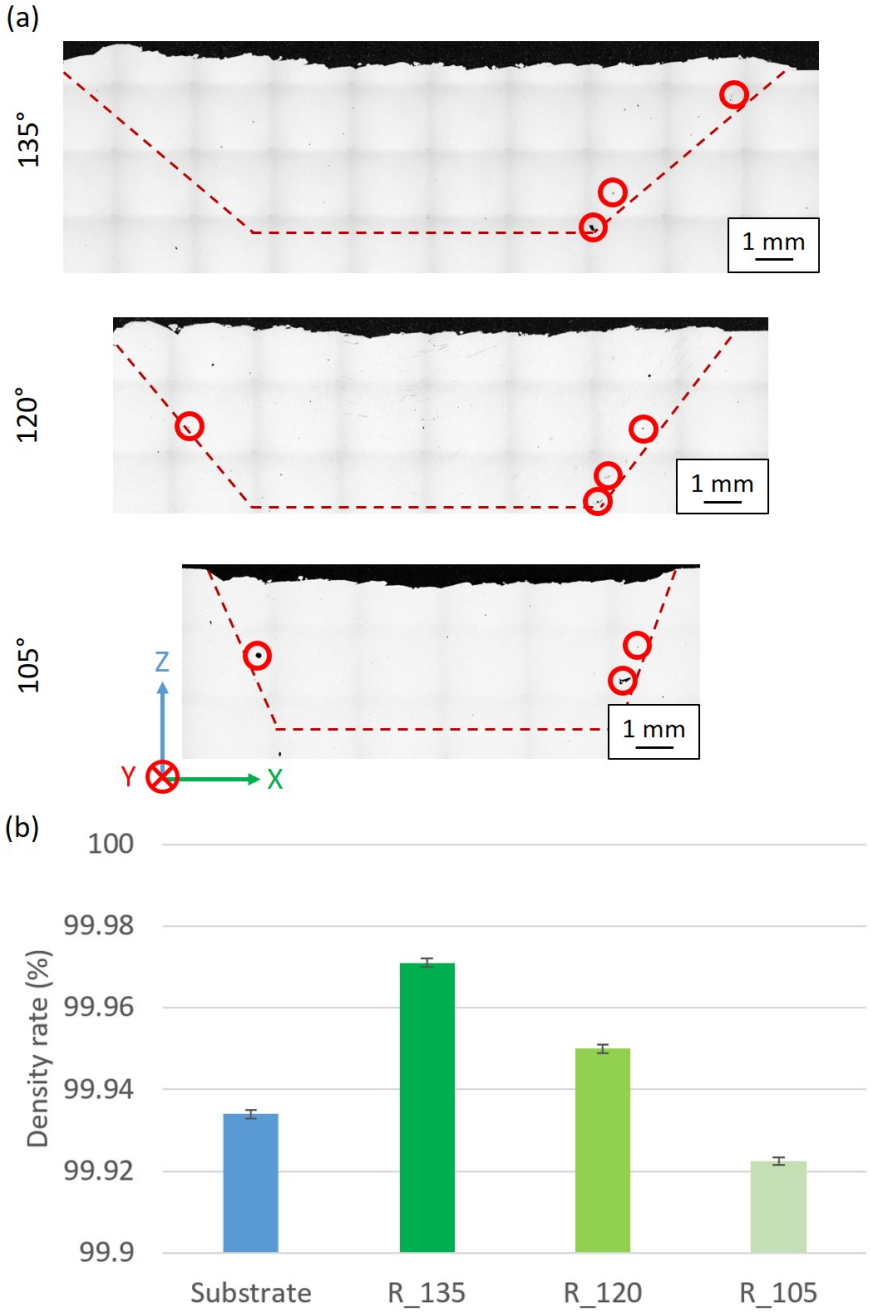

Figure 4.4: (a) Radiographic films, (b) OM observations of the cross-sections and (c) density rate summary of the different repairs.

4.2.3 Microstructure

In order to observe the microstructure of the repair especially at the interface between the substrate and the deposit, SEM observations and EBSD mapping were carried out on the three sides of the repair volume, as shown in Figure 4.5 and Figure 4.6. The

morphology and growth direction of the grains can be examined. The analyses performed are representative of the three opening angles, as no differences were observed between the microstructures of the repairs. The heterogeneous microstructure of the repaired part is characterized by four distinct zones, which are the deposit and the MZ from the FZ and the HAZ and the unaffected substrate from the base metal.

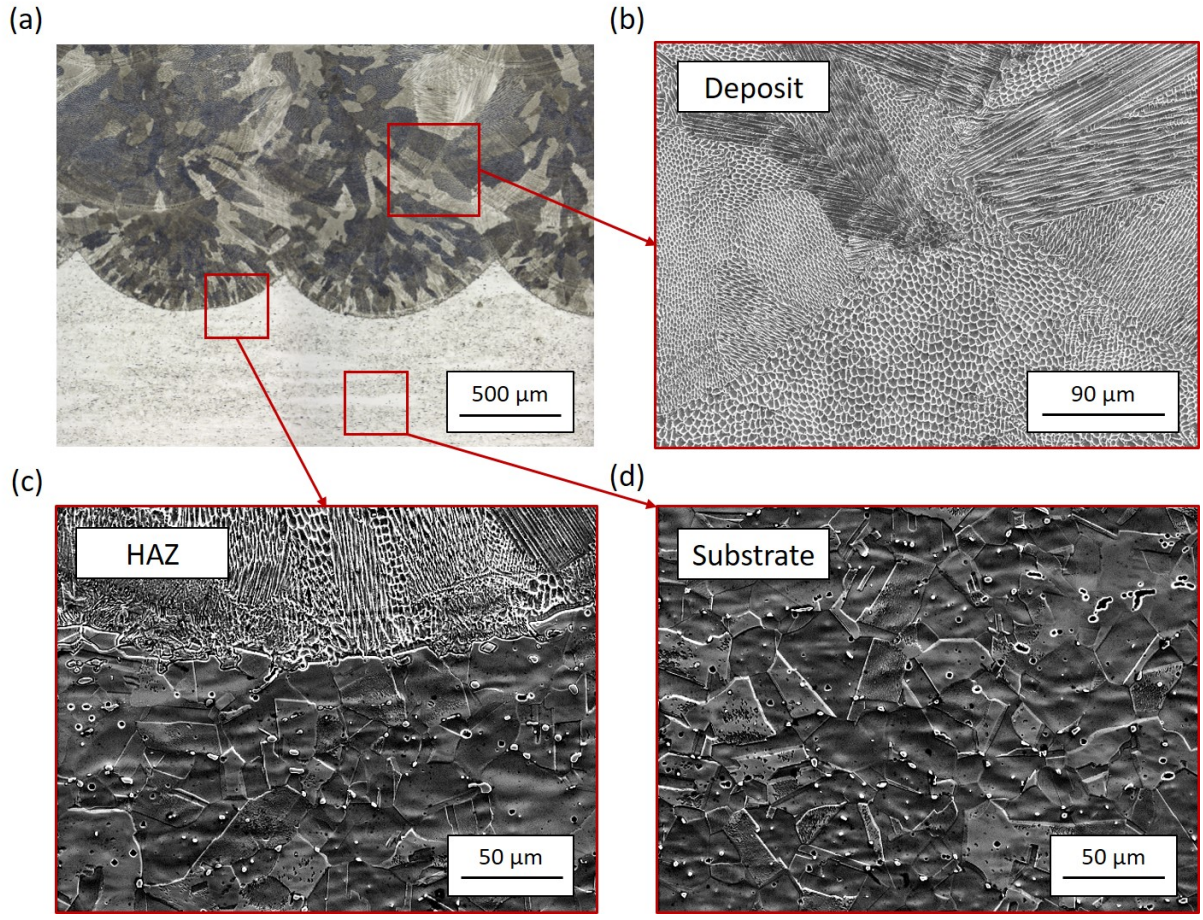

Figure 4.5: (a) OM observation of overall microstructure of the interface, and SEM observation of the enlarged view of (b) the deposit, (c) the HAZ, and (d) the substrate.

The deposit region represents the portion of the FZ where the powder is fused to replace the missing material. Surrounding this region along the fusion boundary is the MZ, delimited by the solidified melt pool boundaries of the beads in contact with the substrate. It consists of melted and resolidified base metal mixed with powder, which forms the first beads in contact with the base metal. These melt pool boundaries are also found within the deposit. The effective height and width of the beads is 500 µm and 1200 µm, respectively. The coarse and columnar grains are clearly visible in Figure 4.5 (a) and Figure 4.6 (c), where the grains are contrasted by electropolishing. The preferential growth direction of the grains is in the direction of the center the melt pool and in

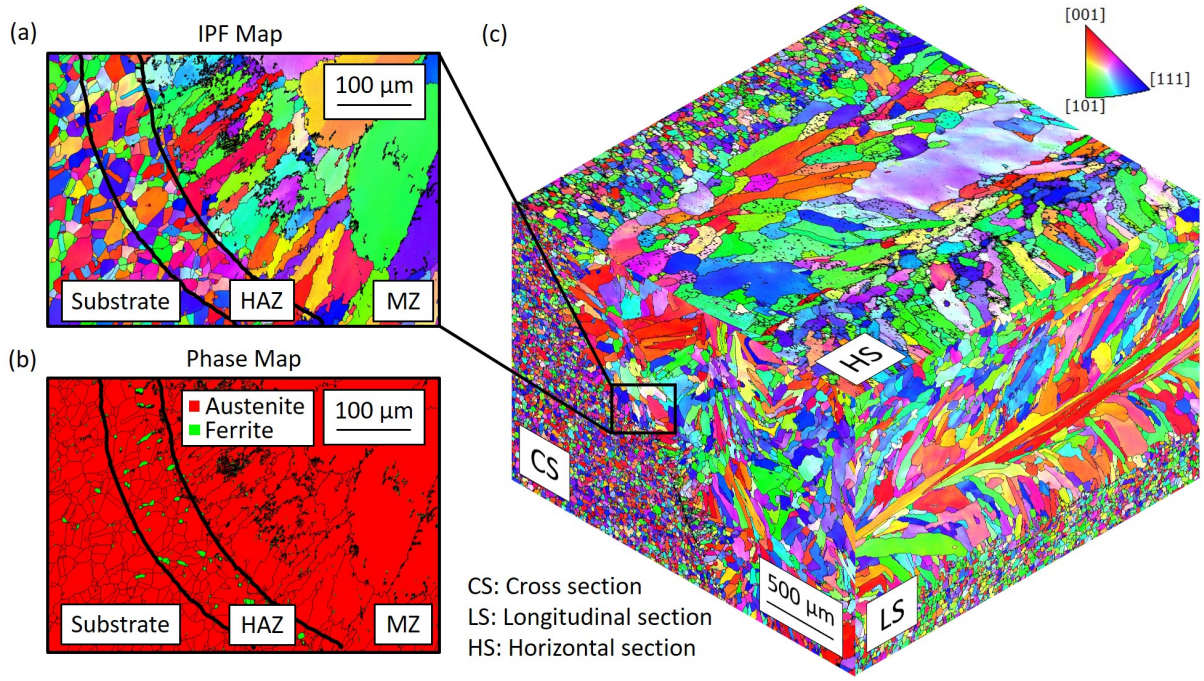

Figure 4.6: EBSD results of the 120°-groove repaired specimen: (a) IPF map and (b) phase map of the interface and (c) pseudo-3D IPF grain map.

the direction of the movement of the nozzle as shown in [81]. These two directions correspond to the directions of the thermal gradient present between the melt pool and the substrate. Figures 4.5 and 4.6 reveal that many grains include the melt pool boundaries. This observation suggests an epitaxial growth of the grains between the substrate and the deposit and between the different layers. This phenomenon contributes to a strong metallurgical bonding throughout the repair. It should be noted that this epitaxial growth results in smaller grains in the MZ with an average area-weighted grain size of 62.5 ± 44.3 µm than in the rest of the deposit, which exhibits an average area-weighted grain size of 121.4 ± 68.4 µm. This observation has already been made in the work of Balit *et al.* [101]. Microscopically, an intragranular cellular substructure is observed in the grains with a cell size around 3 ± 0.6 µm, which is common in LMD-printed parts due to the high cooling rate of the process. Since adjacent cells have the same crystallographic orientation, a cell cannot be considered as a grain [151, 152]. They are the result of a concentration of a high density of dislocations [61] and a micro-segregation of elements in the grain, where the cell boundaries are rich in Cr, Ni, Mo and S, while the centers of the cellular grains are rich in Fe, as observed in Figure 4.7. However, the element Mn is difficult to distinguish in the mapping. Some authors such as Barkia *et al.* [81] report a depletion of Mn at the cell boundaries, while Zietala *et al.* [84] report an enrichment. The first option seems to be more appropriate, since Barkia *et al.* [81] used the same machine, the

same powder and similar deposition parameters as the present study, in contrast to the other authors. The SEM resolution did not allow to distinguish them in the present study, but the authors observe the presence of Si-oxides and Cr-Mo precipitates and Mn-Cr-Mo precipitates in the cell boundaries.

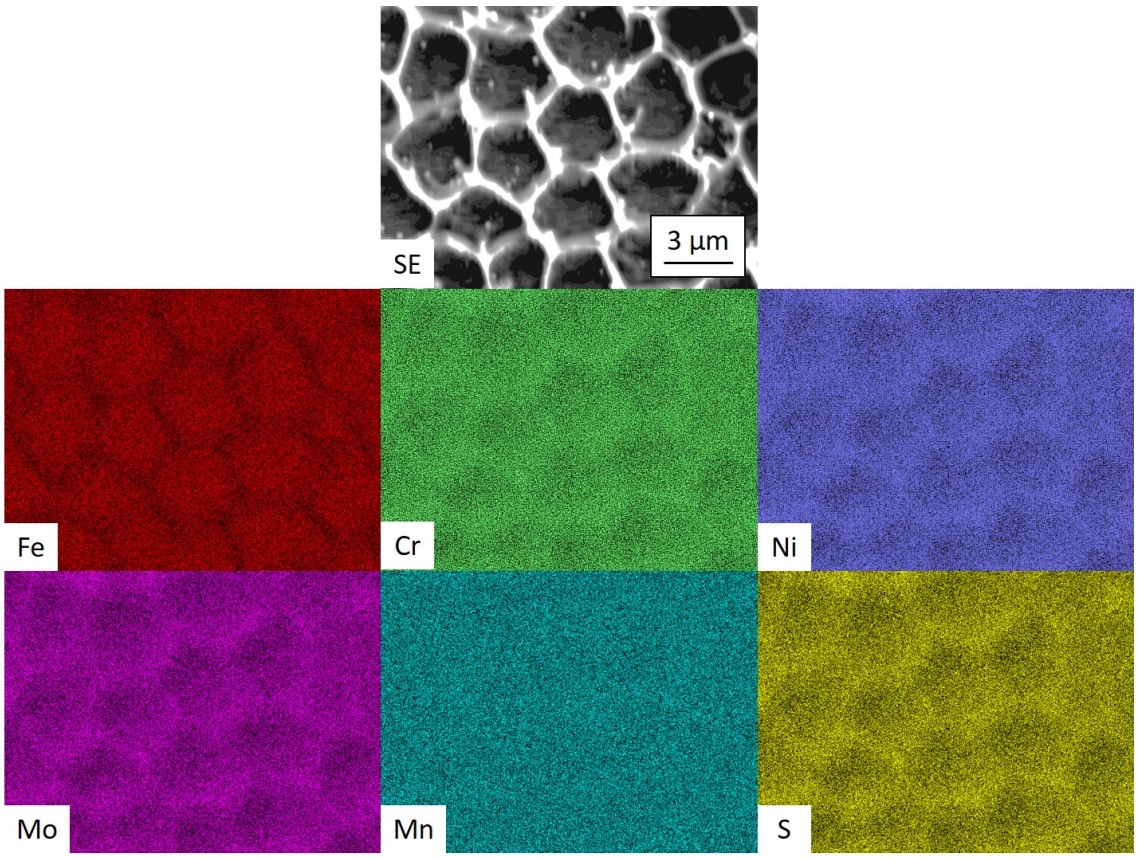

Figure 4.7: EDS mapping of the cellular substructure of the deposit grains.

The HAZ has equiaxed but slightly coarser grains than the substrate not quantified in this study, but apparent, as observed in Figure 4.5 (c). The HAZ is the substrate closest to the deposit that has not received enough energy from the laser to melt, but enough energy to undergo local recrystallization with a possible reduction of twins, local grain growth and phase changes, followed by a very rapid cooling [153]. From Figure 4.6 (b), the HAZ can be estimated at about 100 µm, where an increase in ferrite content relative to the substrate is observed and described below.

The substrate has fine and equiaxed grains with an average area-weighted grain size of 38.5 ± 13.2 µm. These are commonly seen in SS316L hot-rolled parts after heat treatment (solution annealing) [11]. Figure 4.5 (d) highlights the equiaxed microstructure with the presence of impurities and porosities, which are common casting defects found in

blooms. Porosities are spherical caused by gases trapped in the material during the bloom solidification. The excess gases in the molten metal are expelled in the form of bubbles, but some may remain trapped in the metal matrix. The alloying elements interact with each other or with the atmosphere to form inclusions [154].

Heterogeneity of the phases present in the different zones can be observed in addition to the grain size heterogeneity in the repair. As displayed in Figure 4.6 (b), the EBSD analysis highlights that the deposit consists of a single austenite FCC phase, while the substrate and the HAZ consist of austenite FCC and ferrite BCC phases. In contrast, the ferrite content in the substrate is very small and present as a residue. However, because the laser energy has caused recrystallization and phase transformations, the amount of ferrite in the HAZ is higher at a level of 2.4%, compared to 1% of the substrate.

The Schaeffler diagram explains the presence of a higher proportion of ferrite phase in the HAZ [155]. According to the chemical composition of the powder and the substrate, the equivalent chromium and nickel contents are calculated using the following equations 4.1 and 4.2:

$$\%Cr_{equivalent} = \%Cr + \%Mo + 1.5 * \%Si + 0.5 * \%Nb \tag{4.1}$$

$$\%Ni_{equivalent} = \%Ni + 0.5 * \%Mn + 30 * \%C \tag{4.2}$$

Figure 4.8 (a) summarizes the calculation results for the chromium and nickel equivalents, which are 20.7% and 11.4% for the substrate and 21.1% and 15.2% for the powder, respectively. The results indicate that the molten powder theoretically cannot form a ferrite phase. During the LMD process, however, the substrate can theoretically form up to 10% ferrite. The non-repaired substrate has a predominantly austenite structure. This is because it has undergone an anti-ferrite heat treatment after manufacture according to its compliance sheet. However, as the temperature is raised by the laser energy, it forms more ferrite in the HAZ.

The previous results were confirmed by EDS analysis of the repair interface. The chemical composition along the measured line varies more in the deposit than in the substrate. The line passes through the center and edges of several cells of a grain, highlighting the variations in chemical composition between these cells. The presence of ferrite at the interface can be highlighted by chemical elemental analysis. As explained by Tao *et al.* [156], ferrite phase contains less iron and nickel and more chromium and molybdenum than austenite phase, which agrees with our analysis as shown in Figure 4.8 (b).

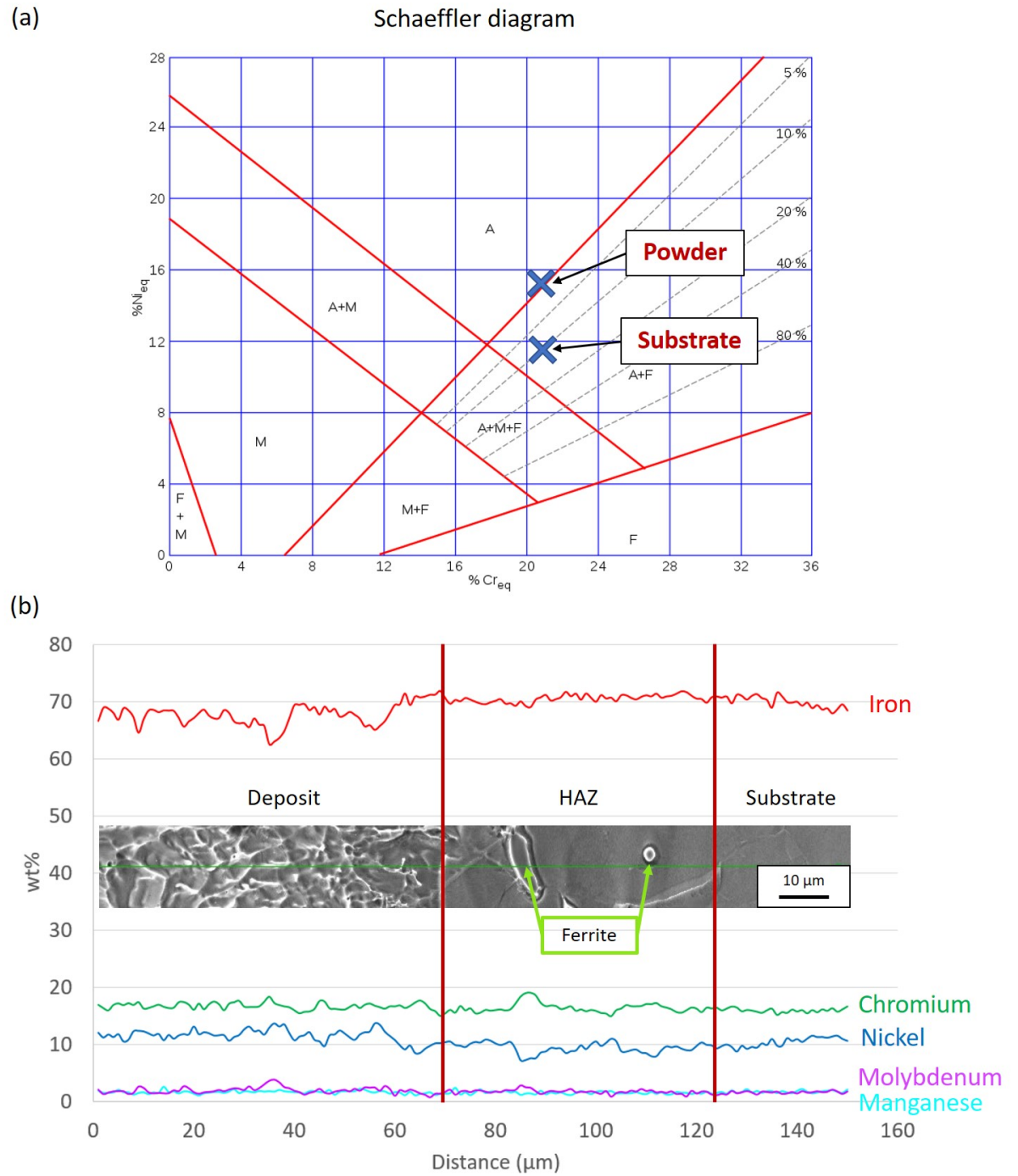

Figure 4.8: (a) Schaeffler diagram with powder and substrate positions and (b) EDS analysis of the repair interface.

4.2.4 Microhardness mapping

To reveal the microhardness gradients across the different areas of the repair, microhardness mapping was performed on the cross sections of the repaired specimens. A

microhardness of 190 HV was obtained for the substrate, 240 HV for the interface, and 200 HV for the deposit (Figure 4.9). Regardless of the groove opening angle, the microhardness value is much higher at the interface, making it more brittle than the other two areas. The hardness peak is located in the HAZ and the first beads in contact with the substrate according to the microhardness mapping.

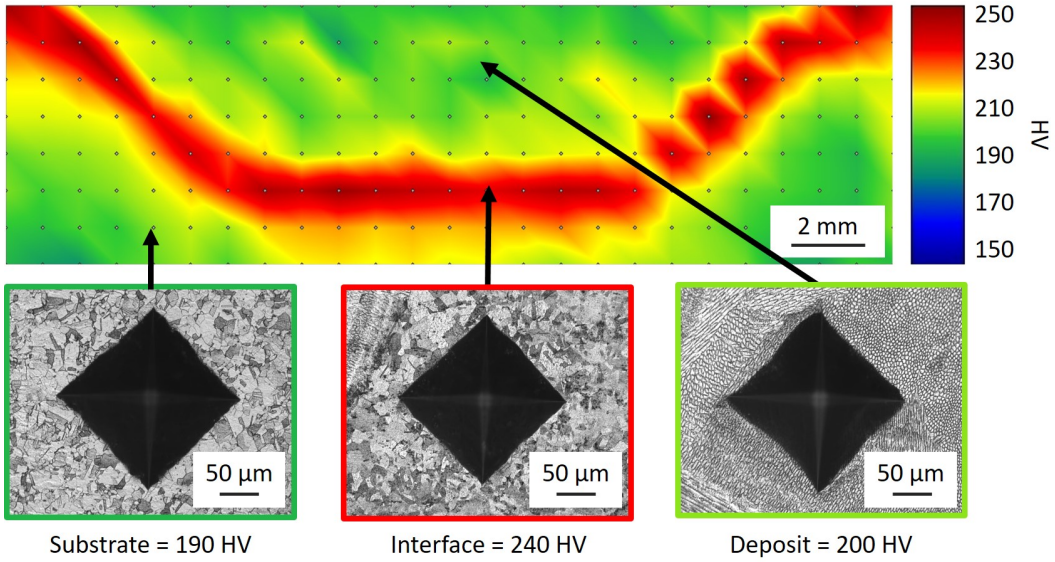

Figure 4.9: Microhardness mapping of the 135°-groove repair.

Literature has reported that the microhardness of SS316L repairs generally varies linearly between the substrate and the deposit, with no hardness peak between the two [108, 157, 158, 145].

However, some authors also report a hardness peak at the interface between the base metal and the fusion zone in their samples. Several mechanisms are involved in the increase in microhardness, including the concentration of residual stresses, the presence of the ferrite BCC phase due to the repair process, the strengthening of the substrate and the smaller grain size in the first deposited layer compared to the rest of the deposit. Indeed, Auzoux *et al.* [159] found that residual stress was generated in SS316L during arc welding, which resulted in significant plastic deformation and strain hardening. They observed the presence of a high density of dislocations in the HAZ and a higher hardness than the base metal. Kannan *et al.* [160] have deposited SS316L using WAAM process. A peak of microhardness is observed at the interface and attributed to the increased presence of residual delta ferrite. For Balit *et al.* [101] the increase in microhardness at the interface is the result of substrate strengthening in the HAZ and finer grains than the rest of the deposit in the MZ due to epitaxial grains growth of the first beads with the

fine grains of the substrate.

Based on these observations in the literature, some phenomena could be identified in this study to explain the rise in microhardness at the interface. In fact, the presence of a BCC ferrite phase in the HAZ and smaller grains in the beads in contact with the substrate are confirmed in this study, as shown in the Section 4.2.3 and can explained the microhardness peak at the interface.

Moreover, the deposit has a higher hardness than the substrate. Nevertheless, the grains have a larger size. According to the Hall-Petch relation, the microhardness should be lower than in the substrate. However, the microstructure of the deposit is particular, since it is multi-scale and is composed of solidified melt pool, grains and a cellular substructure. These elements are obstacles to the diffusion of dislocations. Zhou *et al.* demonstrated that the strengthening mechanism of SS316L parts made in SLM is the combination of these elements [161]. Therefore, the Hall-Petch relationship cannot be used alone to explain the difference in microhardness. It is strongly influenced by the cellular substructure, which has a high dislocation density. This hinders the movement of dislocations and leads to a higher hardness.

4.2.5 Mechanical characterization: tensile properties

Figure 4.10 and Table 4.1 summarize the tensile mechanical properties of the reference substrate and the repairs. A comparison is also made with LMD tensile specimens printed on the same machine, with the same powder and similar deposition parameters, as performed by Barkia *et al.* [81] in 2020. The substrate has mechanical properties similar to those of a conventionally manufactured SS316L part [9].

Table 4.1: Summary of the tensile test values of the repaired parts compared to the reference substrate and LMD-printed deposit.

	UTS (MPa)	YS (MPa)	E (GPa)	EAB (%)	Ref
Substrate	604 ± 10	298 ± 27	149 ± 18	69.9 ± 2.6	This study
R135	593 ± 20	367 ± 61	168 ± 20	22.1 ± 3.8	This study
R120	585 ± 16	351 ± 65	192 ± 36	19.1 ± 2.6	This study
R105	560 ± 83	340 ± 55	159 ± 22	13.3 ± 5.9	This study
Deposit	520	440	-	51.5	[81]
RCC-M standard	> 490	> 175	-	> 45	[9]

For the grooves with 135°, 120°, and 105° opening angles repaired with LMD, the UTS is slightly lower compared to the reference substrate with a decrease of 1.8%, 3.1% and 7.3%, respectively. The substrate EAB is 69.9%, while the repaired specimens have

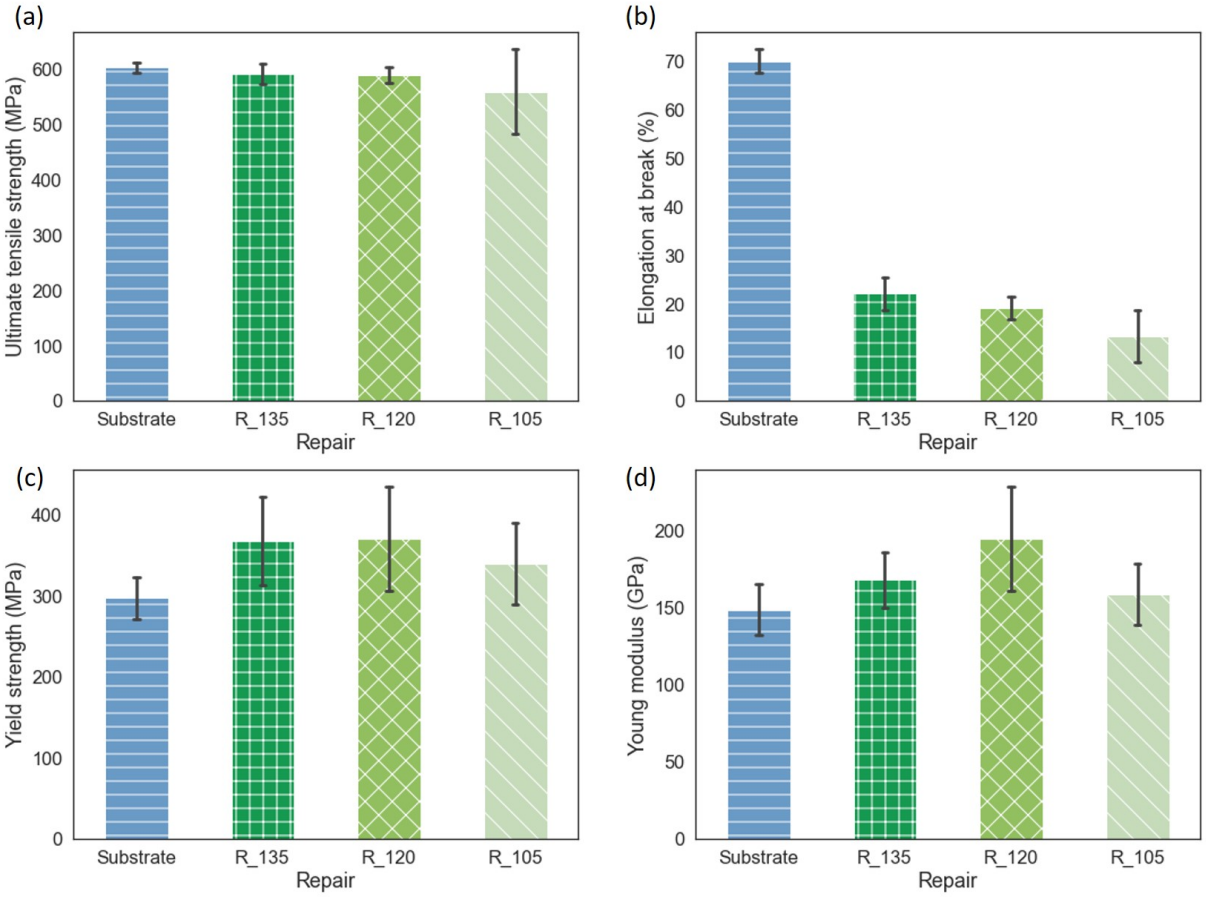

Figure 4.10: Mechanical properties of the substrate and repaired parts: (a) ultimate tensile strength, (b) elongation at break, (c) Young modulus and (d) yield strength.

much lower elongations at break, 22.1%, 19.1%, and 13.3% respectively. However, the YS and Young's modulus of the repairs appear to be higher than the reference substrate, as observed in Figures 4.10 (c) and (d). In fact, the YS of the 135°, 120°, and 105° grooves are 23.5%, 18%, and 14.5% higher, respectively, and the Young's modulus is 12.9%, 28.8%, and 6.8% higher, respectively.

Compared to the fully LMD-printed specimens in the literature, the 135°, 120°, and 105° repairs exhibit better UTS with improvements of 13.9%, 12.6%, and 7.7%, but a decrease of 16.6%, 20.3%, and 22.6% for YS. Similarly, the EAB of the repairs is much lower than that of the LMD-printed tensile specimens.

These results indicate that the repaired parts have better mechanical properties in the elastic regime, but reduced mechanical properties in the plastic regime compared to the reference substrate. On the contrary, the repairs have lower elastic properties than the LMD-printed deposit, but higher plastic properties. The mechanical properties of

the repairs appear to be halfway between the properties of the substrate and the deposit. However, the EAB of the repairs is greatly reduced for all repairs, indicating the presence of a problem of premature crack initiation. These EAB values are too low to meet the standard for stainless steel, which is at least 40%. Furthermore, as observed for all the values measured in these tests, a decrease in the elastic and plastic mechanical properties is observed as the groove opening angle decreases.

To investigate the failure mechanisms under tensile stress, the fractographies of the samples were examined. The reference specimen taken from the substrate shows a ductile fracture surface with a strong striction. This can be seen in Figure 4.11 (a), (e) and (f). However, the repaired samples show a semi-brittle fracture that is located along the interface between the deposit and the substrate, regardless of the opening angles, as shown in Figure 4.11 (b), (c), and (d). The repaired sample R120 has distinct zones such as ductile fracture zones highlighted by the presence of small dimples characteristic of microvoid coalescence (MVC) (Figure 4.11 (g)), lack of fusion zones characterized by the presence of unmelted powder (Figure 4.11 (h)), brittle zones (Figure 4.11 (i)), and interdendritic fracture zones (Figure 4.11 (j)). Oh *et al.* [108] also observed semi-brittle cracking at the interface of DED-repaired specimens after tensile testing, which was caused by delamination of the deposit at the interface due to the effects of groove shape and residual stresses.

In all repaired specimens, the crack propagated along the interface between the deposit and the substrate, as observed in Figure 4.12 (a). The low amplitude porosities observed previously in the cross section turned out to be fine and long porosities along the interface, as shown in Figure 4.12 (b). They were too deep to be detected by X-ray imaging. The porosities are preferential sites for crack initiation and therefore tend to propagate in the most brittle area of the specimen. Thus, the observed trend of decreasing mechanical properties with decreasing opening angle was caused by the increase in porosity rate as the opening angle decreases. In addition, the hardness peak observed in the HAZ also causes an incompatibility of deformation in the tensile specimen, which contributes to the formation of the crack in the interface area.

Furthermore, the interface porosity tends to occupy a greater height in the direction of construction as the groove opening angle decreases, as can be seen from the fractographs of the tensile specimens in Figure 4.11. Figure 4.12 (c) illustrates the phenomenon involved. When the last bead of the layer is placed, it rests on one side on the second last placed bead and on the other side on the slope of the groove, preventing the correct insertion of the last bead in the desired position and causing a lack of fusion. As the opening angle decreases, the slope increases, reinforcing this geometric constraint. This increases the

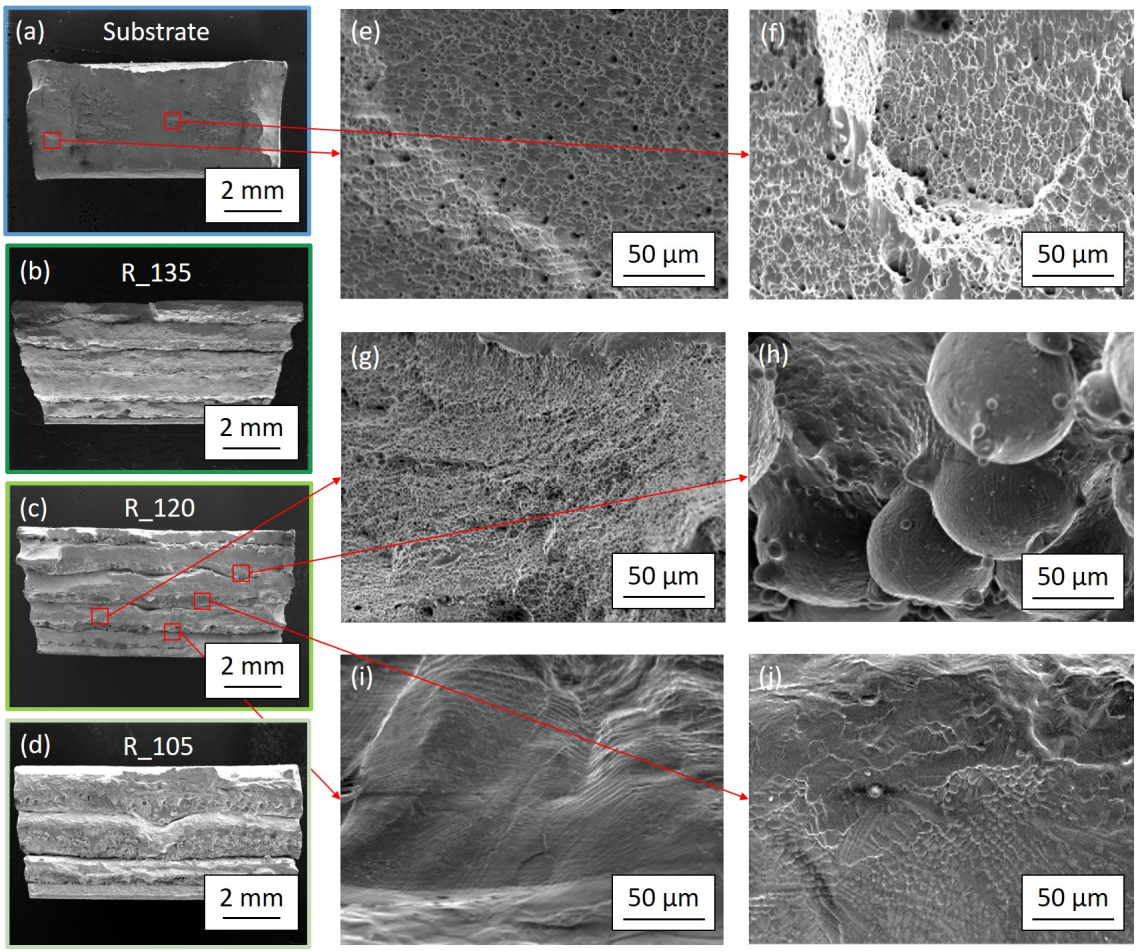

Figure 4.11: SEM observations of the tensile specimens after failure for (a) substrate, (b) R135, (c) R120, and (d) R105 with enlarged views showing: (e), (f) and (g) MVC fracture, (h) lack-of-fusion defects and presence of unmelted powders, (i) brittle fracture, and (j) interdentritic fracture.

height of the porosity in the direction of construction. This causes the cross-sectional area of the specimen to decrease, thereby reducing the tensile mechanical properties.

Notice that Figure 4.12 (c) illustrates the phenomenon in presence, amplified for emphasis. Interface porosity is obviously smaller and much less continuous. In contrast to additive manufacturing on a flat substrate, the repair process is constrained by the edges of the pre-machining shape. It is necessary to adjust the deposition pattern in order to avoid the formation of porosity at the interface and a decrease in the mechanical properties of the repaired parts. Based on this observation, parallel work was carried out to adjust the overlapping rate between the beads for each layer, as explained in Chapter 3.

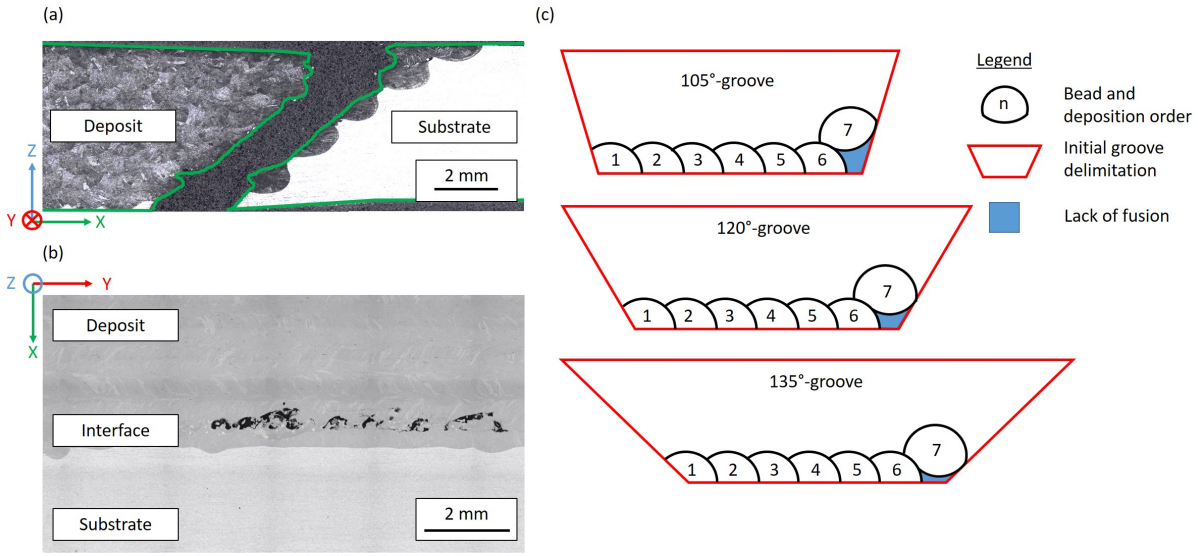

Figure 4.12: OM observations of: (a) cross section of the tensile sample extracted from the R135 after fracture, (b) horizontal section highlighting the porosities present along the groove surface at the interface, and (c) schematic explanation of the porosities size increase at the interface with the decrease of the opening angle.

4.2.6 Fracture behavior: Charpy impact tests

Figure 4.13 (a) summarizes the absorbed energy of the substrate, which is 256 J, while it is 187 J, 189 J, and 200 J for the 135°, 120°, and 105° grooves, respectively. This represents a decrease of 27%, 26% and 22%, respectively. The results highlight that the repaired specimens have lower impact properties than the reference specimen, which can be explained by the differences in their microstructures. Grains are coarse and elongated in the direction of construction in the repaired zone. Therefore, as the crack propagates, less energy is required to propagate through the columnar grains than through the fine and equiaxed microstructure of the substrate [149]. Figure 4.13 (b) is a plot of force versus time for one sample from each family. A bar graph displays the average time for each family for the hammer to reach 0 N in Figure 4.13 (c). The repaired samples fracture almost twice as fast as the reference sample, supporting the phenomenon described above.

It has been shown in the literature that as the number of beads deposited increases, the residual stresses in the deposit are higher due to the repeated heating and cooling cycles [162, 163]. Tensile residual stresses in the deposited beads appear to be higher in the final layers [163]. In addition, according to the work of Ren *et al.* [164], the tensile residual stresses significantly reduce the resistance to crack propagation. However, the repaired parts are subjected to high tensile residual stresses, especially in the deposit, whereas the reference substrate is free of high residual stresses due to its solution annealing

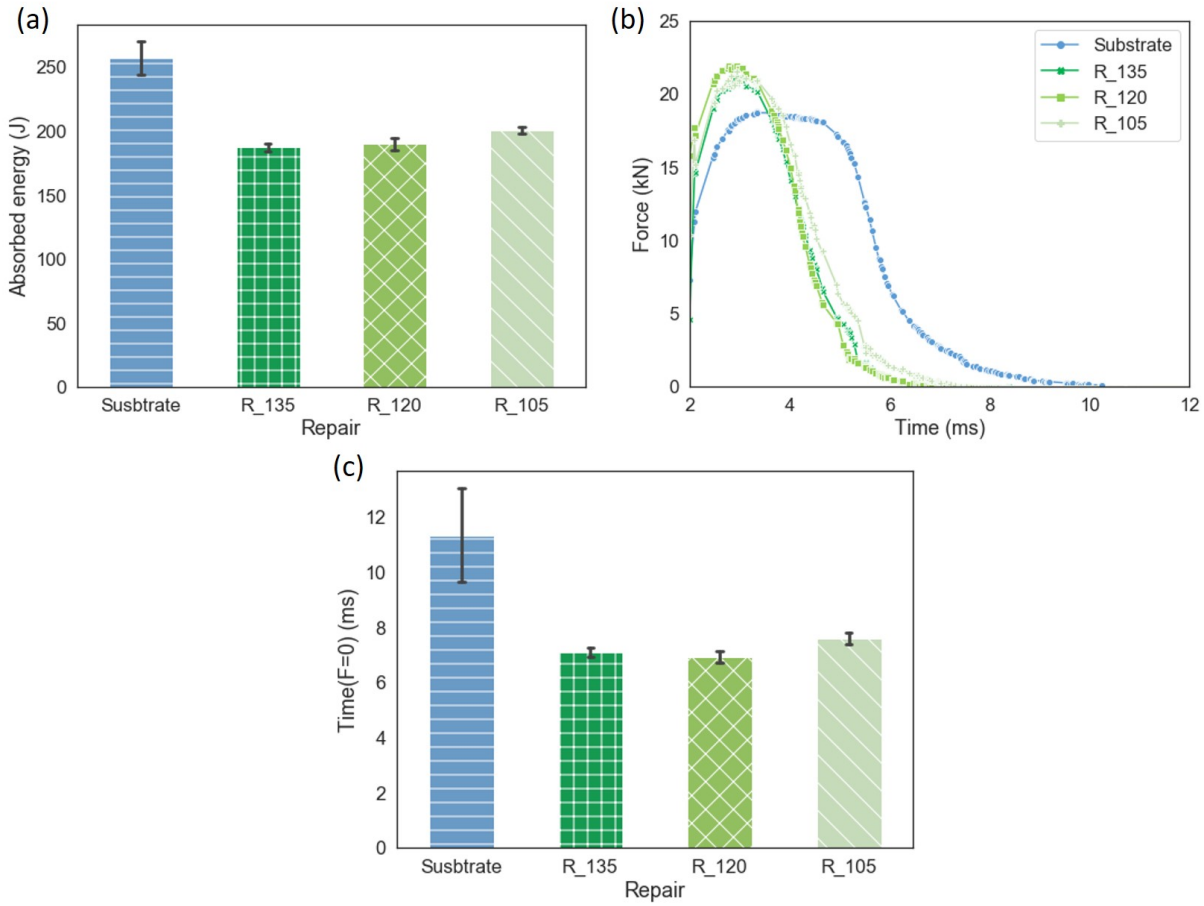

Figure 4.13: (a) Energy absorption of the reference substrate and repaired samples for Charpy impact testing, and (b) the time needed for the hammer to attain a force of 0 N.

heat treatment at the steel mill exit. This hypothesis can be added to the previous one to explain why the energy absorbed by the repaired parts is lower than that absorbed by the substrate.

On the other hand, the latter hypothesis is interesting to explain the tendency of the absorbed energy to increase with the decrease of the opening angle. The cracks in the specimens are located in the center of the deposit. Therefore, it seems unlikely that interfacial porosity is involved in this trend. However, the number of beads required to fill the groove decreases as the opening angle decreases. The introduction of residual tensile stresses into the deposit is also reduced as the number of heating/cooling cycles decreases. Thus, as the resistance to crack propagation increases, the energy absorbed increases.

In the fractured specimens presented Figure 4.14, two zones with different morphologies can be observed. Although both are screw zones with screw rates close to 100% and high ductility, they exhibit slightly different mechanisms. Two shear zones are visible in all

specimens. The first zone near the notch consists of small and elongated dimples as shown in Figure 4.14 (e). In contrast, the second zone opposite the notch is composed of larger dimples, as seen in Figure 4.14 (f), which were created by a very high shear force applied to the rest of the specimen.

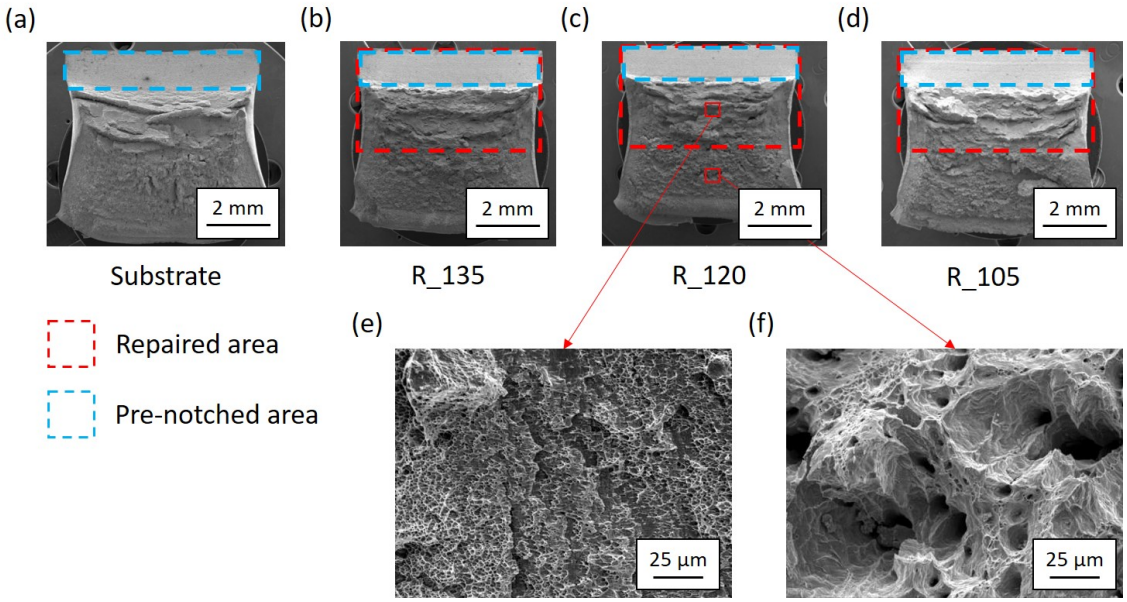

Figure 4.14: SEM micrographs of the Charpy test specimens after failure: (a) substrate, (b) R135, (c) R120, and (d) R105 with enlarged view from R120 highlighting (e) ductile screw failure and (f) ductile MVC failure.

This initial work on the repair of trapezoidal grooves with different opening angles highlighted the heterogeneous characteristics of a part repaired using LMD. Two microstructures are exhibited: fine and equiaxed for the substrate and coarse and columnar for the deposit composed of a cellular substructure. The microhardness of the repairs is heterogeneous with a microhardness peak at the interface caused by the formation of ferrite in the substrate and finer grains in MZ. Finally, the mechanical properties in tension and Charpy impact are reduced compared to the reference substrate. This reduction is caused by the columnar microstructure of the deposit, which is less resistant to crack propagation and porosity formation at the deposit/substrate interface, due to the non-adaptation of the overlapping rate.

Pre-machining opening angle is critical to repair quality. The decrease of the opening angle results in a decrease in the density rate, due to the geometric constraint imposed by the inclined surface of the pre-machining. Tensile mechanical properties decrease caused by the increase of the porosity

size at the interface. However, an improvement in absorbed energy is observed, which could be caused by less introduction of residual stress in the part.

This first part allowed the influence of the opening angle of the pre-machining on the quality of the repair to be determined under adapted conditions. However, the configuration of the LMD process can be problematic in certain situations, such as in the case of deep defects, where the part to be repaired and the projection nozzle are close and interactions can occur. It is therefore necessary to know the conditions to impose on the opening angle of the pre-machining to allow the repair of deep defects while maintaining a high repair density and avoiding collisions between the projection nozzle and the part to be repaired.

4.3 Technical requirements on the opening angle for deep repairs

4.3.1 Experimental protocol

Figure 4.15 (a) displays the cross-sectional geometry of the flat-bottom conical holes milled in the SS316L substrate. To observe the limitations of the LMD process, two depths Z and three opening angles θ are investigated, which can take the following values respectively: 5 mm or 10 mm and 105°, 120° or 135°.

The deposition pattern consists of using a contour path adding zigzag paths with a 90° rotation between each layer, as illustrated in Figure 4.15 (b). Compared to the 180° rotation strategy used in the previous section, this strategy further avoids the formation of preferential grain growth in the repair deposit. In addition, it can be observed whether the beads deposited in the cutting plane and out of the cutting plane have porosity problems or not.

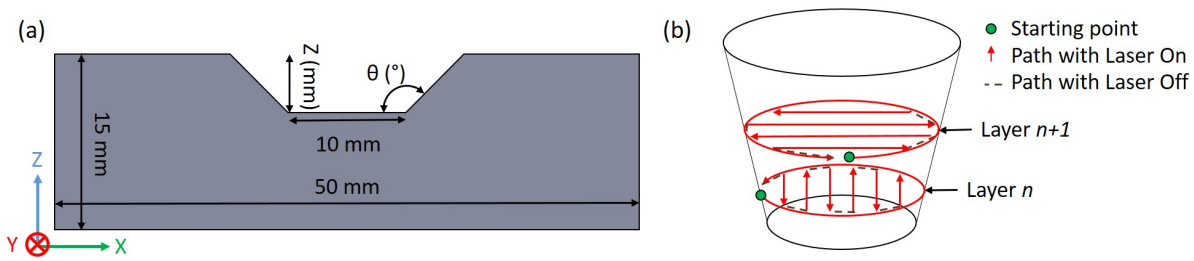

Figure 4.15: (a) Cross-section of the flat-bottom conical hole pre-machining in the substrate and (b) 90°-Zigzag deposition pattern used for this study.

4.3.2 Flat-bottom conical hole repair results

Observations of the cross-sections of the repairs made with the flat-bottom conical holes demonstrate the feasibility of repairing these curved shapes with the LMD process. In fact, as shown in the Figure 4.16, all repairs are dense with no apparent lack of fusion, except for the deepest pre-machining with the smallest opening angle, namely Z = 10 mm and $\theta = 105°$.

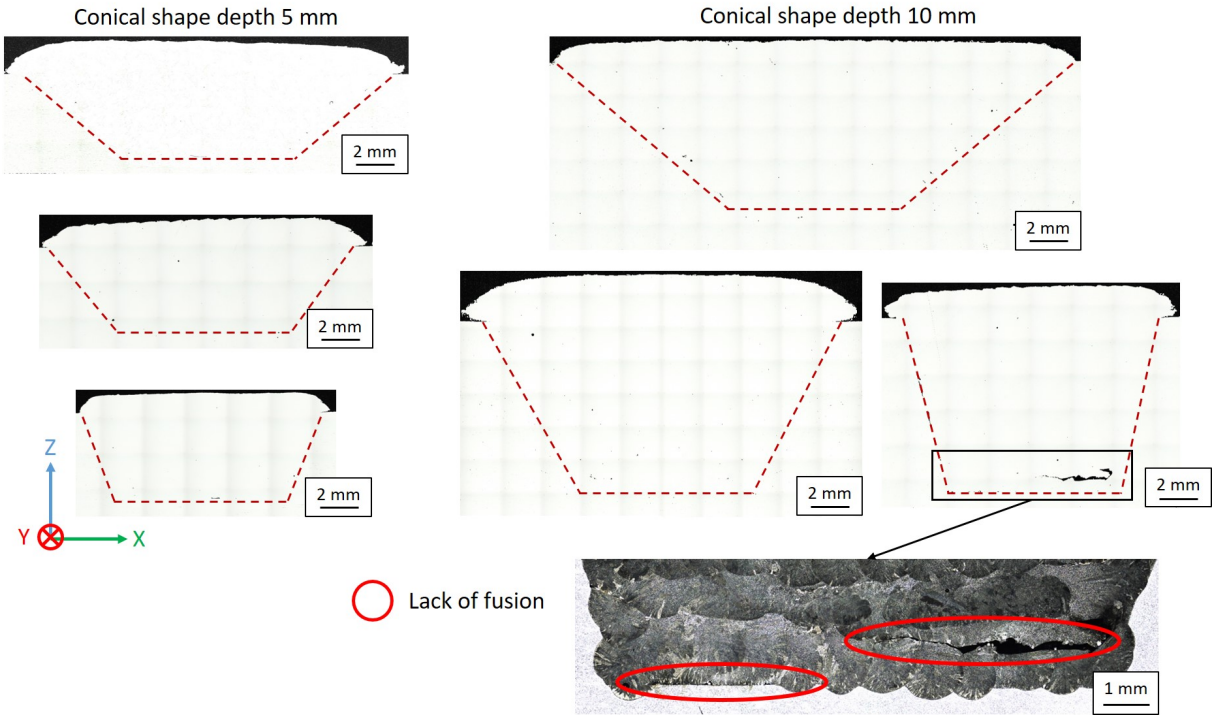

Figure 4.16: OM observations of the repair cross-sections with the flat-bottom conical holes pre-machining.

The configuration of the LMD process is responsible for the formation of these porosities in the most unfavorable pre-machining of this study. As shown in the Figure 4.17, a part of the powder stream is masked by the top surface of the substrate when the opening angle is too small and the depth is too large. The powder mass flow rate and thus melt pool feed are significantly reduced by this masking. As a result, the size of the beads near the edges is significantly reduced, as shown in the right of the first layer in the magnified view in Figure 4.16. These beads are no longer suitable for the developed deposition pattern.

When the projection nozzle moves towards the center of the pre-machining, the powder stream regains its normal visibility and an accumulation of powder occurs at the bottom of the pre-machining. This causes an overbuilding of the beads in the center. Then,

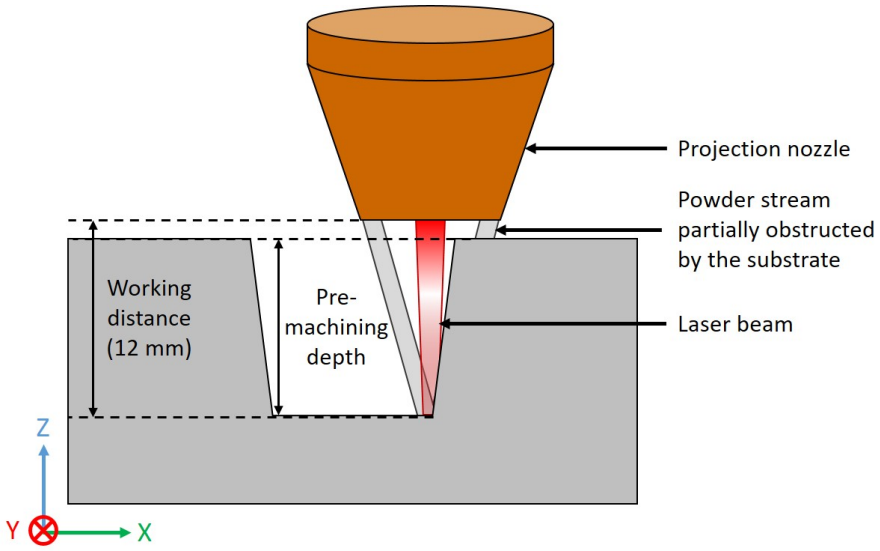

Figure 4.17: Technical limitations imposed by the depth and the low opening angle to the LMD process.

the last beads of the layer will lean on the overbuilt beads of the center because of the overlapping rate, causing an increase in the height of the layer without the possibility of remelting part of the substrate and causing a lack of fusion at the substrate/deposit interface in the end of the deposited layer.

The deposition of the second layer rotated of 90° follows the same principle, but is less accentuated than the first layer. However, the deposition is carried out on a surface with variable height, because as seen previously, the first layer did not have a stable height. The beads of this second layer start at the highest surface and end at the lowest surface (from left to right in the magnified view). Thus, the melt pool solidifies in the underbuilt area before part of the previous layer has been remelted, and lack of fusion appear.

These two phenomena explain the lacks of fusion observed at the bottom of the 105° and 10 mm pre-machining. For the following layers, the depth situation is favorable for the deposition of the beads. This avoids the masking of the powder stream and the accumulation of powder at the bottom of the pre-machining.

4.3.3 Conditions for repairing depth and confined pre-machining

These observations highlight the technical problems associated by the LMD process and pre-machining configurations, in particular for repairing deep pre-machining with small opening angles. The depth and bottom width are imposed parameters that depends of the type and size of the damage defect in the part.

In order to avoid problems during the repair process, conditions must be applied to the opening angle of the pre-machining. The most dangerous situation occurs when the projection nozzle is positioned to deposit the first bead on the bottom edge of the pre-machining. Two situations may occur:

- when the working distance is greater than the depth of the pre-machining (Figure 4.18 (a)), a condition must be imposed on the opening angle to avoid masking the powder stream and inducing underbuilding of the beads close to the edges. This also allows for a constant powder mass flow rate and shielding gas flow and avoids powder accumulation as observed under normal manufacturing conditions;
- when the pre-machining depth is greater than the working distance (Figure 4.18 (b)), it is necessary to impose a condition on the opening angle to avoid collision between the projection nozzle and the part to be repaired.

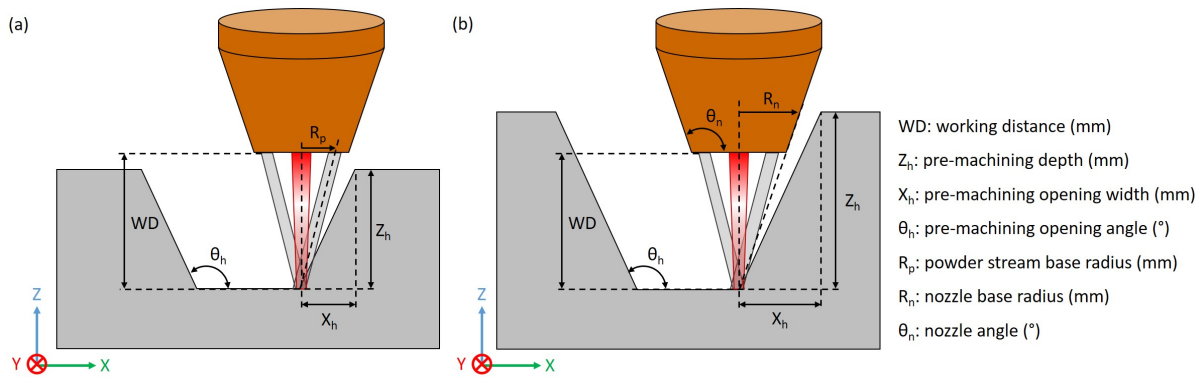

Figure 4.18: (a) Working distance superior to pre-machining depth situation and (b) working distance inferior to pre-machining depth situation.

For the first situation, where $WD > Z_h$, it is necessary that the powder stream is not masked by the upper surface of the pre-machining. To achieve this, the top radius of the powder stream must be smaller than the opening width of the slope. According to Equation 4.3, the opening angle must be superior to the value depending of the top radius of the powder stream and the depth of the pre-machining.

$$R_p < X_h \iff \theta_h > \arctan(\frac{R_p}{Z_h}) + 90 \tag{4.3}$$

For the second situation, where $WD \leq Z_h$, the radius of the nozzle on the upper surface of the substrate must be smaller than the opening width of the slope, knowing that the angle of the projection nozzle θ_n is always obtuse on all LMD technologies. Depending

on the nozzle radius and angle and the working distance, the opening angle condition of θ_h pre-machining is given by Equation 4.4.

$$R_n < X_h \Longleftrightarrow \theta_h > \arctan(\frac{R_n + (WD - Z_h) * \cot(\theta_n)}{Z_h}) + 90 \tag{4.4}$$

The limitations of the LMD process for repairing deep pre-machining have been demonstrated in the repair of flat-bottom conical shapes of various dimensions. In order to avoid obstructing the powder stream by the top surface of the substrate and to avoid collisions between the projection nozzle and the workpiece, conditions must be imposed on the opening angle according to the working distance between the projection nozzle and the deposition surface as a function of the pre-machining depth and machine configuration (powder stream radius, nozzle angle, nozzle base radius).

4.4 Ellipsoid repair with pre-machined volume optimization

4.4.1 Pre-machined volume optimization

Pitting ellipsoidal shape

Minimizing the volume of pre-machining is of great interest in the repair process. In fact, this volume minimization allows to reduce the amount of material to be deposited with the LMD process, thus reducing the time and energy used. In addition, this optimization allows only the damaged defect to be removed, leaving at least the rest of the part for the laser process.

It is interesting to focus on minimizing the repair volume now that the influence of the pre-machining geometry on the mechanical properties of the repaired parts has been determined and conditions have been imposed on the opening angle in relation to the depth of pre-machining and geometry of the projection nozzle. For this purpose, pitting corrosion is chosen as the defect for which the repair volume should be optimized. As a matter of fact, this is a common type of damage encountered in the industry for SS316L.

The shape can be considered as semi-ellipsoidal according to the literature related to pitting corrosion in stainless steel [146, 147, 148]. The ellipsoidal shape is the most representative of this type of corrosion as can be seen in Figure 4.19, which shows examples of pitting corrosion.

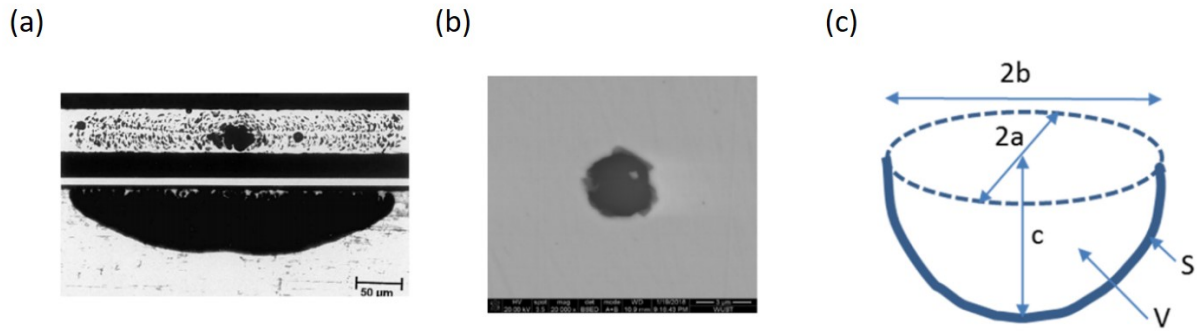

Figure 4.19: Pitting corrosion shape by (a) Ernst *et al.* [146], (b) Cao *et al.* [147], (c) Eguchia *et al.* [148].

The first step of the repair process, not studied in the present work, is to scan the surface of the corroded part to obtain the dimensions of the damaged part and the defect associated, using a surface topography, tomography, 3D scanner or coordinate measuring machine [165]. In addition, it is possible to reconstruct the surface of the part without the defect in order to have the repair volume. It is possible to perform the segmentation to isolate the defect after processing the point cloud obtained from the measurement [166]. Generally, the acquisition allows to have the upper and lower surface of the repair volume.

Once the shape and dimensions of the defect have been determined, the repair volume must be digitally modeled. This is necessary to generate the machining and deposition paths. This step is the construction of an envelope for the representation of the repair volume from an optimization of the ellipsoid parameters. The envelope consists of two surfaces, an upper surface which represents the surface of the part where the defect is, and a lower surface which represents the defect to be repaired. In this study, the optimization minimizes the repair volume from a parallelepiped defect bounding box as shown in Figure 4.20, satisfying the imposed constraints (*i.e.* geometric and technical). The construction of the repair volume and its optimization will be described in detail in the next section. It is important to note that optimization converges to an optimal result depending on surface size discretized in software and numerical resolution.

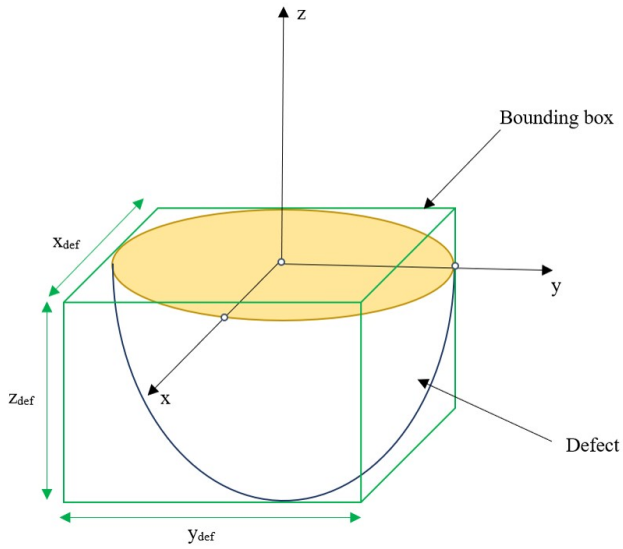

Figure 4.20: Representation of the ellipsoid pit defect in the bounding box.

Modeling of the geometric elements

In order to perform the pre-machining and deposition steps of the repair process, the repair volume must be identified. This volume is contained between an upper surface, which is the part's undamaged surface, and a lower surface, which represents the defect shape to be repaired.

The optimization of the ellipsoid consists in finding the ideal dimensions and the position of the center in order to minimize the repair volume, taking into account the various constraints related to machining and filling.

The upper surface is representative of the part surface without damage and is generated for the demonstration like illustrated in Figure 4.21. The lower surface is an ellipsoidal surface modeled with parametric equations and represents the surface of the defect. The ellipsoid is defined by its dimensions a, b and c, as shown in Figure 4.21 (b). These dimensions represent the half-axis lengths along the three spatial directions, as well as the position of its center in space. Each point on the surface of an ellipsoid satisfies the Equation 4.5.

$$\frac{x^2}{a^2} + \frac{y^2}{b^2} + \frac{z^2}{c^2} = 1 \tag{4.5}$$

Furthermore, depending on the polar angle θ and the azimuth angle ϕ, the coordinates of any point on the surface can be defined according to the system of equations 4.6.

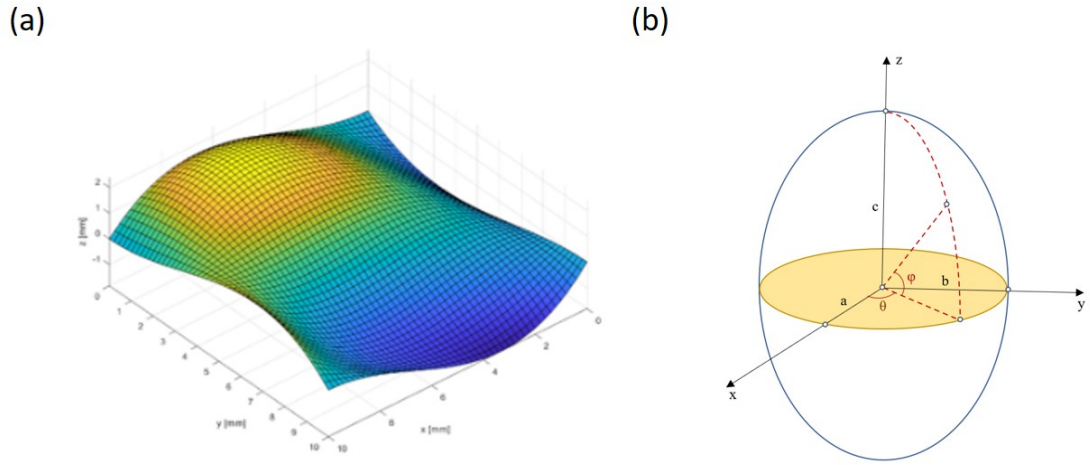

Figure 4.21: (a) Upper surface model and (b) parameters of an ellipsoid.

$$S_{ellipsoide}(\theta,\phi) = \begin{cases} x = a\cos(\theta)\cos(\phi) \\ y = b\sin(\theta)\cos(\phi) \\ z = c\sin(\phi) \end{cases} \tag{4.6}$$

where $\theta \in [0, 2\pi]$ and $\phi \in [-\frac{\pi}{2}, \frac{\pi}{2}]$

In order to define the parameters of the ellipsoid in u and v, the following changes are made to the variables, like described by the Equations 4.7.

$$\begin{cases} \theta = 2\pi u \\ \phi = \pi(v - \frac{1}{2}) \end{cases} \tag{4.7}$$

The system of equations 4.8 is obtained after changing the variables.

$$S_{ellipsoide}(\theta,\phi) = \begin{cases} x = -a\cos(u)\cos(v) \\ y = -b\sin(u)\sin(v) \quad (u,v) \in [0,1]^2 \\ z = c\cos(v) \end{cases} \tag{4.8}$$

The position of the defect on the top face determines the position of the center of this ellipsoid. The assumption is that the defect will be in the center of the top face. The position of the center of the ellipsoid with respect to a reference frame is given by the vector $\vec{z}$.

To find the intersection of the top surface with the ellipsoid surface so that $S_{up} \cap S_{ellipsoid} = C_{intersection}$, the parameters u and v must satisfy the Equation 4.9 for each surface.

$$S_{up}(u_{up}, v_{up}) = S_{ellipsoide}(u_{elps}, v_{elps}) \tag{4.9}$$

Where S_{up} is the upper surface, $S_{ellipsoide}$ the ellipsoid surface, u_{up} the radial unit vector and v_{up} orthoradial unit vector of the upper surface and u_{elps} the radial unit vector and v_{elps} orthoradial unit vector of the ellipsoidal surface.

A numerical resolution is chosen for the selection of all points of the ellipsoid which are closest to the top surface. This part is realized by the calculation of the distance between the points of the ellipsoid and the points of the top surface. Then, a reference distance is chosen to select the points of the corresponding ellipsoid, which allows to have the intersection points, as observed in Figure 4.22.

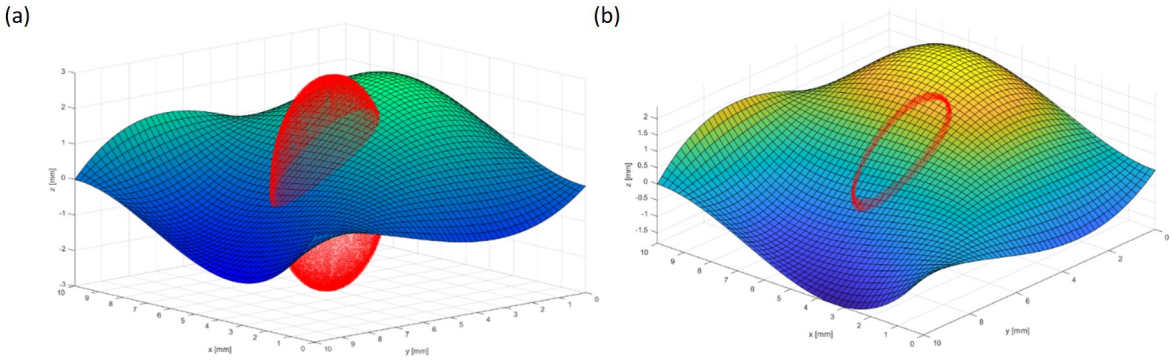

Figure 4.22: Intersection of surfaces (a) positioning of the ellipsoidal surface in the upper surface, (b) intersection points between the ellipsoidal surface and the upper surface.

The lower surface is the surface of the ellipsoid below the upper surface given by Equation 4.10.

$$S_{low}(u, v) = S_{ellipsoide}(u_{low}, v_{low}) \mid S_{ellipsoide}(u_{low}, v_{low}).k \leq S_{up}(u, v).k \tag{4.10}$$

$$\text{with } k = \begin{cases} 0 \\ 0 \\ 1 \end{cases}$$

In the numeric method, the bottom surface can be generated if the points above the intersect points have been deleted. Depending on the parameterization of the ellipsoid, the points above the intersection can be removed line by line, and the result will be the bottom surface. At the end of the process, only the bottom surface remains, as displayed in Figure 4.23.

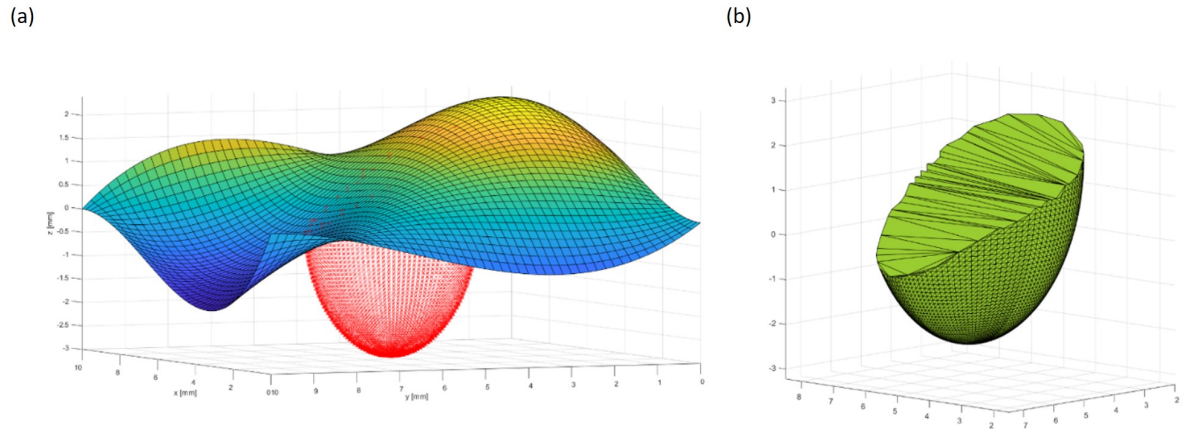

Figure 4.23: Lower surface (a) point removal and (b) repair volume.

Definition of the function and constraints

The defect must be included in the dimensions of the ellipsoid at the intersection and at the depth. The inequalities given by the equation system 4.11 can be written from this constraint:

$$\begin{cases} ix \geq x_{def} \\ iy \geq y_{def} \\ iz \geq z_{def} \end{cases} \tag{4.11}$$

where ix, iy and iz are the dimensions of the repair volume.

For accessibility reasons of the nozzle during the deposition process, it must be ensured that the maximum depth of the bottom surface does not exceed a specific depth determined according to the configuration of the LMD machine.

$$iz \leq depth_{max} \tag{4.12}$$

The values of ix and iy are determined from the intersection points, iz can be calculated from the expression 4.13:

$$iz = c - dz \tag{4.13}$$

Moreover, in order to machine the pre-machining shape, the minimum curvature radius of the bottom surface must be greater than the radius of the machining tool (in this case, a hemispherical tool), defined by the Equation 4.14.

$$r_{min} \geq R_{tool} \tag{4.14}$$

The maximum curvature of the surface, which is calculated from the Gaussian curvature and the mean curvature, must first be calculated in order to calculate the minimum radius of curvature. These curvatures can be calculated from the dimensions of the ellipsoid and the Cartesian coordinates of each point according to the formula developed by Sebahattin Bektas [167] and detailed in Equations 4.15 and 4.16.

$$k_{gauss} = \frac{1}{(abc(\frac{x^2}{a^4} + \frac{y^2}{b^4} + \frac{z^2}{4}))^2} \tag{4.15}$$

$$k_{moy} = \frac{x^2 + y^2 + z^2 - a^2 - b^2 - c^2}{2(abc)^2(\frac{x^2}{a^4} + \frac{y^2}{b^4} + \frac{z^2}{4})^{3/2}} \tag{4.16}$$

The maximum curvature is obtained using the following equation:

$$k_{max} = k_{moy} + \sqrt{k_{moy}^2 - k_{gauss}} \tag{4.17}$$

The minimum radius of curvature is calculated using the following formula:

$$r_{min} = \frac{1}{k_{max}} \tag{4.18}$$

In addition, an opening angle α greater than a certain angle (Equation 4.19) is required for better metallurgical bonding between the substrate and the deposit. The opening angle depends on the position of the ellipsoid at the intersection. Therefore, the smallest value that is calculated will be used.

$$\alpha \geq \alpha_{min} \tag{4.19}$$

This opening angle is calculated at the intersection of the top and bottom surfaces of the repair volume by determining the angle between the tangent vector along the v direction (Sv) at the intersection points and the vector $n(\alpha = \widehat{S_v n})$ with the Equation 4.20, as described in Figure 4.24.

$$\alpha = \arccos\left(\frac{S_v.n}{||S_v||.||n||}\right) \tag{4.20}$$

With: $S_v = \frac{\partial S_{ellipsoide}(u,v)}{\partial v}$

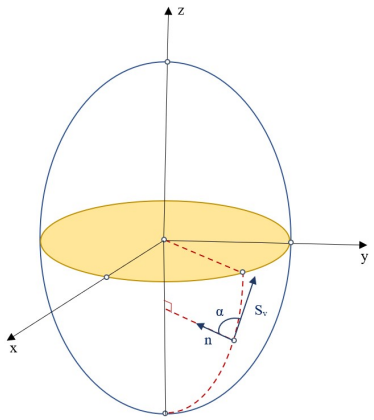

Figure 4.24: Opening angle represented at the intersection between the upper and lower surface.

Finally, the repair volume should be minimized. This will reduce the manufacturing time and the amount of material used. Analytically, the calculation of the repair volume is difficult, especially for complex top surfaces using the Equation 4.21. But this can be done numerically by creating a mesh that allows the repair volume to be calculated for any face.

$$V_{repair} = \int_0^a \int_0^p \int_0^q dx\, dy\, dz \tag{4.21}$$

With $p = b\sqrt{1 - \frac{x^2}{a^2}}$ and $q = c\sqrt{1 - \frac{x^2}{a^2} - \frac{y^2}{b^2}}$

Implementation and optimization example

The repair volume is generated and optimized by the algorithm developed in this work and shown in Figure 4.25. The program generates the bottom surface by deleting the points of the ellipsoid located above the top surface, based on the dimensions and position of the center of the ellipsoidal defect and the top surface. In the next step, the optimization function, which is the repair volume, is calculated at each iteration and the parameters of the ellipsoid are optimized from the initial solution. The algorithm always satisfies the following conditions: the initial solution has dimensions greater than those of the defect, the opening angle has to be greater than a minimum, the minimum curvature has to be greater than the curvature of the tool, and the final solution has to lie within the bounding box of the repair volume.

The case of a defect on a flat surface is tested to validate the correct operation of the

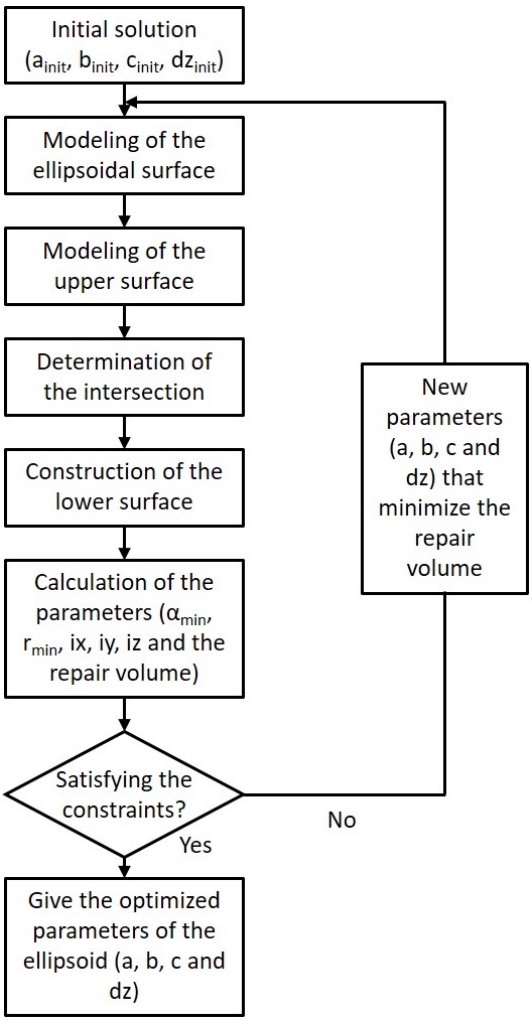

Figure 4.25: Algorithm for the ellipsoid parameters optimization.

developed program. The values of the selected parameters are summarized in Table 4.2. This angle was chosen for optimization because the 120° groove offered a compromise between fast and slow deformation characteristics with good deposition density, as seen in Section 4.2. In order to make a comparison on the same scale, the dimensions of the initial defect are chosen to be slightly smaller than the dimensions of the previously pre-machining.

The computation time is in the order of 200 seconds. An ellipsoid respecting all the constraints imposed is obtained from the optimization. This ellipsoid has dimensions of $10 \times 14 \times 25\ mm^3$ with a center offset of dz = 20 mm, which allows to obtain a hole with dimensions of $10.5 \times 15.75 \times 5\ mm^3$. Thus, the simulated defect, initial, and final pre-machining solutions have volumes of 25.1 mm^3, 75.4 mm^3, and 54.1 mm^3, respectively. Thus, the final pre-machining volume is 115% larger than the defect volume, but the

Table 4.2: Input parameters.

Parameters	Values
Defect dimensions	x_{def} = 8 mm y_{def} = 12 mm z_{def} = 4 mm dz = 0 mm
Initial solution	a_{init} = 6 mm b_{init} = 8 mm c_{init} = 6 mm dz = 0 mm
Milling tool radius	R_{tool} = 3 mm
Opening angle	α_{min} = 120°

optimization algorithm reduced the final volume by 28% compared to the initial solution.

However, it is necessary to check that there are no technical problems with the final dimensions of the pre-machining. The pre-machining depth of 5 mm involves the Equation 4.3 where the working distance is greater than the depth. Knowing that the R_p on the OPTOMEC machine is 2 mm, the results indicate that the minimum angle must be 111.8° to avoid masking the powder stream. The opening angle of 120° was chosen based on the results of the Section 4.2 and meets the technical requirements imposed by the Equation 4.3 defined in the Section 4.3.

With the optimization of the repair volume successfully achieved for the example case of a corrosion pit and respecting the criteria previously defined, experimental tests can be carried out to verify the ability of the LMD process to repair this form of pre-machining.

4.4.2 Experimental protocol of the volume-optimized pre-machining repair

A 3-axis CNC milling machine (DMG HSC 75V) is used to machine the ellipsoids in the substrate, as shown in Figure 4.26 (a). The experimental repair uses the optimized dimensions of the ellipsoid presented previously. From a CAD model of the plate to be machined, the machining paths were generated by CATIA.

The material deposition step uses the same deposition parameters as the grooves and tapered holes. In addition, a Zigzag deposition strategy with a 90° rotation and a contour bead is used to fill the pre-machining as illustrated in the Figure 4.26 (b).

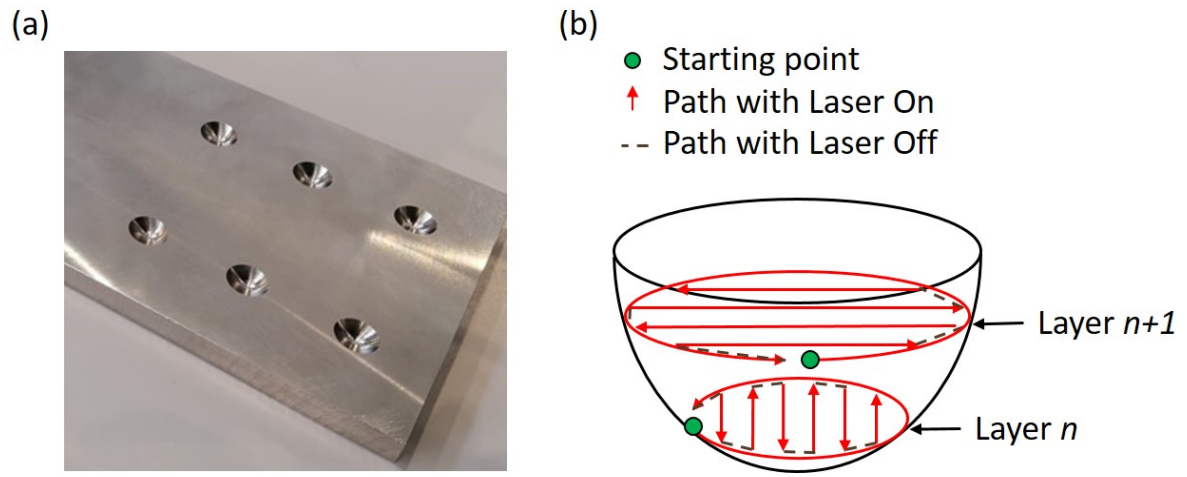

Figure 4.26: (a) Ellipsoidal holes machined in the SS316L substrate and (b) 90°-Zigzag deposition pattern used.

4.4.3 Density and metallurgical bonding

The density of the repair is analyzed by metallurgical observation of the cross section and is shown in Figure 4.27 (a). This analysis highlights the presence of spherical porosity in the deposit, which is common in additive manufacturing. On the other hand, numerous inter-bead lacks of fusion are observed on both sides of the pre-machining. They can be identified by their irregular shape.

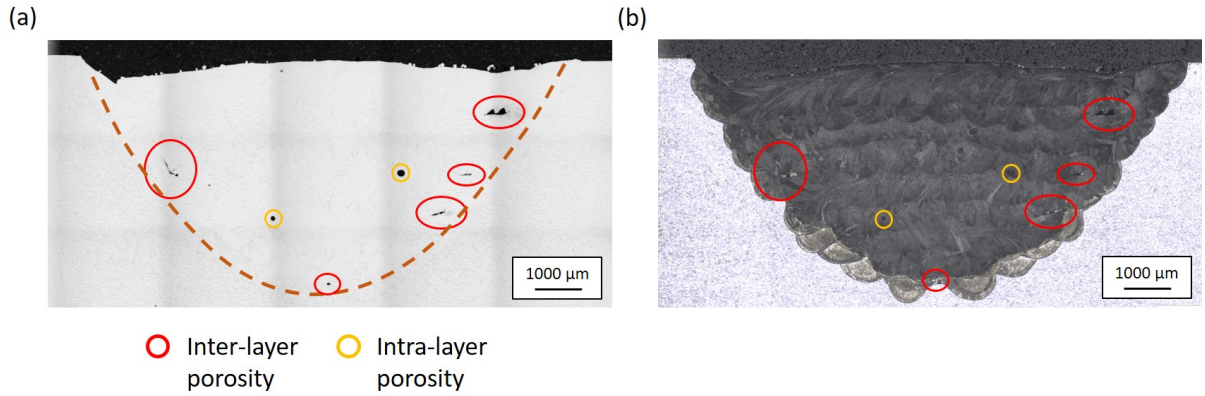

Figure 4.27: OM observations of the cross-sections (a) mirror-polished and (b) after electrochemical etching.

The presence of these porosities is not a problem related to the depth of the pre-machining, nor to the opening angle, which is at least 120°. Furthermore, Figure 4.27 (b) highlights that they are located between the contour bead and the last bead of the Zigzag

strategy. These porosities are therefore caused by the problem of calculating the number of beads per layer presented in Chapter 3. The ellipsoid repair strategies were developed prior to optimizing the deposition strategy by adjusting the inter-bead distance at each layer. As a result, porosities appear at the end of the layer of the Zigzag part with the problem of a missing bead that creates a lack of material or an excess bead that does not penetrate the material.

4.4.4 Microstructure

The microstructure is comparable to that found in Section 4.2. As shown in the Figure 4.28, the deposit is composed of solidified melt pools, which are composed of columnar grains in which the cellular substructure is observed. They are the result of a high density of dislocations formed during the solidification of the LMD process. The substructure is the segregation of the stainless steel elements, as observed in the Section 4.2.3.

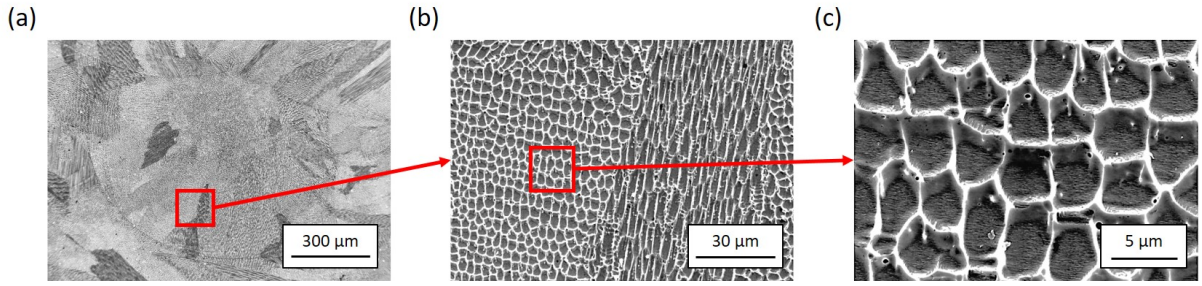

Figure 4.28: SEM observations: (a) solidified melt pool, (b) columnar grains and (c) cellular substructure.

Figures 4.29 (b) and (c) reveal the fine and equiaxed grains of the HAZ and the substrate, which have a similar microstructure. In fact, the substrate has a classic microstructure of a stainless steel produced in steel mills, having been produced by continuous casting, hot rolling and applying a post heat treatment at 1050°C. It is mainly composed of an austenite phase, but has some small grains of residual ferrite that did not disappear during the heat treatment. About 1% of the substrate is ferrite. On the other hand, the HAZ presents slightly larger grains than in the substrate, while remaining equiaxed and with a higher proportion of ferrite in the order of 2.4%.

In Figure 4.30 and Table 4.3, the significant increase in grain size between substrate, interface and deposit can be observed. This observation highlights the heterogeneity of the microstructure due to processes with different kinetics. However, this heterogeneity is

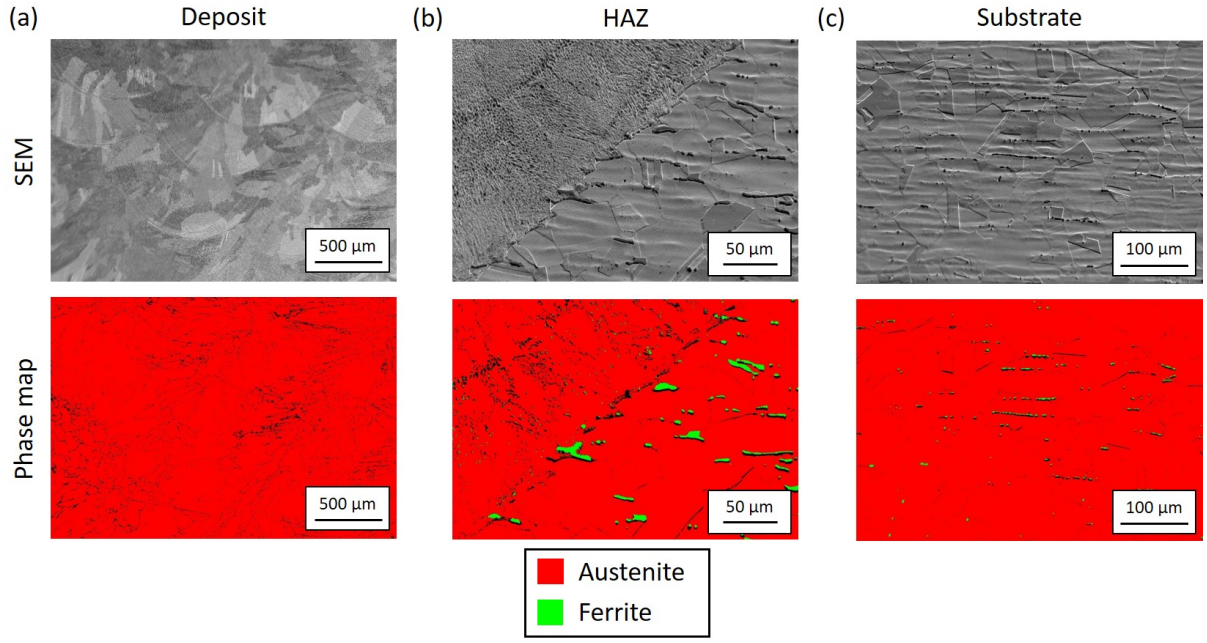

Figure 4.29: SEM observations and phase map: (a) substrate, (b) HAZ and (c) deposit.

already observed in Section 4.2 with a different pre-machining geometry and therefore does not affect the microstructure of the repair.

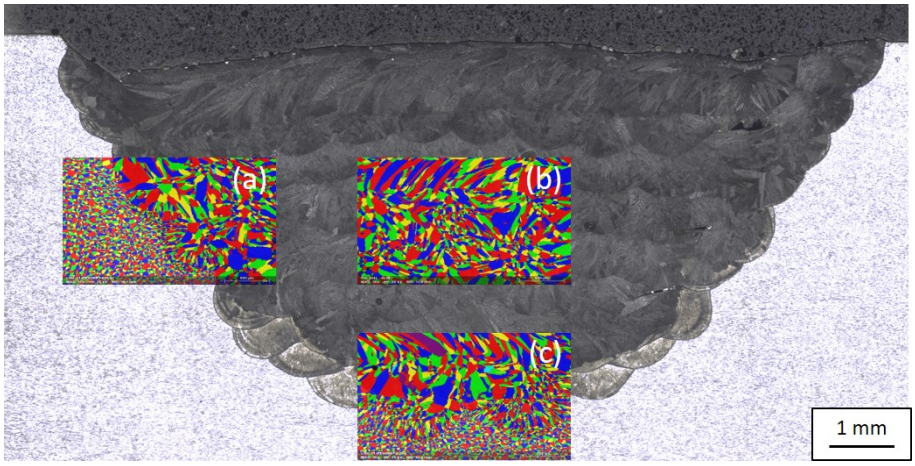

Figure 4.30: Grain size distribution in three areas of the repair.

Ellipsoidal pre-machining has been used to repair a fictive pitting corrosion defect. The volume of the ellipsoids was optimized to minimize the repair volume with a reduction of 28% compared to the initial solution. This allows the removal of the defect and provides good access to the projection nozzle respecting the constraints imposed by the machining tools and the previous

Table 4.3: Statistical values of the volume-weighted average grain size for the areas studied.

Zone	Area-weighted grain size (µm)
Substrate	35.2 ± 15.7
Left interface	75.4 ± 58.4
Bottom interface	64.5 ± 48.5
Deposit center	116.1 ± 70.4

results. The computational process was described by an optimization algorithm that models the surfaces before and after the repair to recover the volume. Experimental tests were carried out and the results led to the same conclusions as for the repairs previously carried out with trapezoidal grooves and flat-bottom conical holes concerning the density, the microstructure and microhardness.

4.5 Summary

This chapter focused on the repair of different shapes and sizes of pre-machined parts to first determine the influence of the geometry of this part on the characteristics of the repair and second to optimize geometric and process parameters for a given geometry. This includes also a study on the minimization of the repaired volume using mathematical tools, which was confirmed by a repair test. The characteristics of the repaired parts were studied for each situation. This work was carried out on the OPTOMEC LENS MTS-500 machine using the same deposition parameters throughout the study and a Zigzag deposition pattern without adaptation of the overlapping rate at each layer.

Overall, this work has demonstrated the feasibility of the LMD process to repair various forms of pre-machining, such as grooves, flat-bottom conical holes and ellipsoids. In fact, the repairs exhibit high density with an average of 99.95%, but lacks of fusion at the interface are observed for all types of pre-machining studied in this chapter, due to the non-adaptation of the overlapping rate between the beads at each layer required for the repair process. Regardless of the pre-machining geometry, the repairs present a heterogeneous microstructure composed of fine and equiaxed grains in the substrate with an average size of 38.5 ± 13.2 µm and coarse and columnar grains in the LMD-printed with an average size of 121.4 ± 68.4 µm deposit where a cellular substructure is present with a small cell size of 3 ± 0.6 µm.

An increase in hardness up to 240 HV is observed in the HAZ and MZ, compared to the 190 HV of the substrate and 200 HV of the deposit. This is respectively attributed to

the formation of the ferrite phase (2.4% in the HAZ compared to 1% in the substrate) and smaller grains in this area compared to the rest of the deposit.

The study on the repair of grooves with different opening angles highlighted the influence of this parameter on the density and global mechanical properties of the repaired parts. In fact, the relative density of the repairs tends to decrease with the opening angle, from 99.75% for the 135°-groove to 99.92% for the 105°-groove. The geometric constraint imposed by the pre-machining surface increases as the opening angle decreases, resulting in a larger lack of fusion.

The repairs exhibit superior elastic mechanical properties with a YS of 351 MPa and a Young's modulus of 192 GPa for the 120° groove, compared to the reference substrate with values of 298 MPa and 149 GPa, respectively. However, the plastic properties are degraded with a UTS of 585 MPa and an EAB of 19.1% compared to 604 MPa and 69.9% of the substrate. This is caused by semi-brittle failure of the repaired specimens due to the presence of the hardness peak and lacks of fusion at the interface, due to deposition pattern without adaptation of the overlapping rate. The decrease in mechanical properties under tensile stress is observed with the decrease in the opening angle from 593 MPa to 560 MPa for the UTS and from 22.1% to 13.3% for the EAB resulting from the increased presence of porosity at the interface and, in particular, the increase in the height of the porosity.

The absorbed energy in the Charpy impact tests is lower for the repairs (189 J for the 120° groove) than for the reference substrate (256 J), due to their coarse and columnar grains, which favor the crack propagation along the grain boundaries. An increase in energy absorption with decreasing opening angle from 187 J to 200 J can be explained by a higher resistance to crack propagation due to a reduced number of beads to fill the grooves at low opening angle.

Thus, from the point of view of the results obtained on the density and mechanical properties in slow and fast deformation, the 120° opening angle groove can achieve a good balance of metallurgical bonding and mechanical properties for repair of SS316L parts using LMD.

The second part regarding flat-bottom tapered hole repairs at various depths (5 mm and 10 mm) and opening angles (135°, 120° and 105°) has proven that deep pre-machining can be repaired if the opening angle meets certain conditions. These conditions are defined by equations, which depend on the depth of the pre-machining and the substrate/nozzle working distance, as well as the configuration of the nozzle itself (powder stream base radius, nozzle base radius and nozzle angle). When the working distance is bigger than the pre-machining depth, they prevent masking of the powder stream by the top surface

of the substrate, which causes problems in feeding the melt pool with powder and changes the geometry of the layers. They also prevent tool/workpiece collision during deep repair, when the working distance is inferior to the pre-machining depth.

In the objective of minimizing the repair volume (to minimize matter, energy, time and cost of the global operation), a last study was performed to develop a specific numerical optimization tool so that only the damaged and contaminated material is removed. In this study, the pitting corrosion was chosen, as defect example. The surface of an ellipsoid, which initial values are slightly larger than the dimensions of the corrosion pit, is generated at each iteration from the new values calculated in the optimization. All points of this surface that are above the nominal surface will be removed. A surface representing the repair volume is generated below the nominal surface. The repair volume optimization calculation then respects the geometric (*i.e.*, initial flaw size and opening angle) and technical (*i.e.*, tool radius) constraints and allows a decrease of 28% of the final volume compared to the initial solution. However, some improvements of the model will allow better optimization of the repair volume. For example, using a shape other than a rectangular box to optimize the repair volume, taking into account the asymmetry of the repair volume, or the orientation of the ellipsoid. The feasibility of repairing ellipsoids using LMD has been demonstrated in experimental tests without significant modification compared to the other pre-machining shape.

The first elements of the specification, which are eliminating the damage defect with the least amount of material removal and producing a dense repair, metallurgically bonded to the substrate, have been demonstrated in this chapter. This work has demonstrated the possibility of repairing different pre-machined shapes with the LMD process, while respecting certain geometric criteria. The importance of adapting the deposition pattern to avoid lack of fusion at the interface has been highlighted and a solution has already been developed in Chapter 3. However, even when a dense and metallurgically bonded repair to the substrate is achieved, the microstructure of the specimen is heterogeneous due to the different processes used, which leads to reduced mechanical properties of the repaired parts compared to a reference part. Complementary methods must be applied to homogenize the characteristics of the specimen and achieve imperceptibility of the repair.

Chapter 5

Effects of thermal treatments on the microstructure, microhardness and corrosion resistance of the repaired parts

Abstract

This chapter presents the results of the study on the influence of different thermal treatments on the density rate, microstructure, mechanical properties, and corrosion resistance of SS316L parts repaired using LMD. These treatments consisted of the application of substrate preheating, interlayer cooling factor, and post heat treatments. The objective was to reach imperceptibility of the repair in the part.

Submitted paper associated to this chapter: T. Cailloux, W. Pacquentin, S. Narasimalu, F. Schuster, H. Maskrot, K. Zhou, F. Balbaud-Celerier, "Influence of substrate preheating, interlayer cooling factor and post heat treatments on laser metal deposition repaired stainless steel 316L parts" submitted to *Journal of Materials Processing Technologies*, 2023

Contents

5.1 Introduction

In the previous chapter, the effect of the pre-machining geometry on the quality of the repair was observed, but also the microstructural and mechanical heterogeneity of the repaired parts was highlighted. A fine and equiaxed microstructure is present in the substrate and a coarse and columnar one in the deposit, with an increase in the ferrite content in the HAZ and the formation of a microhardness peak at the deposit/substrate interface.

Thus, despite a good deposition density, with a metallurgical bonding to the substrate and a fine HAZ, the repaired parts exhibit degraded mechanical properties. This is due to the use of a local laser fusion process for material deposition, which causes changes in the part being repaired and deposits a material with a particular microstructure. This can lead to safety or functional problems when these parts are reused in industrial systems. It is therefore necessary to develop techniques to seek for the imperceptibility of the repair and recover the properties of the initial part. The imperceptibility of the repair consists in obtaining a deposit that is undetectable in terms of microstructure, mechanical properties and corrosion resistance compared to the part to be repaired.

The use of thermal treatments is commonly used in the conventional casting, forging, or welding industries to eliminate residual stresses, homogenize the local chemical composition, recrystallize the microstructure, or soften the metal. These treatments are also emerging in AM as methods to eliminate residual stresses caused by the laser process or to dissolve the cellular substructure of the deposits. This last point is of interest to match the microstructure of the deposit to that of the reference substrate.

As explained in the literature review in Chapter 1, substrate preheating is applied to improve the mechanical properties of the AM-printed, welded and repaired parts by releasing residual stresses [168, 74, 169], and avoiding the formation of cracks [110] or undesired phases [170]. The application of an inter-layer cooling factor is also used to reduce the grain size of the deposit in order to mitigate the grain size heterogeneity between the substrate and the deposit [113, 102], and according to the Hall-Petch relation, to allow the homogenization of the microhardness in the repair. Post-repair heat treatment are used to relieve residual stresses [171], homogenize the microstructure [121] through recrystallization and anti-ferrite treatment, and thus homogenize the hardness distribution in the specimen.

These results show the interest of using these thermal treatments in the repair of metal parts using the LMD process. In fact, they could potentially be a solution to the problem of microstructural and mechanical properties heterogeneity discussed in Chapter 4. Few

studies of thermal treatments have been applied to LMD repairs. Therefore, a study of the influence of these treatments on the characteristics of the repaired parts was performed to determine the optimal combination of processes to obtain imperceptibility of the repair in terms of microstructure, mechanical properties and corrosion resistance. Results of this study are presented in this chapter.

5.2 Experimental protocol

5.2.1 Application of thermal treatments in the repair process

Repair process

According to the results of Section 4.2, a groove with an opening angle of 120° is machined in SS316L substrates, which are used in this study to represent the parts to be repaired. As presented before, this angle allows to obtain a compromise between the density of the repair and the mechanical properties in slow and fast deformation.

The SS316L powder is fed through the coaxial nozzle of the OPTOMEC LENS MTS-500 machine with the optimized parameters determined in Section 3.2.1 to obtain a dense deposit. These parameters are as follows: P = 650 W, V = 600 mm/min, Q = 6.6 g/min and OR = 30%. The deposition pattern used is the 90°-Zigzag strategy with the adaptation of the overlapping rate at each layer developed in the Section 3.4.3. This strategy avoids the formation of porosity at the interface substrate/deposit.

Following the observations made in the previous chapter on the heterogeneity of the microstructure and the mechanical properties, thermal treatments are applied to the LMD repairs in order to homogenize the microstructure and obtain better mechanical properties and corrosion resistance, with the aim of restoring the original properties of the part. The scientific approach to the application of thermal treatments in the repair process is described in Figure 5.1. These treatments are the substrate preheating, the interlayer cooling factor and the post heat treatment, which will be detailed below.

Density rate analyses by Archimedes method and metallographic observations on sections were carried out. The microstructure was analyzed by SEM observations and EBSD mappings. Mechanical properties were determined locally by microhardness mapping. Immersion tests in natural seawater were performed by the company Corrodys in Cherbourg, France, to study the corrosion resistance of the repairs. Finally, analyses of the microorganisms present on the surfaces after immersion in seawater were carried out to study the biofouling.

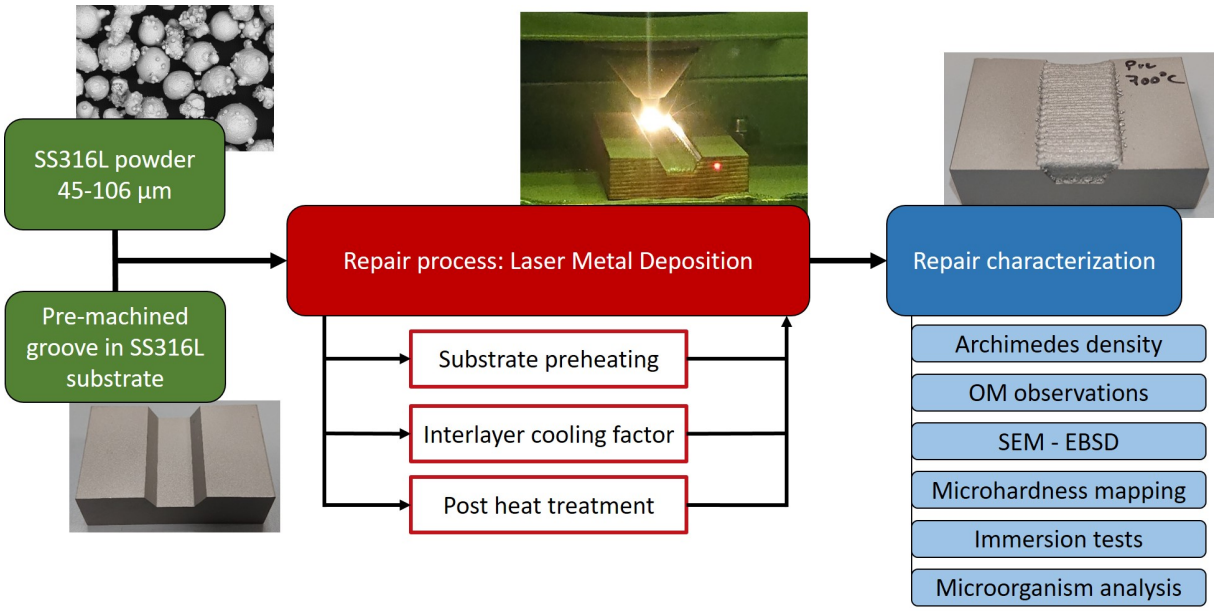

Figure 5.1: Flow chart of the thermal treatments methodology.

Substrate preheating

Substrate preheating was performed using a 6 kW inductor located under the substrate in the OPTOMEC machine, as presented in Figure 5.2 (a). The magnetic fields generated by the inductor induce eddy currents in the stainless steel substrate, which are completely dissipated as heat by Joule heating. The process involved heating the substrate from 20°C to the desired preheating temperature. During the repair of the sample, the inductor remained on to keep the substrate temperature at the set value. The temperature is measured in real time using a pyrometer. At the end of the repair, the inductor was stopped and the part cooled from preheating temperature to 20°C in air. In the following, this thermal treatment will be defined by "P" for preheating, followed by the preheating temperature of the substrate.

Interlayer cooling factor

The interlayer cooling factor was applied to the repair using a deposition dwell time between layers calculated using Equation 5.1. The part is placed in a 20°C argon atmosphere and cooled between the deposition of two layers, as displayed in Figure 5.2 (b). The dwell time is calculated for each layer.

$$d_w = c_f * m_t \tag{5.1}$$

Where d_w is the dwell time between each layer in seconds, c_f is the cooling factor, and m_t is the layer formation time in seconds. In the following, this thermal treatment is defined by "CF" for cooling factor followed by the cooling factor value.

Post-manufacturing heat treatment

The post-heat treatments were applied to the as-built repairs at the desired temperatures for a period of one hour using a convection oven in an air atmosphere, as explained in Figure 5.2 (c). The specimens were air cooled to room temperature after the treatment. In the following, this thermal treatment will be referred to as "HT" for heat treatment, followed by the temperature of the post-heat treatment applied for one hour.

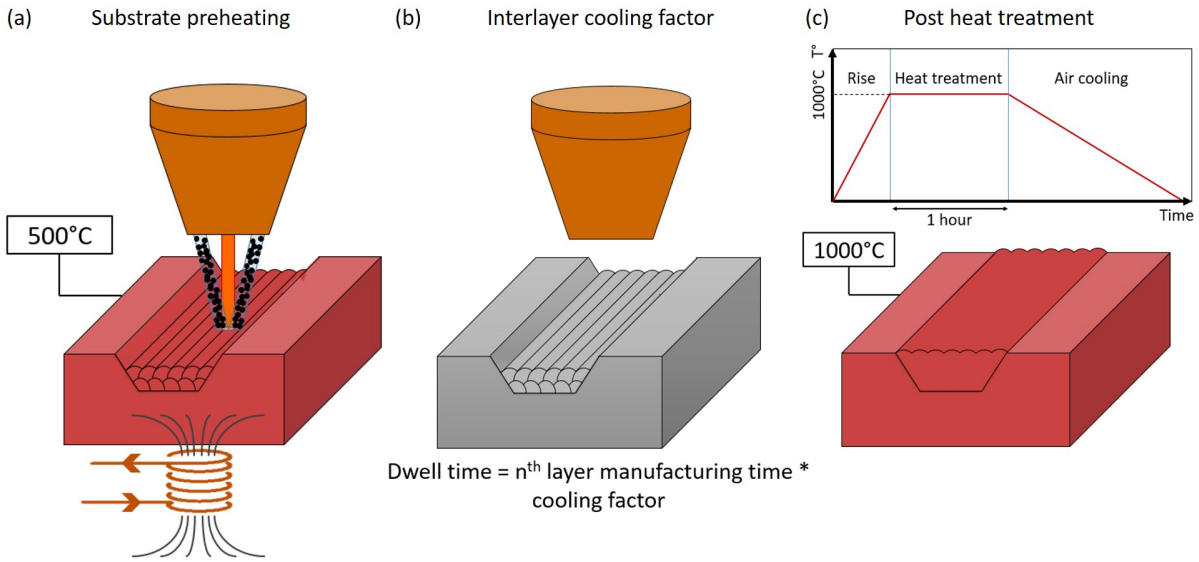

Figure 5.2: Illustration of the (a) substrate preheating, (b) interlayer cooling factor and (c) post heat treatment.

5.2.2 Design of experiment

For this study, two DOE have been developed.

A first DOE focuses on the influence of different treatments: (i) substrate preheating temperature, (ii) variation of interlayer cooling factor and (iii) post heat treatment temperature on the density, microstructure and microhardness of the repair. The different treatments are exposed in Table 5.1. The objective is to determine the influence of each treatment independently on the intrinsic properties of the repairs. An as-built repair is also produced, which is an LMD repaired substrate that has not undergone thermal

treatment as reported in Chapter 4, in order to compare these thermally treated repairs to a reference part. The analyses were carried out on the characterization facilities of the CEA Paris-Saclay.

Table 5.1: DOE 1 for analyses of density, microstructure and microhardness.

Thermal treatment	N°	Name	Description
Without	1	AB	As-built repair without thermal treatment
Substrate preheating	2	P500	Repair with substrate preheating at 500°C
	3	P700	Repair with substrate preheating at 700°C
	4	P900	Repair with substrate preheating at 900°C
Interlayer cooling factor	5	CF1	Repair with cooling factor equal to 1
	6	CF3	Repair with cooling factor equal to 3
	7	CF6	Repair with cooling factor equal to 6
Post heat treatment (1h)	8	HT600	Repair with post heat treatment at 600°C
	9	HT1000	Repair with post heat treatment at 1000°C
	10	HT1200	Repair with post heat treatment at 1200°C

The second DOE concerns the study of the corrosion resistance and microorganism formation of the repaired parts in natural seawater with the application of the different thermal treatments. These tests were carried out in natural environment by the company Corrodys in Cherbourg, France. The treatments selected were those that modify the microstructure the most (*i.e.* substrate preheating and post heat treatment). Table 5.2 summarizes the families of samples produced and studied during these tests. Three specimens were produced per family for the reproducibility of the tests. Their behavior in natural seawater was also compared to an unrepaired SS316L reference substrate and a LMD-printed deposit.

Table 5.2: DOE 2 for analyses of corrosion resistance and microorganism formation.

Thermal treatment	Name	Family number	Sample letter	Description
Without	S	1	A B C	Unrepaired reference substrate
Without	AB	2	A B C	As-built repair without thermal treatment
Substrate preheating	P700	3	A B C	Repair with substrate preheating at 700°C
Post heat treatment (1h)	HT1000	4	A B C	Repair with post heat treatment at 1000°C
Substrate preheating AND post heat treatment (1h)	P700+ HT1000	5	A B C	Repair with preheating at 700°C and heat treatment at 1000°C
Without	LMD	6	A B C	LMD-printed deposit without thermal treatment

5.3 Influence of thermal treatments on the characteristics of the repaired parts

5.3.1 Repair geometry

The repair process was performed using the same parameters for all the samples (*i.e.*, laser power, scanning speed, powder mass flow rate and step-over). However, the height of the deposit (Figure 5.3) or the surface of the material varies with the application of the different thermal treatments.

Indeed, as the preheating temperature increases, the height of the deposit increases. In fact, the energy present in the substrate is increased by substrate preheating. Therefore, the melt pool is wider during deposition than without preheating [172]. However, the step-over of 0.84 mm between two beads remains constant, because it was calculated initially from the overlapping rate of 30% and the normal width of the melt pool measured in Section 3.2.1 during the parametric optimization. So the real overlapping rate increases and, as demonstrated in the studies on laser cladding [71, 70], the height of the layer increases.

The cooling factor, on the other hand, involves the cooling of the substrate between each layer. Compared to a fabrication without dwell time, the energy present in the substrate is reduced [173]. As a result, the melt pool width is smaller, the overlapping rate is lower, and the literature shows that the layer height is also lower [71, 70].

On the samples that have undergone different post-HT treatments, since they are applied after fabrication, no variation in the deposit geometry is observed. On the other hand, the treatment is carried out in an air furnace. This causes the appearance of a fine oxide layer that developed on the sample at 1000°C and thick layer on the sample at 1200°C. No characterizations of this oxide layer were performed.

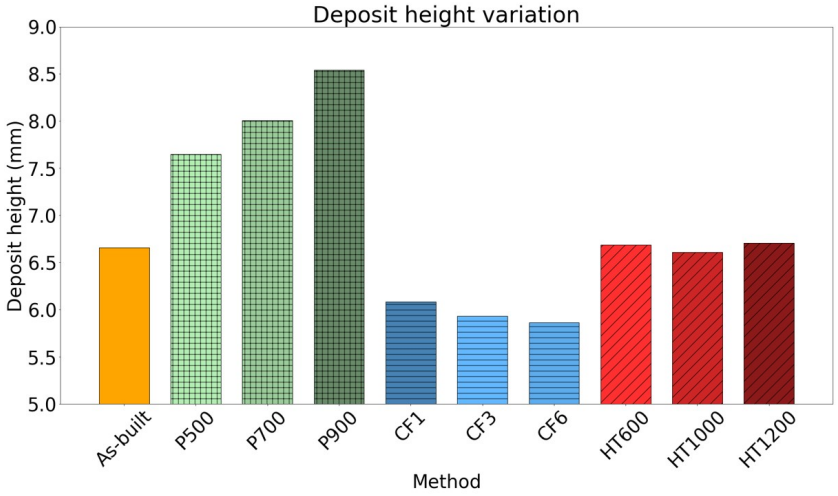

Figure 5.3: Deposit height variation with the different thermal treatment.

5.3.2 Density rate

Metallurgical characterization was performed to determine the density of the repaired samples. The Archimedes method allows the determination of the total density of the sample, and the OM examination of the sections allows to observe the porosity within the material.

Figure 5.4 (a) highlights the variation of the density of the repairs as a function of the thermal treatment by Archimedes measurement. Compared to the as-built repair (99.96%) and the unrepaired reference substrate (99.87%), the specimens with substrate preheating (average of 99.79%) and with cooling factor (average of 99.78%) have a lower density. The samples with post-heat treatments (average 99.93%) have a density comparable to the as-built repair and have a higher density than the reference substrate. This result indicates that the deposit is denser than the substrate and increases the overall density of

the repairs.

Nevertheless, observations of the cross sections shown in Figure 5.4 (b) indicate that all specimens exhibit dense deposition without interbead and interlayer porosity. No lack of fusion is detected at the interface between the deposit and the substrate allowing a strong metallurgical bonding. On the other hand, a decrease in density rate of the samples with substrate preheating and cooling factor is observed compared to the as-built sample and the reference substrate. This is caused by the formation of spherical porosity and intergranular cracks, respectively. With the available observation resolution, this phenomenon is not observed in the as-built and post-heat-treated samples.

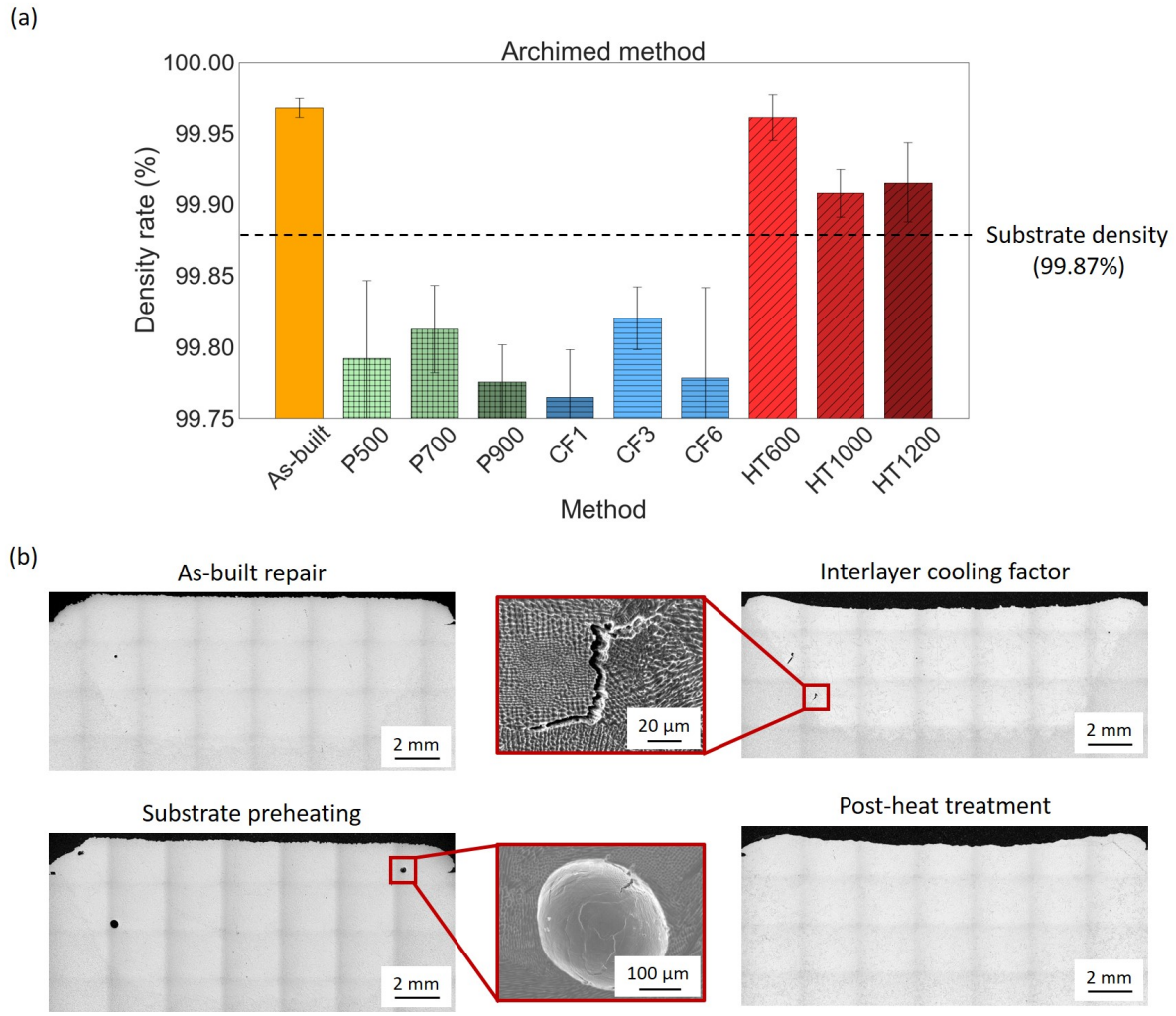

Figure 5.4: (a) Parts density measured by Archimedes method and (b) OM and SEM observations of representative cross sections in function of repair method.

The decrease in density rate (Figure 5.4 (a)) for preheated samples due to spherical porosity formation (Figure 5.4 (b)) is caused by the high energy present in the substrate

due to induction preheating and laser energy input. The alloying elements with a low melting point are vaporized in the melt pool and the gas bubbles remain trapped in the solidified matrix [142].

The cracks observed in Figure 5.4 (b) in the interlayer cooling factor specimens are due to a phenomenon of Ductility Dip Cracking (DDC). They are commonly observed in multi-pass welding of austenitic FCC microstructures [24]. In the present study, they occur in the first bead of each layer. This is where most of the residual stress is introduced. In fact, the substrate cools down between two layers. Therefore, when the first bead of the layer is deposited, the thermal gradient is the most important and causes the introduction of high residual stresses. On the other hand, because the substrate has been locally heated by the deposition of the first bead, the subsequent beads will experience a less significant thermal gradient. Thus, the high residual stresses of the first bead, coupled with a decrease in ductility of the austenitic FCC structure in the temperature range of 800°C - 1150°C, cause the formation of intergranular cracks [24].

As observed in Figure 5.4 (a), the post-manufacturing heat treatments do not change the density of the repairs compared to the as-built sample. These treatments are applied after the repair process only thermally, so the porosity rate cannot be impacted.

The thermal treatments applied during the material deposition (substrate preheating and cooling factor) cause a decrease in the density of the repairs compared to the as-built repair for the deposition parameters obtained in Chapter 3, due to the increase or decrease of the thermal energy present in the substrate, causing evaporation or cracking phenomena. The post heat treatment applied after the material deposition does not affect the density.

5.3.3 Microstructure

Morphology

SEM observations show a heterogeneous microstructure of the repair with the presence of three distinct zones (*i.e.*, deposit, interface, and substrate), as already highlighted in Chapter 4. The observations made on each of the areas of the repair as a function of the thermal treatment are shown in Figure 5.5.

The substrate is made up of fine and equiaxed grains, typical of a cast SS316L that has been hot-rolled with a heat treatment solution annealing at 1050°C. In this type of production, small porosities are detectable and common. The substrate-repair interface is the junction between the deposit and the substrate and is the place of the most important microstructural heterogeneity in the repair. The deposit is characterized by a coarse and

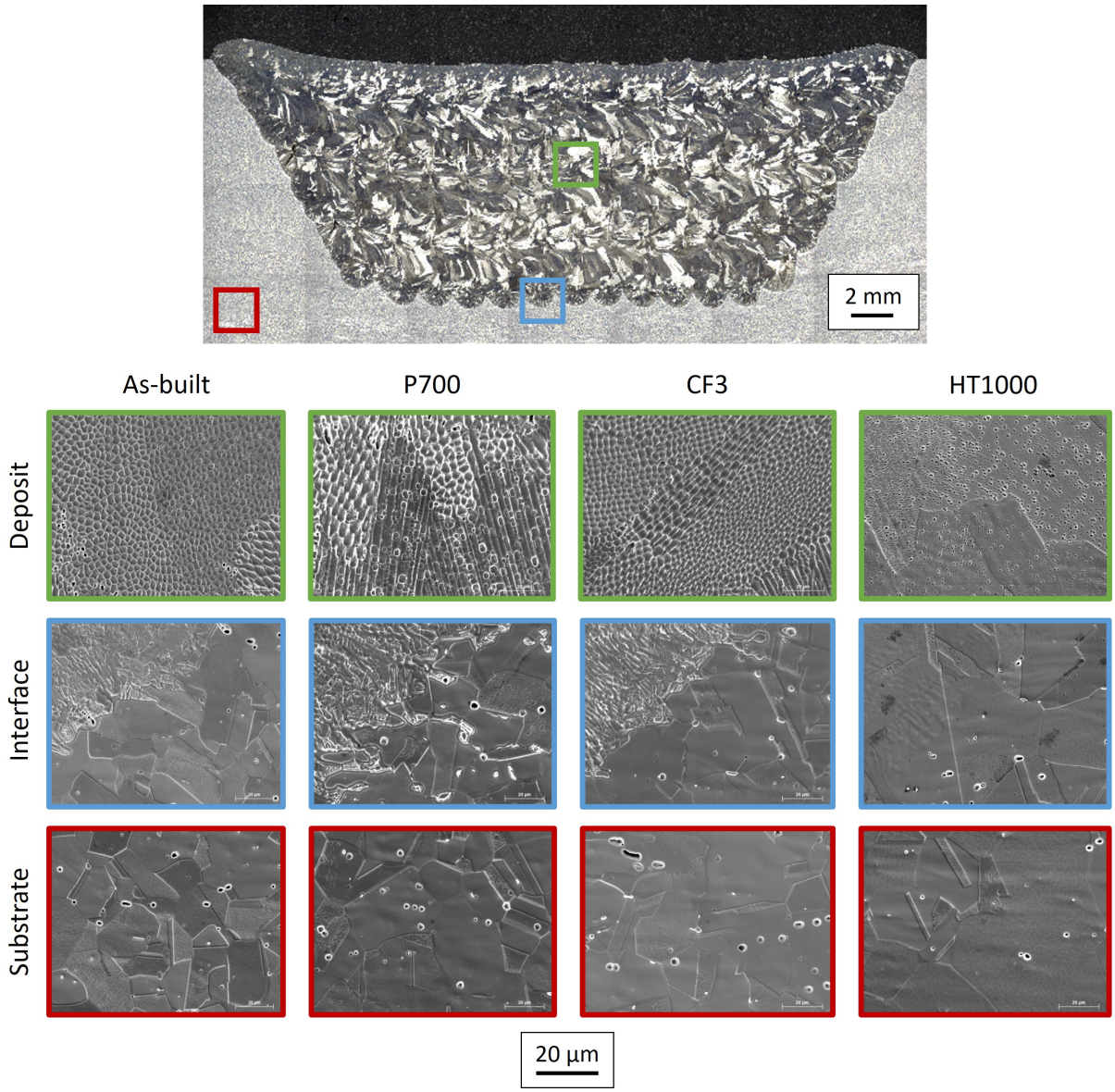

Figure 5.5: SEM observations of substrate, interface and deposit areas for a representative: as-built repair, repairs with substrate preheating, repairs with cooling factor between layers and repairs with high temperature post heat treatment.

columnar microstructure with preferential growth axes. Due to the very fast cooling of the melt pool at the order of 10^4 K/s, the cellular substructure is formed in the grains of the deposit and is characteristic of the LMD process. A high density of dislocations is formed as a result of solidification due to the heterogeneities of heating and cooling during the LMD process and assemble into cellular patterns at cell boundaries [61]. A segregation of the elements of the stainless steel is observed in this substructure: the center of the cells is rich in Fe, while the boundaries are rich in alloying elements such as Cr, Ni, Mo and S, as shown in Section 4.2.3 and the work of Barkia *et al.* [81].

These results show that the microstructural distinction between substrate and deposit is maintained by the different thermal treatments for all of the samples, except in the case of high temperature post-heat treatments, where a structural change is observed. In fact, at 1000°C, a partial dilution of the interface and the cellular substructure of the deposit is observed, as shown in Figure 5.5. The cell boundaries are still partially visible in the deposit and MZ, indicating that the diffusion of chemical elements is not complete. In contrast, for the 1200°C heat treatment, the dissolution of the interface and substructure of the deposit is complete, as the cell boundaries are no longer visible, indicating complete diffusion of the chemical elements. A coarsening of the grains is also observed in the substrate and in the interface region with the high temperature post heat treatments (1000°C and 1200°C).

Substrate preheating, cooling factor, and post heat treatment at 600°C do not change the morphology of the microstructure in the three areas studied. This morphology is similar to that of the as-repaired condition. On the other hand, partial and complete recrystallization takes place at 1000°C and 1200°C, respectively, with diffusion of the chemical elements segregated in the cellular substructure of the grains.

Grain and cell size

EBSD observations were performed on the interface and the deposit center of the repairs. The results are used to evaluate the grain size variation in these two areas and to assess the treatments that most effectively homogenize the microstructure of the repair. Table 5.3 summarizes the main data of the EBSD analysis.

Table 5.3: Summary of the value of measured elements in the microstructure of repairs.

Thermal treatment	Arithmetic grain size		Difference deposit/interface (µm)	Cellular arm spacing (µm)	Calculated cooling rate (°C/s)	Ferrite rate in HAZ (%)
	Left interface (µm)	Deposit center (µm)				
Substrate	6.5 ± 3.2		-	-	-	1
AB	8.8 ± 10.9	45.8 ± 41.7	37 ± 1.2	3 ± 0.3	20586	2.03
P500	7.9 ± 9.1	45.0 ± 41.9	37 ± 1.3	3.6 ± 0.6	12720	2.61
P700	8.6 ± 11.4	47.8 ± 49.2	39.1 ± 1.6	4.7 ± 0.7	5714	2.24
P900	8.9 ± 8.9	51.9 ± 48.7	43 ± 1.6	5.8 ± 1	3069	0.01
CF1	7.4 ± 8.5	42.2 ± 41.6	34.7 ± 1.2	3 ± 0.3	19583	2.42
CF3	8.4 ± 9.4	45.3 ± 41.6	36.8 ± 1.2	2.6 ± 0.2	31157	2.36
CF6	8.9 ± 10.8	44.9 ± 43.4	35.9 ± 1.3	2.1 ± 0.3	59142	2.3
HT600	8.7 ± 9.4	41.6 ± 37.1	32.8 ± 1	3.2 ± 0.5	18773	2.53
HT1000	17.5 ± 15.6	45.4 ± 37	27.7 ± 1.4	Dissolved	-	0.01
HT1200	21 ± 20.9	41.4 ± 39.9	20.3 ± 2.0	Dissolved	-	0.03

Figure 5.6 (a) presents the Inverse Pole Figure (IPF) mapping of the interface of the

repairs. No significant change is observed between the repair methods, except for the high temperature post-heat treatments, which dissolves the interface and produces grain coarsening, especially on the substrate side, as shown in the plot of the average grain size of the maps (Figure 5.6 (b)). An increase of the average grain size of 98.8% is observed for the post heat treatment at 1000°C compared to the as-built repair, and 138.8% at 1200°C.

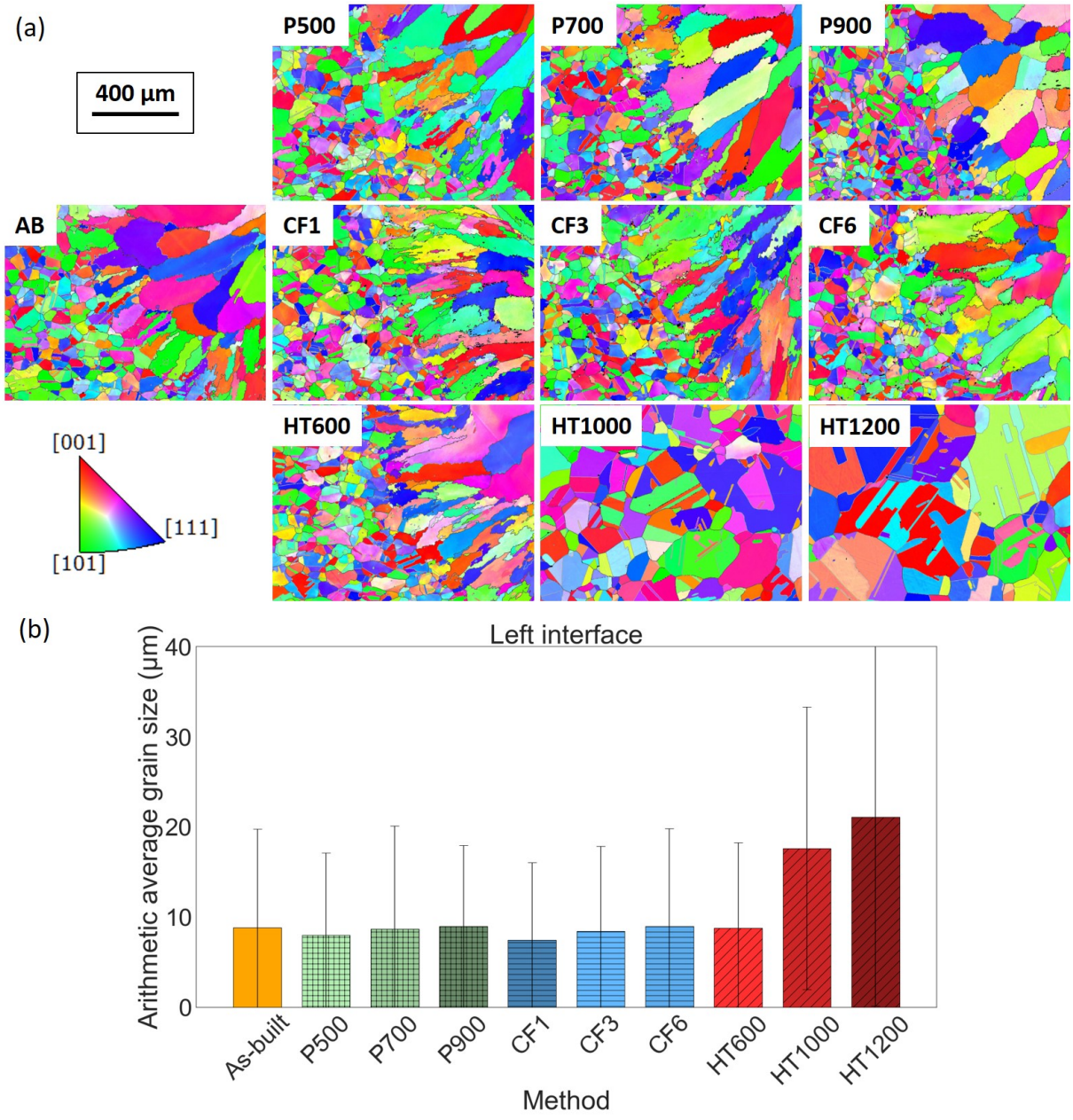

Figure 5.6: EBSD results: (a) IPF maps, (b) arithmetic grain size average of each method for left interface.

Figure 5.7 (a) highlights that during the solidification of the melt pool, the grains of

the deposit grow in the direction of the thermal gradient, *i.e.* towards the center of the melt pool and in the direction of the displacement of the projection nozzle. Similarly, no significant change is observed between the repair methods, except for post-heat treatment at 1200°C, where a recrystallization of the deposit takes place with the formation of equiaxed grains, but does not cause a major variation in the grain size average (Figure 5.7 (b)). It should be noted that there is a slight increase in the grain size of the deposit (15.3% for P900 compared to P500) as the substrate preheating temperature is increased.

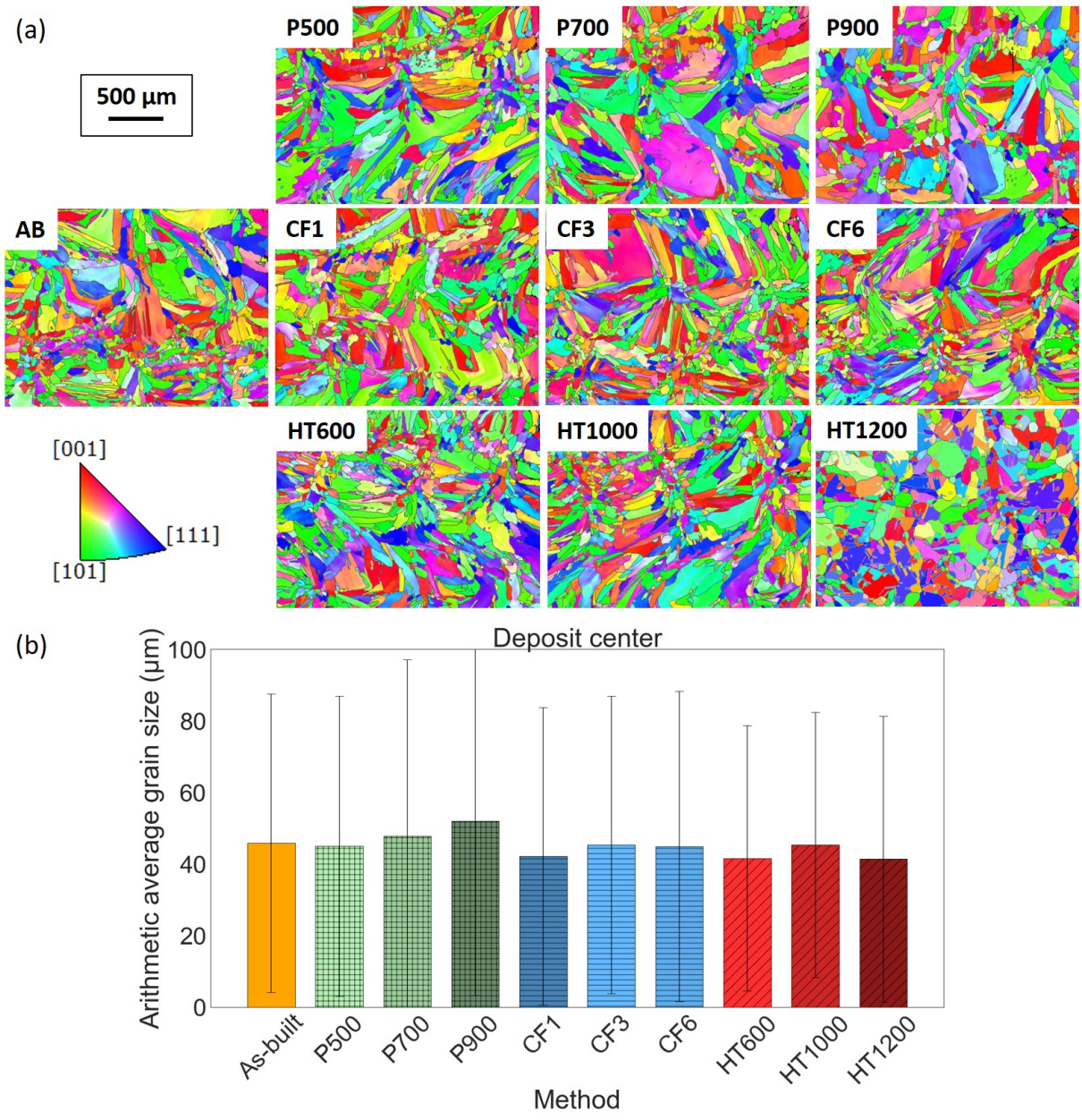

Figure 5.7: EBSD results: (a) IPF maps, (b) arithmetic grain size average of each method for deposit center.

These observations can be summarized in Figure 5.8, which shows the effect of the repair method on microstructure homogenization. Thus, substrate preheating tends to increase the substrate/deposit grain size spacing because the deposit grain size increases with preheating temperature. The substrate/deposit gap is not significantly affected by the interlayer cooling factor. On the other hand, the application of post-heat treatment, especially at high temperature, allows to homogenize the grain size between substrate and deposit grain by increasing the substrate grain size.

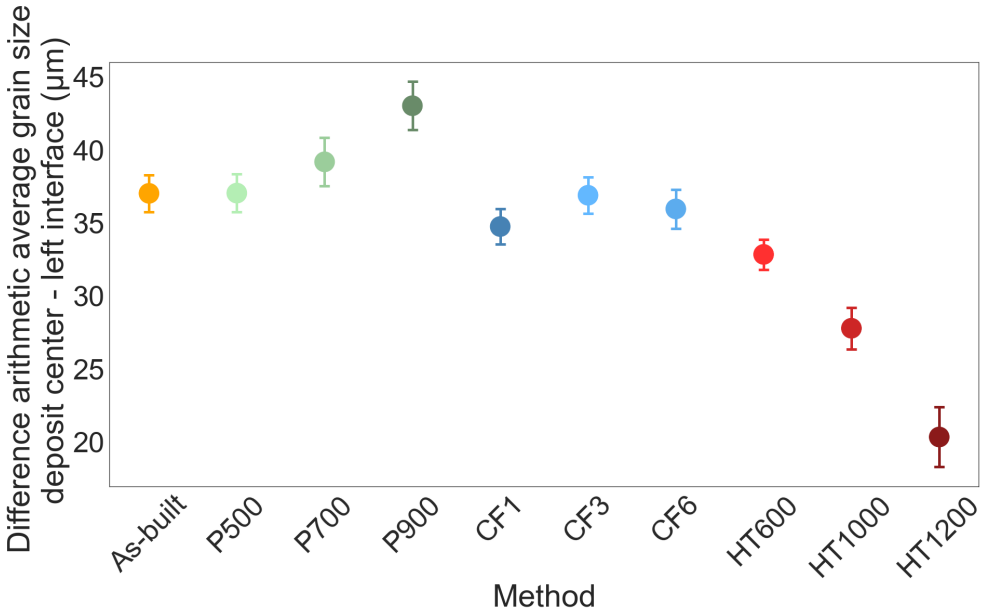

Figure 5.8: Difference of grain size average between deposit center and left interface.

In order to quantitatively compare the Cellular Arm Spacing (CAS) of each sample according to the different thermal treatments, the average CAS of each sample was measured by the triangle method as shown in Figure 5.9. Three midpoints of three adjacent cells form a triangle. The average CAS of the three adjacent cell dendrites can be obtained by measuring and averaging the lengths of the three sides x_1, x_2, and x_3 of the triangle. The measurement is repeated 40 times in several areas of the deposit where the cells are perpendicular to the section plane to reduce errors. The final CAS of the sample can be obtained by averaging the values of all the measured results.

Measuring the cellular substructure using SEM observations revealed that the CAS significantly depends on the repair method used, as it is related to the Cooling Rate (CR) of the part. Increasing the substrate preheating temperature greatly increases the CAS, from 3.6 µm to 5.8 µm for P500 and P900, respectively, representing a increase of 30.5%, as shown in Figure 5.10. Similarly, an increase in the interlayer cooling factor has a tendency to decrease the CAS, from 3 µm to 2.1 µm for CF1 and CF6, respectively,

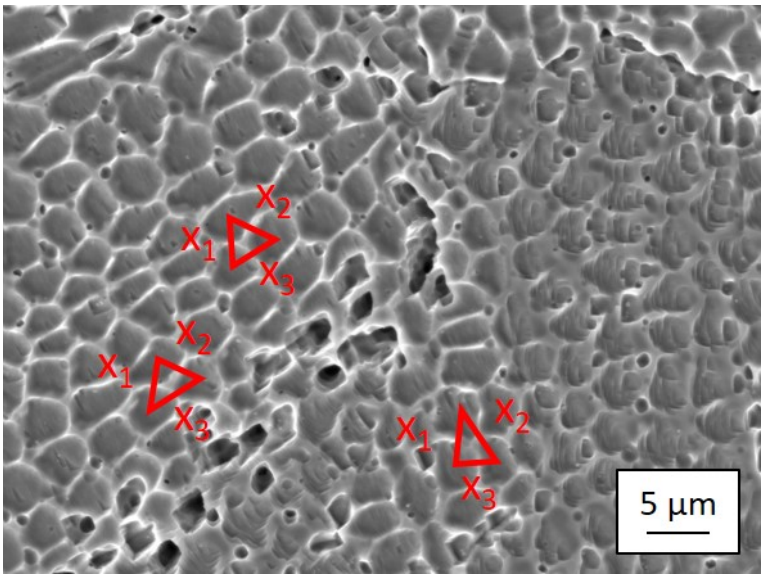

Figure 5.9: Schematic of CAS measurement using the triangle method.

representing a size reduction of 30%. For the high temperature post heat treatments, since the substructure is either partially or completely dissolved, no information is available about the cells. The substructure of the HT600 sample is visible and has a similar cell size to the as-built sample (3 µm). The thermal post-treatment is performed after the sample is fabricated and therefore does not affect the solidification of the melt pool.

In the work of Katayama *et al.* [174], CAS and CR were related by an empirical Equation 5.2. This Equation is obtained from the results of the cooling rate measured during GTA welding of SUS 310S and primary arm spacing measurements of the resulting beads. The curve is extrapolated for high cooling rates and confirmed with primary arm spacing measurements on laser weld beads.

$$CAS = 80 * CR^{-0.033} \tag{5.2}$$

Where the CAS is in µm and the CR is in °C/s. The cooling rate can thus be calculated from the CAS measurements and is shown in Figure 5.10. It can be seen that the cooling rate decreases with increasing preheating temperature and increases with increasing interlayer cooling factor. On the other hand, the post heat treatment at 600°C shows the same cooling rate as the as-built repair.

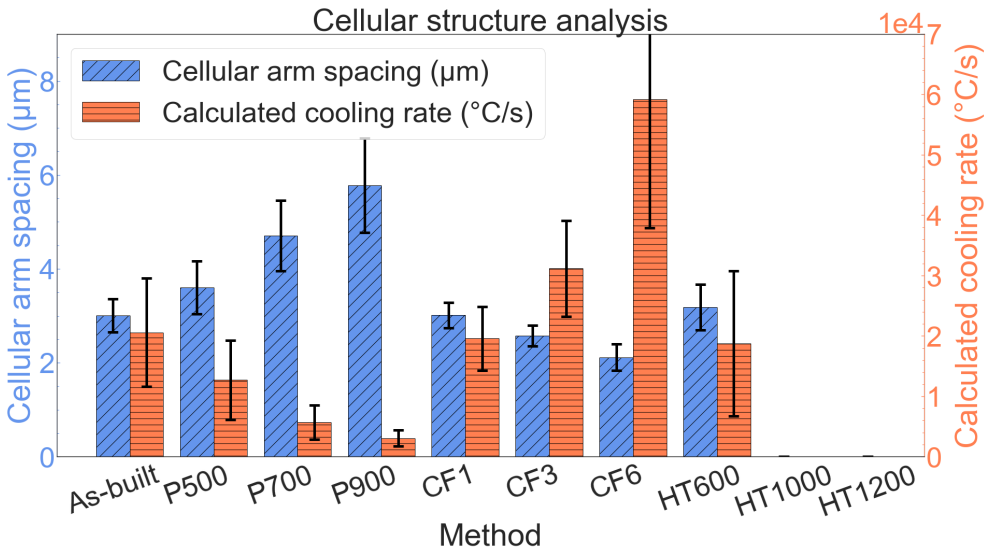

Figure 5.10: Cellular arm spacing measurement and calculated cooling rate of deposit cellular sub-structure.

Phases

Two phases were detected during these analyses, an austenite FCC phase, which constitutes the main matrix and a ferrite BCC phase that appears in small proportions depending on the area observed and the repair method. As highlighted in Figure 5.11 (a), an as-built repair has a fusion zone (deposit + MZ) with a single austenite FCC phase and a base metal (substrate + HAZ) with both austenite FCC and ferrite BCC phases. Like presented in the Chapter 3, the Schaeffler diagram explains the presence of the ferrite BCC phase in the base metal and not in the fusion zone. The calculation results for the equivalent chromium and nickel are 20.72% and 12.68% for the base metal and 21.10% and 14.88% for the powder, respectively. As displayed in Figure 5.11 (c), the powder used as a filler metal for the deposit is in a zone where it has little chance of forming a ferrite phase, which explains the single FCC phase in the fusion zone.

However, the base metal can form up to 7% ferrite. In the unaffected substrate, ferrite is present in trace amounts (1%) because it has undergone a post-manufacturing heat treatment at the steel mill that acts as an anti-ferrite treatment and dissolves this phase. However, the energy delivered by the laser process causes a phase transformation in the HAZ at a thickness of approximately 400 µm. As a result, ferrite grains germinate between the austenite grains and grow in this zone up to 2% for the as-built repair. Table 5.3 and Figure 5.11 (b) summarize the value of the ferrite phase in the HAZ of the left interface for each repair method.

In addition, some repair methods, such as substrate preheating to 900°C or high temperature post-heat treatments (1000°C and 1200°C), avoid the formation of the ferrite phase in the HAZ and only the austenite phase remain in the repair, as shown in Figure 5.11 (b).

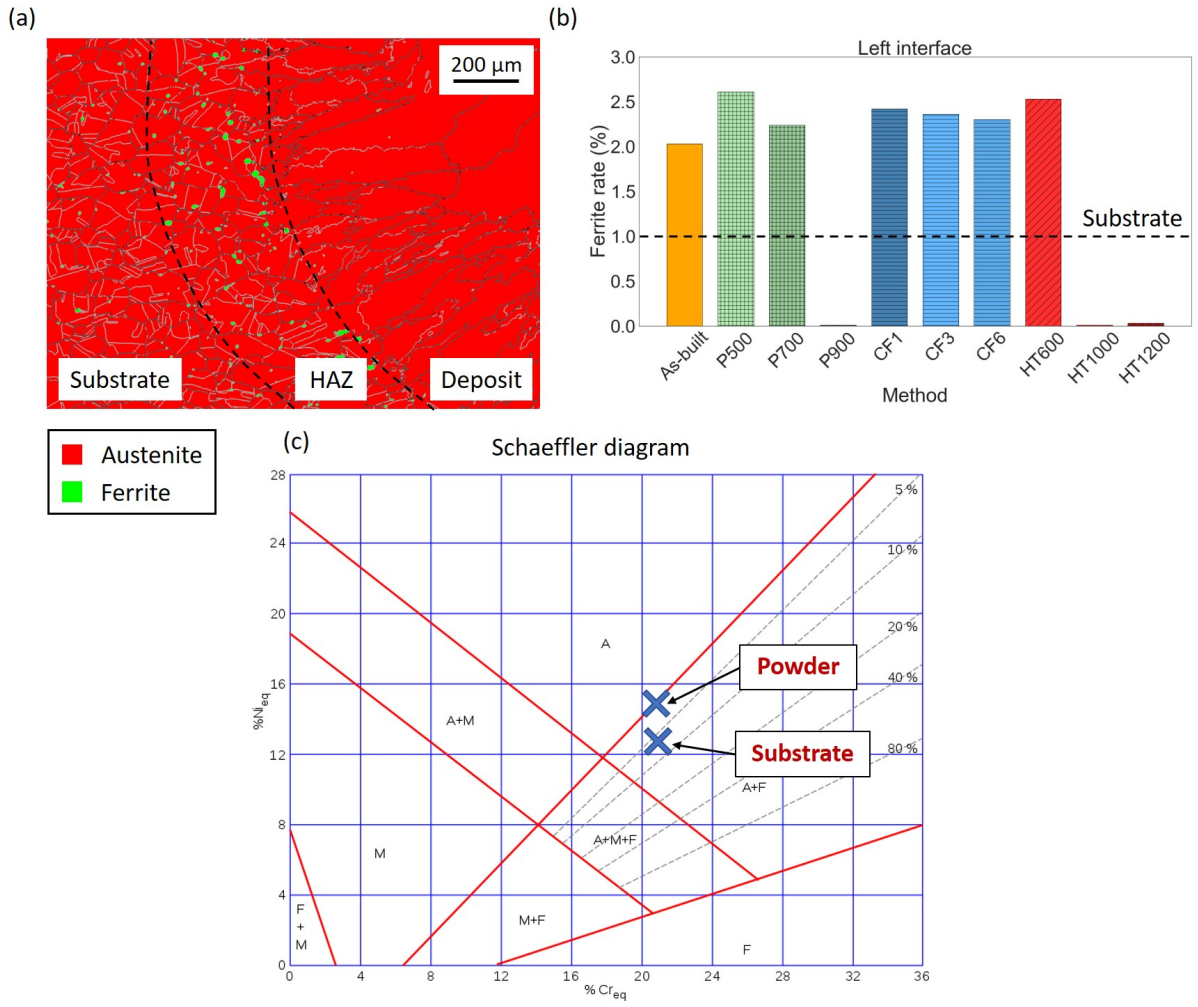

Figure 5.11: (a) Phase map of the as-built repair interface and (b) ferrite phase rate at the left interface in function of the repair method and (c) position of powder and substrate in the Schaeffler diagram.

Discussion

Despite the different preheating temperatures, the morphology of the repair microstructure is similar. However, within the microstructure of the deposit and HAZ, variations are observed. The grain size of the deposit increases slightly with the preheating temperature, but the CAS increases significantly due to the decrease of the CR of the melt pool from

12720 °C/s to 3069 °C/s for the P500 and P900 respectively, as observed in Figure 5.10. In fact, the purpose of the increase in preheating temperature is the reduction of the thermal gradient between the melt pool and the substrate to minimize the introduction of residual stress and to soften the metal. The reduction of the thermal gradient implies consequently a reduction of the cooling rate. Moreover, as the grain size of the deposit increases from 45 µm to 51.9 µm with no big modification of the grain size at the left interface, the gap between the substrate and the deposit grain size increases slightly.

As can be seen in Figure 5.11 (b), the ferrite content decreases to 0% when the substrate is preheated to 900°C, compared to 2.6% and 2.2% for P500 and P700 respectively. The preheating of the substrate is equivalent to a heat treatment that is applied during the repair process. However, the literature reported that heat treatment above 500°C is sufficient to reduce ferrite in a weld [175, 176]. This requires that the treatment is applied long enough to allow the alloying elements to diffuse. Therefore, it can be assumed that the application time of the substrate preheating of about 15 min (heating + repair) is not sufficient to achieve the complete dissolution of the ferrite phase for the temperatures of 500°C and 700°C, but it may be possible at 900°C.

For the application of the interlayer cooling factor, there is no change in the morphology and grain size of the three zones, nor in the phases present. The only variation occurs in the cellular substructure, where the CAS decreases, from 3 µm to 2.1 µm for CF1 and CF6 respectively, with the increase of the interlayer cooling factor. This variation is in agreement with the experiments, since the aim of the cooling factor is to increase the cooling time of the substrate between the deposition of two layers, to allow a greater thermal gradient between the melt pool and the substrate, in order to obtain a finer microstructure. Contrary to the cited works, which report a decrease in grain size with the increase of the cooling factor [113, 102], the present study reports that only the cell substructure shows a decrease in CAS with the increase of the CR. The difference in behavior between this study and the literature is certainly due to the geometry of the deposits. In fact, the two articles in the literature worked on single strand walls where the dissipation of thermal energy is accomplished primarily by convection and conduction through the base of the wall. The application of an interlayer dwell time significantly lowers the overall temperature of the part and results in finer grains. In contrast, in the present study, deposition is performed on a large layer in contact with the substrate from below and from the sides. Therefore, the dissipation of thermal energy is mainly by conduction, and the overall temperature of the part dissipates rapidly even without the application of an interlayer dwell time, changing not the grain size but only the size of

the cellular substructure, which is much more sensitive to the cooling rate.

Finally, a significant change in the morphology of the microstructure is caused by the repair method with post-manufacturing heat treatment. As shown in Figure 5.5, a recrystallization of the microstructure is observed for post heat treatments at high temperatures, *i.e.* above 1000°C. The substructure of the deposit dissolves by diffusion of alloying elements and rearrangement of dislocations formed by the cell network. This disappearance of the cell structure results in the removal of the interface between the deposit and the substrate. It should be noted that for the repairs with heat treatments at 1000°C and 1200°C, respectively, the recrystallization is partial and complete.

In fact, at 1000°C, the grains are still columnar with orientations determined by the solidified melt pool. On the other hand, at 1200°C, the microstructure appears to be equiaxed, indicating a recrystallization of the grains in the deposit, as shown in Figure 5.7 (a). The graphs in Figure 5.6 (b) and Figure 5.7 (b) exhibit an increase in grain size at the interface with increasing post heat treatment temperature, but no change in the deposit. This leads to the reduction of the gap between the microstructure of the interface and the deposit and promotes the homogenization of the grain size of the repair microstructure. Figure 5.12 shows that this homogenization is due to a growth of the small grains at the interface, *i.e.* the substrate grains.

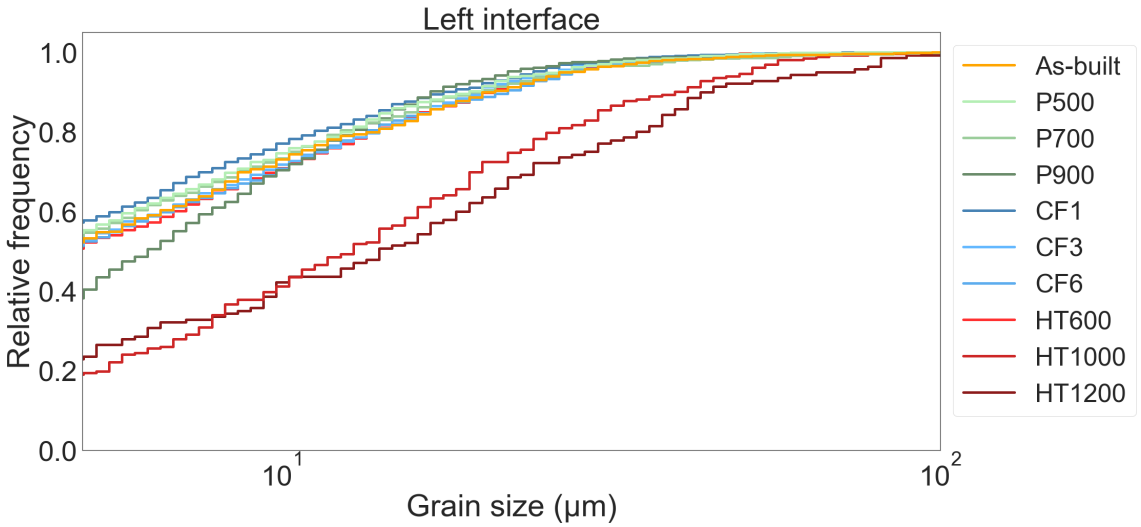

Figure 5.12: Cumulative grain size distribution of each method for the left interface.

These high temperature heat treatments cause a reorganization of the crystal structure, which occurs in two phases. The first phase is recovery. Dislocations become spontaneously mobile and are eliminated either by annihilation or by moving to the free surface of the

metal or to a grain boundary. The second phase is recrystallization, in which new crystallites are nucleated at the triple points and then grow to form the recrystallized microstructure [177].

However, because the repair has a microstructure with heterogeneous morphology between the unaffected substrate, HAZ, MZ, and deposit, each region of the repair evolves differently and at different rates to the post heat treatment. The deposit and the MZ are composed of columnar grains with a cellular substructure characterized by a high density of dislocations and a segregation of chemical elements [61]. Liu *et al.* [178] show that this substructure acts as a barrier to dislocation movement, slowing microstructure recovery. Dislocation movement homogenizes the chemical composition of the grains and contributes to the movement of segregated alloying elements at the cell walls. Recrystallization can begin with nucleation and then growth.

The HAZ consists of fine and equiaxed substrate grains as well as a high density of laser-induced dislocations. Recovery and recrystallization occur faster than in the deposit, as shown by the work of Herrena *et al.* [179], who demonstrated that a cold-rolled SS316L can recrystallize in one hour at 600°C, while incomplete recrystallization without grain growth is observed for an SS316L Selective Laser Melting (SLM) heat treated at 1100°C for one hour [180]. Finally, germination of new grains and their growth occurs rapidly in the substrate free of high dislocation density. These observations help to understand the reason why a growth of grains of the substrate and the HAZ is observed for the two high temperature heat treatments, while the deposit did not completely recrystallize for the treatment at 1000°C and recrystallized without significant growth of grains for the treatment at 1200°C.

5.3.4 Microhardness mapping

Microhardness mapping was performed on the cross sections of the repairs to evaluate the local variations in hardness and to estimate the influence of the repair methods on the homogenization of the mechanical properties.

The maps are shown in Figure 5.13 and highlight that microhardness variations are observed in the repairs depending on the repair methods used. The as-built specimen highlights a deposit and substrate with comparable hardness around 170 HV. However, a microhardness peak is observed at the interface in the HAZ and the MZ. This peak is approximately 400 µm thick on each side. For the HAZ, this increase in hardness can be explained by the formation of delta ferrite, which has a higher plasticity than austenite and causes an increase in hardness [160, 181]. For the fusion zone near the interface, Balit *et al.* [101] explained the presence of a peak of hardness by the finer microstructure of the bead in contact with the substrate and related it to the epitaxial growth of the bead grains on the substrate grains during solidification.

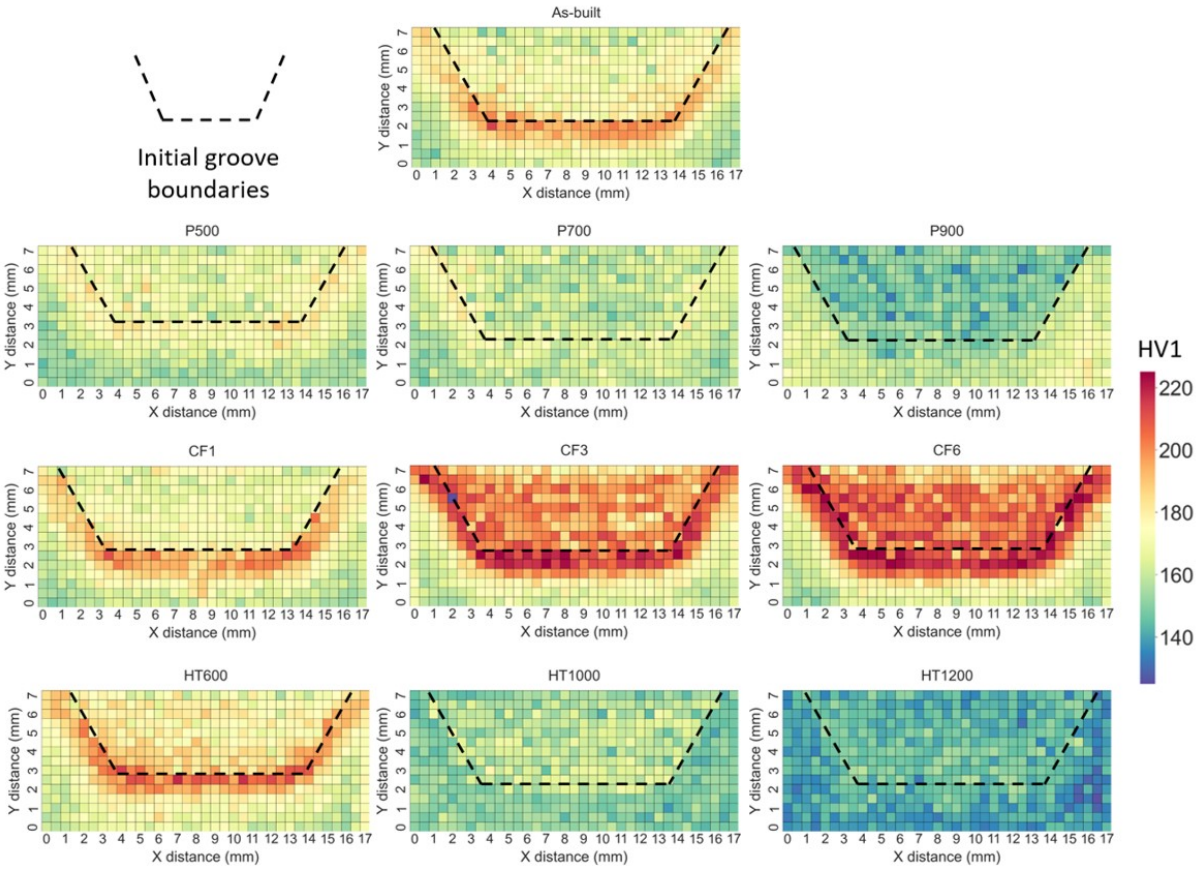

Figure 5.13: Microhardness mappings of the cross sections according to the thermal treatment.

The substrate preheating reduces the microhardness peak with increasing temperature until its complete disappearance for a preheating at 900°C. On the other hand, this temperature also decreases the microhardness of the deposit. An increase of the microhardness of the deposit and of the HAZ is observed with the increase of the cooling factor. The microhardness of the sample is not affected by post-heat treatment at 600°C. On the other hand, high temperature heat treatments dissipate the microhardness peak at the interface and softens the deposit and the substrate.

Figure 5.14 (a) shows the microhardness distributions as a function of the repair method, which can be considered as a combination of Gaussian distributions. By using the expectation maximization algorithm to convergence, each microhardness distribution is decomposed into three Gaussian distributions representing each area of the repair (*i.e.*, substrate, interface, and deposit), whose eigenvalues are shown in Figure 5.14 (b) and summarized in Table 5.4.

Table 5.4: Summary of the microhardness value in the deposit, interface and substrate.

Thermal treatment	Deposit (HV)	Interface (HV)	Substrate (HV)
AB	170.4 ± 8.7	184.4 ± 10.1	167.3 ± 8.5
P500	167.1 ± 3.8	175.8 ± 5.3	156.6 ± 4.4
P700	162.9 ± 3.7	167.5 ± 7	156.5 ± 4.7
P900	149.6 ± 4.2	155 ± 10.7	162.6 ± 4.7
CF1	172.7 ± 4.5	185.9 ± 9.8	162.7 ± 5.2
CF3	193.7 ± 15.7	201.6 ± 9	170 ± 8.6
CF6	196.8 ± 9.9	210.1 ± 8.8	168 ± 8.3
HT600	178.9 ± 6.1	189.8 ± 11.4	167.3 ± 6.3
HT1000	162.3 ± 4	148 ± 3.4	153.5 ± 3
HT1200	141.9 ± 5.1	147.5 ± 4.6	140.2 ± 4.9

These results confirm the previous observations and show that the substrate preheating and the high temperature heat treatments lead to a homogenization of the microhardness in the repairs, while the application of a cooling factor between the layers leads to a heterogenization of the mechanical properties locally.

The preheating of the substrate and the interlayer cooling factor have an effect on the microhardness of the deposit. This can be explained by the Hall-Petch relationship described by Equation 5.3.

$$\sigma_y = \sigma_0 + k * d^{-\frac{1}{2}} \tag{5.3}$$

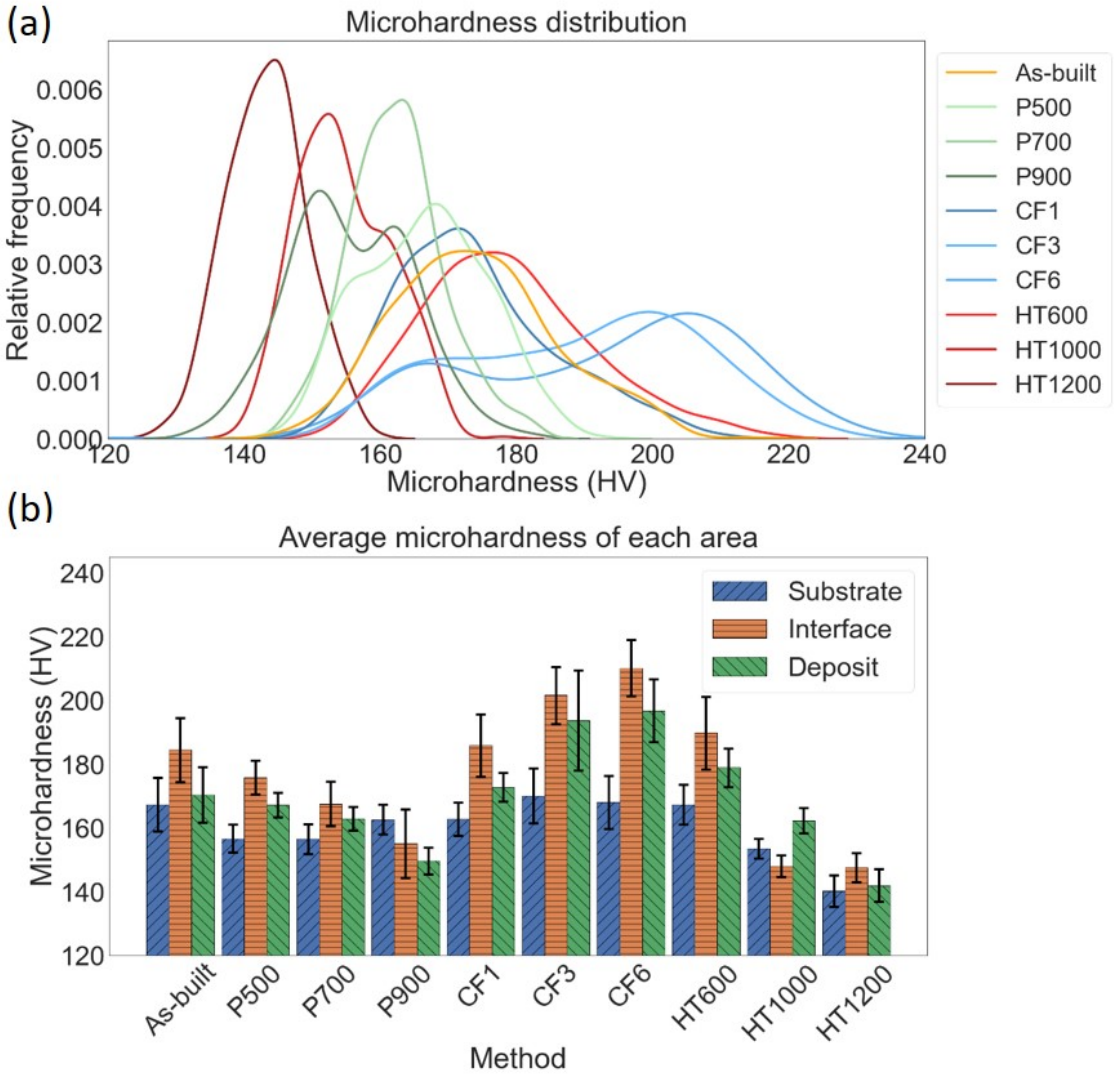

Figure 5.14: (a) Microhardness distributions and (b) microhardness average in substrate, interface and deposit in function of the repair method.

Where σ_y is the yield strength, σ_0 is the resistance of the lattice to dislocation motion, k is the strengthening coefficient, and d is the average grain diameter.

Zhou *et al.* [161] indicate that the cellular substructure has a greater contribution to the YS than the grains. The grain size doesn't change significantly with increasing preheating temperature. On the other hand, there is a significant increase in the dimensions of the cellular substructure. As a result, the hardness of the deposit is reduced.

However, it was observed in the Section 5.3.3 that the grain size of the deposit was not modified for the different values of substrate preheating and cooling factor. On the other hand, these two thermal treatments strongly influence the size of the cellular substructure through the variation of the cooling rate. The size of the cells causes the increase or

decrease of the microhardness of the deposit. A linear regression can be performed between the deposit microhardness and the CAS, and the result leads to the Equation 5.4. Thus, as the cell size increases with the substrate preheating temperature, a decrease in the hardness of the deposit is observed, from 167.1 HV to 149.6 HV for P500 and P900, respectively, as observed in the figure. Similarly, increasing the cooling factor decreases the CAS and increases the deposit hardness in the repairs, from 172.7 HV to 196.8 HV for CF1 and CF6, respectively.

$$HV = -11.8 * CAS + 215.2 \tag{5.4}$$

These two thermal treatments also affect the microhardness peak at the interface (HAZ and MZ), where a dissipation of the peak is observed for the substrate preheating, while a hardening of the peak is observed for the cooling factor. On the MZ side, the microhardness variation can be explained in the same way as for deposition, since this region also contains a cellular substructure whose cell size is sensitive to the cooling rate.

The variation of the microhardness in the HAZ is more complex. In fact, the complete dissolution of the ferrite BCC phase for the P900 specimen could explain the dissipation of the peak in the HAZ for this sample, but P700 present also a microhardness decrease in the HAZ with a value of 162.9 HV compared to the 170.4 HV of the as-built repair, but the ferrite phase is still present in this specimen with a rate of 2.24%. In addition, the increase of the interlayer cooling factor leads to an increase of the microhardness in the HAZ. However, the ferrite content varies little between the different values used, only 5% between CF1 and CF6. Another phenomenon must also affect the hardness of the HAZ for these two heat treatments.

This phenomenon could be the intensity of the residual stresses in the HAZ introduced by the laser process. In fact, the literature has reported the introduction of residual stresses in the HAZ for laser cladding rail repair [171], which could influence the microhardness values obtained on the cross sections of the specimens. The following hypothesis could be made. Increasing the preheating temperature reduces the introduction of residual stresses, as observed in the work of Ding *et al.* [74] on 12CrNi2 deposited by LMD, where the sample preheated to 300°C has 32% lower residual stresses compared to a sample not preheated. This reduction is due to a lower thermal gradient between the melt pool and the substrate. Thus, the hardness of the sample would decrease with the intensity of the residual stresses.

Similarly, the increase in cooling factor leads to an increase of microhardness in the HAZ compared the as-built repair. In contrast to substrate preheating, the thermal

gradient between the melt pool and the part is more important compared to a repair without dwell time, as shown in published work [182, 183]. As a result, the residual stresses introduced in the HAZ affected by the laser could be higher [184], and increase the microhardness in this area.

To confirm this hypothesis, residual stress measurements by XRD were performed on all samples in the substrate, at the interface, and in the deposit. However, the results obtained showed significant variations between each measurement point. It turned out that this type of measurement was not adapted to the samples to be analyzed due to the configuration of the equipment. As explained in Chapter 2, the principle of measuring residual stresses by XRD consists in measuring the shift of the diffraction peak under different angles ϕ and ψ. The hysteresis obtained allows the intensity of the residual stresses to be determined.

In order to obtain a response from the sample, an X-ray beam of 1 mm diameter was used to measure the diffraction peak. However, with the different inclinations of ϕ and ψ, the peak obtained comes from different areas of the repair, as shown in the Figure 5.15. Moreover, the residual stress state in a part repaired with LMD is complex, as shown in the work of Roy *et al.* [171]. This explains the inconsistency of the results obtained. No other residual stress measurements were performed in this thesis.

The microhardness of the samples is also affected by the application of post-heat treatment. The first observation is that a treatment at 600°C for 1 hour is not sufficient for the modification of either the microstructure or the microhardness. On the other hand, the heat treatments at 1000°C and 1200°C have the advantage of eliminating the microhardness peak at the interface by releasing residual stresses and dissolving the ferrite phase contained in the HAZ. In addition, as described in several articles in the literature [113, 121, 185], a general decrease in substrate and deposit hardness is observed. According to the Hall-Petch relation, the increase of the grain size in the substrate causes a decrease of the microhardness in this zone. For the 1000°C and 1200°C treatments, the grain size of the deposit is not changed, but the cellular substructure is partially or completely dissolved. However, Yin *et al.* [186] demonstrate that the dissolution of the cellular substructure causes a decrease in the microhardness of the deposit due to the reorganization of the dislocations. Thus, due to the residual cellular substructure still slightly observed in the microstructure, the deposit at 1000°C (162.3 HV) is harder than that at 1200°C (141.9 HV).

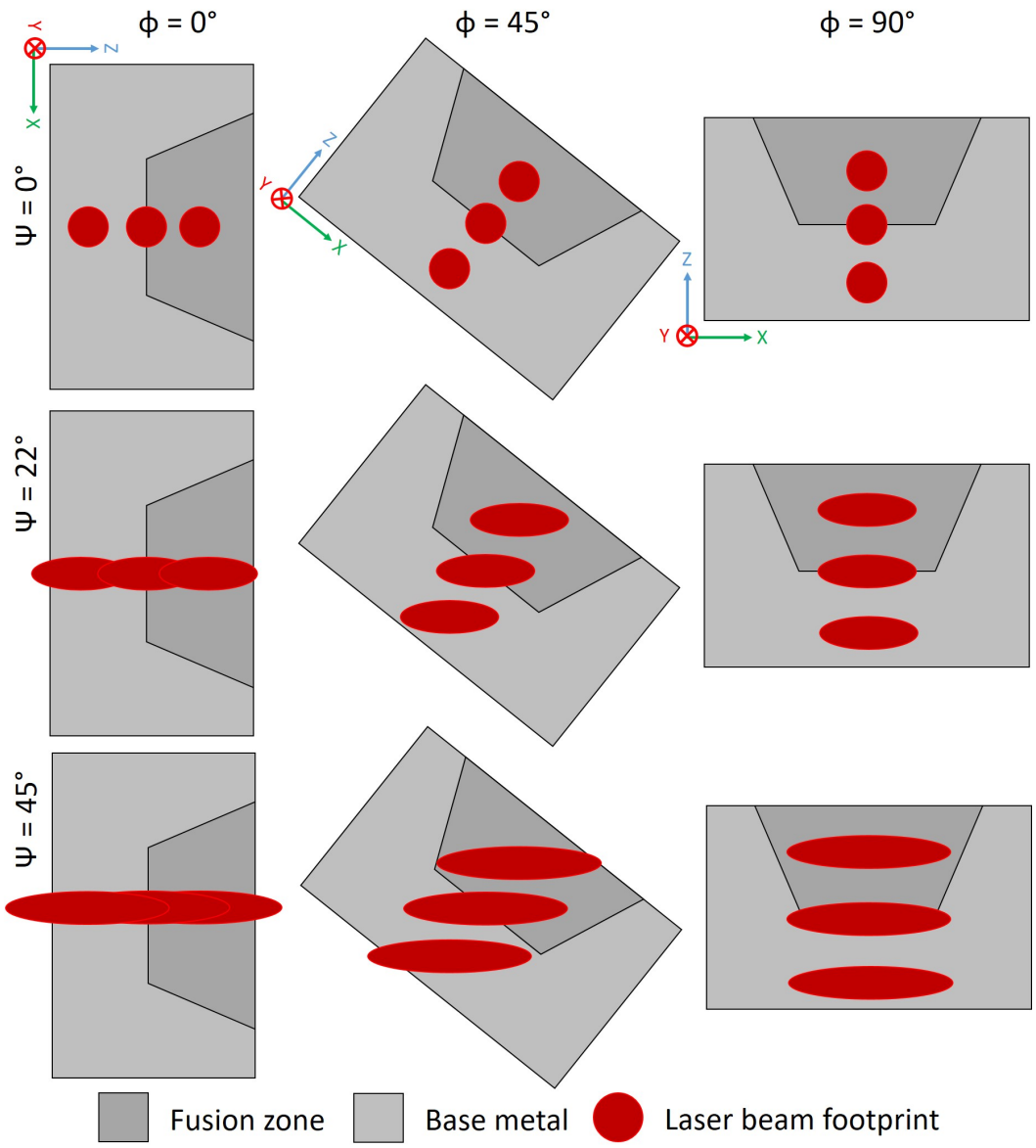

Figure 5.15: Illustration of the problem of overlapping areas of residual stress measurements by XRD for repair.

In this first part of the study on the influence of thermal treatments, three kinds of treatments were applied: substrate preheating, intercooling factor and post-heat treatment. Their effects on the density, microstructure and microhardness of the repairs was analyzed and compared to the properties of an as-built repair and an unrepaired reference substrate. The objective was to determine the most appropriate heat treatment to achieve the desired microstructural and microhardness imperceptibility of the repair. The results show that the interlayer cooling factor, regardless of its value, does not seem

to be adapted to the repair, since it does not cause a major change in the microstructure, except for a reduction in the CAS. Moreover, it leads to a heterogeneity of the microhardness in the repaired area with an increase in the peak hardness at the interface.

Substrate preheating above 700°C showed interest in homogenizing the microhardness within the repair, but did not result in any change in the microstructure except for an increase in the size of the cell substructure. On the other hand, post heat treatments above 1000°C proved to be a promising option to homogenize the microstructure by increasing the substrate grain size and recrystallizing the deposit grains. This transformation allowed the homogenization of the microhardness in the sample. This harmonization of part characteristics would potentially result in better mechanical properties and corrosion resistance compared to an as-built repair as observed in Chapter 4. Mechanical tests such as tensile tests or Charpy impact tests would allow to observe the influence of these treatments on the mechanical properties.

According to the results of this first study, the thermal treatments of substrate preheating at 700°C and post heat treatment at 1000°C for 1h were selected for their interest in homogenizing the intrinsic characteristics of the repaired parts. A second DOE was developed with these two thermal treatments to observe the corrosion behavior and the formation of microorganisms on their surface in natural seawater. A combination of the two thermal treatments was applied to one specimen to observe the effects on the repair. These samples were compared to the reference substrate, an as-built repair, and an LMD-printed deposit, all thermally untreated.

5.3.5 Immersion tests in natural seawater

Free corrosion potential

Figure 5.16 presents the Free Corrosion Potential (FCP) of all samples during the three months of immersion. The potential starts from a value of -0.1 mV/ECS, then it increases immediately after the immersion for about ten days to reach a maximum potential that is between 0.4 and 0.5 mV/ECS. These electrochemical measurements seem to highlight a behavior often found in natural seawater immersion tests for stainless steels, with an increase in the FCP during the first days of immersion, then a stabilization of the potential over time [187, 188, 189, 190]. However, literature results report a maximum potential between 0.3 and 0.35 mV/ECS.

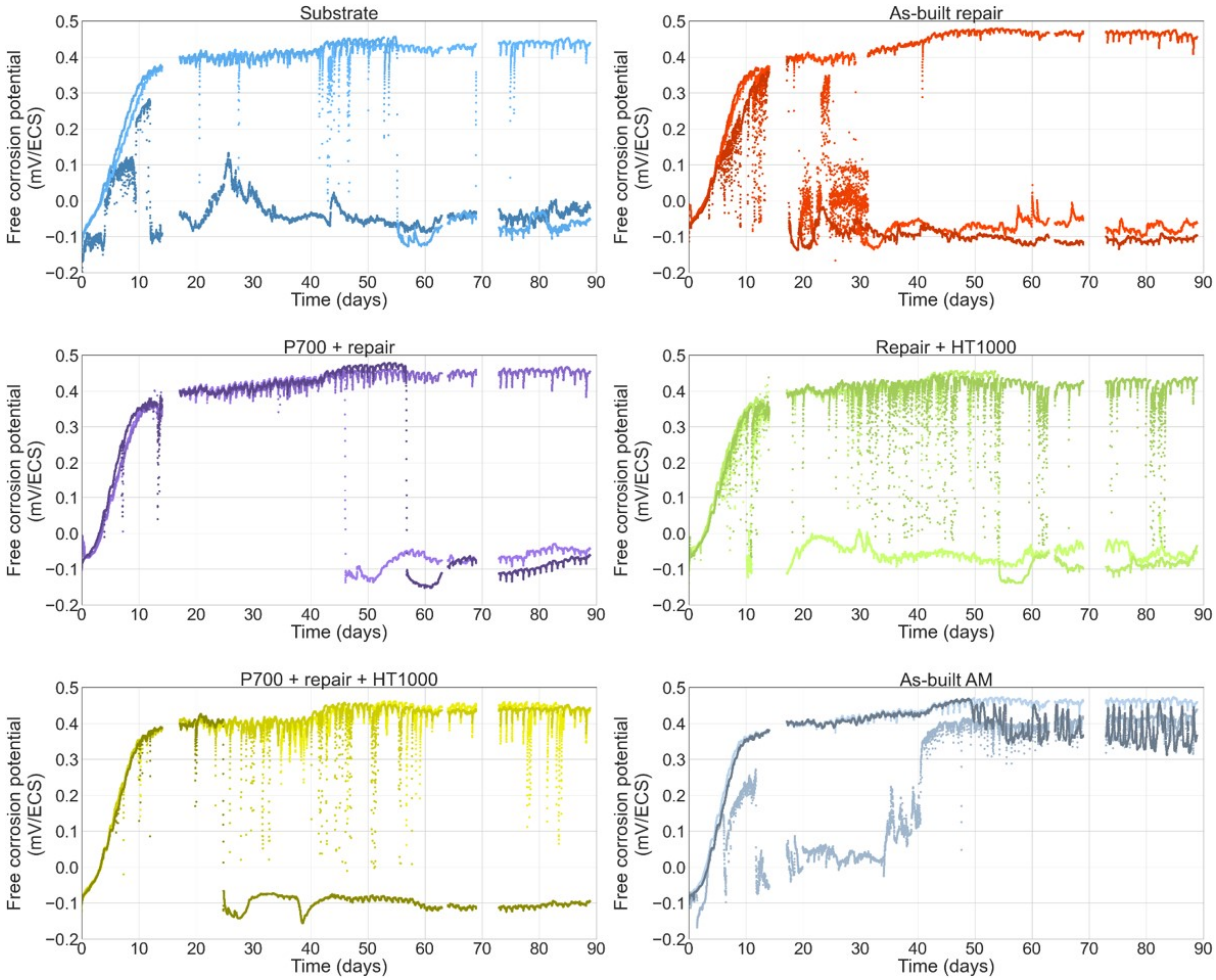

Figure 5.16: Visualization of the FCP for the three samples of each repair method.

The increase in the FCP of stainless steels is related to the formation of biofilm in natural seawater. In fact, as soon as the samples are immersed, organic and inorganic

macromolecules coming from the environment or from microorganisms are adsorbed by the surface of the coupons. The surface properties are modified and allow the irreversible adhesion of bacteria after a few hours of immersion. These bacteria then develop into micro-colonies that form the biofilm [188]. The mass of the biofilm increases simultaneously with the potential at the beginning of the exposure. However, there is no correlation between the maximum potential and the mass of the biofilm when this potential is reached.

The potential increase to a maximum is caused by an increase of the cathodic reaction rate. The reasons for this increase in cathodic reaction rates in natural seawater on stainless steels are still widely discussed and can be divided into three categories:

- Catalysis of oxygen reduction by iron oxides and hydroxides present in the Cr_2O_3 passive layer [190].

- Catalysis of the cathodic reaction by manganese oxides associated with the presence of mangano-bacteria [191, 192].

- Catalysis of oxygen reduction by extracellular compounds present in the biofilm, like the production of hydrogen peroxide [193, 192].

The daily variation of the potential between maximum and minimum corresponds to the variation of the dissolved oxygen content in the water between day and night. In fact, the variation of the oxygen rate is a direct consequence of the photosynthesis of the algae and diatoms present in the seawater and on the coupons. Through their metabolism, they modify the local physico-chemistry and contribute to the variation of the FCP [194].

On the other hand, some coupons exhibited decreases in potential at different immersion times. These coupons correspond to those on which corrosion products formed, as observed in Figure 5.17 (b) of side A after immersion circled in red. The corrosion products appear to originate from the substrate beneath the resin for samples of all families that show a decrease in FCP, with the exception of the LMD printed deposits, which do not show this phenomenon. After cutting and removing the resin, a corrosion phenomenon is located in the substrate under the resin, as shown in the magnified view in Figure 5.17, where the corrosion products originate.

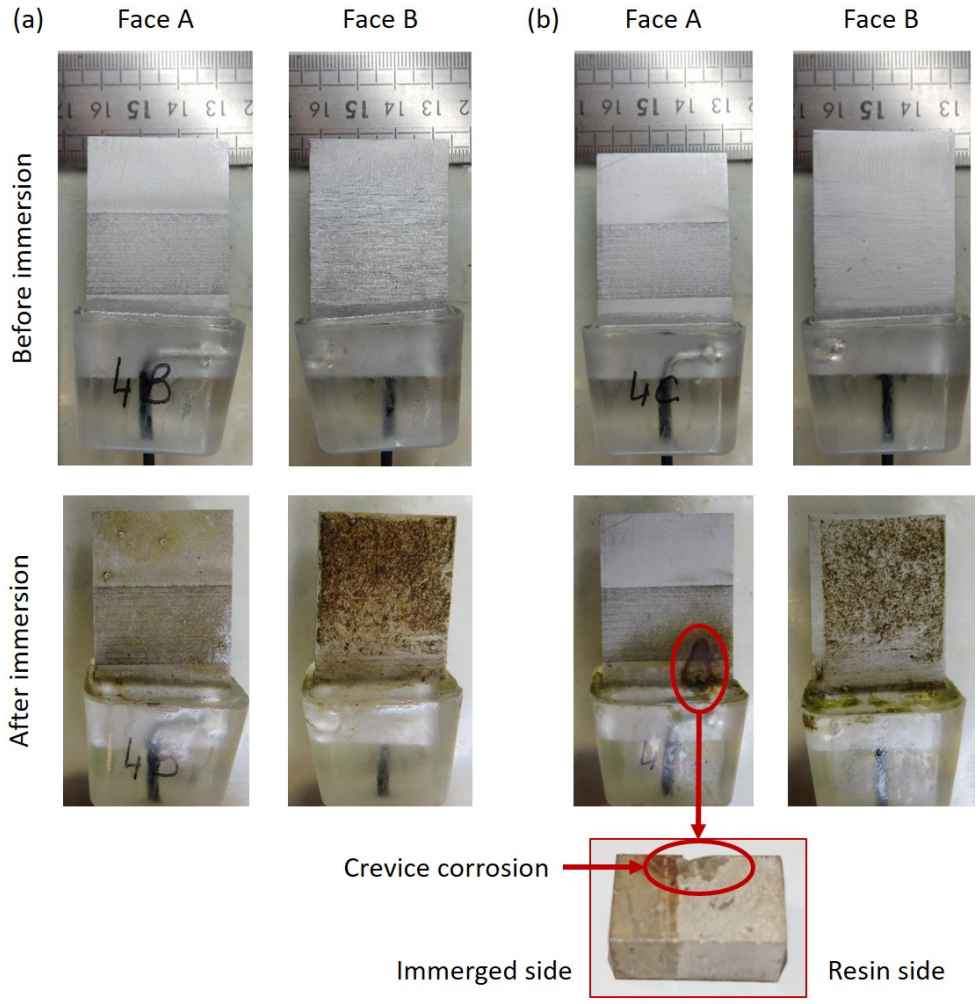

Figure 5.17: Pre- and post-immersion pictures of faces A and B of the substrate preheated repairs (a) B and (b) C, with a magnified view on the corroded area after specimen cutting.

Observations made on the resin montage to protect the electrical connection exhibit a confined area on the underside as illustrated in the Figure 5.18. The resin was immersed only a few millimeters and the water/air interface may have created a confined area, probably with a differential aeration zone, as the environment may be less well renewed at this location compared to the rest of the coupon surface. Moreover, this zone between the coupon and the resin is a preferential zone for the development of microorganisms, which can also accelerate the corrosion phenomenon. Therefore, the geometry of the device resulted in the presence of a confined area that caused crevice corrosion and rapid reduction of FCP in some samples (Figure 5.16). The initiation of crevice corrosion is due to a sudden depassivation of the material, and can be coupled with MIC.

Figure 5.19 highlights the main values of the FCP measurements. For the specimens

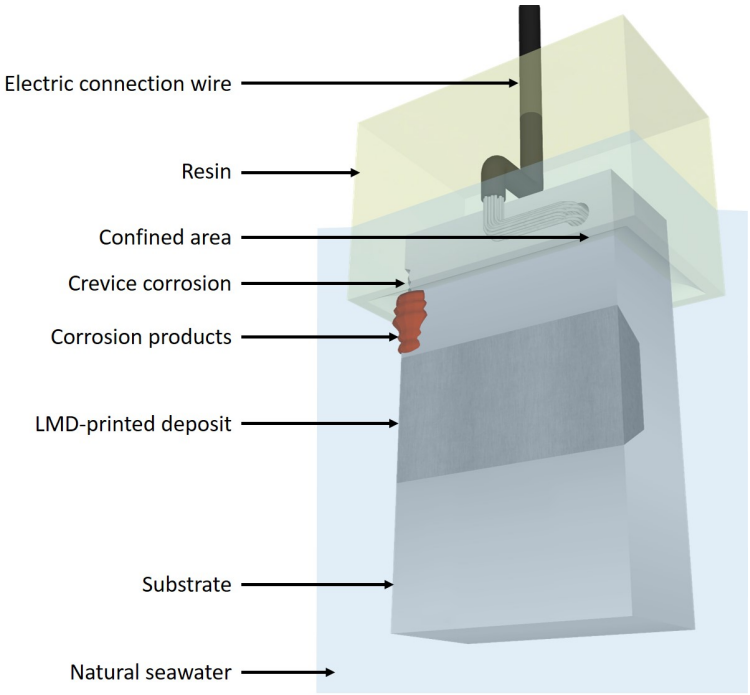

Figure 5.18: Illustration of the montage with the resin protecting the electrical connection with the confined area at the bottom and the position of the corrosion phenomenon and the corrosion products.

with no crevice corrosion observation, the observations made during the 90-day immersion period indicate that the repair areas did not evidence any difference in their corrosion behavior. It was also observed that there was no difference in the electrochemical behavior of the different types of coupons, either regarding the values of the FCP or regarding their evolution over time.

In fact, no trend is observed in the potential value after 3 months of passivation, except for the samples with a low potential due to the formation of corrosion products caused by crevice corrosion observed in Figure 5.19 (a). In the same way, all the samples showed a comparable maximum potential with no specificity depending on the different repair methods (Figure 5.19 (b)). Finally, as observed in Figure 5.19 (c), the slopes are similar between the families of samples. This indicates that the samples passivate at the same rate in natural seawater regardless of the repair method.

However, the Figure 5.19 shows that the samples containing the substrate (substrate only and repairs) are more susceptible to crevice corrosion, with generally two out of three samples experiencing this type of corrosion within the time of immersion in seawater. On the other hand, the samples containing only the LMD printed deposit do not experience crevice corrosion and FCP drop within three months of analysis.

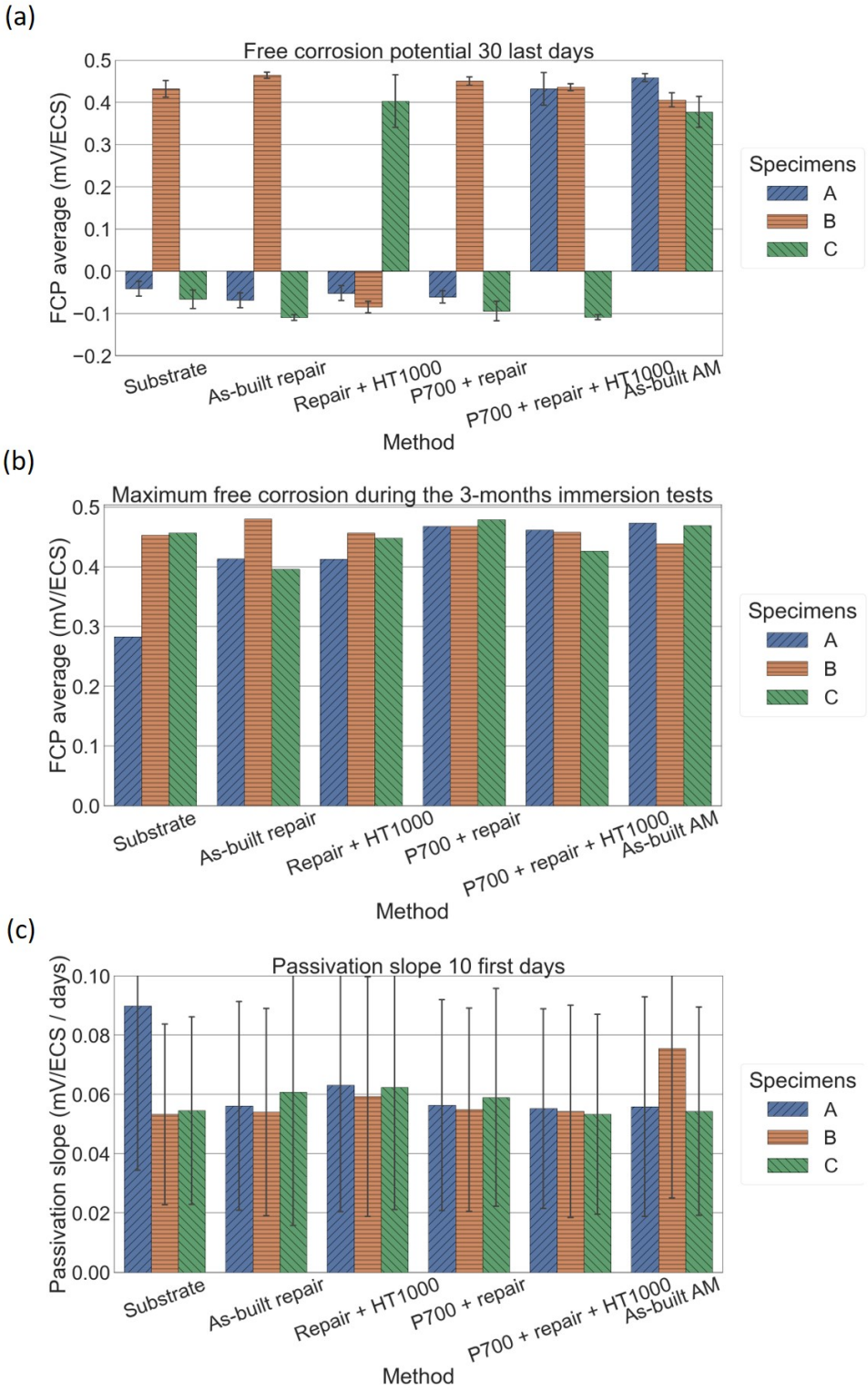

Figure 5.19: (a) FCP average during the last month of immersion, (b) the maximum FCP during the 3-months immersion and (c) passivation slope during the first 10 days of immersion.

This trend can be explained by the chemical composition of the substrate and the powder. The susceptibility to pitting of these two elements can be determined by comparing their Pitting Resistance Equivalent Number (PREN), which is a predictive measure of a stainless steel's resistance to pitting based on its chemical composition and defined by the Equation 5.5. The PREN is often specified when stainless steels are exposed to seawater or other solutions with high chloride content. In general, the higher the PREN, the more resistant the stainless steel is to localized chloride pitting. A PREN > 40 is generally required for use of stainless steel in seawater to resist to pitting and crevice corrosion [190].

$$PREN = \%Cr + 3.3 * \%Mo + 16 * \%N \tag{5.5}$$

According to the chemical compositions of the substrate and the powder, the calculated PREN are 24.02 and 28.26, respectively. This difference is explained by higher chromium and molybdenum in the powders (18.1% and 2.6% respectively) than in the reference substrate (17.3% and 1.6% respectively). These values demonstrate the higher pitting and crevice corrosion resistance of the powder deposit compared to the substrate. Therefore, the LMD-printed deposits (batch 6) do not undergo crevice corrosion during the immersion period, whereas the substrate and the repairs, regardless of their heat treatment, undergo crevice corrosion. Indeed, the montage is such that in the repairs, only the substrate is in a confined area beneath the resin, while the deposit is completely immersed in the seawater, like observed in Figure 5.18.

Microorganism formation

As observed in Figure 5.17, a brown biofilm/deposit is present on all coupons. It is fairly evenly distributed over the entire surface and locally forms small darker clusters (overthicknesses) that have a mossy morphology when observed by SEM analyses (Figure 5.20 (a)). Small tubeworms were observed on almost all surfaces of the coupons. A magnified view is shown in Figure 5.20 (b). Some kind of brown filamentous algae were observed on several coupons. Their development seemed to be unrelated to the type of repair or the location of the coupon. Finally, shells formed randomly on the surface of the specimens (Figures 5.20 (c) and (d)).

The results of the microbiological analyses are summarized in Table 5.5 and Figure 5.21. The average microbial biomass is relatively similar between the different coupons and ranges from 2.0E+07 to 4.0E+07 $microorganisms/cm^2$. The average total aerobic heterotrophic flora (FTa), which ranges from 2.0E+03 to 5.0E+03 CFU/cm^2 shows some variation

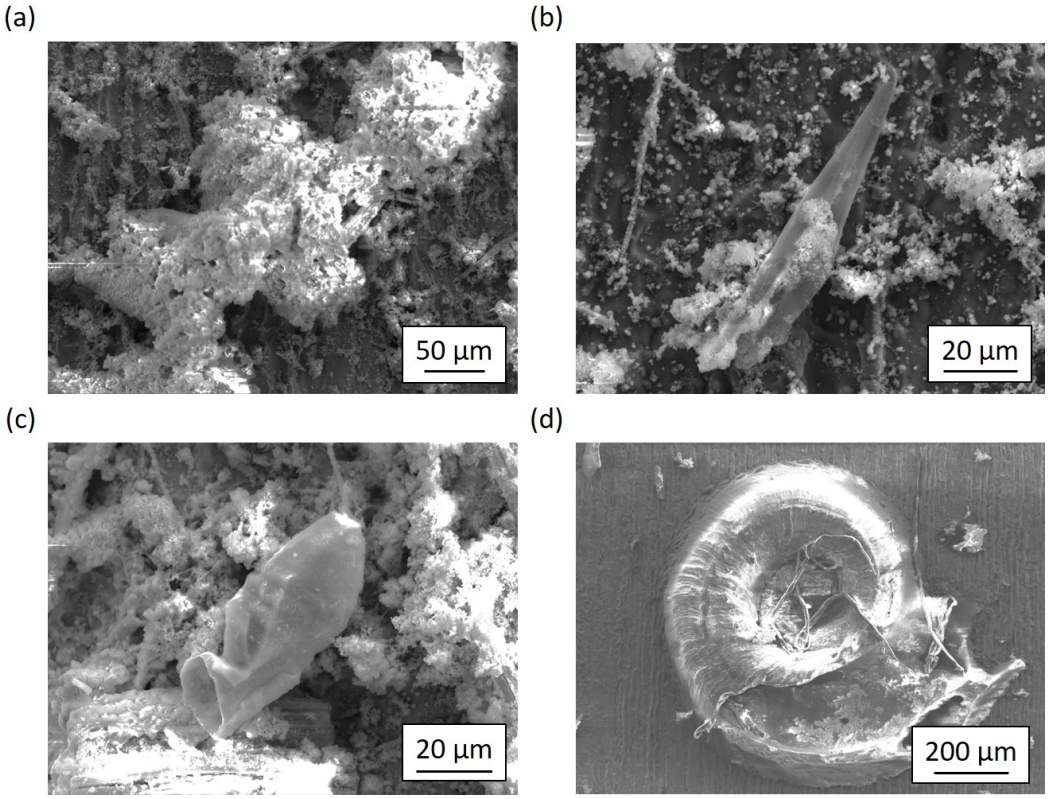

Figure 5.20: SEM observations of (a) the brown biofilm, (b) the tubeworms, (c) and (d) two types of shells.

depending on the coupon, but there does not seem to be a very strong trend depending on the coupon type. For microalgae, counted on Malassez cells, the average concentrations vary between 2.0E+04 and 1.0E+05 $microalgae/cm^2$.

Table 5.5: Summary of the microbiological analyses.

Thermal treatment	Total biomass ($10^6 microorganisms/cm^2$)	Total microalgal biomass ($10^4 CFU/cm^2$)	Total aerobic heterothrophic ($10^3 microalgae/cm^2$)
S	19 ± 3.33	2.50 ± 0.73	2.00 ± 0.2
AB	23 ± 3.33	3.27 ± 1.96	2.90 ± 0.6
P700	29.3 ± 2.22	6.1 ± 2.07	3.27 ± 1.36
HT1000	39.7 ± 11.8	10.8 ± 4.89	4.73 ± 1.69
P700 + HT1000	30.3 ± 8.44	10.5 ± 6.98	3.77 ± 1.24
LMD	4 ± 4.67	13.7 ± 3.56	2.60 ± 0.67

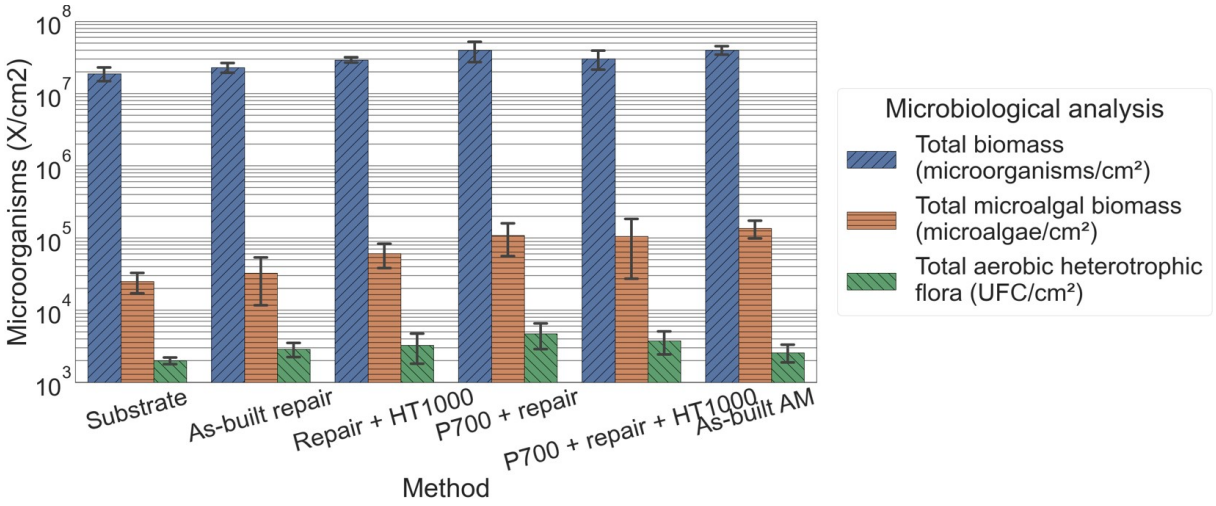

Figure 5.21: Results of the analysis of the microorganisms present on the surfaces of the samples after three months of immersion.

The coupons with the lowest average concentration of microalgae are the substrate and the as-built repair coupons. Those with the highest average concentration are the coupons from the LMD printed deposit. There appears to be a very slight tendency for the coupons from the repairs with thermal treatments (preheating, heat treatment and both) and the LMD-printed deposit alone to have a higher concentration.

This trend can be partially explained by the microstructure of the specimens. In fact, the literature shows that weld beads are more susceptible to the formation of microorganism colonies than the base metal because of their particular microstructure, which consists of a dentritic substructure [195, 196]. The latter leaves a large number of grain sub-joints to which bacteria can adhere and cause MIC in the long term. This could potentially explain why LMD-printed samples alone have the highest rate of microorganisms because they are 100% grain substructure with a very high rate of grain boundaries and cell boundaries. This could also explain why the repairs have a higher rate of microorganisms than the substrate alone, since part of the sample is composed of the LMD-printed deposit.

However, as seen in the Section 5.3.3, the repair with 700°C preheating has fewer cell boundaries because the cells are larger in size as seen in Figure 5.9. Therefore, these samples should have fewer microorganisms than an as-built repair. However, their density ratio is lower. Therefore, microorganisms have an easier time colonizing the spherical porosities created by the vaporization of the low melting elements.

Similarly, the microstructure of the post-heat-treated repairs recrystallized. The grain size of the substrate increased significantly and the cellular substructures partially dissolved into the grains of the deposit, considerably reducing the number of grain boundaries

and thus the site for bacterial adhesion. Javed *et al.* [197] also observed a decrease in the number of micro-colony sites on heat-treated 1010 steel samples compared to an as-received sample. Recrystallization reduced the number of grain boundaries and thus the number of sites suitable for microbial colonization. These samples should also have a lower rate of microorganisms than an as-received repair.

Therefore, our results are not in agreement with those reported in the literature. The position of the samples in the analysis tank is another hypothesis that could explain this difference. In fact, as observed in Figure 2.14 in Chapter 2. The samples of series 3, 4, 5 and 6 are located closer to the water inlet of the tank and in the flow of the water. As a result, the surfaces of these samples would capture a much larger number of microorganisms than the samples in series 1 and 2. This hypothesis is difficult to verify, but could explain this difference.

All of these explanations remain hypothetical at this time due to lack of analysis and would require more detailed analysis to confirm. OM and SEM observations of the cross sections of the specimens, the corroded areas and the immersed surfaces would allow to determine the exact location of the damage and perhaps the reason for the initiation of the crevice corrosion, as well as the state of microorganism formation in the different areas of the repair, such as the equiaxed grains of the substrate or the cellular substructure of the deposit. Similarly, analyses of the thickness of the passivating oxide layer on the different areas of the repair would allow the influence of microstructure and heat treatments on the corrosion resistance of the repair to be known.

5.4 Summary

In this chapter, several thermal treatments have been coupled to the LMD repair process with the objective of achieving a high density of deposition and a strong metallurgical bonding between the substrate and the deposit, as well as the imperceptibility of the repair in terms of microstructure, mechanical properties, and corrosion resistance. The objective is to obtain a repair that is as homogeneous as possible, so that the repaired part has properties that are close to those of the original part. As already highlighted in Chapter 4, the as-built repair has a high density rate (99.96% compared to the 99.87% of the reference substrate), but a heterogeneous microstructure consisting of fine and equiaxed grains in the substrate and coarse and columnar grains in the LMD-printed deposit, with a cellular substructure. The microhardness of the deposit of 170 HV and the substrate are similar 167 HV, but an increase in microhardness is observed in the HAZ and the MZ with a peak at 185 HV, caused respectively by the increase of the ferrite

phase rate (2% compared to the 1% of the substrate) and smaller grains in this area than the rest of the deposit.

This chapter was focused on the influence of the repair method with the application of different thermal treatments (*i.e.* substrate preheating, interlayer cooling factor and post heat treatment) on the final repair quality. The density, microstructure, microhardness and corrosion resistance of SS316L parts repaired by the LMD process was investigated. This work was carried out on the OPTOMEC LENS MTS-500 machine using the same deposition parameters determined in the Section 3.2.1 and the deposition pattern with the adaptation of the overlapping rate at each layer developed in Section 3.4.3.

The substrate preheating causes a widening of the melt pool and a decrease in the density rate of the sample from 99.87% for the as-built repair to an average 99.79% for the preheated substrate, due to the formation of gas bubbles trapped in the metal matrix. It does not strongly change the grain size or morphology, but increases the size of the cellular substructure of the deposit, from 3.6 µm to 5.8 µm for P500 and P900 respectively, due to a lower cooling rate, which decreases the microhardness of the deposit. The microhardness peak at the interface decreases until it disappears with the increase of the preheating temperature due to increase of the cellular substructure and maybe the relaxation of the residual stresses.

The interlayer cooling factor decreases the density of the repairs from 99.87% for the as-built repair to an average 99.78% for the cooled specimens, due to the formation of intergranular cracks caused by a ductility-dip cracking phenomenon. It has no effect on the morphology and size of the microstructure, except for a decrease in the cellular substructure, from 3 µm to 2.1 µm for CF1 and CF6 respectively, which leads to an increase in the microhardness of the deposit from 172 HV to 197 HV. At the interface, increasing the cooling rate decrease the cell size in the MZ and probably introduces higher residual stresses in the HAZ resulting in an increase of the microhardness up to 220 HV.

The density of repairs with post heat treatment (average of 99.93%) is not affected by the thermal treatment and is similar to the as-built repair. Heat treatment at 600°C for one hour has no impact on the characteristic of the repair compared to the as-built repair. On the other hand, the high temperature post heat treatments generate a recrystallization of the substrate and the deposit, with an increase of the grains (increase of 138.8% at 1200°C and 98.8% at 1000°C compared to the as-built repair) and a dissolution of the cellular substructure respectively. This generates a decrease of the microhardness of both areas up to about 145 HV average in the whole repair for the heat treatment at 1200°C. The microhardness peak at the interface is removed by the dissolution of the ferrite phase and surely the residual stress relaxation.

The substrate preheating homogenizes the microhardness without eliminating the deposit/substrate microstructural heterogeneity, which can cause problems during deformation tests. The interlayer cooling factor increases the residual stresses in the repair excessively without significantly changing the microstructure, except for the refinement of cellular substructure. High temperature post heat treatments homogenize the microstructure and microhardness of the repairs, with only 7 HV of difference between the substrate, interface and deposit, compared to the 27 HV for the as-built repair. This type of treatment can be used to homogenize the microstructural and mechanical properties of the SS316L parts repaired using LMD, and aimed at the specification criteria for high density and imperceptibility of the repaired area in terms of microstructure and microhardness. On the other hand, induction substrate preheating can be used as a complementary method when post heat treatment cannot be used. In fact, even if the microstructure of the repair is still heterogeneous and the deposit less dense, the microhardness peak at the interface and the ferrite increase in the HAZ can be eliminated with this technique to aim for the imperceptibility of the repair intrinsic characteristics.

For the corrosion behavior in seawater, the free corrosion potential is unaffected by the thermal treatments applied to the repairs when immersed in natural seawater for 3 months. The reference and different repaired specimens exhibit the same passivation behavior for the duration of the tests. However, some samples exhibit crevice corrosion under the protective resin of the electrical measurement wiring with the corrosion of two samples on three per family except for the LMD-printed deposit. This appears to be related to the montage rather than the different repair methods used. The substrate is more susceptible to crevice corrosion than the LMD-printed deposit because of a lower PREN (24.02 compared to 28.26), due to a lower chemical composition of Cr and Mo. On the other hand, the use of thermal treatments tends to slightly increase the level of microorganisms present on the surface of the specimens, increasing the risk of MIC. The observations revealed that for the duration of the immersion, the different types of repairs did not show any improvement or deterioration in behavior compared to the reference substrate, which indicates promising results for the use of SS316L parts repaired in natural seawater.

This chapter has shown that the addition of thermal treatment to the repair process can approach the imperceptibility of the repair in terms of microstructure and microhardness, while maintaining a high density of repairs with metallurgical bonding with the substrate. However, thermal treatments cannot be applied to all parts to be repaired due to their size or sensitivity to temperature changes. Other methods must be highlighted to achieve the imperceptibility of the repair and meet the last elements of the specifications, which are the return to the original part dimensions and not to modify the structure of the original part.

Chapter 6

Investigation of the additive/subtractive hybrid manufacturing for the repair process

Abstract

This chapter presents the results on the hybridization of the repair process using an ASHM machine. All this part of the work was performed in the Nanyang Technological University in Singapore in the frame of the joint PhD. The time savings and technical issues of this process were investigated. An examination of the quality of repairs using a alternated repair technique between machining and material deposition was performed and compared to a conventional method.

Submitted paper associated to this chapter: T. Cailloux, W. Pacquentin, S. Narasimalu, D. Ho Wee Kiat, Y. Zhen Lek, F. Schuster, H. Maskrot, K. Zhou, F. Balbaud-Celerier, "Contribution of additive/subtractive hybrid manufacturing for the laser metal deposition repair of stainless steel 316L parts" submitted to *Journal of Materials Processing Technologies*, 2023

Contents

6.1 Introduction

In the last chapter, methods were developed to achieve imperceptibility of the repair using thermal treatments. However, not all parts can be heat treated and these treatments tend to modify the structure of the original part with a change in the microstructure of the substrate in the case of post heat treatment. Other methods must therefore be developed to achieve this imperceptibility while maintaining a high deposition density and metallurgical continuity with the substrate, but also ensuring a return to the original dimensions without modifying the structure of the initial part. A promising solution could be the use of the ASHM process, which has been gaining interest in recent years.

ASHM is a technique that allows the use of AM and SM in a single workstation. It allows parts to be manufactured using additive processes and surface finished using milling within the same manufacturing chamber. As a result, the printed part is immediately available with the correct surface roughness, unlike parts produced on additive-only machines, where the roughness is still high due to the nature of the process. This advantage is even more interesting for the repair of parts. Indeed, finishing is important to reduce surface roughness, but more importantly to restore the part to its original dimensions. In addition, as seen in the previous chapters, pre-machining is necessary to remove the damage defect and surface contaminants, but also to provide good access to the spray nozzle in order to obtain a dense repair.

The use of a hybrid process to produce new parts has shown significant time savings, in the order of 68% for producing a hexagon by alternating the additive and subtractive phases [126]. To date, the gain of the hybrid process for repair has not been quantified in the literature. Testing different repair method combinations would allow to quantify the different times needed for the process and highlight the fastest repair method.

The literature is mainly interested in the implementation of the different components of the ASHM process in the production of parts. However, the material quality resulting from the hybrid process is the subject of few studies. Some authors have demonstrated that by alternating the additive and subtractive steps in the manufacturing process, there is a homogenization of the mechanical properties [127] and a reduction of the residual stresses [128] within the parts, conserving a high density of material deposition and metallurgical bonding between the layers. These preliminary results on the use of the hybrid process for the production of parts are of great interest in order to obtain dense repairs with homogeneous properties and thus to avoid the heterogeneity of repairs, as presented in the last chapters.

This chapter focuses on the repair of SS316L substrates using different combinations

of repair methods in an ASHM machine. Repairs are performed with material deposition in one step or alternatively with a machining process or subsequent heat treatment to observe the advantages that ASHM can offer on the quality of the parts and the repair process. The influence of each repair method combinations on the repair time and the quality of the repaired parts is investigated.

6.2 Experimental protocol

6.2.1 Application of the hybrid process in the repair process

Repair process

Figure 6.1 illustrates the approach used in this study to investigate the effect of the ASHM process on the global repair process and the quality of the repaired parts. The DMG Mori LaserTec 65 3D machine was used in this study. It allowed the realization of several steps of the repair process in a single workstation, namely the pre-machining, material deposition by LMD and post-machining finishing steps. For some repairs, a 1 hour post-heat treatment could be applied using an air oven to homogenize the microstructure of the parts, as demonstrated in Chapter 5.

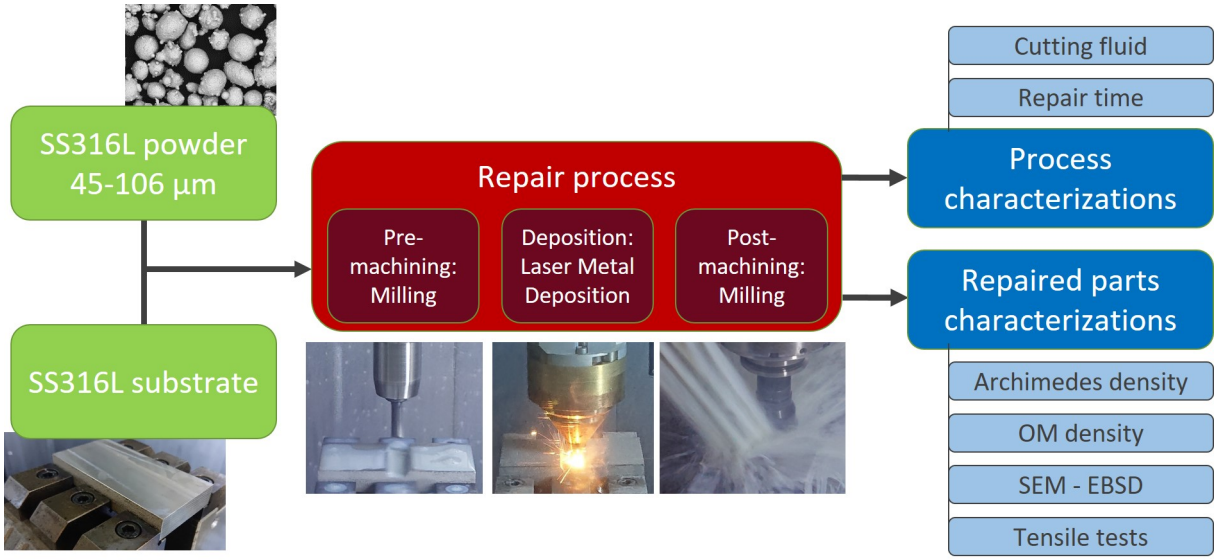

Figure 6.1: Flow chart of the hybrid study methodology.

Different combinations of these steps (pre-machining, material deposition, post machining finishing and post heat treatment) were evaluated and characterized in terms of density rate, microstructure and mechanical properties. The density rate was determined

by Archimedes measurement. Metallographic observations were performed by OM and microstructure was characterized by SEM and EBSD analysis. A global evaluation of the repair time using different processes was performed.

Pre-machining

As mentioned in the previous chapters, pre-machining is an essential step in the repair process, allowing the defect and surface contaminants to be removed and, most importantly, providing good access to the projection nozzle. In Chapter 4, several shapes were optimized and repaired. The 120° groove was chosen as the pre-machining shape to be used in this hybrid repair study for the repeatability.

To pre-machine the groove in the SS316L substrates, an 8 mm diameter milling cutter was used that fits on the machine tool holder. The dimensions of the tool are built into the machine to know its exact position. After measuring the dimensions of the substrate, six steps were required to machine the groove. The machining process is detailed in Figure 6.2 and includes the following steps: rough machining of the straight groove, rough machining of the left edge, rough machining of the right edge, finish machining of the bottom of the groove, finish machining of the left edge, and finish machining of the right edge.

The machining parameters are set at a feed rate of 1000 mm/min and a tool speed of 3500 rpm. The plunge increment into the material is 0.25 mm per pass.

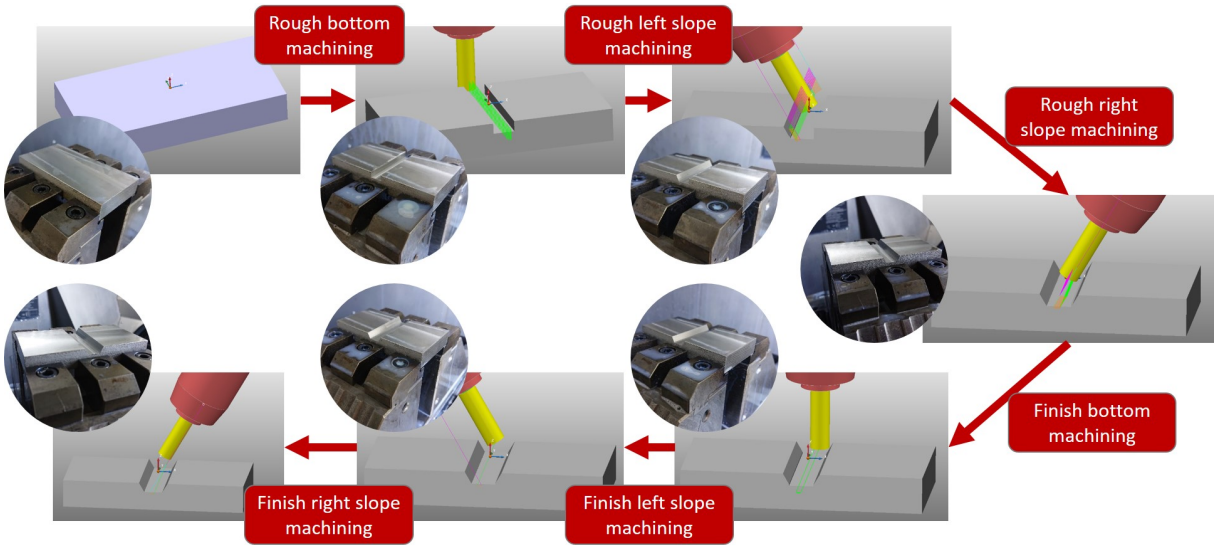

Figure 6.2: Different pre-machining steps required to achieve the 120°-groove.

Material deposition

As presented in Chapter 3, the optimized deposition parameters were determined for the DMG Mori machine and are summarized as follows: P = 1500 W, V = 1000 mm/min, Q = 9.6 g/min, OR = 40%. The 90°-Zigzag deposition pattern was used with adjustment of the overlapping rate between the beads in each layer. It should be noted that the configuration of the additive module of the DMG Mori machine is different from that of the OPTOMEC machine, with a laser beam diameter at the focus point of 3 mm instead of 1.2 mm. The beads deposited have a height and width of 500 µm and 2500 µm respectively. Therefore, with the same height than on the OPTOMEC machine, the beads are 108% wider. However, this does not change the generation of the G-code files, where the Python program adapts to the new bead geometry and the new deposition parameters.

The projection nozzle is attached to the tool holder after the milling cutter is placed in the magazine. These tool change steps are performed automatically by the machine.

Post-machining

The post-machining step allowed the original dimensions of the substrate to be restored by removing the excess material deposited in the groove. To perform this step, the same 8 mm diameter cutter was used to make three passes along the deposit as shown in Figure 6.3. This pass starts at 2 mm above the substrate top surface recorded and then goes down with a step of 0.25 mm to avoid any violent collision between the part and the tool. The machining parameters are set at a feed rate of 1000 mm/min and a tool speed of 3500 rpm.

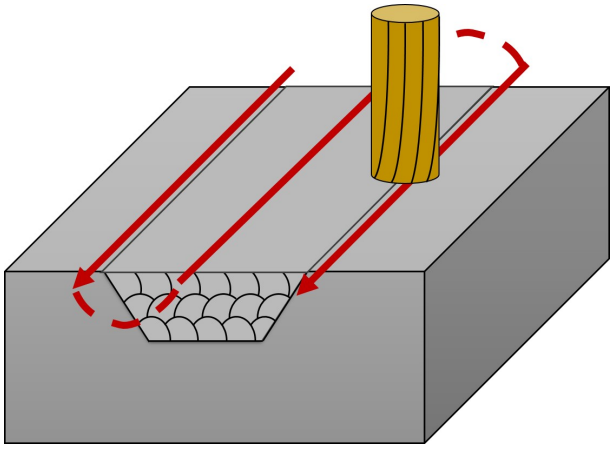

Figure 6.3: Tool path of the milling cutter for the finishing machining.

6.2.2 Design of experiments

The DOE developed in this study aims to observe the influence of different repair methods using an ASHM process on the repair time and the properties of the repaired parts in comparison to an unrepaired reference substrate.

Four repair methods were performed, which are detailed in Figure 6.4.

- The first method, labeled (PSM)+(AM)+(FSM), consisted of performing the pre-machining, material deposition, and post-machining steps separately. The pre-machining was performed by a machinist in France (Maigrot company). The material deposition and post machining steps are performed in the DMG Mori, but simulating the loading and unloading of the parts as if a change of machine (from additive to subtractive) was performed between each step;

- A second method, called (PSM+AM+FSM), focused on performing all three steps at once on a single workstation;

- A third technique, called alternated process, consisted of performing all steps in one machine, but alternating the material deposition and machining steps. After the deposition of a layer, the 8 mm cutter machine 30% of the last deposited layer in order to observe a possible modification of the microstructure due to the passage of the machining cutter. It is called (PSM+I(AM+SM)+FSM);

- Finally, the last repair method is similar to the second one, but a post heat treatment at 1100°C for 1h in an air furnace was performed to recrystallize the microstructure of the repaired parts. It is called (PSM+AM+FSM)+(PHT).

To understand the meaning of the repair methods, the parentheses indicate all the steps performed in the same workstation and the acronyms are detailed below:

- PSM: Pre-Subtractive Manufacturing;

- AM: Additive Manufacturing;

- FSM: Finishing Subtractive Manufacturing;

- I(AM+SM): Intermediate Additive Manufacturing and Subtractive Manufacturing;

- PHT: Post-Heat treatment.

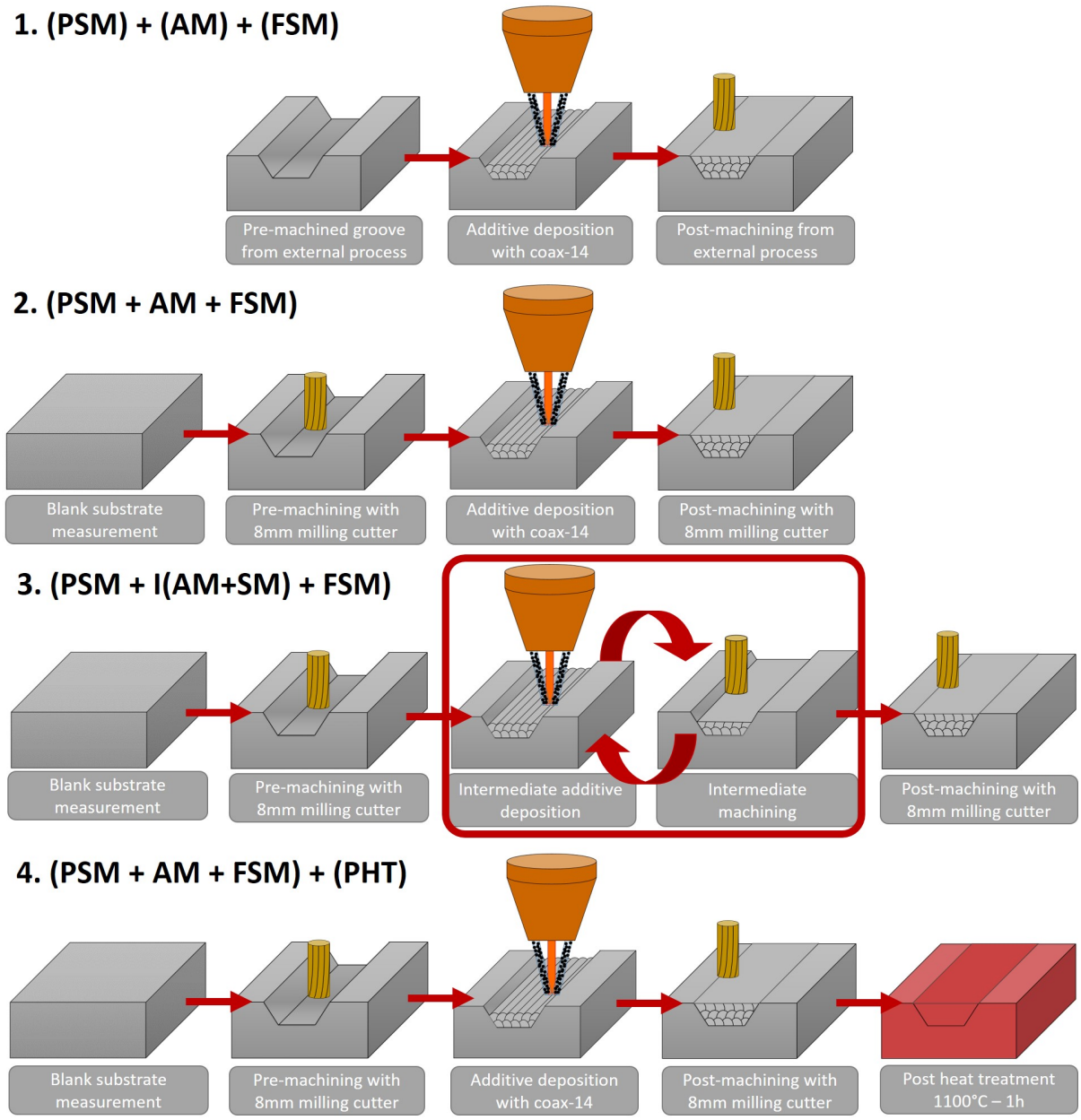

Figure 6.4: Design of experiment developed for the hybrid repair study.

6.3 Technical issues caused by the hybridization of the repair process

6.3.1 Cutting fluids in the manufacturing chamber

During the machining operations, it is essential to use cutting fluids composed of a water/oil mixture between 5% and 10% concentration, which lubricate and cool the tool

and the part during the cutting of the metal scrap. These cutting fluids are generously sprayed into the machining area to ensure that the area is adequately lubricated, as seen in Figure 6.5 (a).

When the machining operation is complete, the machining chamber is filled with the cutting fluids, which cover the walls, the support and the part being repaired, as shown in Figure 6.5 (b). If the cutting fluids are not cleaned, they will have a significant influence on the quality of the manufactured parts, as demonstrated by Cortina *et al.* [198] by performing material deposition on different concentrations of water/oil mixtures. On the one hand, the energy provided by the laser causes water evaporation and creates porosity in the deposit, with the risk of damage to the optical system due to the water vapor [123]. On the other hand, the unmelted powder can agglomerate with the water to form a thick layer. This agglomerate will add to the powder delivered by the coaxial nozzle and cause overbuilding of the beads with little dilution in the substrate [198].

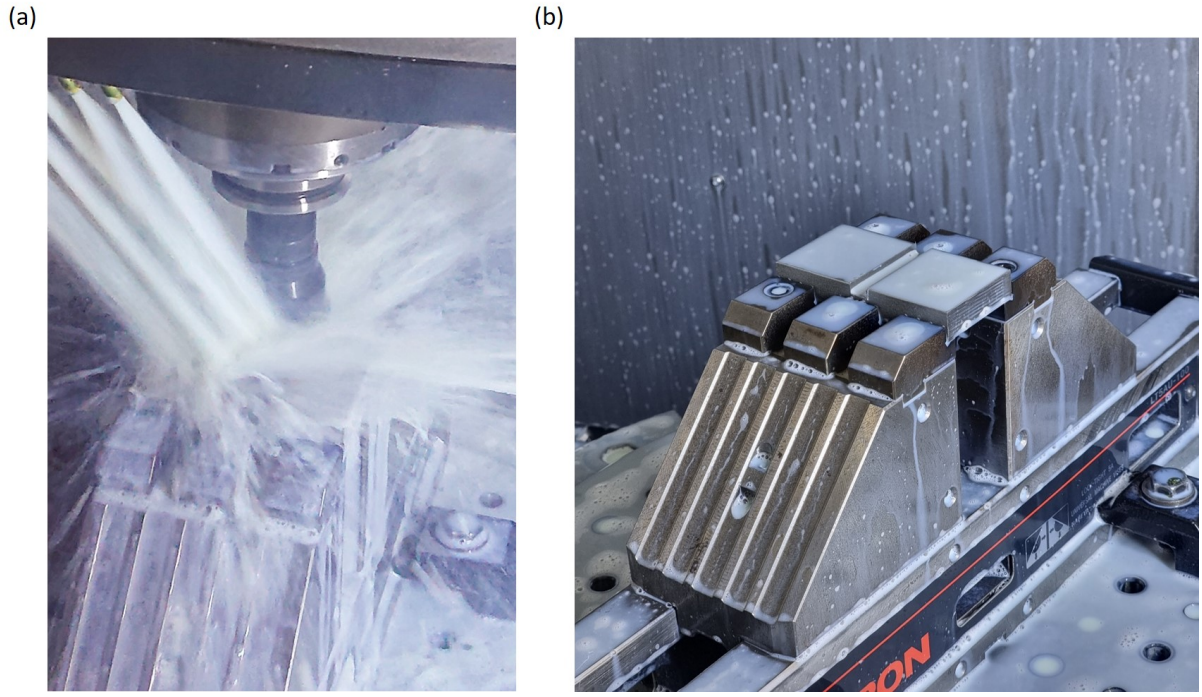

Figure 6.5: (a) Cutting fluid projection during milling operation and (b) cutting fluid residue in the manufacturing chamber after milling.

Therefore, to avoid introducing porosity into the material and damaging the machine, it is necessary to clean the surface after machining. Some authors have studied different ways of cleaning the substrates with the available equipment. Cortina *et al.* [198] eliminated the problem of porosity formation due to cutting fluids by obtaining dense deposits on surfaces cleaned with compressed air or by passing the defocused laser at low power to

evaporate the water. Similarly, Yan *et al.* [199] demonstrated that using the low-power laser on substrates contaminated with water or oil solutions, coupled with compressed air blowing, resulted in dense deposits and did not affect the mechanical properties of the parts in tensile tests. In contrast, the uncleaned deposit had a high density of inclusions and cracks.

To prevent water evaporation from damaging the optics, the laser was not used to clean the surface of the parts being repaired in this study. The surfaces were cleaned with compressed air to remove excess water, then degreased with 99% ethanol. Finally, a final pass of compressed air removed any remaining residue from the surface of the samples.

Even though the part being repaired is free of cutting fluids, the rest of the chamber is still filled with them. This increases the moisture content in the machining chamber as the machining steps are performed. However, Kannan *et al.* [129] have studied the effect of humidity on the quality of deposits in a machining chamber. They showed that the humidity of the atmosphere had a negligible effect on the density of the parts and their mechanical properties. This issue is not studied in this study.

6.3.2 Repair time with various configurations

Repair time is an important factor when repairing damaged components. It determines whether it is economically viable to repair or replace the part. In fact, in addition to the material and energy required, the repair time represents machine and operator time, which are part of the cost of repairing the part. The literature indicates the interest of the ASHM process within the same workstation to reduce manufacturing time [200, 201, 202]. Feldhausen *et al.* [126] report a 68% reduction for a hexagon produced with a hybrid process compared to a distinct additive and subtractive processes. However, no quantification was performed for repair of components.

For each repair method detailed in the DOE, each step presented in Table 6.1 was timed. This allowed quantification and determination of the fastest and therefore least costly method. The results of this analysis are presented in Figure 6.6.

The results show that compared to using separate machines as in (PSM)+(AM)+(FSM), performing the pre-machining, material addition and post-machining steps in a single workstation as in the (PSM+AM+FSM) method reduces the repair time. In fact, the time required to install the part on the support, to move it between machines and to calibrate it is reduced. For the rest, the machining and material deposition times are the same. In the case of the study using the hybrid process compared to separate machines, the time saving is approximately 31%.

Table 6.1: Details of each step measured during the repair process.

Category	Task	Time (PSM)+(AM) +(FSM) (s)	(PSM+AM +FSM) (s)	(PSM+I(AM +SM)+FSM) (s)	(PSM+AM) +FSM)+(PHT) (s)
Substrate initiation	Substrate cleaning with ethanol	102	34	34	34
	Substrate placement on support	48	16	16	16
	Tightening grip	138	46	46	46
	Machine changeover	240	0	0	0
OFFSET setup	Probe loading	57	19	19	19
	X faces middle measurement	273	91	91	91
	Y faces middle measurement	192	64	64	64
	Z face top measurement	117	39	39	39
	Probe unloading	57	19	19	19
Pre-machining	8 mm milling cutter loading	21	21	21	21
	Subtractive program running	644	644	644	644
	8 mm milling cutter unloading	25	25	25	25
	Cutting fluid cleaning with ethanol	115	115	115	115
Adding material	Projection nozzle loading	50	50	550	50
	Additive program running	330	330	865	330
	Machine components cooling	50	50	550	50
	Projection nozzle unloading	45	45	495	45
Interlayer machining	8 mm milling cutter loading	0	0	170	0
	Subtractive program running	0	0	360	0
	8 mm milling cutter unloading	0	0	250	0
	Cutting fluid cleaning with ethanol	0	0	1150	0
Post-machining	8 mm milling cutter loading	17	17	17	17
	Subtractive program running	139	139	139	139
	8 mm milling cutter unloading	25	25	25	25
	Cutting fluid cleaning with ethanol	115	115	115	115
Part removall	Untightening grip	48	48	48	48
	Repaired part marking	50	50	50	50
Post heat treatment	Repaired part loading in furnace	0	0	0	60
	1 hr application	0	0	0	3600
	Air cooling	0	0	0	700

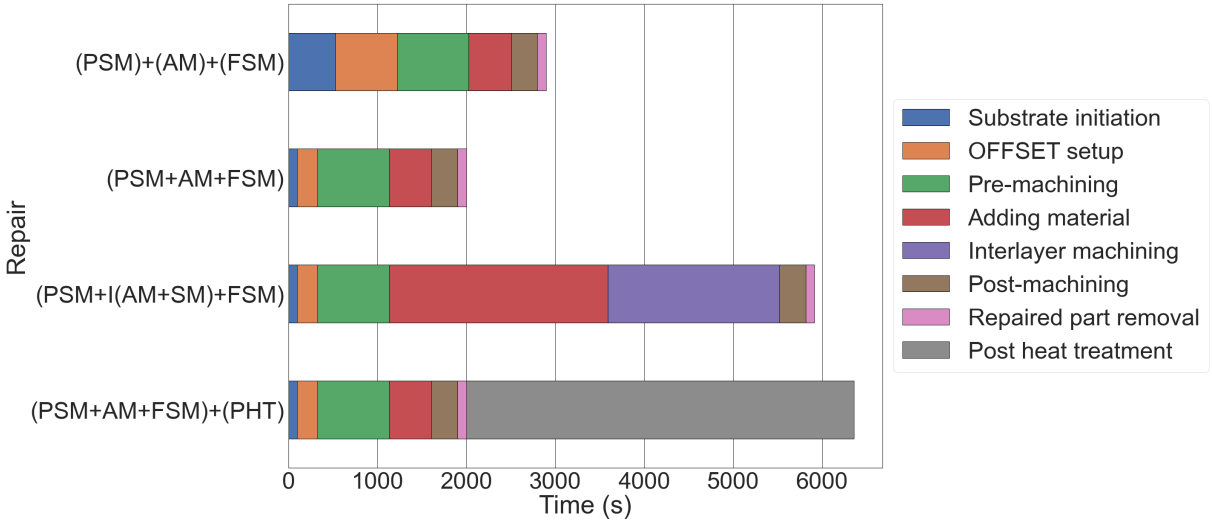

Figure 6.6: Repair time required depending of the method used.

With the alternated process (PSM+I(AM+SM)+FSM), the repair time of the part is significantly increased by alternating the material deposition and machining steps. Even when all steps are performed in one machine, there is a need for cleaning of the part with a blast gun and ethanol after each machining step. The increase in time is also caused by the change of the cutter and the spray nozzle, which use the same tool holder. Finally, there are the idle times to add to the global time where the initialization and program termination steps take place, and the travel times for the tool to reach its loading point at its working point.

The repair time for damaged parts is also significantly increased by applying heat treatment in the (PSM+AM+FSM)+(PHT) method. The time in the hybrid machine is not affected and is similar to the (PSM+AM+FSM) method. The reason for this increase is the realization of the heat treatment on the part with the time of loading in the oven, the time of application for 1h and the cooling in air. However, it should be noted that this additional time does not require the use of the hybrid machine.

6.4 Influence of the additive/subtractive hybrid manufacturing on the quality of the repair

6.4.1 Density

The density rate measurements using the Archimedes method are shown in Figure 6.7. The results show density rates ranging from 99.94% to 99.96% for the repaired samples regardless of the repair method used. The substrate has a density of 99.92%, which is lower than the density of the repairs themselves, but this variation is very small in view of the high density of all the samples.

The substrate has porosities, which are classic casting defects found in blooms. The porosities are spherical caused by gases trapped in the material. Excess gases in the liquid metal are released as bubbles, but some may remain trapped in the metal matrix [154]. These results indicate that the deposits produced by the LMD process are denser than the substrate itself. Thus, they increase the overall density of the part and the repairs appear denser than the substrate.

Figure 6.8 presents the specimens cross-sections observed using OM. No macroscopic porosity, cracks or lack of fusion are observed in the deposit or at the substrate/deposit interface. This indicates that if the LMD process is well optimized prior to the work, the different repair methods do not affect the density of the repaired parts.

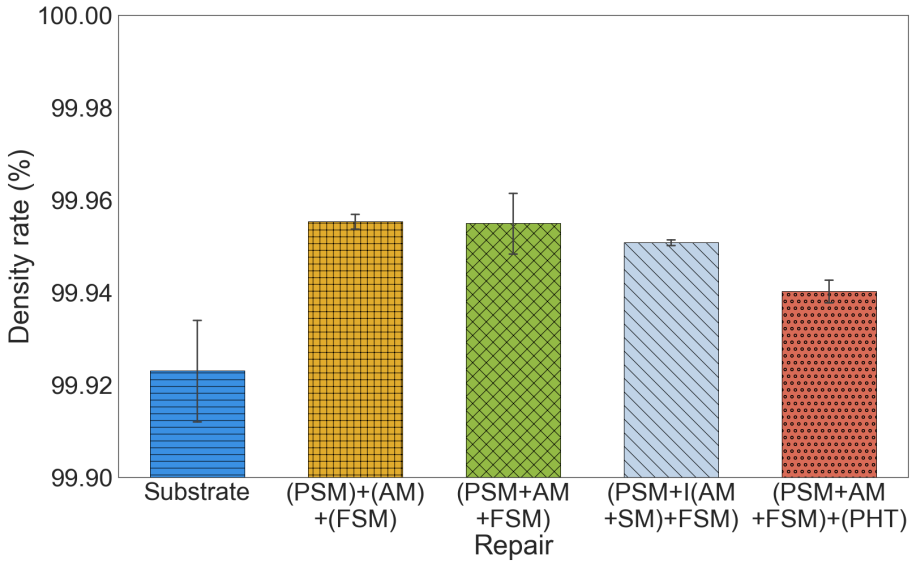

Figure 6.7: Density rate of the repaired parts.

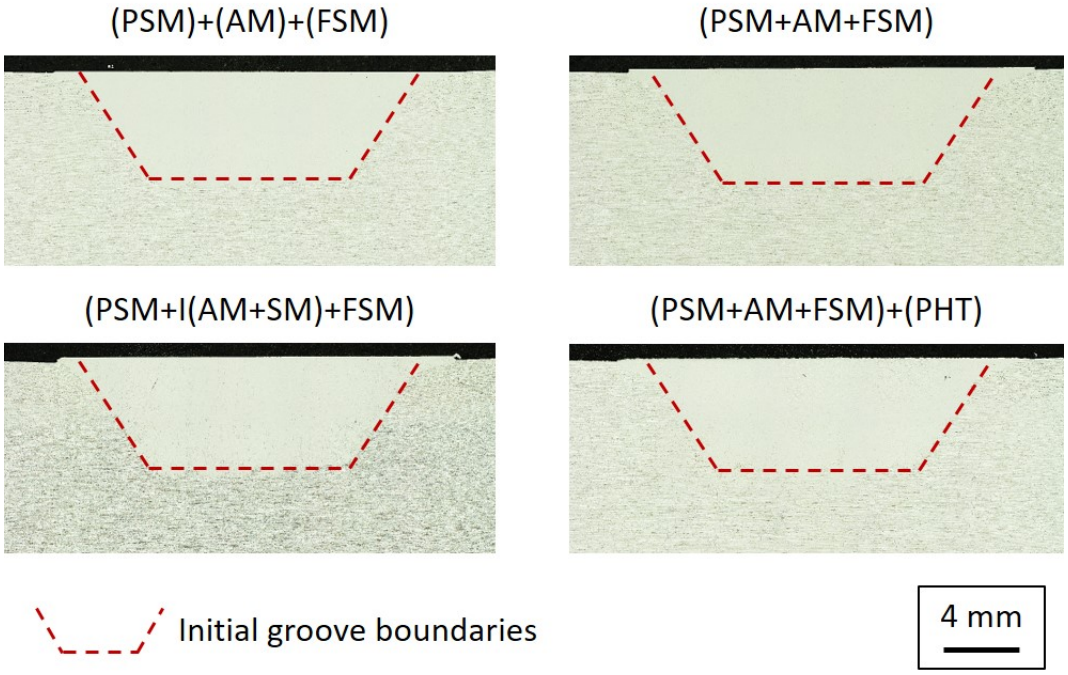

Figure 6.8: OM observations after mechanical polishing exhibiting the density of the repairs.

6.4.2 Microstructure

Morphology

After etching with a Kroll solution, the microstructure of the repairs is revealed. The OM observations presented in Figure 6.9 exhibit the heterogeneous microstructure present within the repairs. Only the heat treated repair deposit reveals a different microstructure. There is no macroscopic change in the microstructure for all other repair methods, using separate machines, using a single workstation, and using a hybrid technique. It can be noted that in the case of the sample (PSM+I(AM+SM)+FSM), 11 layers were necessary for the filling of the pre-machining, instead of 9 layers for the other repairs. In fact, the machining of 30% of the previous layer reduces the effective height of the layer and requires to increase the number of layers to be deposited globally to fill the pre-machining.

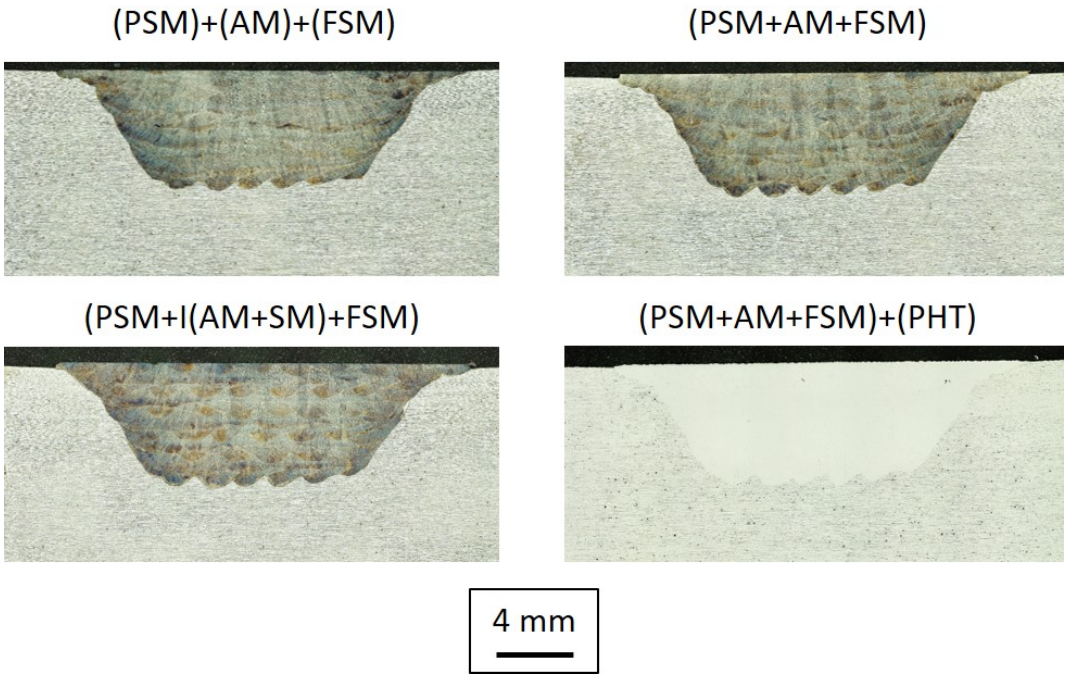

Figure 6.9: OM observations after chemical etching exhibiting the microstructure of the repairs.

The grain morphology is observed by SEM and shown in Figure 6.10. As observed in the Chapter 5, the substrate has fine, equiaxed grains typical of a traditional austenitic stainless steel. The deposit consists of coarse and columnar grains with a cellular substructure inside the grains. Finally, the interface is the area where the most important microstructure difference is concentrated in the repair with the junction between the deposit and the substrate.

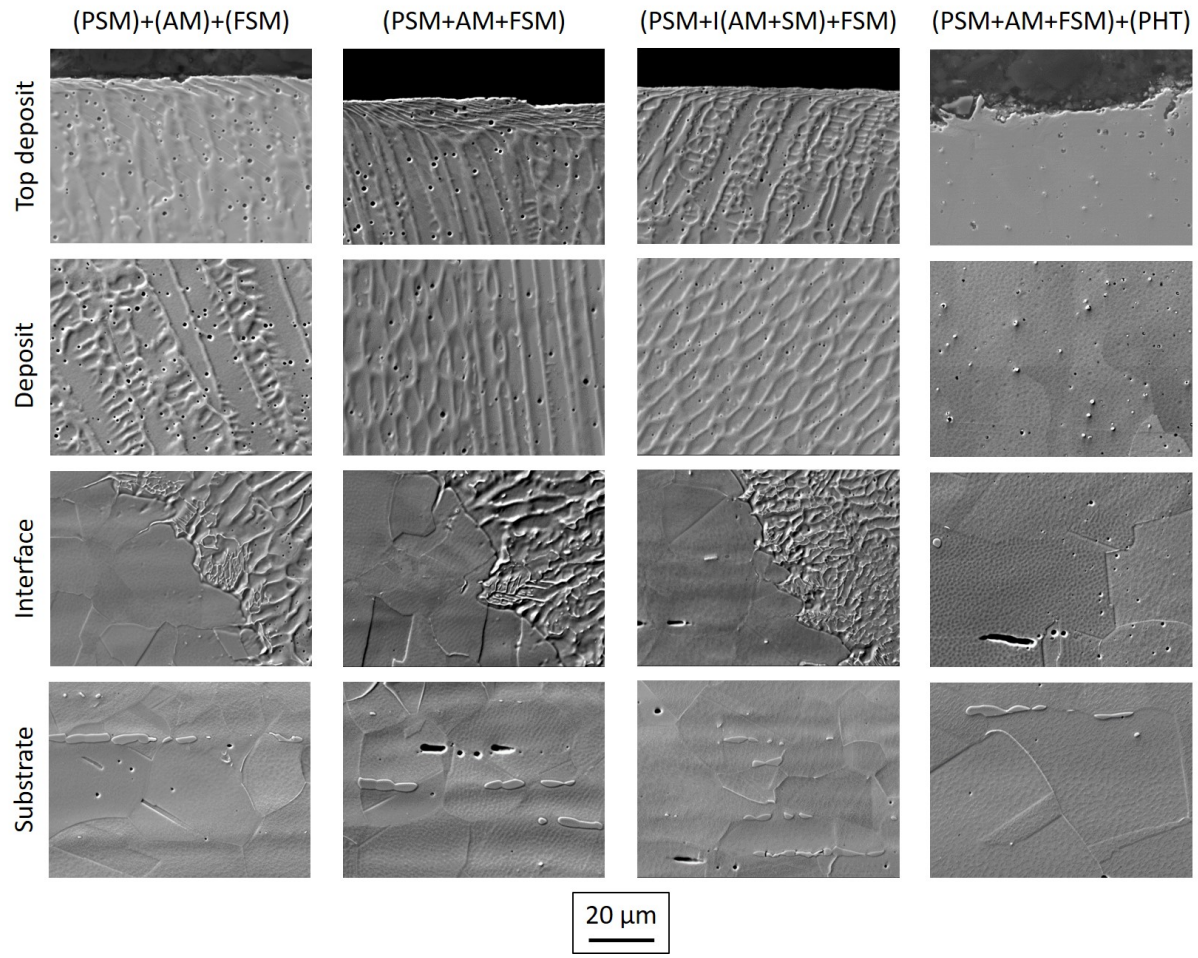

Figure 6.10: SEM observations of substrate, interface, deposit and top deposit areas for each repair method.

For the complete repair followed by high temperature heat treatment, the morphology changes as observed in Chapter 5. The grains of the substrate have grown. The cellular substructure of the deposit has dissolved into the grains, and in the case of this study, completely dissolved. Finally, heat treatment completely dissolved the interface with a grain growth detailed in the next Section.

The interesting area to observe corresponds to the upper part of the deposit. This area was machined after the deposition to remove the excess material and return to the original dimensions of the substrate. Like the rest of the deposit, this area shows a cellular substructure. However, over a thickness of approximately 20 µm in the direction of the tool, the cells have been plastically deformed by the passage of the cutting tool [203, 204]. The heat treated repair exhibits a higher roughness on the machined surface of the sample due to an oxide layer formation during the stay in the air oven.

It is also interesting to note that microporosities are present in the cells of the repair deposits. They are always present after heat treatment, probably due to the process parameters, and are often observed in the literature [205].

The morphology of the microstructure is not influenced by the different repair methods, alternated and additive only. However, the heat treatment homogenizes the overall microstructure of the specimen by recrystallization as already observed and described in the Chapter 5.

Grain and cell size

EBSD analyses were performed to study the size, aspect and orientation of the grains within the repairs. Magnified observations were made in main areas (*i.e.*, substrate, interface and deposit) and then global mapping was performed over the total height of the deposit.

The results of the magnified analysis are displayed in Figure 6.11. They show that the different repair techniques do not influence the grain size in a localized way. No difference in grain size, preferred orientation, or aspect ratio was observed for the first three repair methods. In contrast, as observed in Chapter 5, high-temperature heat treatment significantly increased the grain size of the substrate and interface without changing the morphology and grain size of the deposit.

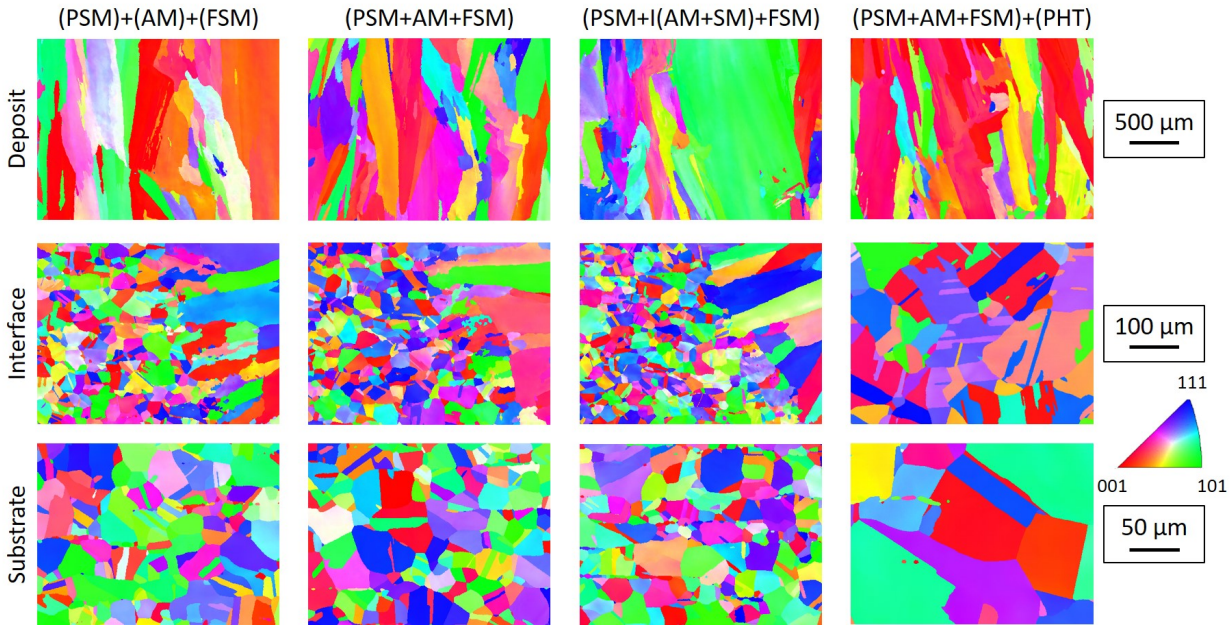

Figure 6.11: IPF maps of the EBSD analysis for each repair method in the deposit, interface and substrate.

A montage of EBSD observations over the entire height of the deposit at its center is shown in Figure 6.12. This type of analysis revealed the microstructure and its evolution throughout the part repair process for each method used in this study.

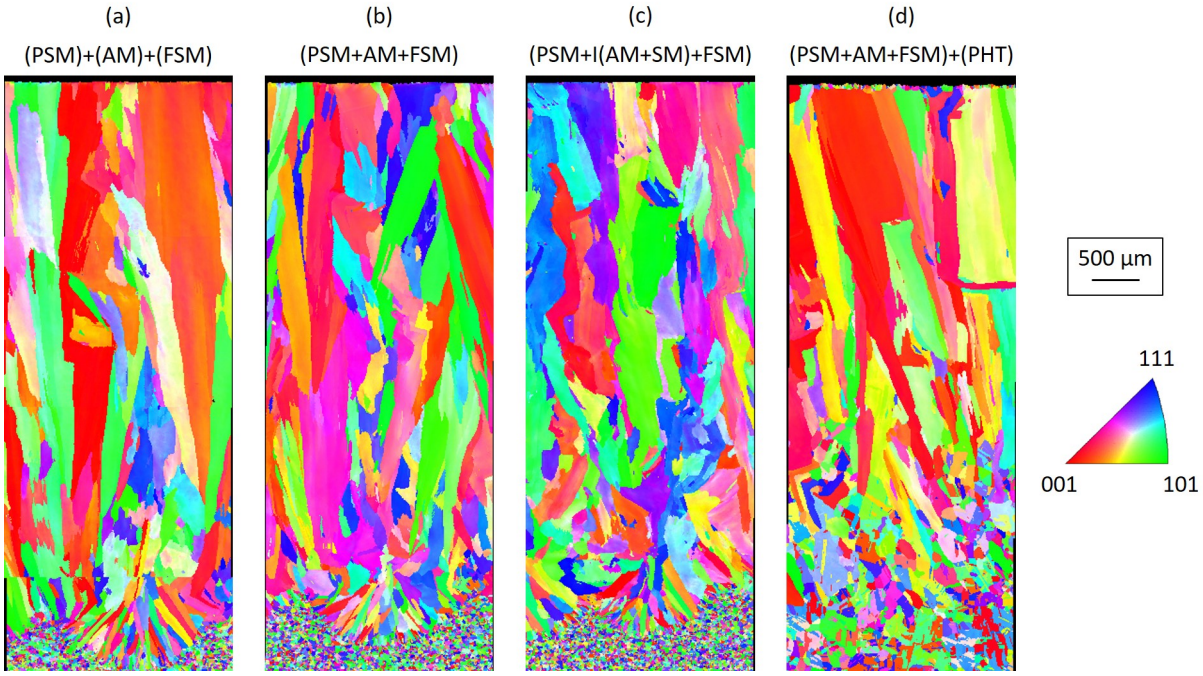

Figure 6.12: IPF maps of the EBSD analysis on the entire cross-section height for each repair method.

The microstructure of the repairs is not affected by performing the pre-machining, material deposition and post-machining steps in multiple steps in separate machines or all at once in the same workstation. In fact, the grains of the beads that are in contact with the substrate grow epitaxially from the grains of the substrate. They are columnar, but finer than the rest of the deposit. The epitaxial growth between the layers then forms coarse and columnar grains that are common to multiple deposited layers.

However, in the alternated technique, the fact that 30% of the previous layer is machined before the next layer is deposited leads to a change in the microstructure of the deposit. In fact, as observed in Figure 6.12 (PSM+I(AM+SM)+FSM), the grains have a less columnar and regular structure than in the cases (PSM)+(AM)+(FSM) and (PSM+AM+FSM). The grains appear to be broken in the process of their growth. This is in contrast to the other repair methods where the grains tend to become wider as they grow. The grains in the alternated process deposit remain columnar, but their width varies between narrow and wider phases and have this undulated shape. This phenomenon is caused by the machining that occurs between each layer, but is not reported in the literature.

In fact, the effect of interlayer machining on the microstructure of two-layer thick single bead walls has been studied by Sadeh *et al.* [206]. This preliminary work showed that the microstructure was affected by this machining pass. The authors suggest that the finer grains are caused by the cooling of the substrate between the two layers during the machining process. The machining pass effectively cools the part and can be compared to a cooling factor between layers. However, the results of the cooling factor repairs in Chapter 5 indicate that the grain size is not affected by this method of repair.

Therefore, another phenomenon is responsible for the microstructure modification in the alternated technique. Several hypotheses can be suggested. More layers are needed to fill the premachining area in the alternated process. Moreover, a deposition strategy with a 90° rotation between each layer is used. Thus, by changing the deposition direction more frequently, the preferential growth of grains is reduced. Another assumption concerns the strain hardening introduced by machining in the top near surface and observed in the work of Sadeh *et al.* [206] compared to a method without machining. When the bead is deposited after machining, grain solidification occurs in a work-hardened region. This forms smaller grains in the lower part of the bead, which widens in the building direction with the solidification of the melt pool. However, the subsequent machining will remove the larger grains at the top of the bead and introduce new residual stresses. The same situation occurs when the next layer is deposited. In contrast to a classical deposition without interlayer machining, the epitaxial growth in each layer takes place on finer grains, resulting in this particular microstructure like illustrated in Figure 6.13.

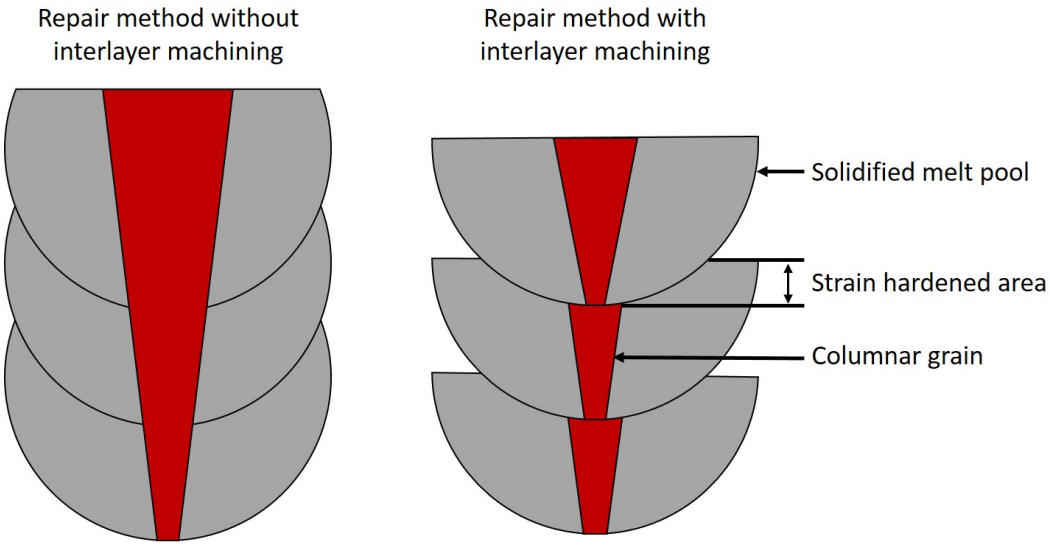

Figure 6.13: Illustration of the phenomenon generating the undulated columnar grains caused by the interlayer machining.

For the sample (PSM+AM+FSM)+(PHT), the first layers of the deposit are completely recrystallized and homogeneous with the substrate. A coarse and equiaxed microstructure is observed. On the other hand, the central and upper parts of the deposit are still coarse and columnar. However, the cellular sub-structure is dissolved as observed in Section 6.4.2. An interesting point is the formation of fine and equiaxed grains in the upper part of the deposit that has been machined. In fact, the plastic deformation caused by the tool causes a work hardening of this zone, which will recrystallize in the form of fine grains with the application of heat treatment to reduce the local residual stresses and dislocations density [207]. This phenomenon is observed in the recrystallization of SS316L plastically deformed by lamination [208] or laser shot peening [209].

Figure 6.14 exhibits the cell size of the grain substructure of the deposit. (PSM)+(AM)+(FSM) and (PSM+AM+FSM) have similar sizes, with a CAS of 8.8 µm and 10.1 µm respectively, while the cells of the alternated repair are smaller (5 µm) due to the cooling of the part with the cutting fluids at room temperature during each machining operation. The thermal history of this repaired part is similar to a repair with a high interlayer cooling factor, as studied in Chapter 5. In fact, as the part is cooled between each layer, the thermal gradient is higher and therefore the cooling rate is also higher, resulting in thinner dendrites as explained by Katayama *et al.* [174]. For the repair with heat treatment, the substructure is dissolved and no observation of its size is possible.

Note that the cell substructure size in this study is higher than in the previous chapters, despite similar GED between OPTOMEC ($54 J/mm^2$) and DMG Mori ($50 J/mm^2$) machines.

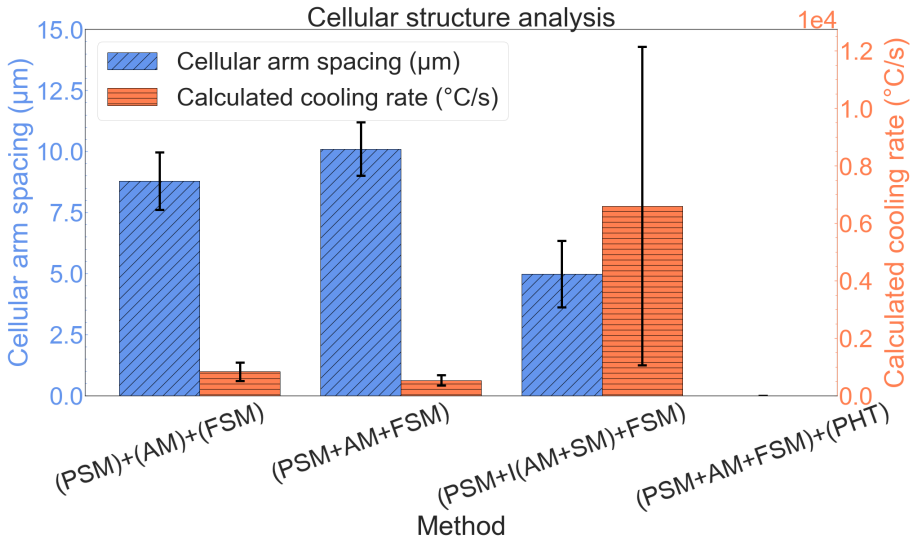

Figure 6.14: Cellular arm spacing measurement and calculated cooling rate of deposit cellular sub-structure.

6.4.3 Mechanical properties: Tensile tests

Tensile tests were performed to determine the mechanical properties of the parts repaired by the different methods. As illustrated in the Figure 2.12 (c), the deposit is located in the center of the specimen to know the mechanical behavior of the entire repair and to know if the interface between the deposit and the substrate is reliable. The mechanical properties were compared to an unrepaired reference substrate. Four tensile specimens were tested for each repair method.

Results of tensile tests are shown in Figure 6.15. Four groups of mechanical tensile behavior were identified among the five families tested. The first group is the unrepaired reference substrate in blue. The second group is the classical repairs made within several machines and within a single workstation (green and orange). Two samples appear to have lower EAB. This decrease is caused by porosities that have formed during the repair process due to a handling error. The third group consists of repairs performed by the hybrid method, alternating machining and material deposition. Finally, the last group (red) consists of repaired specimens heat treated at high temperature. All specimens show ductile cracking in the center of the tensile specimen, namely in the middle of the deposit.

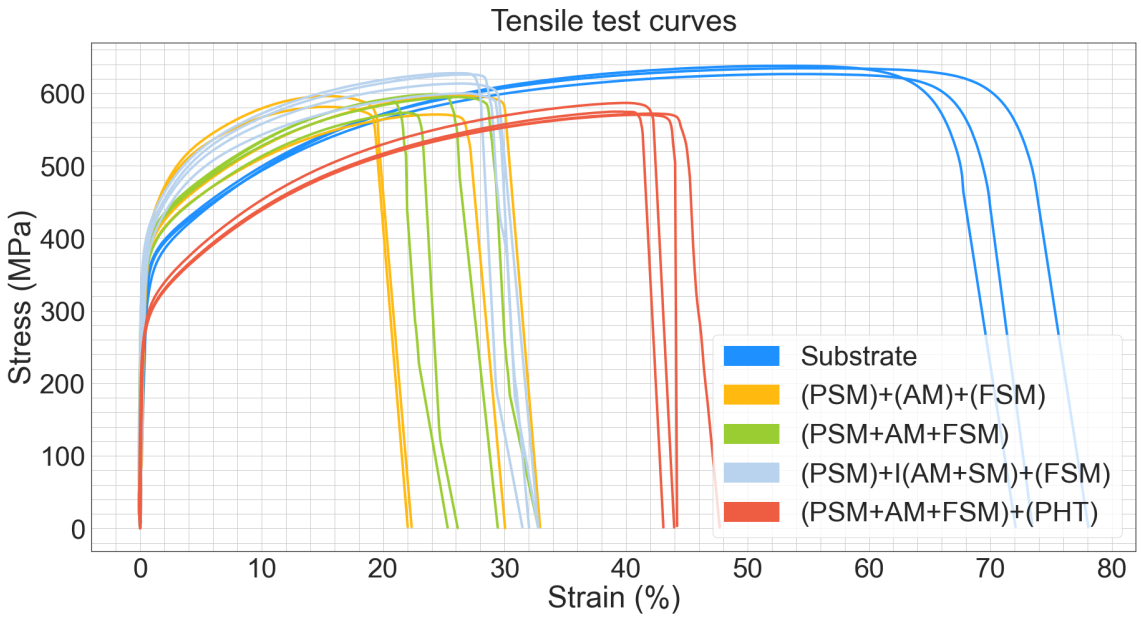

Figure 6.15: Tensile test curves for each repaired specimens.

Figure 6.16 and Table 6.2 summarizes the main values of the tensile tests. In fact, the substrate shows relatively high UTS, YS, and EAB for SS316L, but is in accordance with the RCC-M standard [9], which requires a minimum UTS, YS and EAB at 20°C of 490 MPa, 175 MPa and 45% respectively.

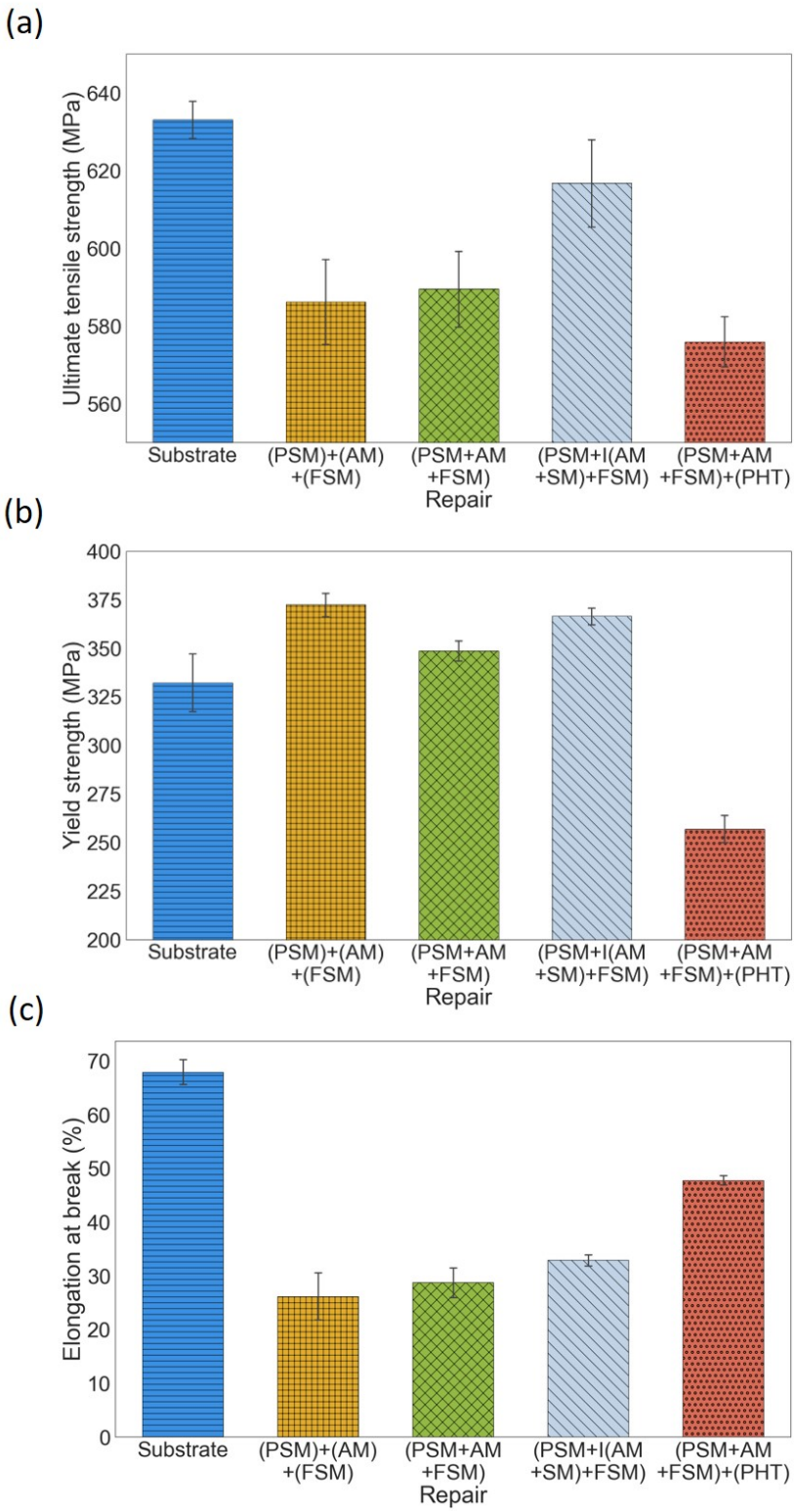

Figure 6.16: Main values of the tensile tests with (a) UTS, (b) YS and (c) EAB.

Table 6.2: Summary of the tensile test values of the repaired parts compared to the reference substrate and LMD-printed deposit.

	UTS (MPa)	YS (MPa)	EAB (%)	Ref
Substrate	632 ± 6	332 ± 18	67.9 ± 2.8	This study
(PSM)+(AM)+(FSM)	586 ± 13	372 ± 7	26.1 ± 5	This study
(PSM+AM+FSM)	589 ± 11	349 ± 6	28.7 ± 3.1	This study
(PSM+I(AM+SM)+FSM)	617 ± 13	366 ± 5	32.8 ± 1.2	This study
(PSM+AM+FSM)+(PHT)	576 ± 7	257 ± 8	47.8 ± 1	This study
R120	585 ± 16	351 ± 65	19.1 ± 2.6	Chapter 4
Deposit	520	440	51.5	[81]
RCC-M standard	> 490	> 175	> 45	[9]

(PSM)+(AM)+(FSM) and (PSM+AM+FSM) repairs have a lower UTS than the reference substrate (586 MPa and 589 MPa compared to 632 MPa), but still within the norm of a traditional SS316L [8]. They have a higher YS than the substrate (372 MPa and 349 MPa compared to 332 MPa). According to the Hall-Petch relationship, the YS is a function of the grain size, but as shown by Zhou *et al.* [161] it is also a function of the cell size. The high YS is explained by the specific microstructure of the grains of the deposit with a cellular substructure containing very small components with an average size of 9.5 µm with a high density of dislocations as observed in the previous Figure 6.14. The UTS and YS of these repairs are comparable to those of the OPTOMEC machine repairs in Chapter 4, which are 585 MPa and 351 MPa, respectively. The EAB is also improved in the present study up to 28.7% for the sample (PSM+AM+FSM) compared to the previous study where the EAB was 19.1% due to the porosities present at the interface. The high density of deposition by adjusting the overlapping rate in each layer to avoid interfacial porosity increased the ductility of the repairs.

However, the low EAB, only 30% on average, is the still the weak point of these repairs compared to the standard (< 45%), the unrepaired reference substrate (67.9%) and also the LMD-printed deposit (51.5%). This weakness can be explained by the composite nature of the specimen due to the heterogeneous microstructure, but also by the heterogeneous microhardness as observed in Chapter 5. As shown by Balit *et al.* [101] by measuring the strain concentration in the microstructure during tensile testing of half-conventional, half-printed SS316L parts, the strain is distributed uniformly only in the substrate at the beginning of the deformation, since this is the area with the lowest YS. This observation can be verified on the sample (PSM+AM+FSM) in the Figure 6.17 at 15% deformation, where only the substrate deforms along the length of the sample, reducing its width. The authors show in their study that the interface is not subjected

to high stresses due to its higher hardness. Finally, as the deformation increases, they observe the formation of high local stresses in the deposit at the melt pool boundaries. This results in significant local plastic deformation as visually observed in the Figure 6.17 at 26% strain. Crack initiation occurs in a region where the stresses (Figure 6.17 at 28% strain) are too high and cause the tensile specimen to crack. Similar to the present study, Balit *et al.* [101] show that the repaired specimen has lower mechanical properties (41% for the repair instead of 46% for an LMD-printed deposit and 85% for the substrate). Thus, the heterogeneous microstructure and microhardness of the repairs cause deformation incompatibilities that lead to degraded properties, even when the deposit is dense, in contrast to the results obtained in Chapter 4 and presented for comparison in Table 6.2, and when porosities were present at the interface.

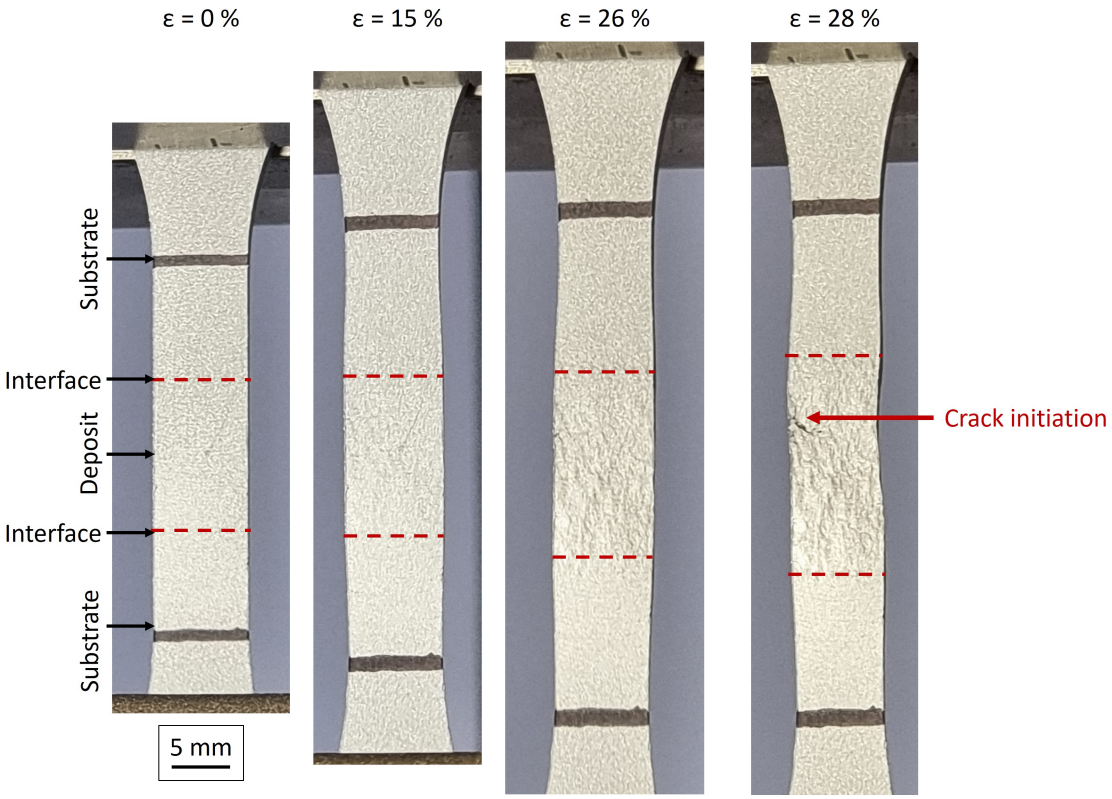

Figure 6.17: Pictures of different stages of deformation of a specimen (PSM+AM+FSM), highlighting the heterogeneous deformation of the repair.

As expected, the alternated repairs (PSM+I(AM+SM)+FSM) show interesting mechanical properties compared to conventional repairs. The UTS is higher (617 MPa) than the other repairs, nearing the reference substrate (632 MPa) and the EAB is slightly improved (32.8% compared to 26.1% for the (PSM)+(AM)+(FSM). The reason for these changes can be explained by the particular microstructure of the alternated deposit

compared to the classical repair methods. In fact, the columnar grains of the deposit are less regular and more undulated. As explained in Figure 6.18, this complicates crack propagation, requiring more energy to propagate through this microstructure [149]. The UTS is therefore higher. At the same time, the grain boundaries are better distributed in all directions in space, allowing a better isotropy of the deposit and a better striction during plastic deformation of the specimen. As a result, the EAB value is slightly higher than that of conventional repairs. However, the YS is not modified despite the finer grains and cellular substructure.

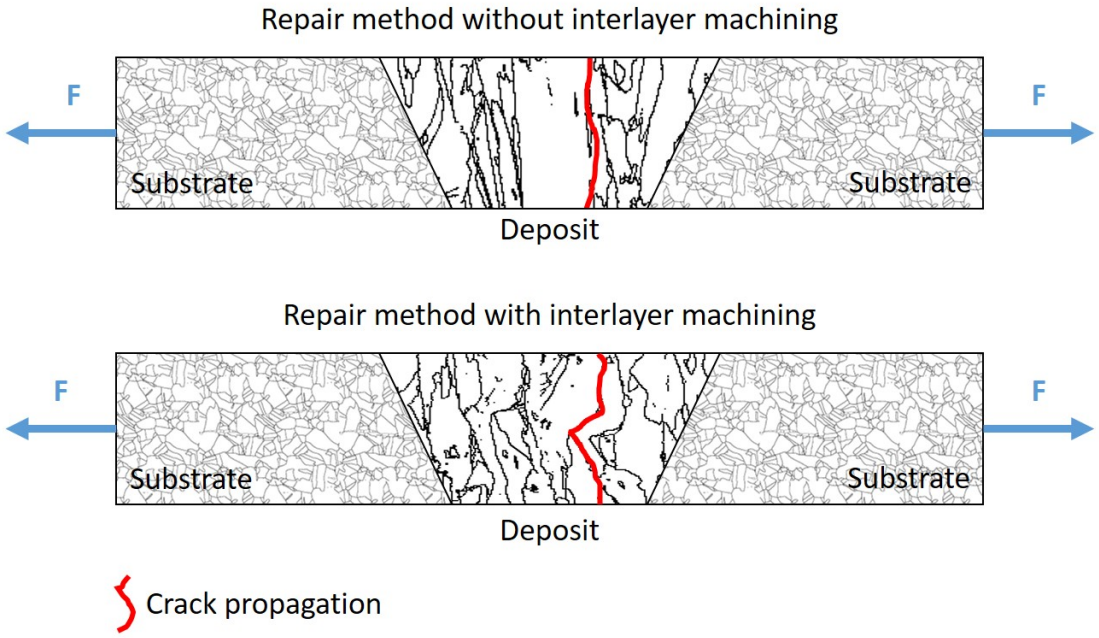

Figure 6.18: Schematic of the crack path in (a) (PSM)+(AM)+(FSM) and (PSM+AM+FSM) and (b) (PSM+I(AM+SM)+FSM).

The high-temperature heat treatment has a strong influence on the tensile mechanical properties of the repair. In fact, the cellular substructure is dissolved and the grains of the substrate and near the interface have quadrupled in size. Thus, according to the Hall-Petch relationship and the results, the YS undergoes a strong decrease as well as the UTS with values of 576 MPa and 257 MPa respectively. On the other hand, the EAB increases to 47.8% compared to the 28.7% of the (PSM+AM+FSM) sample. This phenomenon is observed in the literature in the case of heat treatments applied to conventional and LMD-printed SS316L [116, 120, 185]. According to Wang *et al.* [116], recrystallization reduces dislocation density and low-angle grain boundaries but increases high-angle grain boundaries, which promote uniform repair deformation and result in a rapid increase in elongation but a decrease in yield strength and wear resistance. This post heat treatment

allowed the repair to be modified to meet the RCC-M standard with a minimum UTS, YS and EAB of 490 MPa, 175 MPa and 45% respectively.

6.5 Summary

This study focused on the use of an additive/subtractive hybrid manufacturing machine for the repair of SS316L substrates. Different repair methods related to the operation of this process and post heat treatment were developed and applied to observe the influence on the repair process and the quality of the repairs.

The three steps of the repair process (*i.e.*, pre-machining, material deposition, and post-machining) were performed in separately for a first method and in a single hybrid workstation for a second method. A third technique, called alternated process, consisted of machining 30% of each layer by alternating machining and material deposition. Finally, a final method consisted of performing all steps in a single machine. The repaired part was then subjected to heat treatment at 1100°C for 1 hour to validate the interest for this treatment observed in Chapter 5

The results of this study highlighted a major problem in ASHM, which is the presence of cutting fluid in the manufacturing chamber and on the part to be repaired. This requires blow gun and ethanol cleaning to avoid poor deposit quality and potential damage to the system.

A time savings of approximately 31% for a complete repair within a single machine has been demonstrated using a ASHM versus separate machines. However, repair time increases significantly when additional steps such as post heat treatment (195% more time compared to (PSM+AM+FSM)) or alternation between machining and deposition (217%) are added.

The density of the repaired parts is not affected by the repair method used with results between 99.94% and 99.96%. No lack of fusion or macroscopic defects are found in the repairs. With all methods, microporosity is present in the deposit, but the deposit still appears denser than the substrate, because of the higher density of the repair compared to the reference substrate (99.92%).

The microstructure of most repairs is heterogeneous with fine and equiaxed grains in the substrate and coarse and columnar grains with a cellular substructure in the deposit. Only high temperature post heat treatment dissolves the cellular substructure and increases the grain size in the substrate and near the interface with a factor of 400%. The (PSM)+(AM)+(FSM) and (PSM+AM+FSM) methods do not show differences

between the grains in the deposit. However, the alternated technique changed the morphology of the grains to an undulated shape. The surface work hardening from the machining combined with the removal of the larger grains results in finer columnar grains with specific shapes.

This microstructure results in better mechanical properties than a repair made without alternation. Better UTS and EAB are obtained with this technique with 617 MPa and 32.8% respectively compared to the 589 MPa and 28.7% for the (PSM+AM+FSM) sample, allowing to approach the values specified by the standard for SS316L. The YS of the not heat-treated repairs is also higher (average of 362 MPa) than that of the substrate (332 MPa) due to the cellular substructure of the deposit. The weak point remains the low EAB (average of 30%) caused by the heterogeneous microstructure of the repairs, leading to deformation incompatibility. The heat-treated repair stands out because its UTS and YS are lower (576 MPa and 257 MPa) and the EAB is higher (47.8%) due to the dissolution of the cellular substructure in the FZ, the coarsening of the grain size in the base metal and the homogenization of the overall microstructure caused by the recrystallization.

This study demonstrated the ability to perform a complete repair within an ASHM machine with time savings over separate machines, despite the problem of moisture in the manufacturing chamber. It highlighted the interest of coupling machining and material deposition during pre-machining filling to modify the microstructure and obtain better mechanical properties compared to the additive only process while maintaining a high density rate. Moreover, the post heat treatment at 1100°C for 1h allows the repaired part to have the minimum mechanical properties to meet the RCC-M standards and confirm the interest for this treatment observed in Chapter 5.

General conclusions

Thesis objectives

The repair of damaged components is of great economic and environmental interest, reducing the downtime and costs of industrial equipment and saving energy and resources by restoring only the material damaged by mechanical and corrosive phenomena. This repair process is divided into stages of defect identification, pre-machining, material deposition, post-machining and finally repair characterization. The LMD process was chosen for the deposition of the material because of its advantages recognized in the literature, such as the high deposition density and good mechanical properties, a low HAZ in the part to be repaired and the possibility of automating the repair process thanks to the systematic mounting of projection nozzles on CNC machines.

In this thesis, the repair of stainless steel 316L parts using laser metal deposition was studied in order to optimize the repair process. The objectives were to obtain a dense and crack-free deposit, metallurgically bonded to the substrate and a repair imperceptible in terms of microstructure, mechanical properties and corrosion resistance, without damaging the original part, while restoring its original dimensions.

In order to meet the criteria imposed by the specifications, several research studies were conducted. Firstly, the LMD repair process had to be improved by optimizing the deposition parameters, ensuring good alignment of the parts with the machine and adapting the deposition strategy to this repair application in order to obtain dense deposits that bonded to the substrate. Subsequently, the part preparation step by pre-machining was improved, observing the influence of the pre-machining geometry on the repair quality and the conditions to impose on the geometric parameters to obtain dense deposits by removing a minimum of damaged material. After highlighting the heterogeneity of the repaired parts, which leads to a degradation of the mechanical properties, a study of the imperceptibility of the repair properties was carried out using thermal treatments (substrate preheating, interlayer cooling factor and post-thermal treatment). Microstructural, mechanical and seawater corrosion resistance characterizations have determined the influence of these

parameters on the repairs. Finally, a global evaluation of the repair process was performed using an additive/subtractive hybrid machine allowing in situ machining and material deposition during the year in NTU Singapore. The global time saving of using such type of process could be evaluated.

Laser metal deposition parameters optimization

In the first phase of the thesis, optimization of the additive manufacturing process for repairing parts was performed in order to achieve dense and crack-free deposits, metallurgically bonded to the substrate. The main deposition parameters (*i.e.*, laser power, feed rate, powder mass flow rate and overlapping rate) were identified and varied to observe their influence on bead geometry and deposit density. An important aspect for the beads was to achieve a dilution ratio of about 40% to avoid the formation of porosity and lack of fusion, especially with non-perpendicular surfaces to the laser in the confined pre-machining as observed in the literature.

For both deposition machines used in this work, optimized deposition parameters were obtained for SS316L. The repairs performed on the OPTOMEC LENS MTS-500 machine in CEA Paris-Saclay are as follows: P = 650 W; V = 600 mm/min; Q = 6.6 g/min; OR = 30%, which allowed to obtain beads diluted up to 45% in the previous layer and dense deposits up to 99.993%. For the DMG Mori LaserTec 65 3D machine used in NTU Singapore, the parameters are P = 1500 W; V = 1000 mm/min; Q = 9.6 g/min; OR = 40%, which allow to obtain beads with a dilution of 45% and dense deposits of 99.95%.

It was also shown that the positioning of the parts to be repaired in the machine and their coordinates are essential to ensure a good density of the deposits and to avoid lack of fusion with the edges of the pre-machining. Techniques were thus developed for each machine with the laser guide beam on the OPTOMEC and an automated probe on the DMG Mori and have resulted in dense repairs. The use of modern measuring systems incorporated in the CNC machines and servo-controlled sample holders are of great help in ensuring the correct alignment of the machine axes with respect to the part reference and in knowing its dimensions and position in space.

The generation of the trajectories of the LMD process by CAM software is not adapted to the repair process because the geometric constraints imposed by the pre-machining pose the problem of the formation of porosities at the deposit/substrate interface. Therefore, it was necessary to adapt the trajectories according to the shape and dimensions of the pre-machining, the dimensions of the beads and layers and the deposition parameters by developing a Python program that generates the G-code files that can be read by the

manufacturing machines. A final optimization was made to adjust the overlapping rate at each layer of the repair so that each bead was ideally distributed across the width of the layer being filled. This method eliminated the lack of fusion at the deposit/substrate interface and resulted in high density repairs.

The material deposition step is one of the most important steps in the repair process, as it is during this operation that the replacement material for the damaged material is formed within the part. Therefore, this phase of the work was critical to obtaining dense deposits that were metallurgically bonded to the substrate without lack of fusion at the interface, which is the basis for a successful repair.

Pre-machining shape improvement

In parallel, the pre-machining step was also studied to determine the relationship between the geometry of the pre-machining and the quality of the repair. Several shapes and sizes of pre-machining were repaired with the LMD process in order to observe the influence of the opening angle of the pre-machining on the quality of the repair, to study the conditions to impose to the opening angle of the LMD process for deep repairs, and to study the feasibility of repairing complex and optimized shapes in order to reduce the repair volume.

This initial work on the repair of trapezoidal grooves with different opening angles has highlighted that the pre-machining opening angle is critical on the repair quality. In fact, a decrease in the density rate is observed with a decrease in the groove opening angle, from 99.75% for the 135°-groove to 99.92% for the 105°-groove, because the geometric constraint imposed by the inclined surface of the pre-machining increases the porosity size, which represents less material in the repair. Similarly, tensile tests show a decrease in tensile mechanical properties with decreasing opening angle, from 593 MPa to 560 MPa for the UTS and from 22.1% to 13.3% for the EAB, due to premature specimen failure caused by an increase of the porosity height at the deposit/substrate interface with the decrease of the opening angle. On the other hand, an improvement in absorbed energy with the increase of the opening angle from 187 J to 200 J is observed during Charpy impact tests, which would be caused by a higher resistance to crack propagation due to the introduction of less residual stress in the part, as fewer beads are required for lower opening angles. Based on these results, it is concluded that the 120° opening angle is a good compromise in terms of repair density and mechanical properties.

The second part regarding flat-bottom tapered hole repairs at various depths (5 mm and 10 mm) and opening angles (135°, 120° and 105°) has proven that deep pre-machining

can be repaired if the opening angle meets certain conditions, defined equations. In fact, in order to avoid obstructing the powder stream by the top surface of the substrate (when Z < WD) and to avoid collisions between the projection nozzle and the workpiece (when Z > WD), conditions must be imposed on the opening angle according to the working distance between the nozzle and the substrate as a function of the pre-machining depth.

Ellipsoidal pre-machining has been used to repair fictive pitting corrosion defect. The volume of the ellipsoids was optimized to minimize the repair volume and thus the matter, energy, time and cost of the repair operation. This volume optimization allows the removal of the defect and to provide good access to the projection nozzle. The repair volume optimization calculation then respects the geometric (*i.e.*, initial flaw size and opening angle) and technical (*i.e.*, tool radius) constraints and allows a decrease of 28% of the final volume compared to the initial solution. The whole computational process was described by an optimization algorithm that models the surfaces before and after the repair to recover the volume. Experimental tests were carried out and the results led to the same conclusions as for the repairs previously carried out with trapezoidal grooves and flat-bottom conical holes.

This study demonstrated the feasibility of the LMD process to repair increasingly complex pre-machining with varying dimensions. Certain conditions regarding the opening angle must be observed to ensure a high deposition density, good access to the projection nozzle and to avoid collisions. It also confirmed the importance of adapting the deposition pattern to the case of limited pre-machining repair in order to correctly distribute the beads in the area and avoid the formation of porosities at the substrate/deposit interface.

This study also highlighted the heterogeneous characteristics of a part repaired with the LMD process. In fact, two types of microstructures are exhibited, that of the fine and equiaxed substrate (area-weighted grain size of 38.5 ± 13.2 µm) and that of the coarse and columnar deposit (area-weighted grain size of 121.4 ± 68.4 µm) composed of a fine cellular substructure with a CAS of 3 ± 0.6 µm. The microhardness of the repairs is also heterogeneous with different values in the substrate (190 HV) and in the deposit (200 HV). Similarly, there is a microhardness peak at the interface up to 240 HV caused by the formation of ferrite in the HAZ up to 2.4% compared to the 1% of the unaffected substrate, as well as finer grains in the MZ compared to the deposit. Finally, the tensile mechanical properties are degraded with a UTS of 585 MPa and an EAB of 19.1% compared to 604 MPa and 69.9% of the substrate. Similarly, The absorbed energy in the Charpy impact tests is lower for the repairs (189 J for the 120° groove) than for the reference substrate (256 J). This reduction is caused by the columnar microstructure of the deposit, which is less resistant to crack propagation and porosity formation at the deposit/substrate

interface, since the deposition pattern with the overlapping rate adaptation was not yet applied in this study.

Thus, despite a high deposition density resulting from the optimization of the LMD process parameters and the pre-machining geometry, the heterogeneity of the microstructure and microhardness in the repairs leads to degraded mechanical properties. Additional steps must be added to the repair process to homogenize the properties of the repaired parts and improve their mechanical properties. Similarly, corrosion resistance tests should be performed to evaluate the natural seawater performance of repairs.

Thermal treatments

In view of these results and observations, combined with the findings in the literature, the microstructural and mechanical heterogeneity of the repaired parts, despite a high density rate, is the main reason for the reduced properties. The idea of applying in-situ and post-fabrication thermal treatments to homogenize the properties of the repairs and make the repair imperceptible in terms of mechanical properties and corrosion resistance was developed in this thesis. In order to preheat the substrate by Joule effect prior to material deposition, an inductor was placed under the fabrication support. An interlayer cooling factor was applied to the repairs by maintaining a dwell time depending on the cooling factor and the fabrication time of the layer. Finally, after deposition, the repairs were subjected to post heat treatments in an air oven for a duration of one hour. Several values were used for each thermal treatment and the resulting repairs were compared to an as-built repair and the unrepaired reference substrate to monitor their evolution.

For both the as-built and heat-treated samples, the results of this study exhibited a high density of repairs with a value around 99.96% compared to the 99.87% of the reference substrate. In contrast, the application of substrate preheating and cooling factor reduces the density to 99.78% and 99.78% due to gas bubble formation and ductility dip cracking, respectively, in the deposits.

The morphology and grain size of the repairs are changed only by post heat treatments above 1000°C, which dissolve the cellular substructure and interface and recrystallize the microstructure with a large increase in grain size up to 138.8% for the 1200°C heat treatment. Substrate preheating slightly increases grain size as the initial temperature is increased, but significantly increases the cell size of the substructure from 3.6 µm to 5.8 µm for a preheating temperature of 500°C and 900°C respectively. Conversely, increasing the cooling factor reduces the cell size, from 3 µm to 2.1 µm for CF1 and CF6 respectively, without further changes in the microstructure. The BCC ferrite phase is present in all

repairs with an average of 2.2%, except when preheated to 900°C and post-heat treated at 1000°C and 1200°C, where the ferrite is completely dissolved in the austenite.

The microhardness of the samples changes due to these microstructural changes. The microhardness peak at the interface is attenuated until it disappears as the substrate preheating temperature is increased, due to the dissolution of the ferrite at the interface and the relaxation of the residual stresses. This treatment also reduces the hardness of the deposit due to the increase in cell size. But a difference of only 13 HV is found between the three area of the repair with the substrate preheating at 900°C. On the contrary, increasing the cooling factor increases the microhardness peak up to 210 HV at the interface and the hardness of the deposit due to the refinement of the substructure cells. High temperature heat treatments homogenize the microhardness throughout the repair with the relaxation of the residual stresses and especially the recrystallization of the substrate and the fusion zone with the increase of the grain size and the dissolution of the cellular substructure respectively. For the heat treatment at 1200°C, a difference of only 7 HV is observed between the substrate, the interface and the deposit, demonstrating the great interest of the thermal treatment to reach the imperceptibility of the repair

Repairs subjected to these thermal treatments were immersed in natural seawater. All repairs passivate at the same rate up to a maximum potential, and the evolution of the free corrosion potential is unaffected by the type of thermal treatment. Crevice corrosion appears in the substrate under the protective resin in some specimens due to montage, except for the full LMD-printed specimens. The substrate is more sensitive to crevice corrosion compared to the deposit, due to lower molybdenum and chromium content than the powder. The use of thermal treatments on repairs appears to cause a slight increase in the level of microorganisms on the surface of the samples, which could potentially increase the risk of MIC in the long term. The observations revealed that for the duration of the immersion, the different types of repairs did not show any improvement or deterioration in behavior compared to the reference substrate, which indicates promising results for the use of SS316L parts repaired in natural seawater.

In conclusion, the most interesting thermal methods for repairing stainless steel 316L parts with the LMD process are preheating the substrate to at least 700°C and post heat treatments above 1000°C. With the substrate preheating, there is a homogenization of microhardness, but there is still microstructural heterogeneity. With the post heat treatment, there is a complete homogenization of microstructure and mechanical properties within the repair with recrystallization and relaxation of residual stresses. These thermal treatments do not affect the corrosion resistance of short-term repairs in natural seawater, but special attention must be paid to the chemical composition of the steel in this

environment.

It is therefore possible to homogenize the intrinsic properties of repairs, such as microstructure or microhardness, with thermal treatments to achieve imperceptibility of repairs while maintaining high repair density. However, post heat treatments can be difficult to apply for on-site repairs on non-disassembled parts. Therefore, mobile preheating inductors mounted coaxially to the projection nozzle can be easily used for on-site repairs to at least homogenize the hardness. However, if the part to be repaired cannot be subjected to high-temperature heating, as supported by our results, it is necessary to develop another method that would allow the recovery of the original properties of the part. This technique would also make it possible to restore the original dimensions of the part and thus complete the imposed specifications.

Additive/subtractive hybrid manufacturing

The need to develop a repair process that respects all the constraints imposed by the specifications (high density, imperceptibility, original dimensions) and that can be carried out quickly led to the ASHM process, which combines additive and subtractive manufacturing on a single machine. Thus, after optimizing the pre-machining and material deposition steps, performance of repair obtained in an ASHM machine was evaluated using the DMG Mori machine in NTU Singapore. In this way, a complete repair process could be realized within a single workstation. Different repair methods were studied in order to identify the problems generated by this type of machine, to quantify the duration of the repair according to each method and to observe the influence of a hybrid process on the characteristics of a repair.

A significant time savings of 31% is observed when performing all steps of the repair process within a ASHM machine compared to using separate additive and subtractive machines. However, the addition of post heat treatment or the use of a alternated machining/deposition technique can significantly increase this repair time.

The density of the specimens is not affected by the different repair methods thanks to the preliminary optimization work. The heterogeneous microstructure is found within the repairs with the coarse columnar grains of the deposit composed of a cellular substructure and the fine equiaxed grains of the substrate. The alternated technique, on the other hand, allowed the microstructure of the deposit to be modified. Successive machining passes between each layer deposition in the pre-machining made the columnar grains more wavy with more isotropic grain boundaries. Thus, despite the heterogeneous microstructure between the substrate and the deposit, an improvement in the tensile mechanical properties

is observed compared to repairs performed without interlayer machining.

As previously observed, the post-heat treatment at 1100°C recrystallizes the microstructure, but improves the ductility of the samples to 47.8%, while reducing the UTS and YS to 576 MPa and 257 MPa. However, the values observed in this study are within the standard for mechanical properties of stainless steels 316L, as indicated by the RCC-M standard. Therefore, post heat treatment seems to be one of the best ways to restore the original microstructure and mechanical properties of a conventional SS316L after repair by LMD.

Finally, the use of an ASHM machine has demonstrated the feasibility of this process to perform a complete repair in a single work station with a non-negligible time saving compared to separate machines. Similarly, the alternated repair technique has shown interesting results on the modification of the microstructure of the deposits. Optimization in this way could possibly lead to an equiaxed microstructure in the deposit, thus reducing the heterogeneity of the repair microstructure.

Perspectives

Several perspectives can be proposed to continue this work.

During these studies, characterizations have been made to determine the density rate by Archimedes method or metallographic observations, the microstructure after manufacturing by SEM and EBSD, the mechanical properties by Vickers microhardness, static tensile and Charpy impact tests, as well as the corrosion resistance by immersion in natural seawater. These analyses have provided a great deal of information on the condition of the material and have revealed the phenomena present to explain the mechanical or corrosion behavior of the repaired parts. However, advanced characterizations would allow to analyze the complex behavior of the repaired parts and the behavior of the microstructure during deformations.

The mechanical behavior could be evaluated with advanced tests such as three-point bending to observe the risk of delamination of the deposit in the substrate and the behavior of the interface. Long-term fatigue life of the repaired parts could be determined through fatigue tests. In fact, due to their particular microstructure, LMD-printed deposits are known to be less efficient in fatigue. The use of a half-substrate/half-deposit specimen could accentuate this reduction in performance due to the heterogeneity of the microstructure. Similarly, static tensile tests could be carried out in an SEM, allowing the changes in the microstructure during deformation to be observed. The stress concentration and strain intensity in each zone of the repair could be studied and better understood.

Similarly, the ability of repairs to be reused in corrosive environments would be determined by a more complete characterization of the corrosion resistance of the repairs. Electrochemical polarization testing would allow us to know the corrosion, pitting, and protection potentials of each area of the repair and when the microstructures are mixed within a single specimen. Because of their different microstructures and compositions, each area may have different potentials that can lead to long-term galvanic corrosion. Specific corrosion tests in other environments should also be performed to evaluate the behavior of the repaired component depending on its use.

A study of the behavior of repairs after irradiation would be an interesting analysis if the parts to be repaired were to be used in nuclear environments under irradiation. The effect of neutron irradiation on the deposition and interface regions could be understood by analyzing the microstructure and mechanical properties.

Finally, all the characterizations carried out during this thesis and proposed in perspectives are all destructive tests, which allow to know the characteristics of the parts after repair, but are not applicable to parts that must really be reused within an industrial equipment. Therefore, a state of the art could be realized on all the non-destructive testing means to determine which is the most efficient tool to characterize the quality of a repair, such as tomography to observe the presence and the position of porosities or lack of fusion within the repaired parts. Similarly, new tools could be developed from existing tools to non-destructively monitor the mechanical properties and corrosion resistance of repairs.

This thesis work has demonstrated that the LMD process alone can produce sound and dense repairs with satisfactory mechanical and corrosion resistance properties. However, complete imperceptibility of the repair is not achieved by using this process alone. It must be coupled with other processes, particularly those that modify the microstructure of the LMD deposit and reduce the stresses introduced into the HAZ, such as the use of heat treatments.

The results of the contribution of the ASHM process to repairing damaged components, saving time and improving the quality of the repaired parts, have been presented in this thesis. An in-depth study of the correlation between the machining rate of the layers and the deposition of material could make it possible to obtain repairs with less microstructural heterogeneities and perhaps even improve the mechanical properties of the repaired parts.

Similarly, all steps of the repair process can be fully automated in a single workstation by using hybrid machines. From the measurement, machining and material deposition tools of these machines, algorithms could be developed to identify the damage defect, optimize the repair volume, generate the trajectories of all the tools used, pre-machine the surface, deposit the missing material, post-machine and validate by non-destructive testing.

This approach with the ASHM process opens the way to hybridize the LMD process with other existing techniques described below to improve the properties of repairs. In fact, these techniques have been known in the industry for a long time to modify the condition of the material. For example, it may be interesting to combine the LMD process with hot

rolling. The latter process is known to harden the microstructure that develops after heat treatment fine and equiaxed grains that are desired to approximate the microstructure of the substrate. On the other hand, if this technique can be used for surface repair, as researchers have demonstrated for the repair of shafts [210], it can hardly be integrated in the repair of confined areas, as in a pre-machining, or on surfaces with complex geometry.

The use of other techniques such as Laser Shock Peening (LSP) and Ultrasonic Shock Peening (USP) are known to break up the columnar grains of the welds into a fine, equiaxed microstructure. They also introduce compressive residual stresses into the surface at different depths, depending on the type of peening, which are beneficial for fatigue life or corrosion resistance [211, 212]. The use of these processes with optimized parameters between each layer would make it possible to obtain deposits and interfaces with characteristics very close to the reference substrate and to obtain imperceptible repairs.

Finally, multi-material repair could be important for repairing parts protected by a coating with deep damage. The LMD process has the flexibility to change powders during the deposition process. This makes it a very suitable technology for this type of repair. However, new problems would arise, such as dissolution incompatibility between two dissimilar metals or evaporation of the substrate material at the melting temperature of the coating material, as in the case of tungsten on copper.

The results and perspectives presented in this manuscript show the strong potential of laser metal deposition for repairing damaged components by achieving a repair of excellent quality. Further work is needed to characterize the parts and hybridize the process to make the repair imperceptible in terms of microstructure, mechanical properties and corrosion resistance.

References

[1] Oyewole Adedipe, Feargal Brennan, and Athanasios Kolios. "Review of corrosion fatigue in offshore structures: Present status and challenges in the offshore wind sector". en. In: *Renewable and Sustainable Energy Reviews* 61 (Aug. 2016), pp. 141–154.

[2] François Cattant, Didier Crusset, and Damien Féron. "Corrosion issues in nuclear industry today". en. In: *Materials Today* 11.10 (Oct. 2008), pp. 32–37.

[3] Internationale Atomenergie-Organisation, ed. *Heavy component replacement in nuclear power plants: experience and guidelines*. eng. IAEA nuclear energy series NP-T-3.2. Vienna: IAEA, 2008.

[4] Fred Delany et al. *Advanced joining processes for repair in nuclear power plants*. en-GB. Tech. rep.

[5] Abdollah Saboori et al. "Application of Directed Energy Deposition-Based Additive Manufacturing in Repair". en. In: *Applied Sciences* 9.16 (Aug. 2019), p. 3316.

[6] Robert Odette and Steven John Zinkle, eds. *Structural alloys for nuclear energy applications*. OCLC: on1121057727. Amsterdam: Elsevier, 2019.

[7] ASTM. *ASTM A276 - 10 Standard Specification for Stainless Steel Bars and Shapes*. EN. May 2013.

[8] ASTM. *ASTM A240 - Standard Specification for Chromium and Chromium-Nickel Stainless Steel Plate, Sheet, and Strip for Pressure Vessels and for General Applications*. EN. Nov. 2022.

[9] AFCEN. *Règles de conception et de construction des matériels mécaniques des îlots nucléaires REP. Tome I - Volume B-C-D, Matériels de niveaux 1,2 et 3*. FR. 6ème éd. OCLC: 45898632. Paris: AFCEN, 2018.

[10] G. T. Gray et al. "Structure/property (constitutive and spallation response) of additively manufactured 316L stainless steel". en. In: *Acta Materialia* 138 (Oct. 2017), pp. 140–149.

[11] Ren-Bo Song, Jian-Ying Xiang, and Dong-Po Hou. “Characteristics of Mechanical Properties and Microstructure for 316L Austenitic Stainless Steel”. en. In: *Journal of Iron and Steel Research, International* 18.11 (Nov. 2011), pp. 53–59.

[12] Victor Igwemezie, Ali Mehmanparast, and Athanasios Kolios. “Current trend in offshore wind energy sector and material requirements for fatigue resistance improvement in large wind turbine support structures – A review”. en. In: *Renewable and Sustainable Energy Reviews* 101 (Mar. 2019), pp. 181–196.

[13] Siti Musabikha, I Ketut Utama, and Mukhtasor Mukhtasor. “Corrosion in the Marine Renewable Energy: A Review”. In: Nov. 2016.

[14] IRSN. *Information note : Damage to pipes connected to the main primary system of EDF reactors caused by stress corrosion.* Jan. 2022.

[15] George Bibel. “Significant wastage of a nuclear reactor pressure vessel head”. In: *International Journal of Forensic Engineering* 2.1 (Jan. 2014). Publisher: Inderscience Publishers, pp. 1–14.

[16] Bhaba R. Sarker and Tasnim Ibn Faiz. “Minimizing maintenance cost for offshore wind turbines following multi-level opportunistic preventive strategy”. en. In: *Renewable Energy* 85 (Jan. 2016), pp. 104–113.

[17] Cindy MUYLLE et al. “Repair process using laser metal powder deposition”. Anglais. US20220023948A1 (Nivelles, Belgique). Jan. 2022.

[18] Xinchang Zhang et al. “A Hybrid Process Integrating Reverse Engineering, Pre-Repair Processing, Additive Manufacturing, and Material Testing for Component Remanufacturing”. en. In: *Materials* 12.12 (June 2019), p. 1961.

[19] Kota Kadoi et al. “Crack repair welding by CMT brazing using low melting point filler wire for long-term used steam turbine cases of Cr-Mo-V cast steels”. en. In: *Materials Science and Engineering: A* 666 (June 2016), pp. 11–18.

[20] Kush Mehta. “Advanced Joining and Welding Techniques: An Overview”. en. In: *Advanced Manufacturing Technologies: Modern Machining, Advanced Joining, Sustainable Manufacturing.* Ed. by Kapil Gupta. Materials Forming, Machining and Tribology. Cham: Springer International Publishing, 2017, pp. 101–136.

[21] N. Patel. “A Review on Parametric Optimization of Tig Welding”. In: 2014.

[22] Guifang Sun et al. “Underwater Laser Welding/Cladding for High-performance Repair of Marine Metal Materials: A Review”. en. In: *Chinese Journal of Mechanical Engineering* 35.1 (Jan. 2022), p. 5.

[23] Yongzhe Li et al. “Repairing surface defects of metal parts by groove machining and wire + arc based filling”. en. In: *Journal of Materials Processing Technology* 274 (Dec. 2019), p. 116268.

[24] John C. Lippold. *Welding metallurgy and weldability*. Hoboken, New Jersey: John Wiley & Sons Inc, 2015.

[25] Iman AghaAli et al. “The effect of repeated repair welding on mechanical and corrosion properties of stainless steel 316L”. en. In: *Materials & Design (1980-2015)* 54 (Feb. 2014), pp. 331–341.

[26] Mark Kovalev, Aleksey Shakhmatov, and Aleksey Alhimenko. “Electrochemical studies of welded joints corrosion resistance made from stainless steels”. en. In: *Materials Today: Proceedings* (Feb. 2020).

[27] Wei Tang et al. *ADVANCED WELDING TECHNOLOGY DEVELOPMENT FOR NUCLEAR REACTOR REPAIR*. English. Tech. rep. Oak Ridge National Lab. (ORNL), Oak Ridge, TN (United States), Apr. 2018.

[28] Jae-Hyun Yu et al. “Repairing casting part using laser assisted additive metal-layer deposition and its mechanical properties”. en. In: *Optics & Laser Technology* 106 (Oct. 2018), pp. 87–93.

[29] Jae-Do Kim, Cheol-Jung Kim, and Chin-Man Chung. “Repair welding of etched tubular components of nuclear power plant by Nd:YAG laser”. en. In: *Journal of Materials Processing Technology* 114.1 (July 2001), pp. 51–56.

[30] Wenjing Li et al. “Weldability of irradiated Stainless Steel 304 materials harvested from the National Research Universal (NRU) reactor”. en. In: *Journal of Nuclear Materials* 574 (Feb. 2023), p. 154193.

[31] Wenya Li et al. “Solid-state additive manufacturing and repairing by cold spraying: A review”. en. In: *Journal of Materials Science & Technology* 34.3 (Mar. 2018), pp. 440–457.

[32] Shuo Yin et al. “Cold spray additive manufacturing and repair: Fundamentals and applications”. en. In: *Additive Manufacturing* 21 (May 2018), pp. 628–650.

[33] Sara Bagherifard and Mario Guagliano. “Fatigue performance of cold spray deposits: Coating, repair and additive manufacturing cases”. en. In: *International Journal of Fatigue* 139 (Oct. 2020), p. 105744.

[34] K. Petráčková, J. Kondás, and M. Guagliano. “Fixing a hole (with cold spray)”. en. In: *International Journal of Fatigue* 110 (May 2018), pp. 144–152.

[35] P. Richter. “New value chain for advanced coatings by using cold spray”. In: *Industrial Technologies* (2014).

[36] T. Briefing. “Metal coated particles and defense applications”. In: *CSAT Workshop. Worcester, USA*. 2013.

[37] J. Schell. “Cold spray aerospace applications”. In: *CSAT Workshop, Worcester, USA*. 2016.

[38] Th Stoltenhoff and F. Zimmermann. “LOXPlate® coatings for aluminum aerospace components exposed to high dynamic stresses”. In: *Praxair Surface Technologies GmbH, Ratingen* (2012).

[39] V.P. Lyalyakin, A.Yu. Kostukov, and V.A. Denisov. “Special features of reconditioning the housing of a Caterpillar diesel oil pump by gas-dynamic spraying”. In: *Welding International* 30.1 (Jan. 2016). Publisher: Taylor & Francis _eprint: https://doi.org/10.1080/09507116.2015.1030152, pp. 68–70.

[40] Moridi Atieh. “Cold spray coating: process evaluation and wealth of applications; from structural repair to bioengineering”. EN. PhD thesis. Politechnico Milano, Mar. 2015.

[41] S. M. Hassani-Gangaraj, A. Moridi, and M. Guagliano. “Critical review of corrosion protection by cold spray coatings”. In: *Surface Engineering* 31.11 (Nov. 2015). Publisher: Taylor & Francis _eprint: https://doi.org/10.1179/1743294415Y.0000000018, pp. 803–815.

[42] Pierre Coddet et al. “Mechanical properties of thick 304L stainless steel deposits processed by He cold spray”. en. In: *Surface and Coatings Technology* 277 (Sept. 2015), pp. 74–80.

[43] L. N. Moskowitz. “Application of HVOF thermal spraying to solve corrosion problems in the petroleum industry—an industrial note”. en. In: *Journal of Thermal Spray Technology* 2.1 (Mar. 1993), pp. 21–29.

[44] Rodolpho Fernando Váz et al. “Welding and Thermal Spray Processes for Maintenance of Hydraulic Turbine Runners: Case Studies”. en. In: *Soldagem & Inspeção* 26 (Apr. 2021). Publisher: Associação Brasileira de Soldagem.

[45] Jochen Fiebig et al. “Thermal Spray Processes for the Repair of Gas Turbine Components”. en. In: *Advanced Engineering Materials* 22.6 (2020). _eprint: https://onlinelibrary.wiley.com p. 1901237.

[46] R. W. Rigney et al. “Component Repair and Chrome Plating Replacement with New Thermal Spray in the United States Navy: Successes and the Future”. en. In: ASM International, May 1998, pp. 975–979.

[47] M. F. Smith. “3 - Comparing cold spray with thermal spray coating technologies”. en. In: *The Cold Spray Materials Deposition Process*. Ed. by Victor K. Champagne. Woodhead Publishing Series in Metals and Surface Engineering. Woodhead Publishing, Jan. 2007, pp. 43–61.

[48] *Standard ISO/ASTM 52900:2015. Additive Manufacturing – General Principles – Terminology*. 2016.

[49] Kaufui V. Wong and Aldo Hernandez. “A Review of Additive Manufacturing”. en. In: *ISRN Mechanical Engineering* 2012 (2012), pp. 1–10.

[50] ISO. *ISO 17296-2:2015 Additive manufacturing — General principles — Part 2: Overview of process categories and feedstock*. EN. Jan. 2015.

[51] Anne-Françoise Obaton. “Fabrication additive : contrôles”. FR. In: Techniques de l’ingénieur (Nov. 2022), p. 22.

[52] Dong-Gyu Ahn. “Directed Energy Deposition (DED) Process: State of the Art”. en. In: *International Journal of Precision Engineering and Manufacturing-Green Technology* 8.2 (Mar. 2021), pp. 703–742.

[53] Scott M. Thompson et al. “An overview of Direct Laser Deposition for additive manufacturing; Part I: Transport phenomena, modeling and diagnostics”. en. In: *Additive Manufacturing* 8 (Oct. 2015), pp. 36–62.

[54] Nima Shamsaei et al. “An overview of Direct Laser Deposition for additive manufacturing; Part II: Mechanical behavior, process parameter optimization and control”. en. In: *Additive Manufacturing* 8 (Oct. 2015), pp. 12–35.

[55] T. DebRoy et al. “Additive manufacturing of metallic components – Process, structure and properties”. en. In: *Progress in Materials Science* 92 (Mar. 2018), pp. 112–224.

[56] Adrita Dass and Atieh Moridi. “State of the Art in Directed Energy Deposition: From Additive Manufacturing to Materials Design”. en. In: *Coatings* 9.7 (June 2019), p. 418.

[57] AN Jinoop, CP Paul, and KS Bindra. “Laser-assisted directed energy deposition of nickel super alloys: A review”. en. In: *Proceedings of the Institution of Mechanical Engineers, Part L: Journal of Materials: Design and Applications* 233.11 (Nov. 2019). Publisher: SAGE Publications, pp. 2376–2400.

[58] R. R. Unocic and J. N. DuPont. “Process efficiency measurements in the laser engineered net shaping process”. en. In: *Metallurgical and Materials Transactions B* 35.1 (Feb. 2004), pp. 143–152.

[59] Vincent Jacquier et al. “Melt Pool Turbulence Effects on the Interface between Dissimilar Materials Manufactured by Directed Energy Deposition with Laser and Powder”. en. In: *Journal of Materials Engineering and Performance* 30.12 (Dec. 2021), pp. 8810–8820.

[60] Ian Gibson, David Rosen, and Brent Stucker. *Additive Manufacturing Technologies: 3D Printing, Rapid Prototyping, and Direct Digital Manufacturing*. en. New York, NY: Springer, 2015.

[61] Decheng Kong et al. “About metastable cellular structure in additively manufactured austenitic stainless steels”. en. In: *Additive Manufacturing* 38 (Feb. 2021), p. 101804.

[62] Aziz Chniouel. “Etude de l’élaboration de l’acier inoxydable 316L par fusion laser sélective sur lit de poudre : influence des paramètres du procédé, des caractéristiques de la poudre, et des traitements thermiques sur la microstructure et les propriétés mécaniques.” fr. PhD thesis. Université Paris-Saclay, Nov. 2019.

[63] Ross Cunningham et al. “Analyzing the effects of powder and post-processing on porosity and properties of electron beam melted Ti-6Al-4V”. In: *Materials Research Letters* 5.7 (Nov. 2017). Publisher: Taylor & Francis _eprint: https://doi.org/10.1080/21663831.201 pp. 516–525.

[64] B. H. Rabin, G. R. Smolik, and G. E. Korth. “Characterization of entrapped gases in rapidly solidified powders”. en. In: *Materials Science and Engineering: A* 124.1 (Apr. 1990), pp. 1–7.

[65] U. de Oliveira, V. Ocelík, and J.Th.M. De Hosson. “Analysis of coaxial laser cladding processing conditions”. en. In: *Surface and Coatings Technology* 197.2-3 (July 2005), pp. 127–136.

[66] Hussam El Cheikh et al. “Analysis and prediction of single laser tracks geometrical characteristics in coaxial laser cladding process”. en. In: *Optics and Lasers in Engineering* 50.3 (Mar. 2012), pp. 413–422.

[67] D. P. Bykovskiy et al. “Analysis of microstructure and properties of multilayer coatings produced by laser cladding”. en. In: *Journal of Physics: Conference Series* 691 (Feb. 2016), p. 012008.

[68] Tarun Bhardwaj et al. “Direct Energy Deposition - Laser Additive Manufacturing of Titanium-Molybdenum alloy: Parametric studies, microstructure and mechanical properties”. en. In: *Journal of Alloys and Compounds* 787 (May 2019), pp. 1238–1248.

[69] Yuying Yang et al. “Additive and Subtractive Hybrid Manufacturing (ASHM) of 316L Stainless Steel: Single-Track Specimens, Microstructure, and Mechanical Properties”. en. In: *JOM* 73.3 (Mar. 2021), pp. 759–769.

[70] Ondřej Nenadl et al. “The Prediction of Coating Geometry from Main Processing Parameters in Laser Cladding”. en. In: *Physics Procedia*. 8th International Conference on Laser Assisted Net Shape Engineering LANE 2014 56 (Jan. 2014), pp. 220–227.

[71] Yanxiang Li and Jian Ma. “Study on overlapping in the laser cladding process”. en. In: *Surface and Coatings Technology* 90.1 (Mar. 1997), pp. 1–5.

[72] Yves Valentin, Benoît Verquin, and Sophie Hoguin. *Fabrication additive métallique - les fondamentaux*. français. Ed. by CETIM. 2019.

[73] Gabriele Piscopo, Alessandro Salmi, and Eleonora Atzeni. “Influence of High-Productivity Process Parameters on the Surface Quality and Residual Stress State of AISI 316L Components Produced by Directed Energy Deposition”. en. In: *Journal of Materials Engineering and Performance* 30.9 (Sept. 2021), pp. 6691–6702.

[74] Chenggang Ding et al. “Effects of Substrate Preheating Temperatures on the Microstructure, Properties, and Residual Stress of 12CrNi2 Prepared by Laser Cladding Deposition Technique”. In: *Materials* 11.12 (Nov. 2018).

[75] Xufei Lu et al. “Substrate design to minimize residual stresses in Directed Energy Deposition AM processes”. en. In: *Materials & Design* 202 (Apr. 2021), p. 109525.

[76] Abdollah Saboori et al. “An investigation on the effect of deposition pattern on the microstructure, mechanical properties and residual stress of 316L produced by Directed Energy Deposition”. en. In: *Materials Science and Engineering: A* 780 (Apr. 2020), p. 139179.

[77] Yanis Balit, Eric Charkaluk, and Andrei Constantinescu. “Digital image correlation for microstructural analysis of deformation pattern in additively manufactured 316L thin walls”. en. In: *Additive Manufacturing* 31 (Jan. 2020), p. 100862.

[78] Mingming Ma, Zemin Wang, and Xiaoyan Zeng. “A comparison on metallurgical behaviors of 316L stainless steel by selective laser melting and laser cladding deposition”. en. In: *Materials Science and Engineering: A* 685 (Feb. 2017), pp. 265–273.

[79] Michał Ziętala et al. “The microstructure, mechanical properties and corrosion resistance of 316L stainless steel fabricated using laser engineered net shaping”. en. In: *Materials Science and Engineering: A* 677 (Nov. 2016), pp. 1–10.

[80] Zhi'En Eddie Tan et al. "Characterisation of porosity, density, and microstructure of directed energy deposited stainless steel AISI 316L". en. In: *Additive Manufacturing* 25 (Jan. 2019), pp. 286–296.

[81] Bassem Barkia. "On the origin of the high tensile strength and ductility of additively manufactured 316L stainless steel: Multiscale investigation". en. In: *Journal of Materials Science & Technology* 41 (Mar. 2020), pp. 209–218.

[82] Kai Zhang et al. "Characterization of stainless steel parts by Laser Metal Deposition Shaping". en. In: *Materials & Design* 55 (Mar. 2014), pp. 104–119.

[83] Abdollah Saboori et al. "Microstructure and Mechanical Properties of AISI 316L Produced by Directed Energy Deposition-Based Additive Manufacturing: A Review". en. In: *Applied Sciences* 10.9 (Jan. 2020). Number: 9 Publisher: Multidisciplinary Digital Publishing Institute, p. 3310.

[84] Michał Ziętala et al. "The microstructure, mechanical properties and corrosion resistance of 316L stainless steel fabricated using laser engineered net shaping". en. In: *Materials Science and Engineering: A* 677 (Nov. 2016), pp. 1–10.

[85] Reynier I. Revilla et al. "Microstructure and corrosion behavior of 316L stainless steel prepared using different additive manufacturing methods: A comparative study bringing insights into the impact of microstructure on their passivity". en. In: *Corrosion Science* 176 (Nov. 2020), p. 108914.

[86] Faming Shen et al. "Effect of microstructure on the corrosion resistance of coatings by extreme high speed laser cladding". en. In: *Applied Surface Science* 517 (July 2020), p. 146085.

[87] P. Ganesh et al. "Studies on pitting corrosion and sensitization in laser rapid manufactured specimens of type 316L stainless steel". en. In: *Materials & Design* 39 (Aug. 2012), pp. 509–521.

[88] Geun-Su Jung et al. "Study on Corrosion Properties of Additive Manufactured 316L Stainless Steel and Alloy 625 in Seawater". eng. In: *Corrosion Science and Technology* 18.6 (2019), pp. 258–266.

[89] Majid Laleh et al. "Unanticipated drastic decline in pitting corrosion resistance of additively manufactured 316L stainless steel after high-temperature post-processing". en. In: *Corrosion Science* 165 (Apr. 2020), p. 108412.

[90] Maija Leino, Joonas Pekkarinen, and Risto Soukka. "The Role of Laser Additive Manufacturing Methods of Metals in Repair, Refurbishment and Remanufacturing – Enabling Circular Economy". en. In: *Physics Procedia* 83 (2016), pp. 752–760.

[91] Kumar Kanishka and Bappa Acherjee. “A systematic review of additive manufacturing-based remanufacturing techniques for component repair and restoration”. en. In: *Journal of Manufacturing Processes* 89 (Mar. 2023), pp. 220–283.

[92] M. Brandt et al. “Laser cladding repair of turbine blades in power plants: from research to commercialisation”. In: *International Heat Treatment and Surface Engineering* 3.3 (Sept. 2009). Publisher: Taylor & Francis _eprint: https://doi.org/10.1179/174951409X pp. 105–114.

[93] Boris Rottwinkel et al. “Crack Repair of Single Crystal Turbine Blades Using Laser Cladding Technology”. en. In: *Procedia CIRP* 22 (Jan. 2014), pp. 263–267.

[94] Chun-Ming Lin. “Parameter optimization of laser cladding process and resulting microstructure for the repair of tenon on steam turbine blade”. en. In: *Vacuum* 115 (May 2015), pp. 117–123.

[95] Talu Ünal-Saewe et al. “Process Development for Tip Repair of Complex Shaped Turbine Blades with IN718”. en. In: *Procedia Manufacturing* 47 (Jan. 2020), pp. 1050–1057.

[96] Jennifer Bennett et al. “Control of heating and cooling for direct laser deposition repair of cast iron components”. In: IEEE, Aug. 2016, pp. 229–236.

[97] Jim Foster et al. “Remanufacture of hot forging tools and dies using laser metal deposition with powder and a hard-facing alloy Stellite 21®”. en. In: *Journal of Remanufacturing* 9.3 (Oct. 2019). Number: 3, pp. 189–203.

[98] R. Mudge and Nick Wald. “Laser engineered net shaping advances additive manufacturing and repair”. In: *Welding Journal* (2007).

[99] H. Koehler et al. “Laser reconditioning of crankshafts: From lab to application”. en. In: *Physics Procedia*. Laser Assisted Net Shape Engineering 6, Proceedings of the LANE 2010, Part 1 5 (Jan. 2010), pp. 387–397.

[100] Wook Jin Oh, Yong Son, and Shim Do Sik. “Effect of in-situ heat treatments on deposition characteristics and mechanical properties for repairs using laser melting deposition”. en. In: *Journal of Manufacturing Processes* 58 (Oct. 2020), pp. 1019–1033.

[101] Yanis Balit et al. “High resolution digital image correlation for microstructural strain analysis of a stainless steel repaired by Directed Energy Deposition”. en. In: *Materials Letters* 270 (July 2020), p. 127632.

[102] Camille Guévenoux et al. “Plastic strain localization induced by microstructural gradient in laser cladding repaired structures”. en. In: *Theoretical and Applied Fracture Mechanics* 107 (June 2020), p. 102520.

[103] Tawanda Marazani, Daniel M. Madyira, and Esther T. Akinlabi. “Repair of Cracks in Metals: A Review”. en. In: *Procedia Manufacturing*. 14th Global Conference on Sustainable Manufacturing, GCSM 3-5 October 2016, Stellenbosch, South Africa 8 (Jan. 2017), pp. 673–679.

[104] H. Paydas et al. “Laser cladding as repair technology for Ti–6Al–4V alloy: Influence of building strategy on microstructure and hardness”. en. In: *Materials & Design* 85 (Nov. 2015), pp. 497–510.

[105] Zhichao Liu et al. “Feasibility Exploration of Superalloys for AISI 4140 Steel Repairing using Laser Engineered Net Shaping”. en. In: *Procedia Manufacturing* 10 (Jan. 2017), pp. 912–922.

[106] A J Pinkerton, W Wang, and L Li. “Component repair using laser direct metal deposition”. en. In: *Proceedings of the Institution of Mechanical Engineers, Part B: Journal of Engineering Manufacture* 222.7 (July 2008). Publisher: IMECHE, pp. 827–836.

[107] Benjamin Graf, Andrey Gumenyuk, and Michael Rethmeier. “Laser Metal Deposition as Repair Technology for Stainless Steel and Titanium Alloys”. en. In: *Physics Procedia* 39 (2012), pp. 376–381.

[108] Wook Jin Oh et al. “Repairing additive-manufactured 316L stainless steel using direct energy deposition”. en. In: *Optics & Laser Technology* 117 (Sept. 2019), pp. 6–17.

[109] Lida Zhu et al. “Recent research and development status of laser cladding: A review”. en. In: *Optics & Laser Technology* 138 (June 2021), p. 106915.

[110] Gyeong Yun Baek et al. “Effects of substrate preheating during direct energy deposition on microstructure, hardness, tensile strength, and notch toughness”. en. In: *Metals and Materials International* 23.6 (Nov. 2017), pp. 1204–1215.

[111] Seyed Kiomars Moheimani, Luca Iuliano, and Abdollah Saboori. “The role of substrate preheating on the microstructure, roughness, and mechanical performance of AISI 316L produced by directed energy deposition additive manufacturing”. en. In: *The International Journal of Advanced Manufacturing Technology* 119.11 (Apr. 2022), pp. 7159–7174.

[112] Gunther Mohr, Simon J. Altenburg, and Kai Hilgenberg. “Effects of inter layer time and build height on resulting properties of 316L stainless steel processed by laser powder bed fusion”. en. In: *Additive Manufacturing* 32 (Mar. 2020), p. 101080.

[113] Aref Yadollahi et al. “Effects of process time interval and heat treatment on the mechanical and microstructural properties of direct laser deposited 316L stainless steel”. en. In: *Materials Science and Engineering: A* 644 (Sept. 2015), pp. 171–183.

[114] Erik R. Denlinger et al. “Effect of inter-layer dwell time on distortion and residual stress in additive manufacturing of titanium and nickel alloys”. en. In: *Journal of Materials Processing Technology* 215 (Jan. 2015), pp. 123–131.

[115] M. Shiomi et al. “Residual Stress within Metallic Model Made by Selective Laser Melting Process”. en. In: *CIRP Annals* 53.1 (Jan. 2004), pp. 195–198.

[116] C. Wang et al. “Effect of heat treatment temperature on microstructure and tensile properties of austenitic stainless 316L using wire and arc additive manufacturing”. en. In: *Materials Science and Engineering: A* 832 (Jan. 2022), p. 142446.

[117] Decheng Kong et al. “Mechanical properties and corrosion behavior of selective laser melted 316L stainless steel after different heat treatment processes”. en. In: *Journal of Materials Science & Technology* 35.7 (July 2019), pp. 1499–1507.

[118] Tobias Ronneberg, Catrin M. Davies, and Paul A. Hooper. “Revealing relationships between porosity, microstructure and mechanical properties of laser powder bed fusion 316L stainless steel through heat treatment”. en. In: *Materials & Design* 189 (Apr. 2020), p. 108481.

[119] Alberta Aversa et al. “Effect of Heat Treatments on Residual Stress and Properties of AISI 316L Steel Processed by Directed Energy Deposition”. en. In: *Journal of Materials Engineering and Performance* 29.9 (Sept. 2020), pp. 6002–6013.

[120] M. Kumaran et al. “Effect of heat treatment on stainless steel 316L alloy sandwich structure fabricated using directed energy deposition and powder bed fusion”. en. In: *Materials Letters* 313 (Apr. 2022), p. 131766.

[121] Do Sik Shim et al. “Effects of pre- and post-repair heat treatments on microstructure and tensile behaviors of 630 stainless steel repaired by metal additive manufacturing”. en. In: *Journal of Materials Research and Technology* 13 (July 2021), pp. 980–999.

[122] K. P. Karunakaran et al. “Retrofitment of a CNC machine for hybrid layered manufacturing”. en. In: *The International Journal of Advanced Manufacturing Technology* 45.7 (Dec. 2009), pp. 690–703.

[123] Magdalena Cortina et al. “Latest Developments in Industrial Hybrid Machine Tools that Combine Additive and Subtractive Operations”. en. In: *Materials* 11.12 (Dec. 2018), p. 2583.

[124] L. Ren et al. “Three dimensional die repair using a hybrid manufacturing system”. In: *17th Solid Freeform Fabrication Symposium, SFF 2006* (Jan. 2006), pp. 51–59.

[125] Jason B. Jones et al. “Remanufacture of turbine blades by laser cladding, machining and in-process scanning in a single machine”. EN. In: (Aug. 2012).

[126] Thomas Feldhausen et al. “Mechanical properties and microstructure of 316L stainless steel produced by hybrid manufacturing”. en. In: *Journal of Materials Processing Technology* 290 (Apr. 2021), p. 116970.

[127] Rangasayee Kannan, Peeyush Nandwana, and Thomas Feldhausen. “Comparing the deformation mechanism in 316 L stainless steel fabricated by hybrid and additive manufacturing”. en. In: *Materials Letters* 288 (Apr. 2021), p. 129369.

[128] Yuying Yang et al. “Additive/subtractive hybrid manufacturing of 316L stainless steel powder: Densification, microhardness and residual stress”. en. In: *Journal of Mechanical Science and Technology* 33.12 (Dec. 2019), pp. 5797–5807.

[129] Rangasayee Kannan et al. “Effect of humidity of build chamber in hybrid manufacturing systems on part performance”. en. In: *Manufacturing Letters* 32 (Apr. 2022), pp. 39–43.

[130] *Optomec - 3D PRINTING SOLUTIONS FOR AN ADDITIVE MANUFACTURING WORLD*. en-US.

[131] *DMG MORI - CNC machine tools for all cutting-machining applications*. en.

[132] ASTM B311-17. *Standard test method for density of powder metallurgy (PM) materials containing less than two percent porosity*. English. 2017.

[133] A.B. Spierings, M. Schneider, and R. Eggenberger. “Comparison of density measurement techniques for additive manufactured metallic parts”. In: *Rapid Prototyping Journal* 17.5 (Jan. 2011). Publisher: Emerald Group Publishing Limited, pp. 380–386.

[134] ISO. *ISO 6520-1:2007 - Welding and allied processes — Classification of geometric imperfections in metallic materials — Part 1: Fusion welding*. EN. July 2007.

[135] B. J. Inkson. “2 - Scanning electron microscopy (SEM) and transmission electron microscopy (TEM) for materials characterization”. en. In: *Materials Characterization Using Nondestructive Evaluation (NDE) Methods*. Ed. by Gerhard Hübschen et al. Woodhead Publishing, Jan. 2016, pp. 17–43.

[136] Nicolas Brodusch, Hendrix Demers, and Raynald Gauvin. “Imaging with a Commercial Electron Backscatter Diffraction (EBSD) Camera in a Scanning Electron Microscope: A Review”. en. In: *Journal of Imaging* 4.7 (July 2018). Number: 7 Publisher: Multidisciplinary Digital Publishing Institute, p. 88.

[137] J. Epp. “4 - X-ray diffraction (XRD) techniques for materials characterization”. en. In: *Materials Characterization Using Nondestructive Evaluation (NDE) Methods*. Ed. by Gerhard Hübschen et al. Woodhead Publishing, Jan. 2016, pp. 81–124.

[138] ISO. *ISO 6507-1:2018. Metallic materials — Vickers hardness test — Part 1: Test method*. EN. Jan. 2018.

[139] ISO. *ISO 6892-1:2019. Metallic materials — Tensile testing — Part 1: Method of test at room temperature*. EN. Nov. 2019.

[140] ISO. *ISO 4136:2022. Destructive tests on welds in metallic materials — Transverse tensile test*. EN. Nov. 2012.

[141] ISO. *ISO 148-1:2016. Metallic materials — Charpy pendulum impact test — Part 1: Test method*. EN. Oct. 2016.

[142] M. Naveed Ahsan, Robert Bradley, and Andrew J. Pinkerton. “Microcomputed tomography analysis of intralayer porosity generation in laser direct metal deposition and its causes”. In: *Journal of Laser Applications* 23.2 (May 2011). Publisher: Laser Institute of America, p. 022009.

[143] Shi Da Sun et al. “Effect of laser clad repair on the fatigue behaviour of ultra-high strength AISI 4340 steel”. en. In: *Materials Science and Engineering: A* 606 (June 2014), pp. 46–57.

[144] G. F. Sun et al. “Microstructure and mechanical properties of HSLA-100 steel repaired by laser metal deposition”. en. In: *Surface and Coatings Technology* 351 (Oct. 2018), pp. 198–211.

[145] G. F. Sun et al. “Laser metal deposition as repair technology for 316L stainless steel: Influence of feeding powder compositions on microstructure and mechanical properties”. en. In: *Optics & Laser Technology* 109 (Jan. 2019), pp. 71–83.

[146] P Ernst and R. C Newman. “Pit growth studies in stainless steel foils. I. Introduction and pit growth kinetics”. en. In: *Corrosion Science* 44.5 (May 2002), pp. 927–941.

[147] Yuxin Cao et al. “DFT study on the mechanism of inclusion-induced initial pitting corrosion of Al-Ti-Ca complex deoxidized steel with Ce treatment”. en. In: *Physica B: Condensed Matter* 558 (Apr. 2019), pp. 10–19.

[148] Kenichiro Eguchi, Timothy L Burnett, and Dirk L Engelberg. “X-Ray tomographic characterisation of pitting corrosion in lean duplex stainless steel”. en. In: *Corrosion Science* 165 (Apr. 2020), p. 108406.

[149] “Effects of cladding path on workpiece geometry and impact toughness in Directed Energy Deposition of 316L stainless steel”. In: *CIRP Annals* 67.1 (Jan. 2018), pp. 233–236.

[150] H. L. Wei, J. Mazumder, and T. DebRoy. “Evolution of solidification texture during additive manufacturing”. en. In: *Scientific Reports* 5.1 (Dec. 2015).

[151] K. Saeidi et al. “Transformation of austenite to duplex austenite-ferrite assembly in annealed stainless steel 316L consolidated by laser melting”. en. In: *Journal of Alloys and Compounds* 633 (June 2015), pp. 463–469.

[152] K. Saeidi et al. “Hardened austenite steel with columnar sub-grain structure formed by laser melting”. en. In: *Materials Science and Engineering: A* 625 (Feb. 2015), pp. 221–229.

[153] R. G. Thiessen and I. M. Richardson. “A physically based model for microstructure development in a macroscopic heat-affected zone: Grain growth and recrystallization”. en. In: *Metallurgical and Materials Transactions B* 37.4 (Aug. 2006), pp. 655–663.

[154] Jianzheng Guo and Mark Samonds. “Modeling of Casting and Solidification Processes”. en. In: *Metals Process Simulation*. Ed. by D.U. Furrer and S.L. Semiatin. ASM International, Nov. 2010, pp. 168–195.

[155] “Aciers inoxydables - Critères de choix et structure : Dossier complet - Techniques de l’Ingénieur”. In.

[156] Ping Tao et al. “Characterization on stress-strain behavior of ferrite and austenite in a 2205 duplex stainless steel based on nanoindentation and finite element method”. en. In: *Results in Physics* 11 (Dec. 2018), pp. 377–384.

[157] Jianli Song et al. “Rebuilding of metal components with laser cladding forming”. en. In: *Applied Surface Science* 252.22 (Sept. 2006), pp. 7934–7940.

[158] Lijun Song et al. “Repair of 304 stainless steel by laser cladding with 316L stainless steel powders followed by laser surface alloying with WC powders”. en. In: *Journal of Manufacturing Processes* 24 (Oct. 2016), pp. 116–124.

[159] Quentin Auzoux. “Fissuration en relaxation des aciers inoxydables austénitiques - Influence de l’écrouissage sur l’endommagement intergranulaire”. fr. PhD thesis. École Nationale Supérieure des Mines de Paris, Jan. 2004.

[160] A. Rajesh Kannan et al. “Microstructural characterization and mechanical integrity of stainless steel 316L clad layers deposited via wire arc additive manufacturing for nuclear applications”. In: *Materialwissenschaft und Werkstofftechnik* 52.6 (June 2021), pp. 617–623.

[161] Baogang Zhou et al. “Microstructure and Anisotropy of the Mechanical Properties of 316L Stainless Steel Fabricated by Selective Laser Melting”. en. In: *Metals* 11.5 (May 2021). Number: 5 Publisher: Multidisciplinary Digital Publishing Institute, p. 775.

[162] Youxiang Chew et al. “Thermo-mechanical model for simulating laser cladding induced residual stresses with single and multiple clad beads”. en. In: *Journal of Materials Processing Technology* 224 (Oct. 2015), pp. 89–101.

[163] Parisa Farahmand and Radovan Kovacevic. “An experimental–numerical investigation of heat distribution and stress field in single- and multi-track laser cladding by a high-power direct diode laser”. en. In: *Optics & Laser Technology* 63 (Nov. 2014), pp. 154–168.

[164] X. B. Ren, Z. L. Zhang, and B. Nyhus. “Effect of residual stresses on ductile crack growth resistance”. en. In: *Engineering Fracture Mechanics* 77.8 (May 2010), pp. 1325–1337.

[165] Xinchang Zhang et al. “Evaluation of component repair using direct metal deposition from scanned data”. en. In: *The International Journal of Advanced Manufacturing Technology* 95.9 (Apr. 2018), pp. 3335–3348.

[166] Xinchang Zhang, Wei Li, and Frank Liou. “Damage detection and reconstruction algorithm in repairing compressor blade by direct metal deposition”. en. In: *The International Journal of Advanced Manufacturing Technology* 95.5 (Mar. 2018), pp. 2393–2404.

[167] Sebahattin Bektas. “Curvature of the Ellipsoid with Cartesian Coordinates”. en. In: *Landscape Architecture and Regional Planning* 2.2 (Mar. 2017). Number: 2 Publisher: Science Publishing Group, p. 61.

[168] Damien Buchbinder et al. “Investigation on reducing distortion by preheating during manufacture of aluminum components using selective laser melting”. en. In: *Journal of Laser Applications* 26.1 (Nov. 2013). Publisher: Laser Institute of AmericaLIA, p. 012004.

[169] C. Li et al. “Residual Stress in Metal Additive Manufacturing”. en. In: *Procedia CIRP* 71 (2018), pp. 348–353.

[170] Quan Lai et al. “Investigation of a novel functionally graded material for the repair of premium hypereutectoid rails using laser cladding technology”. en. In: *Composites Part B: Engineering* 130 (Dec. 2017), pp. 174–191.

[171] Taposh Roy et al. “Residual stress in laser cladded heavy-haul rails investigated by neutron diffraction”. en. In: *Journal of Materials Processing Technology* 278 (Apr. 2020), p. 116511.

[172] Jessica Dill, Masakazu Soshi, and Kazuo Yamazaki. “A study on the effect of directed energy deposition substrate energy on clad geometry”. en. In: *The International Journal of Advanced Manufacturing Technology* 109.1 (July 2020), pp. 315–333.

[173] L. Costa et al. “Rapid tooling by laser powder deposition: Process simulation using finite element analysis”. en. In: *Acta Materialia* 53.14 (Aug. 2005), pp. 3987–3999.

[174] Seiji Katayama and Akira Matsunawa. “Solidification microstructure of laser welded stainless steels”. en. In: *International Congress on Applications of Lasers & Electro-Optics* 1984.2 (Sept. 2018). Publisher: Laser Institute of America LIA, p. 60.

[175] V. S. Raghunathan et al. “The influence of post weld heat treatments on the structure, composition and the amount of ferrite in type 316 stainless steel welds”. en. In: *Metallurgical Transactions A* 10.11 (Nov. 1979), pp. 1683–1689.

[176] B. Gill et al. “Transformation of Delta-Ferrite during the Postweld Heat Treatment of Type 316 L Stainless Steel Weld Metal”. In: (May 1986).

[177] Ghania BENCHABANE. “Les mécanismes de recristallisation et de croissance des grains dans les métaux et alliages métalliques légers”. en. phd. Université Mohamed Khider Biskra, 2009.

[178] Leifeng Liu et al. “Dislocation network in additive manufactured steel breaks strength–ductility trade-off”. en. In: *Materials Today* 21.4 (May 2018), pp. 354–361.

[179] C. Herrera, Ronald Lesley Plaut, and Angelo Fernando Padilha. “Microstructural Refinement during Annealing of Plastically Deformed Austenitic Stainless Steels”. en. In: *Materials Science Forum* 550 (2007). Conference Name: Fundamentals of Deformation and Annealing ISBN: 9780878494347 Publisher: Trans Tech Publications Ltd, pp. 423–428.

[180] Md. Shamsujjoha et al. “High Strength and Ductility of Additively Manufactured 316L Stainless Steel Explained”. en. In: *Metallurgical and Materials Transactions A* 49.7 (July 2018), pp. 3011–3027.

[181] Artem Aleksandrovich Voropaev et al. “Influence of Laser Beam Wobbling Parameters on Microstructure and Properties of 316L Stainless Steel Multi Passed Repaired Parts”. en. In: *Materials* 15.3 (Jan. 2022). Number: 3 Publisher: Multidisciplinary Digital Publishing Institute, p. 722.

[182] Yangyang Lei, Jun Xiong, and Rong Li. “Effect of inter layer idle time on thermal behavior for multi-layer single-pass thin-walled parts in GMAW-based additive manufacturing”. en. In: *The International Journal of Advanced Manufacturing Technology* 96.1 (Apr. 2018), pp. 1355–1365.

[183] Régis Henrique Gonçalves e Silva et al. “Analysis of Interlayer Idle Time as a Temperature Control Technique in Additive Manufacturing of Thick Walls by Means of CMT and CMT Pulse Welding Processes”. en. In: *Soldagem & Inspeção* 25 (Feb. 2020). Publisher: Associação Brasileira de Soldagem.

[184] Sergei Yu Ivanov et al. “Effect of Inter-Layer Dwell Time on Distortion and Residual Stresses of Laser Metal Deposited Wall”. en. In: *Key Engineering Materials* 822 (2019). Conference Name: New Materials and Technologies in Mechanical Engineering ISBN: 9783035716115 Publisher: Trans Tech Publications Ltd, pp. 445–451.

[185] M. Kumaran et al. “Influence of heat treatment on stainless steel 316L alloy fabricated using directed energy deposition”. en. In: *Materials Today: Proceedings*. International Conference on Emerging Trends in Material Science and Technology-2022 62 (Jan. 2022), pp. 5307–5310.

[186] Houshang Yin et al. “Thermal stability and microstructural evolution of additively manufactured 316L stainless steel by laser powder bed fusion at 500–800 ℃”. en. In: *Additive Manufacturing* 41 (May 2021), p. 101981.

[187] S. C. Dexter and G. Y. Gao. “Effect of Seawater Biofilms on Corrosion Potential and Oxygen Reduction of Stainless Steel”. In: *Corrosion* 44.10 (Oct. 1988), pp. 717–723.

[188] Chantal Compere and Nathalie Lebozec. “Behaviour of stainless steel in natural seawater”. In: Dec. 1997.

[189] C. Marconnet et al. “Comportement d’aciers inoxydables en eaux naturelles”. fr. In: *Matériaux & Techniques* 93 (2005). Publisher: EDP Sciences, s.83–s.90.

[190] D. Féron. *Marine Corrosion of Stainless Steels*. en. Ed. by D. Féron. 1st ed. CRC Press, Apr. 2021.

[191] W. H. Dickinson, F. Caccavo, and Z. Lewandowski. “The ennoblement of stainless steel by manganic oxide biofouling”. en. In: *Corrosion Science* 38.8 (Aug. 1996), pp. 1407–1422.

[192] Cyril Marconnet et al. “Stainless steel ennoblement in freshwater: From exposure tests to mechanisms”. en. In: *Corrosion Science* 50.8 (Aug. 2008), pp. 2342–2352.

[193] Isabelle Dupont, Damien Féron, and Georges Novel. “Effect of glucose oxidase activity on corrosion potential of stainless steels in seawater”. en. In: *International Biodeterioration & Biodegradation* 41.1 (Jan. 1998), pp. 13–18.

[194] S Maruthamuthu et al. “Effects of microfouling and light/dark regimes on the corrosion potentials of two stainless alloys in seawater”. In: *Biofouling* 7.4 (Dec. 1993). Publisher: Taylor & Francis _eprint: https://doi.org/10.1080/08927019309386258, pp. 257–265.

[195] Kurissery R Sreekumari, Kanavillil Nandakumar, and Yasushi Kikuchi. “Bacterial attachment to stainless steel welds: Significance of substratum microstructure”. In: *Biofouling* 17.4 (Dec. 2001). Publisher: Taylor & Francis _eprint: https://doi.org/10.1080/08927010109378490, pp. 303–316.

[196] Kurissery R. Sreekumari, Kanavillil Nandakumar, and Yasushi Kikuchi. “Effect of Metal Microstructure on Bacterial Attachment: A Contributing Factor for Preferential MIC Attack of Welds”. en. In: OnePetro, Mar. 2004.

[197] M.A. Javed et al. “The effect of metal microstructure on the initial attachment of Escherichia coli to 1010 carbon steel”. In: *Biofouling* 29.8 (Sept. 2013). Publisher: Taylor & Francis _eprint: https://doi.org/10.1080/08927014.2013.820826, pp. 939–952.

[198] Magdalena Cortina et al. “Analysis of the Influence of the Use of Cutting Fluid in Hybrid Processes of Machining and Laser Metal Deposition (LMD)”. en. In: *Coatings* 8.2 (Feb. 2018). Number: 2 Publisher: Multidisciplinary Digital Publishing Institute, p. 61.

[199] Lei Yan et al. “Investigation of machining coolant residue cleaning methods for Ti6Al4V part fabrication through hybrid manufacturing process”. en. In: *Manufacturing Letters* 16 (Apr. 2018), pp. 10–13.

[200] José Luis Dávila et al. “Hybrid manufacturing: a review of the synergy between directed energy deposition and subtractive processes”. en. In: *The International Journal of Advanced Manufacturing Technology* 110.11 (Oct. 2020), pp. 3377–3390.

[201] Moses O. Oyesola et al. “Hybrid-additive manufacturing cost model: A sustainable Through-Life Engineering support for Maintenance Repair Overhaul in the Aerospace”. en. In: *Procedia Manufacturing*. Proceedings of the 8th International Conference on Through-Life Engineering Services – TESConf 2019 49 (Jan. 2020), pp. 199–205.

[202] J. P. M. Pragana et al. “Hybrid metal additive manufacturing: A state–of–the-art review”. en. In: *Advances in Industrial and Manufacturing Engineering* 2 (May 2021), p. 100032.

[203] Zhipeng Pan, Yixuan Feng, and Steven Y. Liang. “Material microstructure affected machining: a review”. en. In: *Manufacturing Review* 4 (2017). Publisher: EDP Sciences, p. 5.

[204] Yusuf Kaynak and Ozhan Kitay. “Porosity, Surface Quality, Microhardness and Microstructure of Selective Laser Melted 316L Stainless Steel Resulting from Finish Machining”. en. In: *Journal of Manufacturing and Materials Processing* 2.2 (June 2018). Number: 2 Publisher: Multidisciplinary Digital Publishing Institute, p. 36.

[205] V. B. Vukkum and R. K. Gupta. “Review on corrosion performance of laser powder-bed fusion printed 316L stainless steel: Effect of processing parameters, manufacturing defects, post-processing, feedstock, and microstructure”. en. In: *Materials & Design* 221 (Sept. 2022), p. 110874.

[206] Sepehr Sadeh et al. “Interlayer machining effects on microstructure and residual stress in directed energy deposition of stainless steel 316L”. en. In: *Journal of Manufacturing Processes* 94 (May 2023), pp. 69–78.

[207] Francesco Careri et al. “Machining and heat treatment as post-processing strategies for Ni-superalloys structures fabricated using direct energy deposition”. en. In: *Journal of Manufacturing Processes* 61 (Jan. 2021), pp. 236–244.

[208] C. Herrera, Ronald Lesley Plaut, and Angelo Fernando Padilha. “Microstructural Refinement during Annealing of Plastically Deformed Austenitic Stainless Steels”. en. In: *Materials Science Forum* 550 (2007). Publisher: Trans Tech Publications Ltd, pp. 423–428.

[209] Sara Bagherifard et al. “Nanoscale surface modification of AISI 316L stainless steel by severe shot peening”. en. In: *Materials & Design* 102 (July 2016), pp. 68–77.

[210] Hongtu Xu et al. “In-situ hot rolling directed energy deposition-arc repair of shafts”. en. In: *Additive Manufacturing* 61 (Jan. 2023), p. 103362.

[211] Erfan Maleki et al. “The effects of shot peening, laser shock peening and ultrasonic nanocrystal surface modification on the fatigue strength of Inconel 718”. en. In: *Materials Science and Engineering: A* 810 (Apr. 2021), p. 141029.

[212] W. W. Deng et al. “Effect of laser shock peening on tensile properties and microstructure of selective laser melted 316L stainless steel with different build directions”. en. In: *Materials Science and Engineering: A* 850 (Aug. 2022), p. 143567.